

**MODELING MUNICIPAL SOLID
WASTE GASIFICATION: MOLECULAR-LEVEL
KINETICS AND SOFTWARE TOOLS**

by

Scott Ryan Horton

A dissertation submitted to the Faculty of the University of Delaware in partial fulfillment of the requirements for the degree of Doctor of Philosophy in Chemical Engineering

Spring 2016

© 2016 Scott Ryan Horton
All Rights Reserved

ProQuest Number: 10156547

All rights reserved

INFORMATION TO ALL USERS

The quality of this reproduction is dependent upon the quality of the copy submitted.

In the unlikely event that the author did not send a complete manuscript and there are missing pages, these will be noted. Also, if material had to be removed, a note will indicate the deletion.



ProQuest 10156547

Published by ProQuest LLC (2016). Copyright of the Dissertation is held by the Author.

All rights reserved.

This work is protected against unauthorized copying under Title 17, United States Code
Microform Edition © ProQuest LLC.

ProQuest LLC.
789 East Eisenhower Parkway
P.O. Box 1346
Ann Arbor, MI 48106 - 1346

**MODELING MUNICIPAL SOLID
WASTE GASIFICATION: MOLECULAR-LEVEL
KINETICS AND SOFTWARE TOOLS**

by

Scott Ryan Horton

Approved: _____
Abraham M. Lenhoff, Ph.D.
Chair of the Department of Chemical & Biomolecular Engineering

Approved: _____
Babatunde A. Ogunnaike, Ph.D.
Dean of the College of Engineering

Approved: _____
Ann L. Ardis, Ph.D.
Senior Vice Provost for Graduate and Professional Education

I certify that I have read this dissertation and that in my opinion it meets the academic and professional standard required by the University as a dissertation for the degree of Doctor of Philosophy.

Signed:

Michael T. Klein, Sc.D.
Professor in charge of dissertation

I certify that I have read this dissertation and that in my opinion it meets the academic and professional standard required by the University as a dissertation for the degree of Doctor of Philosophy.

Signed:

Francis P. Petrocelli, Ph.D.
Member of dissertation committee

I certify that I have read this dissertation and that in my opinion it meets the academic and professional standard required by the University as a dissertation for the degree of Doctor of Philosophy.

Signed:

Dionisios G. Vlachos, Ph.D.
Member of dissertation committee

I certify that I have read this dissertation and that in my opinion it meets the academic and professional standard required by the University as a dissertation for the degree of Doctor of Philosophy.

Signed:

April M. Kloxin, Ph.D.
Member of dissertation committee

I certify that I have read this dissertation and that in my opinion it meets the academic and professional standard required by the University as a dissertation for the degree of Doctor of Philosophy.

Signed:

Prasad S. Dhurjati, Ph.D.
Member of dissertation committee

ACKNOWLEDGMENTS

First and foremost, I would like to acknowledge my advisor, Professor Michael T. Klein. His support and direction was invaluable during this thesis work. Mike was a great advisor. He simultaneously kept me on track, in terms of graduating, while allowing for enough freedom to encourage creativity. He also actively encouraged professional development which allowed me to do two internships: at Air Products then later at Aspen Technology. When each of these opportunities came up, his comment was the same both times: “I’ve found that internships are beneficial to both the students and the companies.” This statement, in a way, summarizes his selfless style of advising. His actions and decisions have consistently been in my best interest. I am looking forward to continuing work with Mike for the next year as a post-doc.

I would like to acknowledge my collaborators at Air Products: Rebecca Mohr, Yu Zhang, and Frank Petrocelli. Rebecca helped keep the MSW gasification project grounded and going in a useful direction. Working with Rebecca helped also helped hone my technical writing skills and, more importantly, the ability to write to a larger audience. Yu Zhang’s feedback and guidance helped in using the MSW gasification model for the plasma-arc gasifier especially in the development of the coke gasification model. Frank was a great mentor, and was really like a second advisor on the gasification project. He has continued his guidance through the dissertation by agreeing to be on my thesis committee.

I would also like to acknowledge the academic members of my thesis committee: Dionisios Vlachos, April Kloxin, and Prasad Dhurjati. Their feedback

helped to improve my dissertation and our discussions provided interesting areas for future work in MSW gasification. Dion provided guidance as an expert in catalysis, kinetics, and biomass pyrolysis. My meetings with both Dion and members of his group have often inspired new ideas for modeling techniques and future model development. Historically, our research group hasn't done much work with plastics; April provided great insight for the MSW gasification model as a polymer expert. Prasad provided great out-of-the-box discussion in both my qualifying exam and committee meeting.

I would like to thank my research group. Craig Bennett and Zhen Hou are long-term group members and are the real experts of our software tools, and without their guidance, this dissertation would have been impossible. Craig was, and will continue to be, my go-to expert for software discussion. Brian Moreno was my first true collaborator in the group; he was my first 'user' and target audience for many of my software apps. Linzhou Zhang, a visiting scholar, was an amazing collaborator on our work with resid; his sheer rate of productivity is an inspiration to this day. Juan Lucio is my partner in crime in the shift of our group's focus to 'app development'; Juan is also the driving force behind the next big revision of our tools. Triveni Billa continues to be a joy to work with and is my role model when it comes to work-life balance. The newest member of our group is Pratyush Agarwal. He has helped a great deal in editing my papers, and I look forward to collaborating with him on his thesis work. I could not have asked to work with a better group of people.

One of the amazing things about my research group is that every member started as a colleague but became a friend. Chatting and getting lunch with Brian, Craig, and Zhen (initially) and later Linzhou, Prat, Juan was one of the things that I

looked forward to most at work. When traveling to India, I really got to know Triveni by spending time with her family in her hometown. Recently, I was fortunate enough to visit Linzhou in Beijing where he is an aspiring lecturer at his university. Luckily, I am staying on as a post-doc, but when I do leave the group I will miss every one of my group members.

I would also like to thank my classmates and friends in the chemical engineering department. Specifically, I would like to thank Marguerite Mahoney. Her tireless work makes many events for our research group and the UDEI possible. She often goes above and beyond the call of duty to be helpful.

Finally, I would like to thank my family. My parents, Joe and Linda Horton, for raising encouraging me in all of life's decisions; they have been my role models for as long as I can remember. My siblings, Derek and Leanna, for always paving the way; hopefully continuing forward into the working world. Hannah, for her support during both the good and hard times that come with grad school. Her adventuresome spirit always encourages me to never be complacent: to go new places, try new things; this mentality is certainly reflected in my research and this dissertation.

TABLE OF CONTENTS

LIST OF TABLES	xiii
LIST OF FIGURES	xviii
ABSTRACT	xxvii

Chapter

1	INTRODUCTION	1
1.1	Municipal Solid Waste: Burden or Resource?	1
1.2	Waste-to-Energy Technologies	3
1.3	Plasma-Arc Gasification.....	5
1.4	MSW Gasification Modeling	8
1.5	Research Objectives	12
1.6	Dissertation Scope	13
2	MOLECULAR-LEVEL KINETIC MODELING IN THE KINETIC MODELER'S TOOLKIT	16
2.1	Material Balance.....	16
2.2	Initial Conditions from the Composition Model Editor	17
2.2.1	Computational Representation of Molecules	19
2.3	Reaction Network Constructed using the Interactive Network Generator	19
2.3.1	Reaction Families	20
2.3.2	History of Reaction Network Generation in KMT	22
2.3.2.1	Computational Representation of Reactions	25
2.4	Equations Written, Solved, and Optimized using the Kinetic Model Editor	26
2.4.1	Reactor Type	27
2.4.2	Rate Laws and Linear Free Energy Relationships	28
2.4.3	Model Solution	30

2.4.4	Kinetic Parameter Optimization	31
2.5	Summary.....	33
3	MOLECULAR-LEVEL KINETIC MODELING OF THE GASIFICATION OF COMMON PLASTICS	35
3.1	Abstract.....	36
3.2	Introduction	37
3.3	Molecular Representation of Plastics	39
3.3.1	Flory-distributed Linear Polymers	40
3.3.2	Gamma-distributed Linear Polymers	41
3.4	Reaction Chemistry of Gasification of Plastics.....	42
3.4.1	Depolymerization	42
3.4.1.1	Random Scission of Flory Polymers	43
3.4.1.2	Random Scission Method for a Generalized Polymer Size Distribution.....	44
3.4.1.3	Depolymerization Chemistry – PE.....	49
3.4.1.4	Depolymerization Chemistry – PET	50
3.4.1.5	Depolymerization Chemistry – PVC.....	51
3.4.1.6	Depolymerization Chemistry – PS	53
3.4.2	Pyrolysis of Oligomers	54
3.4.3	Gasification of Oligomers	57
3.5	Network Generation	58
3.6	Model Equations and Kinetics.....	59
3.7	Model Evaluation	61
3.7.1	Model Evaluation – PE.....	61
3.7.2	Model Evaluation – PET	64
3.7.3	Model Evaluation – PVC.....	67
3.7.4	Model Evaluation – PS.....	69
3.7.5	Reaction Family Rate Constants	70
3.8	Conclusions	72
4	MOLECULAR-LEVEL KINETIC MODELING OF BIOMASS GASIFICATION	73
4.1	Abstract.....	74

4.2	Introduction	75
4.3	Molecular Representation of Biomass.....	78
4.3.1	Linear Polymer Composition Models: Cellulose and Hemicellulose	79
4.3.2	Cross-linked Polymer Composition Model: Lignin	83
4.3.3	Combined Biomass Composition Model.....	94
4.4	Reaction Chemistry of Biomass Gasification.....	96
4.4.1	Cellulose and Hemicellulose	97
4.4.1.1	Depolymerization	97
4.4.1.2	Pyrolysis	104
4.4.1.3	Gasification.....	106
4.4.2	Lignin	107
4.4.2.1	Interconversion of Attributes.....	107
4.4.2.2	Core Reactions.....	107
4.4.2.3	Linkage and Side Chain Reactions.....	108
4.4.2.4	Light Gas Reactions	109
4.5	Network Generation	110
4.6	Model Equations and Kinetics.....	111
4.7	Model Evaluation	114
4.8	Tar Prediction and Reaction Family Analysis.....	117
4.9	Kinetic Rate Constants	120
4.10	Conclusions	121
5	IMPLEMENTATION OF A MOLECULAR-LEVEL KINETIC MODEL FOR PLASMA-ARC MUNICIPAL SOLID WASTE GASIFICATION	123
5.1	Abstract.....	124
5.2	Introduction	124
5.3	Kinetic Model Development of Municipal Solid Waste Gasification...	129
5.3.1	MSW Composition Model	129
5.3.2	Reaction Chemistry and Network	132
5.3.3	Kinetic Model Details.....	135
5.4	Kinetic Model Development of Coke Gasification	135
5.4.1	Coke Structure and Composition.....	135

5.4.2	Gasification Reactions of Coke	136
5.4.3	Reaction List and Rate Laws	138
5.4.4	Intrinsic Kinetics and Diffusional Limitations	140
5.4.5	Analysis of Kinetics in Coke Bed	142
5.5	Reactor Simulation of Plasma-arc Gasifier	145
5.5.1	MSW Gasification I/O Converter	146
5.6	Trending Studies	149
5.7	Summary and Conclusions	156
6	MOLECULAR-LEVEL KINETIC MODELING OF RESID PYROLYSIS	158
6.1	Abstract	159
6.2	Introduction	160
6.3	Molecular Representation of Resid	163
6.4	Feedstock Composition	166
6.5	Reaction Chemistry	170
6.6	Network Generation	174
6.7	Model Equations	175
6.8	Kinetics	178
6.9	Model Evaluation	179
6.10	Conclusions	187
7	ENHANCING THE USER-MODEL INTERFACE THROUGH THE DEVELOPMENT OF SOFTWARE APPS	188
7.1	Increasing the Scientific and Mathematical Understanding of the Model through Apps	193
7.1.1	Reaction Network Visualizer	199
7.1.2	KME Results Analyzer	204
7.2	Enabling the Usage of Model to Predict Measured Outputs from Measured Inputs	209
7.2.1	MSW Gasification I/O Converter	210
7.2.2	Naphtha Reforming I/O Converter	211
7.3	Furthering Kinetic Model Development Capabilities	212
7.3.1	KME Flowsheet Application	214
7.3.2	TGA Simulator	217

7.3.3	Physical Property Database Interface	220
7.4	Current and Future App Development	226
7.4.1	Data Audit Application.....	226
7.4.2	Update of User Interfaces	228
7.5	Summary.....	229
8	SUMMARY AND CONCLUSIONS.....	230
8.1	Summary and Conclusions	230
8.2	Recommendations for Future Work	232
8.2.1	MSW Composition.....	232
8.2.1.1	Individual Polymer Composition	232
8.2.1.2	Combined Composition of MSW	234
8.2.2	Parameter Tuning and Confidence Intervals	235
8.2.3	Optimizing Experimental Data for Molecular Models.....	237
8.3	Closing Remarks on MSW Gasification	238
	REFERENCES	239
	Appendix	
	PUBLISHED WORK COPYRIGHT CLEARANCE PERMISSIONS	252

LIST OF TABLES

Table 1.1: Leach tests on vitrified slag. Table reproduced from source material. [6]....	5
Table 2.1: Reaction families added by Bennett[44] and Moreno[45] to INGen.	24
Table 2.2: The two types of measurements in the objective function.	32
Table 3.1: Experimental and predicted ultimate analyses for PE, PVC, and PET. The literature values are from Arena et al.[23] for PE, Heikkinen et al[63] for PET, and Zhu et al. for PVC[64]. The Xn' s for these results are 291, 998, and 5 for PE, PET, and PVC respectively.....	41
Table 3.2: Literature measurements for polystyrene and corresponding gamma predictions. Mw was reported in Liu et al[67], approximate literature PDI values were used to approximate Mn . The gamma parameters for these values were calculated to be: $a = 13037.43$, $d = 20$	42
Table 3.3: Probability of bonds broken within a 4-mer.....	46
Table 3.4: Description of terms Equation 3.11. The notation is <i>mrow, column</i> for the breakdown matrix. The row corresponds to total number of bonds breaking in the <i>i-mer</i> . The column corresponds to the production of smaller <i>j-mers</i> from the breakdown of <i>i-mer</i>	48
Table 3.5: Stable radicals and products from included mechanisms in polystyrene degradation.	54
Table 3.6: Pyrolysis cracking reaction families, reaction matrices, and example reactions. The reaction matrix contains -1 for bond-breaking and -1 for bond-making during reaction.....	55
Table 3.7: Pyrolysis reactions used to build aromatic, polyaromatic char molecules..	56
Table 3.8: Gasification reactions included in the model. The reversibility of light gas reactions was determined based on the equilibrium constants at reactor conditions.	57
Table 3.9: Reaction network diagnostics for the plastics model.	59

Table 3.10: Utilized experiments from Arena et al[23].	62
Table 3.11: HCl and char from all experiments in Slapak et al.[82] Q1 and Q2 are uncatalyzed (quartz sand bed). A1, A2, and all A3 experiments were under alumina support. *- data points not used in char analysis due to catalyst effects on char formation.	68
Table 3.12: Experimental weight percent values for monoaromatics, diaromatics and triaromatics in pyrolysis output at different temperatures[67]. All values are in weight percent of initial polystyrene.	70
Table 3.13: Reaction family rate constants at 1000 K relative to Acyclic Thermal Cracking. $\log(k)_{\text{relative},1000} = \log(k)_{\text{AcyclicThermalCracking},1000} - \log(k)_{\text{ReactionFamily},1000}$.	71
Table 4.1: Ultimate analysis of cellulose samples in Chang et al. (2011)[99].	81
Table 4.2: Comparison between experimental data and predictions from the Linear Polymer Composition Editor. Experimental data came from Chang et al.[99] and Couhert et al.[100], [101] for cellulose and hemicellulose, respectively. The simulated average degree of polymerizations for cellulose and hemicellulose were 232 and 5.	83
Table 4.3: C9 units of Lignin[103].	84
Table 4.4: Attribute Identities as parsed by CME from the Freudenberg model for lignin.	87
Table 4.5: Mole fraction calculation from sampled molecules.	89
Table 4.6: Experimental Data used in the optimization of the lignin compositional model. All data are from Hage et al. (2009)[104].	90
Table 4.7: Adjustable parameters in optimization. *obtained by difference, not an adjustable parameter. In simulations 1 and 2, bolded terms were optimized on.	92
Table 4.8: Experimental data currently used in the optimization of the lignin compositional model. All data are from Hage et al. (2009)[104]. The data shown here is a subset of data reported; CME adjustments are required to make use of more data.	93
Table 4.9: Ultimate analysis for each subcomponent of biomass from preceding sections.	94

Table 4.10: Biomass splits for each of the biomasses under study by Li et al.[13] SPF is spruce, pine, fir mixed sawdust. PS is 50% each of pine bark and spruce whitewood mix.....	96
Table 4.11: Depolymerization reactions representing conversion of attribute representation to molecular representation for linear polymers.	101
Table 4.12: Depolymerization reaction rate laws representing conversion of attribute representation to molecular representation for hemicellulose.	102
Table 4.13: Depolymerization reaction rate laws representing conversion of attribute representation to molecular representation for cellulose.	103
Table 4.14: Pyrolysis reactions used to breakdown cellulose and hemicellulose into small molecules.	105
Table 4.15: Pyrolysis reactions used to build aromatic, polyaromatic char molecules.....	106
Table 4.16: Gasification reactions in hemicellulose and cellulose networks.	107
Table 4.17: IL and SC gasification to hydrogen side chains to retain stable cores.	109
Table 4.18: Thermodynamic details of the specific gas-phase reactions. Superscripts represent temperatures (K).	109
Table 4.19: Reaction network diagnostics for the biomass model.....	111
Table 4.20: Analysis of adjustable parameters and constraints in the model.....	113
Table 4.21: Biomass type, temperature, and gas composition for each utilized experimental run from Li et al (2004). For biomass type, the abbreviations are Cyp – cypress, hem – hemlock, SPF- spruce, pine, fir. PS – pine, spruce.	115
Table 4.22: Observed and predicted values for data sets in Li et al. All values in the table are in mol/s.	116
Table 4.23: Weight fraction of tar in output stream for all data sets.....	118
Table 4.24: Rate constants at 1000K relative to Acyclic Thermal Cracking. $\log(k)_{\text{relative},1000} = \log(k)_{\text{AcyclicThermalCracking},1000} - \log(k)_{\text{ReactionFamily},1000}$. Reaction families that were assumed to be equilibrated are not included in the table.	121

Table 5.1: Pyrolysis reaction families in MSW gasification. These families include both categories of pyrolysis chemistry: cracking and tar-formation. This table was adapted from tables in prior work[54], [83].	133
Table 5.2: Included gasification reactions. Table is directly from Horton et al[54].	134
Table 5.3: Ultimate analysis of coke fed to the gasifier.	136
Table 5.4: Reaction network for the coke gasification model. Definitions: $cR = CO/CO_2$ ratio, r_{net} is the net rate taking into account both intrinsic kinetics and diffusional limitations. C_0, H_0, S_0, N_0 are the relative initial amounts of each element in the coke (Units in either Mol/s or Mol/L).	140
Table 5.5: Comparison of MSW compositions. All data points used equivalence ratio of 0.3. The syngas flow rate was defined as the flow rate sum of CO, CO ₂ , H ₂ , and CH ₄ . Relative syngas flow rate was the ratio of the flow rate to minimum flow rate amount the data sets.	154
Table 6.1: The mole fraction calculation for selected molecules from attributes. P_{core} , P_{IL} , and P_{SC} represent the three attribute PDFs. P_{BS} and P_{CS} represent the binding site and cluster size distributions.	164
Table 6.2: Number of molecules for the two common sampling methods for different cluster sizes using 100 cores, 2 linkages, and 50 side chains.	165
Table 6.3: Cracking reaction families, sites, matrices, and examples. These details are discussed in the PhD Thesis by Zhang[130]. The reaction matrices define the bond making (1) and bond breaking (-1) in a reaction type.	172
Table 6.4: Aromatization reaction families, sites, matrices, and examples for aromatization reactions. These details are discussed in the PhD Thesis by Zhang[130].	173
Table 6.5: Reaction network diagnostics including total number of reactions, attributes, and irreducible molecules. These details are discussed in the PhD Thesis by Zhang[130].	175
Table 6.6: Experimental data for resid pyrolysis at 500 °C and 0.101 MPa for 40 minutes. All data were collected at the State Key Laboratory of Heavy Oil Processing, China University of Petroleum.	180

Table 6.7: Total error and error associated with experiments and quantitative structure property correlations for the measurements in the objective functions. Values for error were estimated based on experience in our prior work[46] with similar data in the objective function.	182
Table 6.8: Tuned parameters for kinetic model for each reaction family. $a_j = \ln(A_j) - E_{0(j)}/RT$ and $b_j = -\alpha_j/RT$. For aromatic ring condensation, α_j is the scaling factor, as shown in Equation 6.7. The value for the gas constant used is $R = 1.987 \times 10^{-3}$ kcal/(mol*K) and $T = 773$ K.....	184
Table 7.1: The types and goals of kinetic model users.....	189
Table 7.2: The categories of apps as organized by objective, corresponding design method, and a list of apps developed	192
Table 7.3: The KMT software supported by each App discussed in this thesis.....	193
Table 7.4: Information types, relevant KMT software, how the information is organized, and how well the user comprehends the information. *the comprehension of the reaction network depends on the network size. .	198
Table 7.5: Ethane pyrolysis reaction network before and after seeding.....	204
Table 7.6: Reaction rate information from KME.	205
Table 7.7: Apps excluded from the current chapter.	213
Table 7.8: Block Types and Descriptions included in KME Flowsheet Application.	216
Table 7.9: Some common molecules divided into Benson Groups and predicted heats of formation versus the values found in the NIST database.	222
Table 7.10: Order of preference for sources of molecular properties.	223
Table 7.11: Inputs, observed quantities, minimum and possible values at reactor outlet, and whether a heuristic returns a red flag.	227
Table 8.1: Experimental[64] and predicted ultimate analyses for PVC. Also given are the ultimate analyses if the for a monomer and infinite polymer, and pure polyene structure. The partially depolymerized polymer was 93.6% PVC repeat units with 6.4% polyene repeat units.....	233

LIST OF FIGURES

Figure 1.1: MSW management technologies from 1960-2013. Figure from source material[1].	2
Figure 1.2: Net energy to grid per ton of MSW. Figure reproduced from source material[6].	4
Figure 1.3: Alter NRG Plasma Gasifier. Image from source[6].....	7
Figure 1.4: MSW breakdown in 2013 for the United States[1]. This composition represents the discarded (<i>i.e.</i> , post-recycling) MSW.....	8
Figure 1.5: Urban and rural MSW waste descriptions in the United Kingdom[25].....	8
Figure 1.6: Artificial Neural Net from Xiao and coworkers. Image directly from source material[37].....	11
Figure 2.1: CME Optimization loop which converts available experimental measurements to a molecular composition.	18
Figure 2.2 Bond electron matrix representation of propan-1-ol from Moreno[45]. Figure from source material.	19
Figure 2.3: Generalized Alcohol Dehydration Reaction.	21
Figure 2.4: Cellulose monomer, glucose.	21
Figure 2.5: alcohol dehydration of propan-1-ol to propene and water.	25
Figure 2.6: Chemical reaction as a matrix operation for propan-1-ol dehydration. Figure from source material[45].....	26
Figure 2.7: Separation of the full bond electron matrix post-reaction into product molecules.	26
Figure 2.8: Figure from Horton and Klein[47]. (a) Figure reproduced Mochida and Yoneda[49] showing the dealkylation of alkylaromatics reaction family on a SA-1-Na-3 catalyst. The numbers represent experimental rates of dealkylation on different alkyl aromatics.	30

Figure 2.9: Example parity plot for the pyrolysis of naphtha for an experimental carbon number distribution. Figure from source material[42].	33
Figure 3.1: Plastics generation and recovery from the EPA report on Municipal Solid Waste (MSW)[1].	37
Figure 3.2: Repeat Unit Structures for PE, PVC, PET, and PS (Left to Right).	39
Figure 3.3: Conceptual goal of random scission for a generalized polymer size distribution. Top and bottom figures are representative n-mer distributions.	45
Figure 3.4: Illustration (top) and breakdown matrix representation (bottom) of possible bond breaking events in a 4-mer. Values in the matrix are relative initial amount of 4-mer.	47
Figure 3.5: Radical propagation steps for polyethylene depolymerization. The H-abstraction step shown here is inter-molecular and can occur with any radical in the system.	49
Figure 3.6: Oligomers with 6-carbons produced during polyethylene depolymerization. These are the starting molecules from polyethylene for the full pyrolysis and gasification network.	50
Figure 3.7: Link cleavage in polyethylene terephthalate (concerted mechanism).	51
Figure 3.8: Two-step depolymerization of polyvinyl chloride.	52
Figure 3.9: Tuning results for all data sets. The linear fit has the equation $y_{\text{predicted}}=0.952*y_{\text{experimental}}+0.0036$. Tar yield is in units of (g/s/25); it was rescaled to have a similar value as the light gas flow rates (mol/s).	63
Figure 3.10: Comparison of experimental and model predicted results for liquid/gas ratio (mass basis) for all data sets.	63
Figure 3.11: Experimental error and the effects of temperature deviation in model predictions for Run 6. Effects of a 10 degree temperature variation are shown using error bars.	64
Figure 3.12: Logic for the TGA Simulator C# application	65

Figure 3.13: TGA model results (lines) compared with experiment (points). Colors correspond to different heating rates: red, 5 °C/min; green, 10 °C/min; blue, 20 °C/min; orange, 40 °C/min. The left plot gives the TGA curves, the right plot is a parity plot of the results. The maximum decomposition rates in units of wt%/°C are 0.018, 0.17, 0.015, and 0.041 in order of increasing heating rate.	66
Figure 3.14: TGA Simulator results showing persistence of char in the absence of oxygen for PET depolymerization at a heating rate of 40 °C/min.	67
Figure 3.15: Results for HCl (all runs) and Char (only Q1 and Q2). The outlet flow rate units for HCl and char are in mol/s and g/s/50 respectively.	69
Figure 3.16: Parity plot for monomer-trimer predictions for polystyrene pyrolysis. A least-squares linear fit of the data gives $y_{\text{predicted}} = 0.9595y_{\text{experimental}} + 0.0217$	70
Figure 4.1: Literature lumped kinetic models. (Left) Sequential lumped model[86] of biomass gasification. (Right) parallel lumped model of biomass gasification where V_1 - V_5 are lumped volatile products.[87]	76
Figure 4.2: Cellulose polymeric n-mer of β 1 \rightarrow 4 linked D-glucose units (Left). Hemicellulose representation as an n-mer of poly-xylan (Right).	79
Figure 4.3: Linear Polymer Composition Editor optimization loop.....	82
Figure 4.4: Adapted Freudenberg Structure[102]. This structure was parsed to yield the attribute identities.	85
Figure 4.5: Binding site types on the phenol core.	88
Figure 4.6: Logic of MSW Bulk Composition solver applied for biomass. All numbers in this figure are in wt%. The plastics and carbon support segments of the figure are truncated as the weight fraction within biomass is 0 for each. *-Lignin fraction is dependent on cellulose and hemicellulose.	95
Figure 4.7: Cellulose Depolymerization Pathways.	98
Figure 4.8: Complete cracking of a cellulose 4-mer showing final monomeric products.	98
Figure 4.9: Starting molecules of full cellulose pyrolysis network: linear levoglucosan (left) and linear glucose (right).....	99

Figure 4.10: Depolymerization pathways for hemicellulose.....	100
Figure 4.11: Linear forms of anhydro-xylopyranose (left) and xylose (right). These are the starting point of the full pyrolysis network.	100
Figure 4.12: Example of stepwise gasification reactions of cores. Each reaction is written for both incomplete combustion and steam reforming. The alternate reactions where the phenol ring is gasified first were also written.....	108
Figure 4.13: Parity plot of tuned data sets for Li et al data. After a linear fit, the formula comparing experiment to model results is $y_{\text{predicted}}=y_{\text{obs}}*0.928+0.0003$. The R^2 relative to $y=x$ is 0.918 for the tuned data sets.	116
Figure 4.14: All viable datasets from Li et al (2004) using tuned parameters from data sets 3, 4, and 11. Squares represent tuned results, circles are predicted results. After a linear fit, the formula comparing experiment to model results is $y_{\text{predicted}}=y_{\text{obs}}*0.989-0.007$. The R^2 relative to $y=x$ is 0.861 for all data sets.....	117
Figure 4.15: Tar weight fraction as a function of the ratio of dry biomass to supplied oxygen (blue, left axis). The fraction of CO and H ₂ in overall dry syngas (nitrogen excluded) is also shown (orange, right axis).	119
Figure 4.16: Relative importance of reaction families in the reactor model integration for Data Set 11. All analysis was done using an in-house C# application, <i>KME Results Analyzer</i>	120
Figure 5.1: MSW management technologies from 1960-2013. Figure from source material[1].	125
Figure 5.2: Average landfill tipping fees in the US 1982-2013. Prices are in USD.[1]	126
Figure 5.3: MSW Fractions in the United States in 2013. A. Overall fractions as reported by the EPA. B. MSW divided into four categories. The biomass-derived category includes food, wood, yard trimmings, textiles, and paper. The ‘not modeled’ category includes metals, glass, other, and rubber and leather. C. the cellulose hemicellulose and lignin splits predicted in prior work[83] using data from Li and coworkers[13]. D. The relative amounts of included plastics, renormalized from EPA data[1].	130

Figure 5.4: Screenshot from the MSW Bulk Composition Solver. In this screen, the checkboxes on the left allow the user to select which fractions are adjusted during the optimization procedure.	131
Figure 5.5: Comparison of initial reaction rates for 4” (top) and 6” (bottom) particles for gasification with oxygen. Data labels give values for diffusion limitations at 1200K to show comparison in particle sizes....	143
Figure 5.6: Damköhler number as a function of temperature for 4” and 6” particles.	144
Figure 5.7: Reaction rate contributions as a function of temperature for CO ₂ gasification from the Cupula Handbook[121]. In the low temperature region (w ₁), kinetic limitations dominate. The middle range temperatures, w ₂ , both kinetics and diffusion contribute to the overall rate. At high temperatures (w ₃), diffusional limitations dominate.	145
Figure 5.8: Gasification unit depiction from Young[6] (left) and conceptual organization of idealized reactors for each reaction zone(right).	145
Figure 5.9: Screenshot of the main screen from the MSW Gasification I/O Converter. Measurable process inputs are on the left, the reactor layout is given in the diagram, and measurable process outputs are on the right.....	147
Figure 5.10: Edit MSW Composition window within the MSW User Friendly Gasification Model.	149
Figure 5.11: Tar composition analysis screen in the MSW Gasification I/O Converter.	149
Figure 5.12: Relative tar fraction and relative syngas quality as a function of equivalence ratio. The tar fraction is defined as the weight fraction of species with boiling point greater than or equal to benzene. Syngas quality here is the mass ratio of CO+H ₂ to CO+H ₂ +CH ₄ +CO ₂	151
Figure 5.13: Tar composition leaving the freeboard zone. Left: overall tar molecule mass fractions. Right: composition of lignin tar molecules.	152
Figure 5.14: Seasonal Dependence of UK MSW, winter and summer[25].	153
Figure 5.15: Comparison of Tar Compositions for different MSW compositions: Left(UK-Summer), Right(Synthesized 2).	154

Figure 5.16: Effect of α on relative syngas quality (orange) and tar flow rate (blue) at equivalence ratios of 0.4 (top) and 0.3 (bottom).	155
Figure 6.1: Comparison of Attribute Reaction Modeling and Conventional Modeling methods.	162
Figure 6.2: Example resid molecule and attribute groups: cores (blue), inter-core linkages (red), and side chains (green).	163
Figure 6.3: Differences in binding sites for complete sampling and main methyl method.	166
Figure 6.4: Examples of both hydrocarbon and heteroatom-containing core attributes.	167
Figure 6.5: The four side chain types and two inter-core linkages. The side chain types are, top-to-bottom, n-alkyl, iso-alkyl, carboxylic acid, and sulfide.	167
Figure 6.6: Side chain (left) and Inter-core linkage (right) PDFs. The side chain PDF is only shown for n-alkyl side chains (normalized to 1). Similar PDFs can be created for the other side chain types.	168
Figure 6.7: Selected cores from the core PDF, mole fractions normalized for the selected cores.	169
Figure 6.8: Binding site (left) and cluster size (right) PDFs for feedstock composition. Results are from model presented by Zhang et al.[46]....	169
Figure 6.9: Molecular weight distribution of the sampled molecules. Figure reproduced from attribute distributions in Zhang et al[46].	170
Figure 6.10: Most stable cracking pathways for an alkyl aromatic.	171
Figure 6.11: Aromatic ring condensation example reaction.	174
Figure 6.12: Conversion of continuous attribute pdfs to discrete PDFs during the generation of initial conditions for the reactor kinetic model.	177
Figure 6.13: The alteration of attribute PDFs through model solution.	178

Figure 6.14: Parity plot comparing experimental and predicted results. The $y=x$ line corresponds to exact prediction. All weight percent values were converted to weight fractions, the average molecular weight for gas-oil was normalized to be on the same scale as other data. The R^2 value relative to $y=x$ is 0.944.	183
Figure 6.15: Observed versus experimental including error bars for σ_{total} ; the error bars were chosen to be drawn on the experimental values. The average molecular weight for gas-oil was normalized to be on the same scale as other data.	184
Figure 6.16: Before (left) and After(right) distributions for MW, aromatic ring number, and naphthenic ring numbers.	186
Figure 7.1: Main software packages that make up the Kinetic Modeler's Toolkit	190
Figure 7.2: (Left) Typical lumped model of coal pyrolysis. (Right) Conceptual representation of the information complexity in coal pyrolysis versus simple lumped models.	194
Figure 7.3: Trade-offs of the comprehension and scientific rigor of models as a function of the number of equations.	195
Figure 7.4: Information sources and amounts within a molecular-level kinetic model. Values are relative and qualitative. The relatively low value for rate parameters is due to a linear free energy relationship (LFER) basis.	196
Figure 7.5: Sample screenshot from the Reaction Network Visualizer. Graph image rendered using GraphViz[132].	199
Figure 7.6: Reaction families and some example reactions from ethane pyrolysis. The primary form of mass increase from ethane is first via olefin addition reactions. Once large olefins form, Diels-alder additions allow for the formation of cyclic structures. Beta-scission can then lead to aromaticity and the product of interest, xylene.	201
Figure 7.7: Number of equations by rank in an ethane pyrolysis model with ethane as the only seed. The black dots represent the location of xylenes before and after seeding.	202
Figure 7.8: Some major reaction paths visualized using the Reaction Network Visualizer. Images rendered using GraphViz.	203

Figure 7.9: Full reaction network generation in a Naphtha Reforming model.	206
Figure 7.10: Reaction families responsible for the production of 3-methyldecane. ..	207
Figure 7.11: Visualization of Bulk Properties in the KME Results Analyzer.....	208
Figure 7.12: Window allowing the addition of bulk properties to the KME Results Analyzer. The bulk property added here is 1-3 ring aromatics.	209
Figure 7.13: Sample Screenshot from the MSW Gasification I/O Converter.....	210
Figure 7.14: Sample Screenshot from Naphtha Reforming I/O Converter	212
Figure 7.15: Sample screenshot from the KME Flowsheet Application. The flowsheet layout images in the KME Flowsheet Application are rendered using the open-source GraphViz software[132].....	214
Figure 7.16: Solution order of blocks in the example flowsheet.....	217
Figure 7.17: Conceptual Diagram of a Thermogravimetric Analysis experiment.	218
Figure 7.18: Selected screenshots from TGA Simulator. Upper Left: opening screen where user can select the KME model. Upper right: Experimental data Input. Lower Left: simulation settings. Lower right: results and comparison with experiments.....	219
Figure 7.19: TGA Simulator Logic. Image from source [54].	220
Figure 7.20: Boiling point options in TGA Simulator	220
Figure 7.21: Screenshot of Physical Property Database Interface.	224
Figure 7.22: Export molecule list window in the Physical Property Database Interface. The left side shows a search of the database for all species with 1 or more aromatic ring. The right side gives the current list of selected molecules and details on which properties are being exported.....	225
Figure 7.23: Basic reaction network layout for heuristic example.....	227
Figure 7.24: Comparison of user interfaces in Windows Forms Applications (Left, App: INGen Network Merge) and Windows Presentation Foundation (WPF, Physical Properties Database Interface).	229

Figure 8.1: 95% confidence intervals on A-factors relative to the value of the A-factor. For instance, the confidence interval is $\pm 0.169 * \log A$ for dehydrogenation.	236
Figure 8.2: Comparison of DBE versus Carbon Number for single pyrrolic ring structures for experimental(right) and predicted (left) results. Figure taken directly from source and was Figure 15 in the source material.[46]	238
Figure A.1: RightsLink permission obtained from ACS for reproduced work published by author[47].....	252
Figure A.2: RightsLink permission obtained from ACS for reproduced work published by author[54].....	253
Figure A.3: RightsLink permission obtained from ACS for reproduced work published by author[83].....	253
Figure A.4: RightsLink permission obtained from ACS for reproduced work published by author[109].....	254

ABSTRACT

Municipal Solid Waste (MSW) is a valuable energy resource that is underutilized by today's society. Waste-to-Energy (WTE) is a low-hanging fruit in a multifaceted energy landscape that incorporates conventional fuels and a plethora of renewable alternatives. From an environmental standpoint, WTE reduces the storage of MSW in landfills which can contaminate groundwater and release methane, a potent greenhouse gas. The most attractive WTE technology is gasification, a process where nonstoichiometric amounts of oxygen or air are fed to a high temperature reactor. The output from gasification is syngas, a ubiquitous product that can be used for a range of purposes, including liquid fuel synthesis and conversion to electricity via combustion. Plasma-arc gasification is an extension of conventional gasification that utilizes a plasma torch to obtain extreme reactor temperatures. The solid by-product from plasma gasification is an inert vitrified slag, which is usable as a construction material. Plasma-arc gasification successfully utilizes the entire MSW feedstock, thereby removing the need for landfills. However plasma-arc gasification is a relatively new WTE technology, and there is a need to better understand the underlying chemistry in order to optimize process parameters.

Molecular-level kinetic modeling has proven valuable in gaining insight on process chemistries ranging from naphtha reforming to biomass pyrolysis. To this end, this dissertation focuses on the development and application of a molecular-level kinetic model for MSW gasification. For model development, the MSW stream was divided into plastics and biomass. Kinetic models were constructed separately for the

gasification of each of these streams, using literature data. These models were then combined to construct the MSW gasification model. This model was used to simulate a 1000 metric ton per day plasma-arc gasifier that was divided into three zones for MSW: combustion, gasification, and freeboard. The reactor model was utilized to study the effects of process parameters on syngas quality and tar formation. Increasing the relative oxygen flow to the bed was found to reduce tar formation at the cost of syngas quality. Variations in MSW composition affected the oxygen content in tar molecules but had little impact on syngas quality. Lastly, the localized extreme temperatures in the combustion zone had a potentially negative impact on both syngas quality and tar production due to the oxidation of CO.

While studying MSW gasification, modeling approaches were developed for the depolymerization of both linear and cross-linked polymers that could be applied to other complex feedstocks and processes. In particular, this dissertation focuses on heavy oil resid pyrolysis. Resid pyrolysis is an attractive field for modeling due to recent advances in experimental techniques. This study highlighted the ability of molecular-level kinetic models to predict >50,000 molecules from detailed mass spectrometry measurements.

Orthogonal to kinetic model development, this thesis focused on the construction of software tools. Software tool development highlighted the interface between molecular-level kinetic models and users. There are three types of users of kinetic models: model developers, research collaborators, and process engineers. Each user has their own goals while using the model. For instance, software tools for model developers or research collaborators might focus on organizing the incredible amount of information contained in a molecular-level kinetic model. To address this aim, one

tool focused on the visualization of the reaction network to understand the network structure. In contrast, software tools designed for process engineers target measured inputs and outputs while abstracting the underlying molecular detail. This allows a process engineer, regardless of training in detailed kinetics, to reap the benefits of a molecular model and study the effects of operation parameters such as temperature or feed variation. These examples showcase the ability of software tools to increase the accessibility of detailed kinetics by molding the user-model interface to correspond to the user's needs.

This dissertation focused on gasification of waste, and culminated in a reactor model for the most environmentally friendly of WTE option: plasma-arc gasification. This work was then taken one step further by developing the software necessary to increase the accessibility of the model to a wider audience, ranging from process engineers to model developers. This accessibility makes the model not only fundamental, but also practical for industrial partners. Gasification and other WTE technologies have been, and will continue to be, a future topic of research. Undoubtedly, detailed kinetic models will play a central role in the future conversion of waste to energy

Chapter 1

INTRODUCTION

1.1 Municipal Solid Waste: Burden or Resource?

By its very designation, municipal solid waste (MSW) is viewed as a problem in today's society. The term *waste*, as defined by the Oxford dictionary, is a "material that is not wanted; the unusable remains or byproducts of something." Historically, this term was valid; according to the Environmental Protection Agency (EPA), essentially all MSW in the United States was placed in landfills before 1960, as shown in Figure 1.1[1]. Landfills can have issues in terms of the environment and public perception. First, waste stored in landfills can contaminate groundwater. Second, waste degradation by microbes in landfills produces methane[2], a greenhouse gas with a global warming potential roughly 25 times higher than carbon dioxide[3]. Additionally, in terms of public perception, landfills are an eyesore. They are one of the most common examples of the NIMBY, or "not in my backyard", effect. MSW that is discarded in landfills truly merits being called waste.

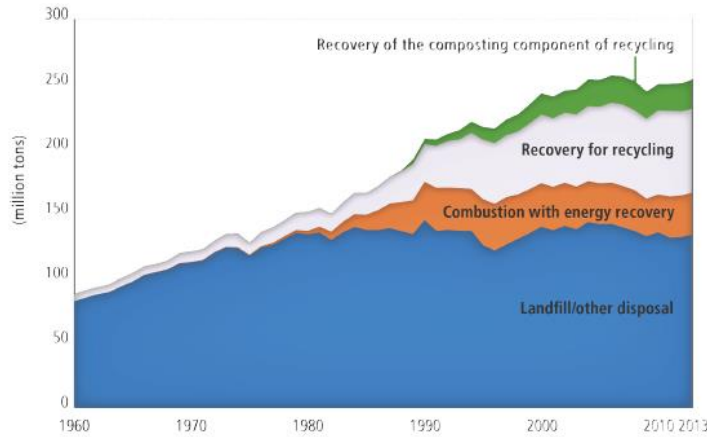


Figure 1.1: MSW management technologies from 1960-2013. Figure from source material[1].

Beginning around 1970, society began ways to utilize MSW. Between 1970 and 2000, there was a gradual increase in the fraction of waste recovered for recycling. Furthermore, in this time period, industry began to realize that MSW contains considerable energy, giving rise to combustion as the first waste-to-energy technology to be used at the industrial scale. Today, around half of MSW still goes to landfills, where this energy source is left untapped. The energy landscape in a modern society is quickly becoming multi-faceted, involving renewables, traditional fuels, and nuclear power. In this landscape, waste-to-energy is a low-hanging fruit requiring little research to obtain significant results. Other countries have utilized this resource; for example, Sweden made news in 2015 because they transport trash to fuel waste-to-energy facilities from surrounding countries[4]. If this is any indication of the future of MSW in the United States, it will be considered a *resource*, rather than *waste*.

1.2 Waste-to-Energy Technologies

There are numerous waste-to-energy (WTE) technologies that are currently feasible. These technologies include methane recovery from landfills, incineration, gasification, and plasma-arc gasification. Each of these technologies has advantages and disadvantages in terms of environmental concerns, energy obtained, and ease of implementation.

Methane recovery from landfills, also called landfill gas, is a WTE technology that focuses on waste after it has been deposited in landfills. There are two benefits. First, the methane can be burned to generate energy. Second, capturing and burning methane produces CO₂, a much less potent greenhouse gas. This technology is being actively pursued in the United States. According to the EPA, 645 landfills have been retrofitted to recover methane for energy production (as of March 2015), generating power for 1.2 million homes with 440 candidate landfills for future development[3].

Landfill gas recovery is a good short-term technology for obtaining energy from landfilled MSW; however, there are many drawbacks. First, all other disadvantages of landfills (*e.g.*, potential groundwater contamination) still exist. It is difficult to compare the energy obtained from landfill gas to other WTE technologies due to differences in timescales. Methane recovery is dependent on the rate at which microbes break down the material, which is significantly longer than the other techniques. Intuitively, the total energy recovered from a slow, partial breakdown via microbes is lower than a fast, near-complete breakdown by any other WTE technology. For these reasons, WTE technologies that minimize, or even exclude, the use of landfills are better long-term solutions.

The oldest, and currently most popular, WTE technology is incineration. This process entails the complete combustion of waste: excess oxygen is fed to the process,

which converts the waste entirely to CO₂. The heat from this process is utilized to generate electricity. The inherent simplicity of this process is compromised by the production of ash and pollutants. Of the original waste, 20-30% is categorized as non-hazardous ash and 2-6% as hazardous ash[5]. Incinerator ash is typically deposited in landfills[6]. The excess oxygen also promotes the formation of SO_x, NO_x, dioxins, and furans[7]. Laws such as the Clean Air Act[8] regulate the release of pollutants into the atmosphere, and incineration facilities must be designed to meet these standards.

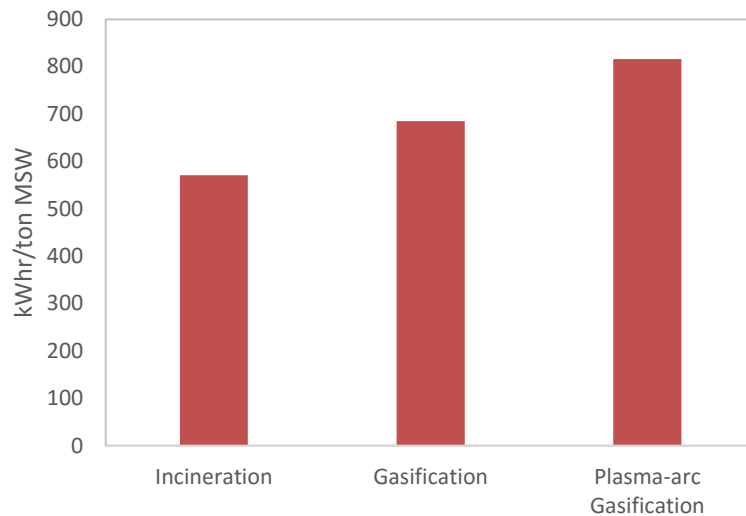


Figure 1.2: Net energy to grid per ton of MSW. Figure reproduced from source material[6].

Gasification addresses many of the issues with incineration by reducing the oxygen flow to the bed. The final product is a syngas—or synthesis gas—stream predominantly composed of CO and H₂. This ubiquitous outlet can be used to create chemicals or liquid fuel. Most often, however, the syngas stream is burned to generate electricity. Gasification has been applied extensively to more conventional feedstocks, *e.g.*, coal[9]–[12] or biomass[13]–[20]. This process is more efficient than

incineration, which is reflected in the larger net energy to grid per ton of MSW, as shown in Figure 1.2[6]. In conventional gasification, the final solid by-product of gasification is an ash material that ends up in landfills.

The ash byproduct from gasification has been addressed in a more recent type of gasifier that utilizes a plasma torch. This technique, termed “plasma-arc gasification”, melts the ash at extreme temperatures in the gasification bed, that can exceed 7000 °F[6]. The final solid byproduct is a vitrified slag which passes groundwater leach tests (shown in Table 1.1) and can be utilized as a construction material. The major disadvantages of plasma-arc gasification are capital costs for a new facility and the risks associated with new technologies. Plasma-arc gasification is the only technology currently in use that completely removes the need for landfills.

Table 1.1: Leach tests on vitrified slag. Table reproduced from source material. [6]

	EPA Permissible Conc. (mg/L)	Vitrified Slag Conc. (mg/L)
Arsenic	5	<0.1
Barium	100	0.47
Cadmium	1	<0.1
Chromium	5	<0.1
Lead	5	<0.1
Mercury	0.2	<0.1
Selenium	1	<0.1
Silver	5	<0.1

1.3 Plasma-Arc Gasification

A general plasma-arc gasification reactor is depicted in Figure 1.3. MSW is fed near the middle of the gasifier. The waste falls and forms a bed in the gasification zone. Along the height and circumference of this bed are inlets for the gasification

agent: typically air, oxygen-enriched air, or pure O₂[21]. The zone of open space above the MSW bed is called the freeboard zone, where primarily equilibrium reactions, such as water-gas shift, occur. After the freeboard zone, syngas leaves the top of the reactor. The other output is the vitrified slag, which exits the bottom of the gasifier and is molten at reactor conditions. In the diagram, the plasma torch is shown inside the gasifier; however, it can also be separate. In this scenario, a vapor stream carries the heat from the torch to the gasifier bed[22].

There are multiple categories of plasma-arc gasification units, but they generally fall into two categories: one-stage and two-stage. The category described here, and studied in this thesis, is an example of a one-stage gasifier. Two-stage examples include multi-reactor designs where the initial waste is fed to a conventional gasification unit. The plasma gasifier can then be used to convert the tar molecules in syngas or vitrify the ash into slag.

The primary product from the process is syngas. Depending on reactor conditions, this syngas can contain measurable amounts of tar molecules, defined here as molecules with higher boiling points than benzene. These tar molecules must be processed in downstream units[23]. The quality of the syngas is dependent on the gasification medium. The energy content, on a per volume basis, can be doubled with oxygen-enriched air or pure oxygen instead of natural air. This increased energy density allows for the use of a wider range of gas turbines to make electricity[21]. Syngas composition is dependent on the original feedstock[24], MSW. Most of the complexity and variability of the process is in the MSW inlet stream.

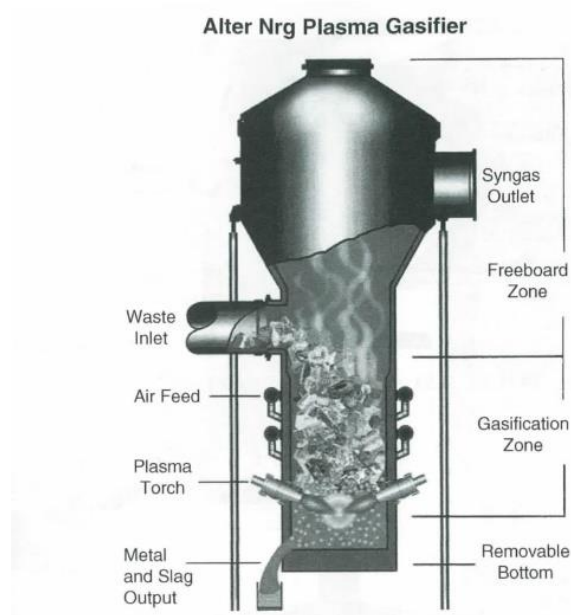


Figure 1.3: Alter NRG Plasma Gasifier. Image from source[6].

The main inlet to the plasma-arc gasifier is MSW, a mixed feedstock that can be broken down into a number of categories as shown in Figure 1.4. The most interesting thing about this composition is that it is inherently variable. This is demonstrated using the breakdown of United Kingdom (UK) waste in Figure 1.5[25]. The composition of UK waste is different than the US. Specifically, plastics are a much higher fraction of waste in the US. This is important as plastics, which are derived from oil, have lower oxygen content than biomass and therefore have a higher energy content. Also, even within the UK, the waste composition changes in urban and rural settings. The complexity and variability of MSW as a feedstock is a major motivator for process modeling of MSW gasification.

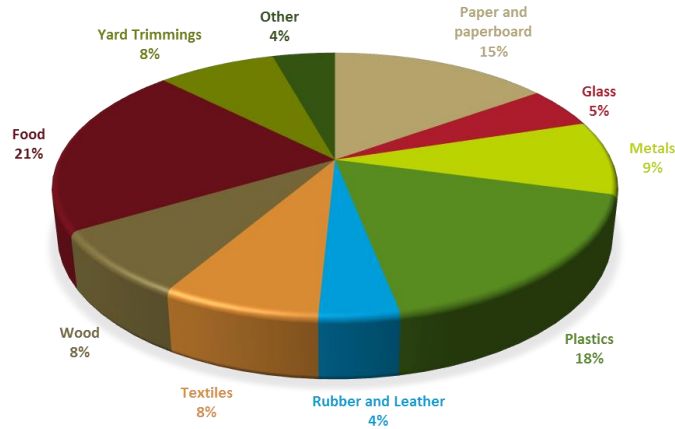


Figure 1.4: MSW breakdown in 2013 for the United States[1]. This composition represents the discarded (*i.e.*, post-recycling) MSW.

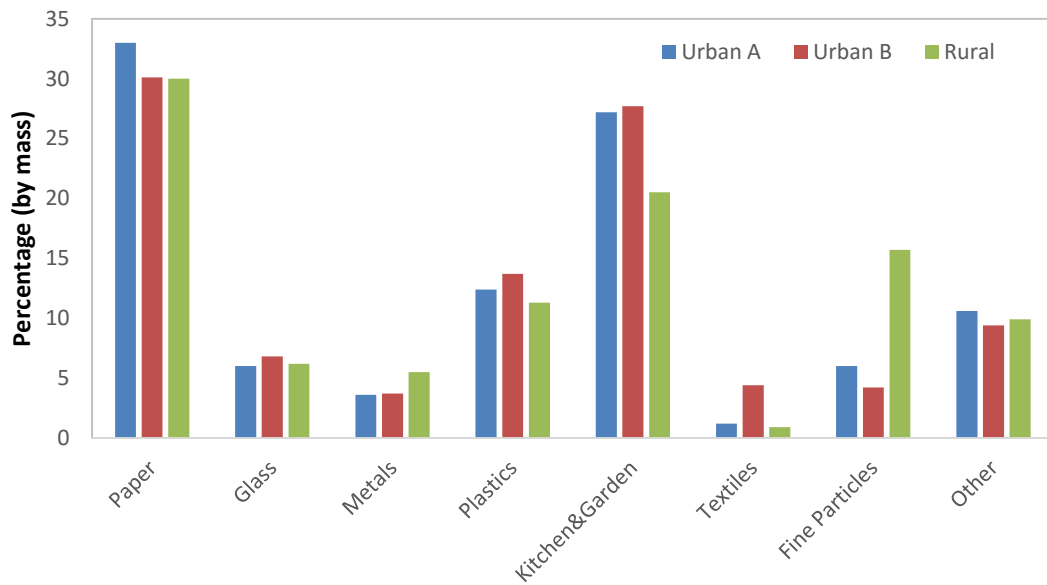


Figure 1.5: Urban and rural MSW waste descriptions in the United Kingdom[25].

1.4 MSW Gasification Modeling

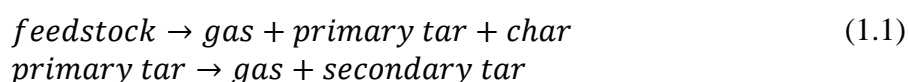
The aim of mathematically modeling of a chemical process is twofold: practical and scientific. The practical application of modeling is in the design and

control of the commercial reactor. For MSW gasification, the goal of process engineers is to control syngas production and composition. Modeling can help guide the choice of process parameters such that the energy content is maximized while high molecular weight tar molecules are minimized. The scientific application of modeling is in the understanding of the physics and chemistry of the process. This is more important to researchers and future projects as it can answer bigger questions about the process. For example, scientific understanding can be used to design a MSW stream to increase syngas energy content or control the composition of tar molecules.

The simplest model for gasification is a model based on the assumption of thermodynamic equilibrium [13], [16], [25]–[32]. By assuming the system reaches equilibrium, these models assume a reactor outlet composition based on the temperature of the system. Equilibrium models can handle changes in MSW feedstock through ultimate analyses. Returning to the aims of modeling gasification, there are a number of issues with equilibrium models. Equilibrium models do not contain detailed reactions and cannot help with understanding the underlying chemistry of the gasification process. Also, at the temperatures in a plasma-arc gasifier, tar molecules are not predicted at equilibrium. If tar molecules are observed, then the system is not at thermodynamic equilibrium and reaction kinetics must be taken into account.

The most basic type of kinetic models are lumped models[34], [35]. An example of a lumped model is given below in Equation 1.1[34], where chemical reactions are represented simply between lumped categories. A major advantage of lumped models is the model simplicity; these models are easy to build and understand. The mathematical solution is also fast, thereby allowing the kinetics to be easily paired with more complex descriptions of heat and mass transfer. The limitation of lumped

models is that they lack detail beyond the definition of the lumps. Each lump in the model might represent hundreds or thousands of chemical species. For instance, the model in Equation 1.1 would have trouble answering questions about the effects of MSW composition on predicted tar composition. In terms of scientific understanding, lumped models are based on experimental observations; however, they are ill-equipped to answer molecular-level questions about the formation of particular product molecules.



Artificial neural nets (ANNs) are kinetic models that are based on how neurons form connections in the brain[36]. Applied to a chemical process, ANN models have connections from measured inputs to measured outputs as shown in Figure 1.6[37]. The connections formed are based entirely on the data, and ANNs are ideal in the scenario where there is no knowledge in how inputs become outputs. This characteristic is also the key weakness of ANN models. Because there is no chemistry in the model, the model cannot help explain the underlying science of the physical process.

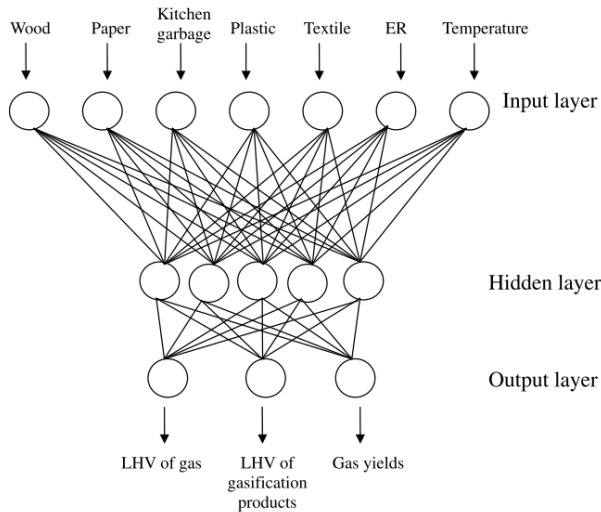


Figure 1.6: Artificial Neural Net from Xiao and coworkers. Image directly from source material[37].

Molecular models address the weaknesses of lumped and ANN models by tracking observable molecules in the reactor. The feed is represented as a set of molecules and mole fractions. These molecules undergo chemical reactions based on mechanistic and pathways levels of process chemistry. The reaction integration utilizes the reaction network to obtain the molecular outputs. This type of modeling inherently addresses the aims of modeling MSW gasification. First, the model can inform a process engineer of how process conditions impact measured quantities such as syngas and tar compositions. Second, because the input is molecular, it can account for the variable nature of MSW. Third, because the reaction network is based on reaction chemistry, the model conveys an understanding of the underlying science of gasification.

1.5 Research Objectives

There are two orthogonal sets of objectives in this dissertation: developing models and model-building tools. Due to the relative scarcity of data on plasma-arc gasification, model development focused primarily on a general reaction model for the gasification of MSW. This model was later applied to a specific reactor configuration of a plasma-arc gasification unit. Similar modeling methods were also utilized for the development of a kinetic model for the pyrolysis of heavy oil. In terms of model-building tools, this dissertation work has exposed the importance of the user-model interface for detailed kinetic models.

The primary objective of this research was the development of a molecular-level kinetic model for MSW gasification. Due to the complexity of MSW as a feedstock, a three-stage approach was adopted. In the first stage, a kinetic model was constructed for common mixed plastics; this model was optimized and validated using literature gasification data on each of the polymers. The second stage of MSW model development was the construction of a model for biomass gasification. This model utilized literature data to optimize and probe the predictive ability of the model. The final stage of MSW gasification model development focused on merging together the plastics and biomass models. At this stage, the merged model was a general gasification reaction model and contained the major components of MSW. This general model was then applied to a specific MSW plasma-arc gasification process. The resulting reactor model was utilized to perform trending studies on important process parameters.

The development of the MSW gasification model led to advances in the modeling framework for linear and cross-linked polymers. These advances are applicable to other high molecular weight feedstocks such as coal or heavy oil.

Although the chemical makeup and physical properties for these feedstocks are different from MSW, the polymeric complexity can be approached using the same mathematical tools. Specifically, this dissertation also focuses on the development of a model for the pyrolysis of a vacuum residue.

The second set of objectives for this dissertation pertained to software tool development. There are three users of kinetic models: model developers, research collaborators, and process engineers. Each type of these users has a different aim, and effective software tools must address these needs. For example, a tool for a process engineer focuses on measured inputs and outputs to a process. In contrast, tools for model developers might focus on enhancing the scientific and mathematical understanding of the model. An example of this is the visualization of a reaction network to gain in-depth understanding of the network structure. Through this logic, a completely different style of tool development has arisen. Rather than focusing on major software packages with many features, this dissertation focuses on single-purpose ‘apps.’ This style minimizes the learning curve for a given tool and allows for more fluid and personalized development for users.

1.6 Dissertation Scope

Chapter 2 provides a background on the Kinetic Modeler’s Toolkit (KMT) and how it is utilized for building kinetic models. The focus of the chapter is on the system of material balance differential equations that represent the kinetic model. The chapter discusses the three main steps of molecular modeling: feedstock composition, reaction network generation, and kinetic model solution.

Chapter 3 develops a kinetic model for the gasification of mixed plastics, including polyethylene, polyvinyl chloride, polyethylene terephthalate, and

polystyrene. Each polymer was simulated as linear with a constant repeat unit structure. Statistical methods are utilized for the initial breakdown of the polymeric macromolecules. A pyrolysis and gasification network is developed for the reaction of small oligomers. The model parameters are optimized for literature data, and comparisons are made.

Chapter 4 discusses the construction of a kinetic model for the gasification of biomass. The focus of the work is on three biopolymers: cellulose, hemicellulose, and lignin. Cellulose and hemicellulose are approximated as linear polymers, and similar methods are utilized as in the plastics model. Lignin is modeled as a cross-linked polymer and the structure is modeled using structural attributes. The model is tuned to literature data across different biomass types. The predictive ability of the model was probed using additional data.

Chapter 5 combines the kinetic models of plastics and biomass gasification to develop a model for MSW gasification. A model for coke gasification is also developed. The MSW and coke reaction models are applied to a plasma-arc gasifier. The resulting reactor model is organized in an app called the MSW Gasification I/O Converter. This app allows for trending studies to examine key operation parameters such as the effect of waste composition.

Chapter 6 demonstrates the use of similar modeling methods to the pyrolysis of heavy oil resid. Specifically, resid was modeled using the attribute methodologies utilized in lignin modeling. This study showcased the ability of the attribute reaction modeling to simulate systems with hundreds of thousands of molecules.

Chapter 7 examines the theory of ‘app’ development for kinetic modeling and showcases the apps developed over the course of this dissertation. This chapter

highlights the goals of the different types of users of kinetic models: developers, research collaborators, and process engineers. Apps were divided into three categories. The first category targeted the comprehension of the scientific and mathematical aspects of a kinetic model. The second category focuses on measured inputs and outputs to a process, while abstracting other complexity away from the user. The third category of apps aims to increase the capabilities of the Kinetic Modeler's Toolkit.

Chapter 8 summarizes the findings of this dissertation and discusses target areas of future work for both experimentalists and modelers in the areas of MSW gasification.

Chapter 2

MOLECULAR-LEVEL KINETIC MODELING IN THE KINETIC MODELER'S TOOLKIT

2.1 Material Balance

At the heart of a kinetic model is a system of material balances, given in Equation 2.1. The derivation of the mass balance is straightforward; the amount of each component can change from inlet or outlet flow and consumption or production by chemical reactions. There is one mass balance equation for every molecular species. Assuming no accumulation, this equation describes the change in amount of each species as a function of time. When applied to every species, the model is system of ordinary differential equations (ODE). This system is the basis for a kinetic model; the focus of this chapter is how the Kinetic Modeler's Toolkit (KMT) builds the system of material balances. Other complexities, such as the inclusion of the overall energy balance are within the capabilities of the software, but outside the scope of this chapter.

$$\frac{d\bar{y}}{dt} = \bar{r}_{in} - \bar{r}_{out} + \sum_{i, \text{reactions}} \bar{v}_i * rate_i \quad (2.1)$$

$$y(0) = \text{feed composition}$$

In the system of material balances, \bar{y} is a vector denoting the molar flow of every molecular species in the system. The flow in and out of the reactor is denoted using the vectors \bar{r}_{in} and \bar{r}_{out} , respectively. The reaction term is summed over all reactions, and for each reaction, a vector of stoichiometric coefficients, \bar{v}_i , is

multiplied by the rate of the reaction. For example, if the reaction is $CH_4 + \left(\frac{3}{2}\right) O_2 \rightarrow 2H_2O + CO$ then the consumption of methane would be equal to the reaction rate and the production of water would be twice the reaction rate.

KMT is an in-house software suite, developed over the last twenty years[38]–[45], that builds molecular-level kinetic models. Each piece of software addresses different terms in Equation 2.1. First, the Composition Model Editor (CME) gives the initial conditions. Next, the Interactive Network Generator (INGen) writes the reaction list[44]. Finally, the Kinetic Model Editor (KME) writes out the system of differential equations[40]. In this final step, the user specifies the rate laws and reactor types. At this stage, all terms have been completely defined and KME integrates the system of equations.

2.2 Initial Conditions from the Composition Model Editor

The solution of a reactor model is an initial value problem (IVP) as shown in Equation 2.2. For a molecular-level kinetic model, the initial values are the molar flow rates of the feed stream to the reactor. For simple processes, such as ethane pyrolysis, the feed stream is known and can be exactly defined. For more complex systems, such as the pyrolysis of heavy oil resid, the feed composition itself must be modeled as it can obtain $O(10^5)^1$ uniquely identifiable molecular structures.

¹ $O(10^5)$ means ‘on the order of’ 10,000

$$\frac{d\bar{y}}{dt} = \bar{r}_{in} - \bar{r}_{out} + \sum_{i, reactions} \bar{v}_i * rate_i \quad (2.2)$$

$$\boxed{y(0) = \text{feed composition}}$$

Compositional models of complex feedstocks are found using the Composition Model Editor, or CME. In general, CME takes available experimental measurements and uses an optimization loop to find a molecular composition that best represents the data. A simplified optimization diagram is shown below in Figure 2.1. CME predicts a composition then uses quantitative structure property relationships (QSPRs) to obtain a list of simulated properties. These properties are compared with experimental values to obtain a value of an objective function. The composition is adjusted to calculate a new simulated composition that can restart the optimization loop until a satisfactory objective function value is obtained. After optimization, the feed composition consists of a list of molecular structures and mole fractions. Much more information can be found in the literature on CME that goes into more depth on the optimization procedure and how CME has been applied to a wide variety of feedstocks[5],[9]–[12].

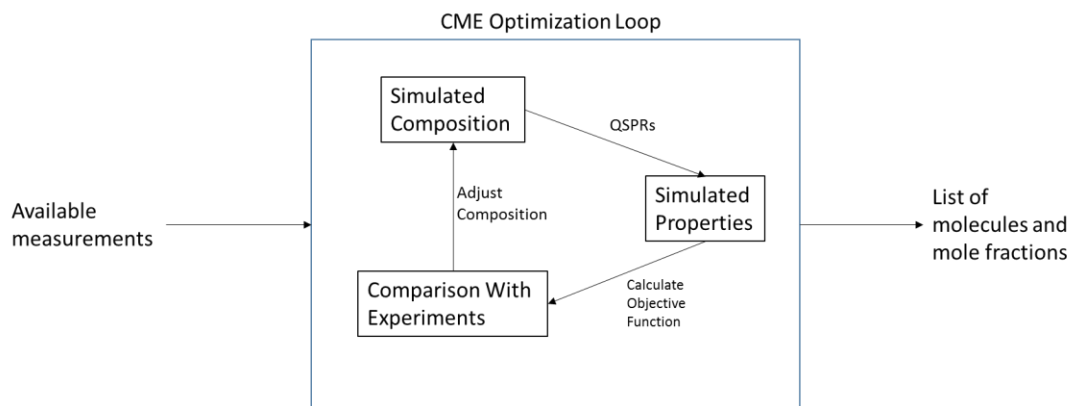


Figure 2.1: CME Optimization loop which converts available experimental measurements to a molecular composition.

2.2.1 Computational Representation of Molecules

In the process of modeling composition, a fundamental concept is the representation of molecular structures on a computer. To represent these structures, KMT utilizes the concept of bond electron matrices. An example is shown for propan-1-ol in Figure 2.2. In this matrix, 1 entries represent single bonds between the row and column intersection and 0 entries represent the absence of a bond. The matrix is symmetric as every atom is listed as a column and a row. Every molecule in the composition model has a unique bond-electron matrix.

	C ₁	C ₂	C ₃	O ₁	H ₁	H ₂	H ₃	H ₄	H ₅	H ₆	H ₇	H ₈
C ₁	0	1	0	1	0	1	1	0	0	0	0	0
C ₂	1	0	1	0	0	0	0	1	1	0	0	0
C ₃	0	1	0	0	0	0	0	0	0	1	1	1
O ₁	1	0	0	0	1	0	0	0	0	0	0	0
H ₁	0	0	0	1	0	0	0	0	0	0	0	0
H ₂	1	0	0	0	0	0	0	0	0	0	0	0
H ₃	1	0	0	0	0	0	0	0	0	0	0	0
H ₄	0	1	0	0	0	0	0	0	0	0	0	0
H ₅	0	1	0	0	0	0	0	0	0	0	0	0
H ₆	0	0	1	0	0	0	0	0	0	0	0	0
H ₇	0	0	1	0	0	0	0	0	0	0	0	0
H ₈	0	0	1	0	0	0	0	0	0	0	0	0

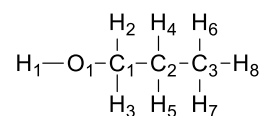


Figure 2.2 Bond electron matrix representation of propan-1-ol from Moreno[45].
Figure from source material.

2.3 Reaction Network Constructed using the Interactive Network Generator

The core of a molecular-level kinetic model is the process chemistry which defines the conversion from molecular input to output. Chemistry is the underlying science for a kinetic model. A correct understanding of chemistry allows for model robustness, and the ability of the model to be used as a predictive tool. In KMT, the

software responsible for utilizing our chemical knowledge to build a reaction network is the Interactive Network Generator, or INGen.

$$\frac{d\bar{y}}{dt} = \bar{r}_{in} - \bar{r}_{out} + \sum_{i, reactions} \bar{v}_i * rate_i \quad (2.3)$$

$$y(0) = \text{feed composition}$$

In the kinetic model, the reaction network appears in two locations in the material balances, reproduced in Equation 2.3. First, the reaction network defines the entire species footprint, or the size of the \bar{y} vector. Second, the reaction network gives the number of reactions and the stoichiometry vector, \bar{v}_i . The size of this network depends on the complexity of the process chemistry. The most detailed networks have thousands to tens of thousands of reactions.

2.3.1 Reaction Families

Even the most detailed, largest reaction networks contain many instances of a few reaction types, or reaction families. For instance, take alcohol dehydration as a reaction type, shown in Figure 2.3. This one reaction can be applied to any molecule in the system with an alcohol group and a hydrogen on an adjacent carbon. For example, alcohol dehydration can occur on ethanol or propanol but not methanol. Some molecules could even have multiple reaction sites for alcohol dehydration. For instance, glucose, the monomeric unit of cellulose, has five sites for alcohol dehydration. If the feedstock is biomass, it's easy to imagine hundreds of alcohol dehydration reactions, each occurring with the exact same underlying chemical mechanism.

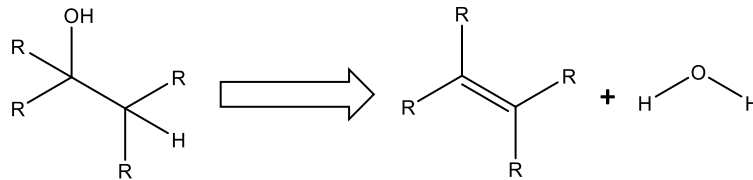


Figure 2.3: Generalized Alcohol Dehydration Reaction.

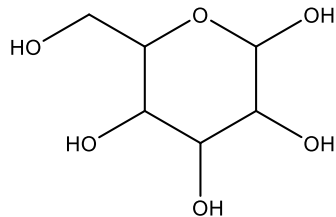


Figure 2.4: Cellulose monomer, glucose.

The most important step in building the reaction network is the correct selection of reaction families. Reaction family selection is process-dependent; for example, naphtha reforming would not include the same reaction families as a MSW gasification. To build a chemically-relevant model, the user must have an understanding of the chemistry that can occur in the system based on prior knowledge and/or the open-literature.

After selecting the process chemistry, the second requirement for network generation are the seed molecules, or the starting point from which to build a reaction network. The logical starting point for the network, in most cases, is the feed to the system. For example, if the model represents the pyrolysis of ethane, then a good seed molecule would be ethane. In more complex systems, the identities of the seed molecules come from the output of CME.

Network generation is an iterative process of finding reactive sites and adding to the reaction list. The species list begins as the set of seed molecules. Generation proceeds by searching the first seed molecule and writing all reactions that can occur. Next, the products of these reactions are checked for any new species. These new species are added to the species list. Network generation continues through the list of seeds and product molecules, each time searching for sites and adding valid reactions. When the end of the species list is reached, all products of all reactions have been searched for reactive sites. This process has been automated using INGen which has been developed over many years of research.

2.3.2 History of Reaction Network Generation in KMT

In the Klein research group, automatic generation of molecular-level reaction networks was originally a tool called NetGen, or Network Generator. This tool was originally developed by Linda Broadbelt and Scott Stark[38]. NetGen laid out the groundwork in terms of the representation of molecules and reactions computationally. At this stage, many features such as reaction types were hard-coded. As such, each project required expertise in computer science and a deep understanding of the NetGen tool.

INGen, written by Craig Bennett[44], is the current network-generating software in KMT. While it is fundamentally based on NetGen, it has many improvements in terms of the user-interface, the list of pre-made reaction chemistries, and the simplicity of adding new chemistry. The user-interface is a simple, easy-to-use Excel interface written in VBA (Visual Basic for the Excel Application). This interface communicates/runs the back-end program (written in C), which is the

workhorse behind network creation. This communication allows a user with minimal programming experience to build reaction networks.

The interface also allows the user to select reaction chemistries, set reaction rules (e.g., max carbon number), and select seed molecules from which to begin network creation. Because of the sheer magnitude of pre-built reaction chemistries, many kinetic models can be constructed using INGen without program modifications. Table 2.1 shows the reaction families currently in INGen. Many of the hydrocarbon, radical, and ion chemistries were added by Bennett in his doctoral thesis. More recently, the work of Brian Moreno on biomass pyrolysis greatly expanded INGen's capabilities by adding new hydrocarbon, nitrogen, sulfur, and radical reaction families. Most significantly, this work added oxygen chemistry.

INGen contains reaction families at both the mechanistic and pathways levels. Mechanistic reaction families involve reactive intermediates. In comparison, the pathways-level reaction families are based on implied mechanisms, such that the steps involving immeasurable reactive intermediates are lumped into the overall pathway. Depending on the desired complexity of the reaction network, the user can select mechanistic or pathways reaction families. Despite the long list of reaction families, new kinetic models sometimes require the addition of new chemistries. INGen has streamlined the process of this addition; an expert user can add a new reaction family in a matter of a few hours.

Table 2.1: Reaction families added by Bennett[44] and Moreno[45] to INGen.

Hydrocarbon	Methyl Shift	Keto-Enol Taut.
Paraffin Methyl Shift	β -scission	Enol-Keto Taut.
Path A Par. Methyl Shift	Hydrogen Abstraction	Alkyl Oxidation
Path B1 Par. Methyl Shift	Protonation/Deprotonation	Aldehyde Oxidation
Path B2 Par. Methyl Shift	5-Member Ring Closure	Alcohol Oxidation
Path C Par. Methyl Shift	Ring Expansion	Hydroperoxide Rearr.
Olefin Methyl Shift	Addition	Pyran Ring Saturation
Path A Olefin Methyl Shift		Furan Ring Saturation 4H
Path B1 Ole. Methyl Shift	Sulfur	Decarbonylation
Path B2 Ole. Methyl Shift	Desulfonation	Decarboxylation
Path C Olefin Methyl Shift	Thiopyran Ring Sat.	Depolymerization
Aromatic Methyl Shift	Thiophene Ring Sat. 2H	Hydrolysis
Acyclic Thermal Cracking	Thiophene Ring Sat. 4H	Ester Hydrolysis
Cyclic Thermal Cracking	Hydrodesulfurization	Olefin Hydration
Hydrogenation	Sulfur Saturation	Aldehyde Hydration
Double Bond Shift		Ketone Hydration
Isomerization	Oxygen	O-O Hydrogenolysis
Cyclization	Oxide Thermal Cracking	C-O Hydrogenolysis
Hydrogenolysis	Retro-Aldol Condensation	C-O Hydrogenolysis 5
Cracking	Aldol Condensation	C-O Hydrogenolysis 6
Dehydrogenation	Alcohol Condensation	C-O Hydrogenolysis 7
	Peracid Condensation	Aldehyde Cycl. 5
Nitrogen	Water Gas Shift	Aldehyde Cycl. 6
Pyrrole Ring Sat. 2H	Hydroxyl Shift	Ketone Cyclization 5
Pyrrole Ring Sat. 4H	Alcohol Dehydration	Ketone Cyclization 6
Pyridine Ring Sat. 2H	Pinacol Rearrangement	Carboxyl Cycl. 5
Pyridine Ring Sat. 6H	Ortho Acid Dehydration	Carboxyl Cycl. 6
Denitrogenation	Alcohol Dehydrogenation	Alcohol Cyclization 5
	Primary Alcohol Dehydro.	Alcohol Cyclization 6
Radical	Secondary Alcohol Dehydro.	Alcohol Cyclization 7
CX Bond Fission	Carbonyl Hydrogenation	Alcohol Ring Closure 5
HX Bond Fission	Aldehyde Hydrogenation	Alcohol Ring Closure 7
OX Bond Fission	Ketone Hydrogenation	O Ring Isomerization
Rad Beta-Scission	Carboxyl Hydrogenation	Esterification
Rad H-Abstraction	Ester Hydrogenation	Transesterification
Rad Oxidation	Lactone Hydrogenation	
	Tautomerization	
Ion	Alde-Enol Tautomerization	
Hydride Shift	Enol-Alde Tautomerization	

2.3.2.1 Computational Representation of Reactions

In building reaction networks, INGen represents reactions on a computer. As in CME, the molecules in INGen are represented using bond-electron matrices. Reactions extend the matrix analogy and are simply matrix transformations. For example, the alcohol dehydration of propan-1-ol is given in Figure 2.5. In this representation, the conversion of reactant to product molecules is governed by the alcohol dehydration reaction matrix. This matrix and the matrix operation is shown in Figure 2.6. First, the reduced reactant matrix are atoms whose connectivities will change in the reaction. The reaction matrix defines how the atomic connectivities change in the reaction. All reactions within a given reaction family have the same reaction matrix. Finally, the updated values are represented in the reduced product matrix. A key concept is that all reactions in the reaction family have the same reduced reactant matrix, reaction matrix, and reduced product matrix. The reduced product matrix is used to update the full product matrix as shown in Figure 2.7. In this case, the full product matrix is split into two separate molecules.

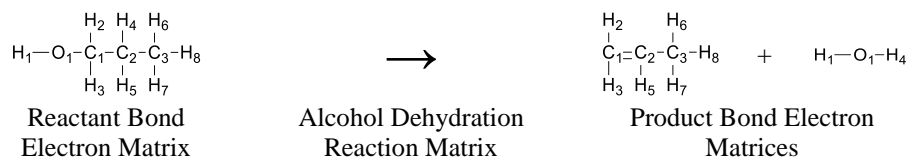


Figure 2.5: alcohol dehydration of propan-1-ol to propene and water.

<table border="1" style="border-collapse: collapse; text-align: center;"> <tr><th></th><th>O₁</th><th>C₁</th><th>C₂</th><th>H₄</th></tr> <tr><th>O₁</th><td>0</td><td>1</td><td>0</td><td>0</td></tr> <tr><th>C₁</th><td>1</td><td>0</td><td>1</td><td>0</td></tr> <tr><th>C₂</th><td>0</td><td>1</td><td>0</td><td>1</td></tr> <tr><th>H₄</th><td>0</td><td>0</td><td>1</td><td>0</td></tr> </table> <p>Reduced Reactant Matrix</p>		O ₁	C ₁	C ₂	H ₄	O ₁	0	1	0	0	C ₁	1	0	1	0	C ₂	0	1	0	1	H ₄	0	0	1	0	+	<table border="1" style="border-collapse: collapse; text-align: center;"> <tr><th></th><th>O₁</th><th>C₁</th><th>C₂</th><th>H₄</th></tr> <tr><th>O₁</th><td>0</td><td>-1</td><td>0</td><td>1</td></tr> <tr><th>C₁</th><td>-1</td><td>0</td><td>1</td><td>0</td></tr> <tr><th>C₂</th><td>0</td><td>1</td><td>0</td><td>-1</td></tr> <tr><th>H₄</th><td>1</td><td>0</td><td>-1</td><td>0</td></tr> </table> <p>Reaction Matrix</p>		O ₁	C ₁	C ₂	H ₄	O ₁	0	-1	0	1	C ₁	-1	0	1	0	C ₂	0	1	0	-1	H ₄	1	0	-1	0	=	<table border="1" style="border-collapse: collapse; text-align: center;"> <tr><th></th><th>O₁</th><th>C₁</th><th>C₂</th><th>H₄</th></tr> <tr><th>O₁</th><td>0</td><td>0</td><td>0</td><td>1</td></tr> <tr><th>C₁</th><td>0</td><td>0</td><td>2</td><td>0</td></tr> <tr><th>C₂</th><td>0</td><td>2</td><td>0</td><td>0</td></tr> <tr><th>H₄</th><td>1</td><td>0</td><td>0</td><td>0</td></tr> </table> <p>Reduced Product Matrix</p>		O ₁	C ₁	C ₂	H ₄	O ₁	0	0	0	1	C ₁	0	0	2	0	C ₂	0	2	0	0	H ₄	1	0	0	0
	O ₁	C ₁	C ₂	H ₄																																																																											
O ₁	0	1	0	0																																																																											
C ₁	1	0	1	0																																																																											
C ₂	0	1	0	1																																																																											
H ₄	0	0	1	0																																																																											
	O ₁	C ₁	C ₂	H ₄																																																																											
O ₁	0	-1	0	1																																																																											
C ₁	-1	0	1	0																																																																											
C ₂	0	1	0	-1																																																																											
H ₄	1	0	-1	0																																																																											
	O ₁	C ₁	C ₂	H ₄																																																																											
O ₁	0	0	0	1																																																																											
C ₁	0	0	2	0																																																																											
C ₂	0	2	0	0																																																																											
H ₄	1	0	0	0																																																																											

Figure 2.6: Chemical reaction as a matrix operation for propan-1-ol dehydration.
Figure from source material[45].

<table border="1" style="border-collapse: collapse; text-align: center;"> <tr><th></th><th>O₁</th><th>C₁</th><th>C₂</th><th>H₄</th><th>C₃</th><th>H₁</th><th>H₂</th><th>H₃</th><th>H₅</th><th>H₆</th><th>H₇</th><th>H₈</th></tr> <tr><th>O₁</th><td>0</td><td>0</td><td>0</td><td>1</td><td>0</td><td>1</td><td>0</td><td>0</td><td>0</td><td>0</td><td>0</td><td>0</td></tr> <tr><th>C₁</th><td>0</td><td>0</td><td>2</td><td>0</td><td>0</td><td>0</td><td>1</td><td>1</td><td>0</td><td>0</td><td>0</td><td>0</td></tr> <tr><th>C₂</th><td>0</td><td>2</td><td>0</td><td>0</td><td>1</td><td>0</td><td>0</td><td>0</td><td>1</td><td>0</td><td>0</td><td>0</td></tr> <tr><th>H₄</th><td>1</td><td>0</td><td>0</td><td>0</td><td>0</td><td>0</td><td>0</td><td>0</td><td>0</td><td>0</td><td>0</td><td>0</td></tr> <tr><th>C₃</th><td>0</td><td>0</td><td>1</td><td>0</td><td>0</td><td>0</td><td>0</td><td>0</td><td>0</td><td>1</td><td>1</td><td>1</td></tr> <tr><th>H₁</th><td>1</td><td>0</td><td>0</td><td>0</td><td>0</td><td>0</td><td>0</td><td>0</td><td>0</td><td>0</td><td>0</td><td>0</td></tr> <tr><th>H₂</th><td>0</td><td>1</td><td>0</td><td>0</td><td>0</td><td>0</td><td>0</td><td>0</td><td>0</td><td>0</td><td>0</td><td>0</td></tr> <tr><th>H₃</th><td>0</td><td>1</td><td>0</td><td>0</td><td>0</td><td>0</td><td>0</td><td>0</td><td>0</td><td>0</td><td>0</td><td>0</td></tr> <tr><th>H₅</th><td>0</td><td>0</td><td>1</td><td>0</td><td>0</td><td>0</td><td>0</td><td>0</td><td>0</td><td>0</td><td>0</td><td>0</td></tr> <tr><th>H₆</th><td>0</td><td>0</td><td>0</td><td>0</td><td>1</td><td>0</td><td>0</td><td>0</td><td>0</td><td>0</td><td>0</td><td>0</td></tr> <tr><th>H₇</th><td>0</td><td>0</td><td>0</td><td>0</td><td>1</td><td>0</td><td>0</td><td>0</td><td>0</td><td>0</td><td>0</td><td>0</td></tr> <tr><th>H₈</th><td>0</td><td>0</td><td>0</td><td>0</td><td>1</td><td>0</td><td>0</td><td>0</td><td>0</td><td>0</td><td>0</td><td>0</td></tr> </table>		O ₁	C ₁	C ₂	H ₄	C ₃	H ₁	H ₂	H ₃	H ₅	H ₆	H ₇	H ₈	O ₁	0	0	0	1	0	1	0	0	0	0	0	0	C ₁	0	0	2	0	0	0	1	1	0	0	0	0	C ₂	0	2	0	0	1	0	0	0	1	0	0	0	H ₄	1	0	0	0	0	0	0	0	0	0	0	0	C ₃	0	0	1	0	0	0	0	0	0	1	1	1	H ₁	1	0	0	0	0	0	0	0	0	0	0	0	H ₂	0	1	0	0	0	0	0	0	0	0	0	0	H ₃	0	1	0	0	0	0	0	0	0	0	0	0	H ₅	0	0	1	0	0	0	0	0	0	0	0	0	H ₆	0	0	0	0	1	0	0	0	0	0	0	0	H ₇	0	0	0	0	1	0	0	0	0	0	0	0	H ₈	0	0	0	0	1	0	0	0	0	0	0	0	→	<table border="1" style="border-collapse: collapse; text-align: center;"> <tr><th></th><th>C₁</th><th>C₂</th><th>C₃</th><th>H₂</th><th>H₃</th><th>H₅</th><th>H₆</th><th>H₇</th><th>H₈</th></tr> <tr><th>C₁</th><td>0</td><td>2</td><td>0</td><td>1</td><td>1</td><td>0</td><td>0</td><td>0</td><td>0</td></tr> <tr><th>C₂</th><td>2</td><td>0</td><td>1</td><td>0</td><td>0</td><td>1</td><td>0</td><td>0</td><td>0</td></tr> <tr><th>C₃</th><td>0</td><td>1</td><td>0</td><td>0</td><td>0</td><td>0</td><td>1</td><td>1</td><td>1</td></tr> <tr><th>H₂</th><td>1</td><td>0</td><td>0</td><td>0</td><td>0</td><td>0</td><td>0</td><td>0</td><td>0</td></tr> <tr><th>H₃</th><td>1</td><td>0</td><td>0</td><td>0</td><td>0</td><td>0</td><td>0</td><td>0</td><td>0</td></tr> <tr><th>H₅</th><td>0</td><td>1</td><td>0</td><td>0</td><td>0</td><td>0</td><td>0</td><td>0</td><td>0</td></tr> <tr><th>H₆</th><td>0</td><td>0</td><td>1</td><td>0</td><td>0</td><td>0</td><td>0</td><td>0</td><td>0</td></tr> <tr><th>H₇</th><td>0</td><td>0</td><td>1</td><td>0</td><td>0</td><td>0</td><td>0</td><td>0</td><td>0</td></tr> <tr><th>H₈</th><td>0</td><td>0</td><td>1</td><td>0</td><td>0</td><td>0</td><td>0</td><td>0</td><td>0</td></tr> </table>		C ₁	C ₂	C ₃	H ₂	H ₃	H ₅	H ₆	H ₇	H ₈	C ₁	0	2	0	1	1	0	0	0	0	C ₂	2	0	1	0	0	1	0	0	0	C ₃	0	1	0	0	0	0	1	1	1	H ₂	1	0	0	0	0	0	0	0	0	H ₃	1	0	0	0	0	0	0	0	0	H ₅	0	1	0	0	0	0	0	0	0	H ₆	0	0	1	0	0	0	0	0	0	H ₇	0	0	1	0	0	0	0	0	0	H ₈	0	0	1	0	0	0	0	0	0	+	<table border="1" style="border-collapse: collapse; text-align: center;"> <tr><th></th><th>O₁</th><th>H₁</th><th>H₄</th></tr> <tr><th>O₁</th><td>0</td><td>1</td><td>1</td></tr> <tr><th>H₁</th><td>1</td><td>0</td><td>0</td></tr> <tr><th>H₄</th><td>1</td><td>0</td><td>0</td></tr> </table>		O ₁	H ₁	H ₄	O ₁	0	1	1	H ₁	1	0	0	H ₄	1	0	0
	O ₁	C ₁	C ₂	H ₄	C ₃	H ₁	H ₂	H ₃	H ₅	H ₆	H ₇	H ₈																																																																																																																																																																																																																																																																																					
O ₁	0	0	0	1	0	1	0	0	0	0	0	0																																																																																																																																																																																																																																																																																					
C ₁	0	0	2	0	0	0	1	1	0	0	0	0																																																																																																																																																																																																																																																																																					
C ₂	0	2	0	0	1	0	0	0	1	0	0	0																																																																																																																																																																																																																																																																																					
H ₄	1	0	0	0	0	0	0	0	0	0	0	0																																																																																																																																																																																																																																																																																					
C ₃	0	0	1	0	0	0	0	0	0	1	1	1																																																																																																																																																																																																																																																																																					
H ₁	1	0	0	0	0	0	0	0	0	0	0	0																																																																																																																																																																																																																																																																																					
H ₂	0	1	0	0	0	0	0	0	0	0	0	0																																																																																																																																																																																																																																																																																					
H ₃	0	1	0	0	0	0	0	0	0	0	0	0																																																																																																																																																																																																																																																																																					
H ₅	0	0	1	0	0	0	0	0	0	0	0	0																																																																																																																																																																																																																																																																																					
H ₆	0	0	0	0	1	0	0	0	0	0	0	0																																																																																																																																																																																																																																																																																					
H ₇	0	0	0	0	1	0	0	0	0	0	0	0																																																																																																																																																																																																																																																																																					
H ₈	0	0	0	0	1	0	0	0	0	0	0	0																																																																																																																																																																																																																																																																																					
	C ₁	C ₂	C ₃	H ₂	H ₃	H ₅	H ₆	H ₇	H ₈																																																																																																																																																																																																																																																																																								
C ₁	0	2	0	1	1	0	0	0	0																																																																																																																																																																																																																																																																																								
C ₂	2	0	1	0	0	1	0	0	0																																																																																																																																																																																																																																																																																								
C ₃	0	1	0	0	0	0	1	1	1																																																																																																																																																																																																																																																																																								
H ₂	1	0	0	0	0	0	0	0	0																																																																																																																																																																																																																																																																																								
H ₃	1	0	0	0	0	0	0	0	0																																																																																																																																																																																																																																																																																								
H ₅	0	1	0	0	0	0	0	0	0																																																																																																																																																																																																																																																																																								
H ₆	0	0	1	0	0	0	0	0	0																																																																																																																																																																																																																																																																																								
H ₇	0	0	1	0	0	0	0	0	0																																																																																																																																																																																																																																																																																								
H ₈	0	0	1	0	0	0	0	0	0																																																																																																																																																																																																																																																																																								
	O ₁	H ₁	H ₄																																																																																																																																																																																																																																																																																														
O ₁	0	1	1																																																																																																																																																																																																																																																																																														
H ₁	1	0	0																																																																																																																																																																																																																																																																																														
H ₄	1	0	0																																																																																																																																																																																																																																																																																														

Figure 2.7: Separation of the full bond electron matrix post-reaction into product molecules.

2.4 Equations Written, Solved, and Optimized using the Kinetic Model Editor

The Kinetic Model Editor (KME) first defines the remaining terms on the material balance, and, then, it writes, solves, and optimizes the kinetic model. There are two remaining groups of terms in the mass balance, reproduced in Equation 2.4. The first set of terms is a function of reactor type and represents inlet flows and the form of the differential equation. The second term represents the reaction rates, determined by rate laws and underlying rate constants. To write the equations, KME first utilizes the reaction network produced by INGen. After the equations are written,

solution proceeds as an initial value problem where the feed composition is provided by CME. Finally, KME optimizes rate parameters by comparing model results with experimental data.

$$\frac{d\bar{y}}{dt} = \boxed{\bar{r}_{in} - \bar{r}_{out}} + \sum_{i, \text{reactions}} \bar{v}_i * \boxed{\text{rate}_i} \quad (2.4)$$

$$y(0) = \text{feed composition}$$

2.4.1 Reactor Type

Reactor type is among the most important design decision in developing a chemical process model. The type of reactor determines the residence time of reactants, the effective concentrations of reactants and products, and the temperature profile in the reactor. Often when modeling a process, idealized reactors are used individually or in a configuration that mimics the real system. Within KME, the following reactor types are available: batch reactor, plug-flow reactor (PFR), continuous stir-tank reactor (CSTR), radial flow reactor (RFR), semibatch reactor, PFR with sidestream, and continuous catalytic reformer (CCR).

In the material balance equation, reactor type affects the differential term and the inlet-outlet flows. For example, in a batch reactor, the flow terms are zero and drop out of the equation. Alternatively, in a PFR, the differential equation is in terms of reactor length rather than time. The rate expressions are invariant with reactor type, but reaction rates can be drastically affected as different reactor types affect the effective concentrations of reactants and products.

2.4.2 Rate Laws and Linear Free Energy Relationships²

For every reaction in the network there is a rate law, which is a mathematical model that predicts the rate at which reactants are consumed and products are produced. The rate law must be determined from experiments and cannot be inferred simply by looking at the reaction equation. A few rate law types that have proven value for many chemistries include the law of mass-action (or micro-kinetic model), power-law, and Langmuir-Hinshelwood-Hougen-Watson (LHHW) model. KME builds the rate laws for each reaction based on the user-selected option. Regardless of rate law, every reaction has a rate constant.

$$\ln k_i = \ln A_i - \frac{E_i^*}{RT} \quad (2.5)$$

Rate constants expressed using the Arrhenius equation, shown in Equation 2.5 for reaction i . For complex systems like coal or biomass, a molecular-level kinetic model can contain as many as $O(10^5)$ reactions. Equation 2.5 shows that there are two parameters A_i and E_i^* for each reaction. Optimizing tens of thousands of parameters is intractable due to both amount of required data and computational complexity. An interesting phenomenon, observed in the literature[49], [50], is that, for a given reaction type, there is a linear relationship between the rate constants and the enthalpy change on reaction, as shown in Figure 2.8, for molecules that have a similar functional group. Linear free energy relationships (LFERs) make use of this observation to reduce parameter complexity of each rate law. The basic assumption of

² Material paraphrased with permission from **Horton, S.R.** and Klein, M.T. “Reaction and Catalyst Families in the Modeling of Coal and Biomass Hydroprocessing Kinetics” *Energy & Fuels*. 2013, 28, 37-40. DOI: 10.1021/ef401582c. Copyright 2014. American Chemical Society. [47]

LFERs is that the rate constants of mechanistically similar reactions of similar molecules are dependent on the thermodynamic properties of the reactants and products. The Bell-Evans-Polanyi[51], [52] LFER, for example, is shown as Equation 2.6. The Polanyi relation correlates the activation energy of a given reaction i in a reaction family j , $E_{i,j}^*$, to the change in enthalpy of reaction, ΔH_i .

$$E_{i,j}^* = E_{0(j)} + \alpha_j * \Delta H_i \quad (2.6)$$

The second parameter in Arrhenius Equation is the pre-exponential factor, A_i . As a first-order approximation, this factor is assumed to be only a function of reaction family, or A_j . The substitution of the LFER relationship into the Arrhenius equation allows for a more general form of the equation to be written for the rate constant, as shown in Equation 2.7.

$$\ln k_{i,j} = \ln A_j - \frac{E_{0(j)} + \alpha_j * \Delta H_i}{RT} \quad (2.7)$$

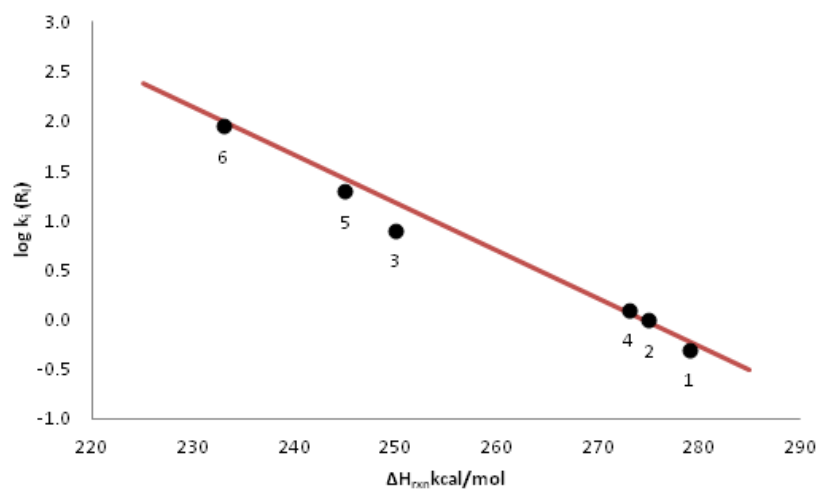


Figure 2.8: Figure from Horton and Klein[47]. (a) Figure reproduced Mochida and Yoneda[49] showing the dealkylation of alkylaromatics reaction family on a SA-1-Na-3 catalyst. The numbers represent experimental rates of dealkylation on different alkyl aromatics.

The major impact of using LFERs for reaction families is the massive reduction in the number of adjustable parameters in the kinetic model. Relating back to the original mass balance equation, the adjustable parameters in a molecular-level kinetic model are within the rate constants for each of the reactions where there are two rate parameters per rate constant. As it was shown, LFERs reduce the number of adjustable parameters down to three per reaction family. This drastically reduces the experimental data and computational time required to optimize a kinetic model.

2.4.3 Model Solution

At this stage, the material balance equations have been completely defined. KME takes these concepts and automatically writes the material balance differential equations[2],[3],[42]. Within KME, the differential equation solver suite is the open-

source Livermore Solver for Ordinary Differential Equations (LSODE)[53]. LSODE is a robust solver that allows for the solution of both stiff and non-stiff systems of differential equations. The output from the model is a list of molecules and molar flows. This output can be used to calculate output bulk properties. Molar flows and bulk properties allow for comparison with a wide variety of experimental information which becomes the basis for kinetic parameter optimization.

2.4.4 Kinetic Parameter Optimization

In parameter optimization, the objective function, F , is a measure of model goodness of fit. For the case of a kinetic model, the objective function is a measure of how well the output stream matches experimental measurements, as shown in Equation 2.8. The output stream is a function of the conditions in the reactor, the reactor type, the reaction network, and the rate parameters. Of these terms, the reactor conditions, reactor type and sizing are likely preset for these measurements. Assuming the reaction network adequately models the process chemistry, the only parameters upon which to optimize are the rate parameters.

$$F = \sum_{i, meas} \left(\frac{measured_i - predicted_i (rate\ parameters)}{w_i} \right)^2 \quad (2.8)$$

The measurements in the objective function come in two forms: direct measurements of the molar flow of species and measurements of the bulk properties as shown in Table 2.2. For measurements that yield data on individual species, such as gas chromatography, the model comparison is calculated directly. For bulk properties,

the comparison is made implicitly by converting the product composition to predicted properties via structure property correlations.

Table 2.2: The two types of measurements in the objective function.

Overall Objective Function	<i>Molar Flow Terms + Bulk Property Terms</i>
Molar Flow Terms	$\sum_{i, \text{ species}} \left(\frac{(\text{measured flow})_i - (\text{predicted flow})_i}{w_i} \right)^2$
Bulk Property Terms	$\sum_{i, \text{ properties}} \left(\frac{(\text{measured property})_i - (\text{predicted property})_i}{w_i} \right)^2$

Using the objective function, KME optimizes the model to experimental data. The major optimization routine is simulated annealing, a global optimization algorithm. Global optimization techniques are specifically designed to find the global minimum in a problem with a high number of parameters. Most global optimization algorithms rely on randomly sampling new parameter values from the range of allowable parameter values. Another characteristic of global optimizers is that they have some probability of allowing *uphill steps*, or steps that increase the value of the objective function. This may seem counter-intuitive, but it is this characteristic which allows the solution to escape local minima. Global optimizers are the only feasible way to solve high-parameter optimization problems.

Once the numerical optimizer reaches a satisfactory objective function value, the result is a list of tuned kinetic parameters and the corresponding comparison of predicted to measured experimental results. A common plot drawn to analyze the fit of these results is a parity plot as shown in Figure 2.9. In parity plots, the model

predictions are on the y-axis, and experimental measurements are on the x-axis. The line $y=x$ corresponds then to a perfect model prediction.

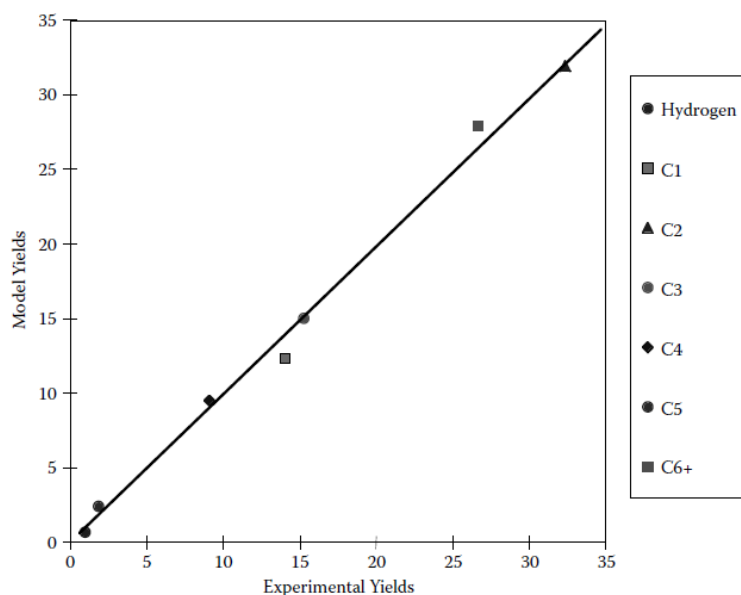


Figure 2.9: Example parity plot for the pyrolysis of naphtha for an experimental carbon number distribution. Figure from source material[42].

2.5 Summary

In summary, a molecular-level kinetic model is fundamentally a system of material balance differential equations with one equation per species. The three software tools that make up KMT each build different terms in the differential equations. CME finds the initial value of the system by finding the optimal feed composition for a set of experimental measurements. INGen builds a reaction network by utilizing the feed composition and an understanding of process chemistry. With this reaction network, KME writes the material balances using user-defined rate laws and reactor types. After constructing the system of equations, KME solves the reactor model. The adjustable parameters are reaction family LFER parameters. Comparison

with experimental measurements allows for an optimization of the kinetic parameters. The results from optimization are a set of tuned LFER parameters. The optimization results can be analyzed using a parity plot showing model predictions and experimental measurements.

Chapter 3

MOLECULAR-LEVEL KINETIC MODELING OF THE GASIFICATION OF COMMON PLASTICS

Scott R. Horton¹, James Woeckener¹, Rebecca Mohr², Yu Zhang², Francis Petrocelli², and Michael T. Klein¹

¹*University of Delaware Energy Institute and Department of Chemical and Biomolecular Engineering, University of Delaware, Newark, DE 19716*

²*Air Products and Chemicals Incorporated. Allentown, PA, 18195*

Reproduced by permission from **Horton, S.R.**; Woeckener, J.; Mohr, R.; Zhang, Y.; Petrocelli, F.; Klein, M.T. “Molecular-level kinetic modeling of the gasification of common plastics.” *Energy & Fuels*. 2015 (Web).

DOI:10.1021/acs.energyfuels.5b02047. Copyright 2015. American Chemical Society.[54]

3.1 Abstract

A molecular-level kinetic model was developed for the gasification of common plastics including poly-ethylene (PE), polyethylene terephthalate (PET), polyvinyl chloride (PVC), and polystyrene (PS). Model development was divided into three steps: molecular characterization of the feed, generation of a pathways-level reaction network, and creation of the material balance differential equations (DEs). The structure of all polymers was modeled as linear with known repeat units. For PE, PVC, and PET Flory-Stockmayer statistics were used to describe the initial polymer size distribution; PS was described using a two-parameter gamma distribution. The parameters of all polymer size distributions were tuned using data from the open literature.

The chemistry of plastics gasification contains depolymerization, pyrolysis, and gasification reactions. The initial depolymerization of PE and PET was modeled using random scission and Flory-Stockmayer statistics. A statistical method was created extending random scission to a generalized polymer size distribution and applied here to the breakdown of polystyrene. The depolymerization of PVC was modeled as two-step: poly-ene formation followed by benzene production. Pyrolysis reactions were included on small oligomers and were broken down into two categories: cracking and formation of tar and char molecules. For gasification, incomplete combustion and steam reforming were included to break down oligomers, tar, and char molecules. Also, light gas reactions, e.g., water-gas shift, were added to the network. The final network contained 283 reactions and 85 species.

After construction of the material balance DEs, kinetic parameters were tuned using literature data on each plastic. These studies involved gasification, pyrolysis,

and TGA experiments each probing different aspects of depolymerization, pyrolysis, and gasification kinetics. Model results matched experimental data well.

3.2 Introduction

Plastics made up 35 million tons, or 12.8%, of municipal solid waste (MSW) in the United States in 2013 as shown in Figure 3.1[1]. Of this waste, just 9% or 3 million tons were recovered directly for recycling. Therefore, plastic degradation is a key aspect in waste-to-energy technologies such as MSW gasification. In a MSW gasification unit, plastics are broken down into light gas molecules and higher-molecular weight tar and char molecules. In the design and operation of a gasification process, a primary goal is to minimize tar and char production while maximizing the energy content of light gases. In order to probe the gasification performance of a variety of plastics, mathematical models are needed to predict the breakdown from long-chain polymers to light gases, char, and tar molecules.

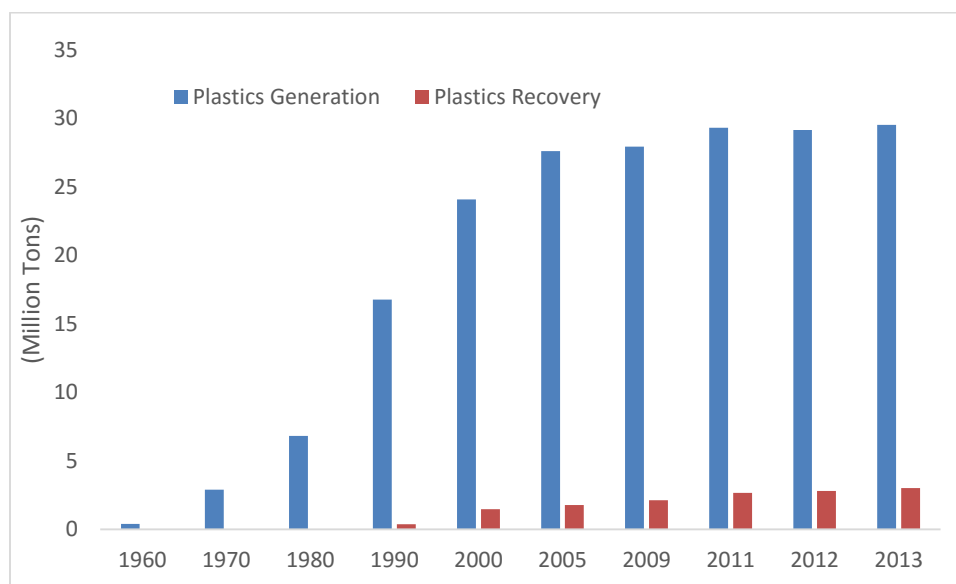


Figure 3.1: Plastics generation and recovery from the EPA report on Municipal Solid Waste (MSW)[1].

Prior work in the mathematical modeling of depolymerization of plastics can be divided into two categories: pyrolysis and gasification. For pyrolysis, there have been some very detailed studies of chemical kinetics at the radical level for individual common polymers. For example, polystyrene has been studied extensively by Broadbelt and coworkers[55],[56]. Similarly, there is a mechanistic understanding of the pyrolysis of ethane[57]; which is directly applicable to polyethylene. There has also been detailed work on the pyrolysis of plastic mixtures[58]. The detail of mathematical models in the gasification literature is far less prevalent and complex. Some studies fit lumped kinetic parameters to Thermogravimetric Analysis (TGA) data[59],[60]; however, complex kinetic models at the molecular-level are missing from the plastic gasification literature.

The current modeling work is the first representation in the open literature of a molecular-level kinetic model for the gasification of common plastics; specifically, PE, PET, PVC, and PS. Modeling kinetics at the molecular-level requires molecular detail at every step in the model-building process. First, the feed is modeled as a collection of molecules and mole fractions. Next, the reaction network utilizes fundamental chemistry to describe the mapping from reactant to product molecules. This network is used to construct a set of material balance differential equations for each molecular species. The feed composition specifies the initial values of these differential equations. The kinetic model can be integrated for a given set of reactor conditions and reactor type. The adjustable parameters in the model are the kinetic parameters to each reaction chemistry. Experimental data from the open literature allows for both kinetic parameter tuning and model evaluation.

3.3 Molecular Representation of Plastics

The first step in building a molecular-level kinetic model is the molecular representation of the feedstock. If the polymers are assumed to be linear, then the composition is defined by the repeat unit structure and a polymer-size distribution. The repeat unit structures for the polymers in this study are shown below in Figure 3.2. In this report, the polymers were described using two types of polymer size distributions. A single-parameter Flory distribution is used for PE, PVC, and PET, and a two-parameter gamma distribution is used for polystyrene. The adjustable parameters in the composition model are then the parameters of the distribution; these parameters were optimized using literature data on each of the polymers.

The molecular structure of a polymer can also be conceptualized as cores with inter-core linkage (IL) and side chain (SC) substituents. Cores are connected by ILs to form polymers, and SCs are terminal end groups. For example, in polyethylene, the core identity is C_2H_4 , the IL is the bond between cores, and a SC is a terminal bond to hydrogen. Each core has two binding sites for substituents, filled by either ILs or SCs. Because SCs are terminal, each linear polymer chain only has two SCs. In a linear polymer, an *i-mer* contains *i* cores, *i-1* ILs, and 2 SCs.

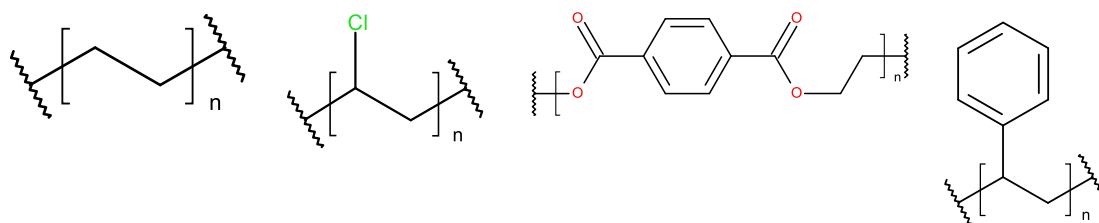


Figure 3.2: Repeat Unit Structures for PE, PVC, PET, and PS (Left to Right).

3.3.1 Flory-distributed Linear Polymers

One of the most commonly used polymer-size distributions is the single-parameter Flory distribution[61], given in Equation 3.1. The p used in this equation is commonly the extent of polymerization, and is equivalently the fraction of core binding sites contained within linkages, given in Equation 3.2. A common measure of linear polymers is the number average degree of polymerization, \overline{X}_n , which is calculated directly from p using Equation 3.3. The composition of a Flory-distributed linear polymer is therefore defined by repeat unit structure and average degree of polymerization.

$$x_i = (1 - p) * p^{i-1} \quad (3.1)$$

$$p = \frac{2 * [IL]}{2 * [IL] + [SC]} \quad (3.2)$$

$$\overline{X}_n = \frac{1}{1 - p} \quad (3.3)$$

For each Flory-distributed linear polymer, literature ultimate analyses were used to find optimal values of \overline{X}_n . For these optimizations, an in-house software tool called Linear Polymer Composition Editor was utilized. Further detail on this tool can be found in prior work[54]. The results for the composition models are summarized below in Table 3.1. In these results, PE and PET matched well with experimental data. The minor discrepancies in polyvinyl chloride could be explained by the presence of plasticizers, a common PVC additive[62], in the experimental sample that are absent in the composition model. The role of these plasticizers in the composition and subsequent kinetic model is assumed to be a second-order effect, but is an opportunity for future work. Although more detailed distribution information, such as polydispersity index (PDI), was not measured experimentally, the agreement with

available data suggests the Flory distribution is applicable to PE, PET, and PVC in the composition model.

Table 3.1: Experimental and predicted ultimate analyses for PE, PVC, and PET. The literature values are from Arena et al.[23] for PE, Heikkinen et al[63] for PET, and Zhu et al. for PVC[64]. The \overline{X}_n 's for these results are 291, 998, and 5 for PE, PET, and PVC respectively.

Element	Polyethylene		Polyethylene Terephthalate		Polyvinyl Chloride	
	Experimental	Predicted	Exp.	Pred.	Exp.	Pred.
C	85.0	85.6	62.51	62.49	41.55	38.1
H	13.8	14.4	4.19	4.20	4.81	5.44
O	0.00	0.00	33.30	33.3	0.00	0.00
Cl	0.00	0.00	0.00	0.00	52.95	56.38

The Flory distribution is not well-suited as a composition model for all polymers; this is exemplified by polystyrene. At the lab scale, polystyrene is often synthesized via anionic polymerization with typical PDI values of 1.05[65], [66]. These samples were found to behave similarly to commercial polystyrene under pyrolysis conditions[65]. At long chains, the Flory distribution converges on a polydispersity index (PDI) of 2.00. Due to the discrepancy in PDI, polystyrene was instead modeled using a 2-parameter gamma distribution.

3.3.2 Gamma-distributed Linear Polymers

The two-parameter gamma distribution is given in Equation 3.4 where a and d are shape and scale factors, respectively. Experimental measurements were used to optimize the parameters for the distribution. In this case, the data for polystyrene are the number average molecular weight, \overline{M}_n , and weight average molecular weight, \overline{M}_w . After finding optimal gamma parameters, a comparison of experimental results

and predictions are given below in Table 3.2. The results fit the data well suggesting that the gamma distribution is appropriate for polystyrene.

$$x_i(a, d) = \frac{i^{d-1} * e^{-\frac{i}{a}}}{a^d * \Gamma(d)} \quad (3.4)$$

Table 3.2: Literature measurements for polystyrene and corresponding gamma predictions. \overline{M}_w was reported in Liu et al[67], approximate literature PDI values were used to approximate \overline{M}_n . The gamma parameters for these values were calculated to be: $a = 13037.43$, $d = 20$.

Parameter	Experimental Value	Value from Gamma Distribution
$\overline{M}_n \left(\frac{g}{mol} \right)$	260749	260637
$\overline{M}_w \left(\frac{g}{mol} \right)$	273786	273571
PDI = 1.05	1.05	1.049

3.4 Reaction Chemistry of Gasification of Plastics

The second step of building a molecular-level kinetic model is the generation of the reaction network. This network contains the fundamental process chemistry for the gasification of plastics. In this model, first the long-chain polymers are depolymerized into smaller oligomers via depolymerization reactions. The small oligomers then react further via more detailed pyrolysis and gasification chemistry to form light gas, tar, and char molecules.

3.4.1 Depolymerization

Depolymerization chemistry breaks down the initial polymer backbone. Although these chemistries are polymer specific, there are common types of

depolymerization. For example, many mechanisms occur randomly along the polymer backbone and are known as random scission mechanisms. Due to the random nature of the mechanism, it is possible to predict the changes in the polymer size distribution over the course of depolymerization. This allows the model to account for large mers without the unnecessary computational burden of individually tracking hundreds to thousands of mers over the course of depolymerization.

3.4.1.1 Random Scission of Flory Polymers

Random scission depolymerization is most easily applied to Flory polymers. In polymerization, the Flory distribution assumes that all end-groups are equally reactive and therefore linkages are randomly formed in the system. Random scission is simply the reverse of this process, and the Flory distribution, given before in Equation 3.1, still applies to the product polymer. Because the distribution is still applicable, depolymerization simply decreases the value of p .

Depolymerization can also be related to the concept of cores, ILs, and SCs. If depolymerization is represented using a single link cleavage reaction in Equation 3.5, then the change of ILs in the system can be related to the Flory parameter as shown in Equation 3.6. The constant, C , follows from the link cleavage reaction and represents the number of substituent sites in the system.



$$\frac{dp}{dt} = \frac{2}{C} * \frac{d[IL]}{dt}, \quad C = 2 * [IL] + [SC] \quad (3.6)$$

As described previously, this statistical description is utilized only for the initial breakdown, and more detailed pyrolysis and gasification chemistry will be utilized on small oligomers. The output from the statistical method, $\frac{d[IL]}{dt}$, must therefore supply the input to the explicit material balances for the oligomers in the

molecular model. The Flory distribution is scaled such that the boundary oligomers occur at $i=l$. This effectively transforms the l -mer from a monomer to an oligomer in the distribution. The oligomer molar flow rate is then given in Equation 3.7 and represented by N_1 . Equation 3.8 gives the increase in N_1 from depolymerization.

$$N_1 = \frac{C}{2} * (1 - p)^2 \quad (3.7)$$

$$\frac{dN_1}{dt} = \frac{C}{2} * -2 * (1 - p) * \frac{dp}{dt} = -2 * (1 - p) * \frac{d[IL]}{dt} \quad (3.8)$$

3.4.1.2 Random Scission Method for a Generalized Polymer Size Distribution

For polymers modeled using more complex polymer size distributions, the random scission method is not as easily applied. For instance, in this work, polystyrene was represented using a gamma distribution. Rather than utilizing a method specific to gamma distributions, the far more interesting derivation is for a generalized polymer-size distribution. In the general case, consider the polymer size distribution as a histogram, as illustrated in Figure 3.3, where the mole fraction of every mer is independent. The goal, as before, is to correlate the changes in linkage concentration to the changes in molar flow rates of mers in the system. This allows for a prediction of the histogram after depolymerization.

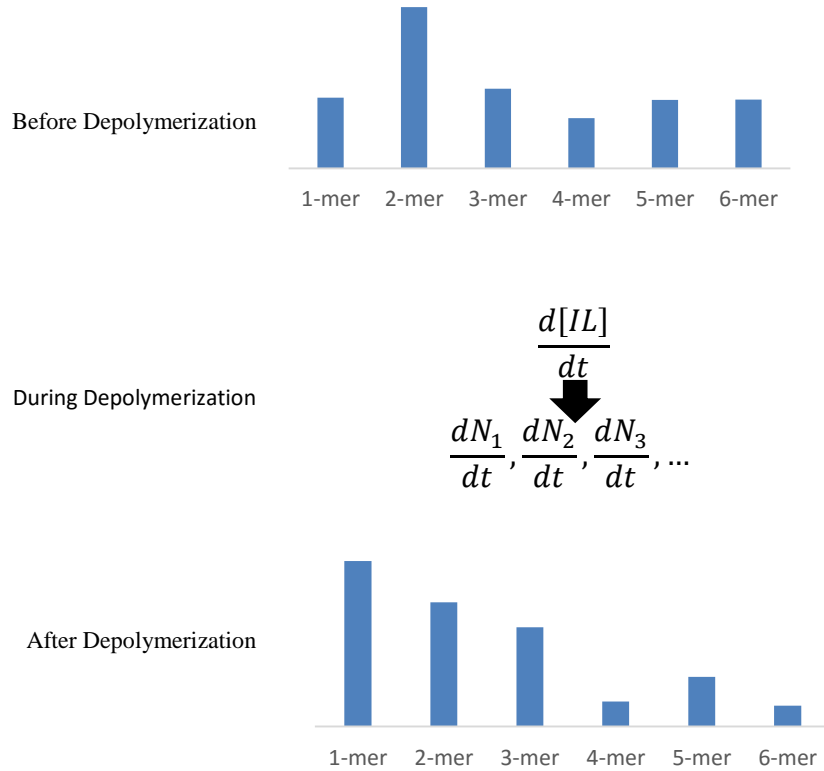


Figure 3.3: Conceptual goal of random scission for a generalized polymer size distribution. Top and bottom figures are representative n -mer distributions.

The aim of this derivation is to map ΔN_{IL} (equivalently $\frac{d[IL]}{dt}$) to ΔN_i for all i -mers. The probability of a bond breaking in the backbone is given in Equation 3.9 and is independent of polymer size due to the assumption of random scission. For a given i -mer, up to $(i-1)$ bond breaking events can occur as shown in the 4-mer example in Table 3.3. The probability of each event follows a simple binomial distribution. The more general equation is given in Equation 3.10 for n bond breaking events.

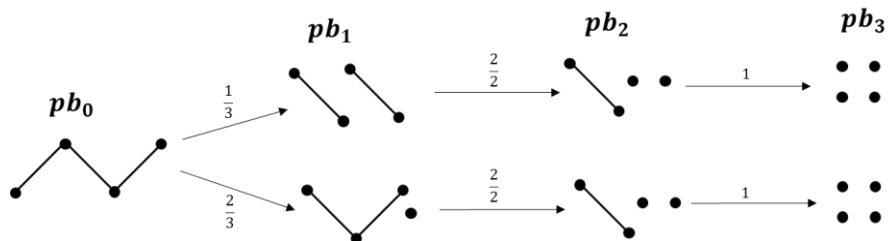
$$p_{break} = \frac{\Delta N_{IL}}{N_{IL}} \quad (3.9)$$

$$pb_n = (1 - p_{break})^{i-1-n} * p_{break}^n * \binom{i-1}{n} \quad (3.10)$$

Table 3.3: Probability of bonds broken within a 4-mer.

Bonds Broken	Probability
0	$pb_0 = (1 - p_{break})^3 * \binom{3}{0}$
1	$pb_1 = (1 - p_{break})^2 * p_{break} * \binom{3}{1}$
2	$pb_2 = (1 - p_{break}) * p_{break}^2 * \binom{3}{2}$
3	$pb_3 = p_{break}^3 * \binom{3}{3}$

After calculating the probability of bond breaking events in an i -mer, the next step is to calculate the amount of smaller mer production. For example, 4-mer breakdown is shown in Figure 3.4. If a single bond breaking event occurs in a 4-mer, there are three possible bonds to break. Two of the three bonds produce a trimer and a monomer, and the other bond produces 2 dimers. The expected production from one bond breaking event is therefore $\frac{2}{3}$ of each smaller mer. This method is extended to multiple bond breaking events. The breakdown matrix format is easier to visualize, each row corresponds to a bond breaking event. The columns correspond to the relative amounts of each j -mer produced by that specific event.



	1-mer	2-mer	3-mer	4-mer
pb_0	0	0	0	1
pb_1	$\frac{2}{3}$	$\frac{2}{3}$	$\frac{2}{3}$	0
pb_2	2	1	0	0
pb_3	4	0	0	0

Figure 3.4: Illustration (top) and breakdown matrix representation (bottom) of possible bond breaking events in a 4-mer. Values in the matrix are relative initial amount of 4-mer.

Each *i-mer* has its own unique breakdown matrix; however, all breakdown matrices can be filled using a generalized formula, given in Equation 3.11. The terms of this equation are described using Table 3.4. The general logic is that each row in the matrix is filled sequentially. The first row is known, if zero bond breaking events occur, then the *i-mer* remains unreacted. For subsequent rows, each column (*j-mer*) is calculated using a standard balance format: (value from previous bond breaking event) – (consumption in this bond breaking event) + (production in this bond breaking event).

$$m_{n+1,j} = m_{n,j} - m_{n,j} * \frac{j-1}{i-j} + \sum_{k=j+1}^{i-n+1} m_{n,k} * \frac{k-1}{i-n} * \left(\frac{2}{k-1}\right) \quad (3.11)$$

Table 3.4: Description of terms Equation 3.11. The notation is $m_{row,column}$ for the breakdown matrix. The row corresponds to total number of bonds breaking in the i -mer. The column corresponds to the production of smaller j -mers from the breakdown of i -mer.

Term	Description
$m_{n+1,j}$	Breakdown matrix value for row (n+1), column j.
$m_{n,j}$	Value from the previous break for j-mer.
$m_{n,j} * \frac{j-1}{i-j}$	Amount of j-mer breaking down in this bond breaking event
$\sum_{k=j+1}^{i-n+1} m_{n,k} * \frac{k-1}{i-n} * \left(\frac{2}{k-1}\right)$	j-mer production from larger k-mers

With the breakdown matrices filled for all i -mers, the remaining step is to calculate the new values for molar flow rates of each i -mer, $N_{i,new}$. The formula, given by Equation 3.12, simply loops over all larger mers and utilizes the values from the breakdown matrices to calculate the new flow rate. This result gives the complete updated histogram for a change in IL concentration.

$$N_{i,new} = \sum_{j=i}^{max} N_{j,old} * \left(\sum_{k=0}^{(j-1)} pb_k * (m_{k,i}) \right), \text{ where } max \text{ is the largest mer} \quad (3.12)$$

In order to address numerical issues with large n-mers, two simplifications can be made in the use of this algorithm. Because this method is used in conjunction with a system of differential equations, ΔIL in any given time step is small. This allows for the simplification that only a few bond breaking events occur in any given reaction

step. This reduces the numerical complexity that arises in the combinatorial term in the binomial calculation in Equation 3.10. The second simplification is to lump similarly-sized mers. For example, if histogram only tracks every 20-mers, then much longer mers can be calculated quickly while only losing the more minute detail.

3.4.1.3 Depolymerization Chemistry – PE

The thermal depolymerization of polyethylene proceeds via a radical cracking mechanism[68] containing two primary mechanistic steps: H-abstraction and β -scission, shown in Figure 3.5. The products from depolymerization arise from relative stabilities of radicals. For instance, after a cracking reaction, the instability of the primary product radical means unzipping is unlikely to occur, and monomer yield is low[68]. Instead, the product from β -scission is likely to abstract a hydrogen either intramolecularly or intermolecularly. In the intramolecular case, H-abstraction occurs on the same chain, likely at the 6-carbon location due to a 6-member ring transition state[69]; this step is often called backbiting. If H-abstraction occurs intermolecularly, then the depolymerization has random-scission type behavior. In order to accommodate both mechanisms, the initial breakdown was performed using random scission, and 3-mer was selected as the largest oligomer for full pyrolytic detail.

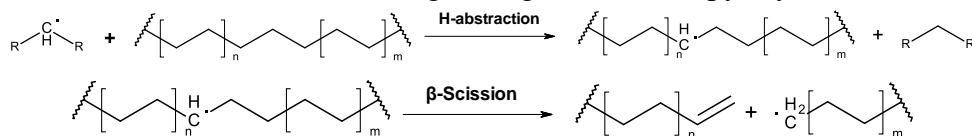


Figure 3.5: Radical propagation steps for polyethylene depolymerization. The H-abstraction step shown here is inter-molecular and can occur with any radical in the system.

There are three possible 6-carbon oligomers from the thermal cracking of polyethylene: hexane, hex-1-ene, and hexa-1,5-diene shown in Figure 3.6. In this mechanism, each bond breaking event produces one double bond end group and one single bond end group. It therefore follows that there should be approximately a 1:2:1 ratio of these products. If the assumption is made that all initial end groups are saturated, then the ratio is slightly skewed toward hexane. During depolymerization, the link cleavage reaction in Equation 3.5 keeps track of the relative amounts of single bond and double bond end groups. This allows for the ratio of 6-carbon oligomers to be calculated at any time.

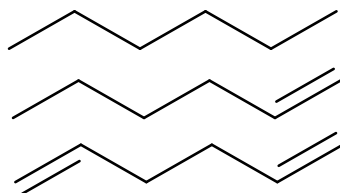


Figure 3.6: Oligomers with 6-carbons produced during polyethylene depolymerization. These are the starting molecules from polyethylene for the full pyrolysis and gasification network.

3.4.1.4 Depolymerization Chemistry – PET

The thermal depolymerization of PET follows the mechanism[70],[71] shown in Figure 3.7. Because this mechanism is concerted and thermal, the random scission assumption applies. For PET, a dimer was chosen as the oligomer size for more detailed chemistry. This allowed the inclusion of a charring mechanism to occur on the PET linkage as will be shown later when discussing pyrolysis. Again, there are three possible 2-mers based on the different combinations of end groups.

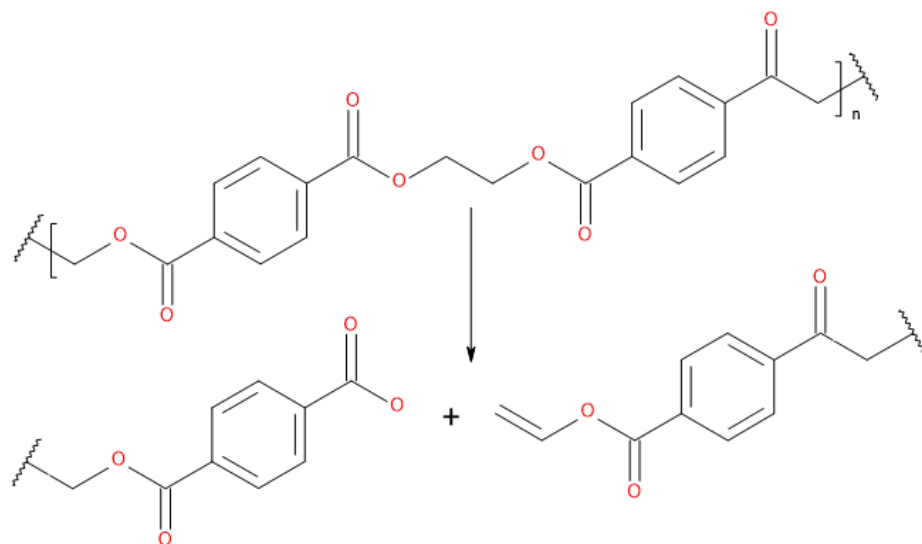


Figure 3.7: Link cleavage in polyethylene terephthalate (concerted mechanism).

3.4.1.5 Depolymerization Chemistry – PVC

The depolymerization of polyvinylchloride is modeled as a two-step depolymerization given in Figure 3.8. The first step, dehydrochlorination, occurs very quickly producing HCl and a poly-ene structure[68], [72]. The second step of PVC breakdown is less well understood and far slower. Benzene is one of the most common volatile products from thermal breakdown[73]. To account for benzene production, a pinch-off mechanism[72] was utilized to further breakdown the polyene structure.

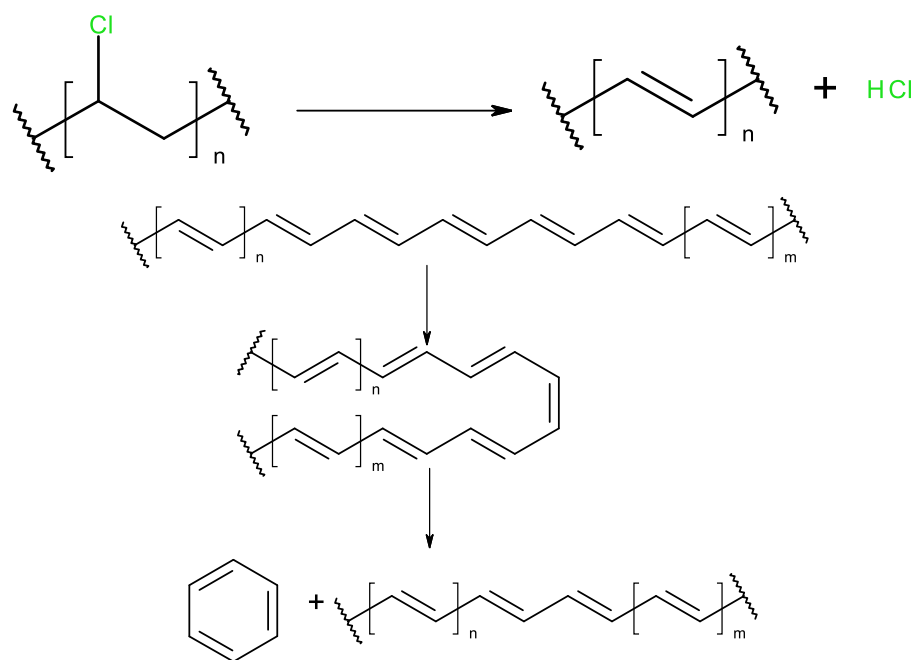
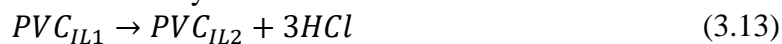


Figure 3.8: Two-step depolymerization of polyvinyl chloride.

Unlike PE and PET, PVC is not modeled using a random scission mechanism. Instead, there are two reactions, given in Equation 3.13 and Equation 3.14. Dehydrochlorination occurs on the original PVC molecule and produces 3 HCl for every 6 carbons. This step also changes the backbone to a polyene structure, represented here by PVC_{IL2} . The pinch-off mechanism occurs only on the poly-ene structure and produces a benzene every link cleavage; thereby eliminating the need to track the polymer size distribution during depolymerization. The transition point to full pyrolysis and gasification chemistry occurs at benzene for PVC.

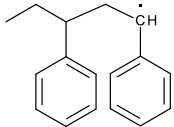
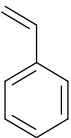
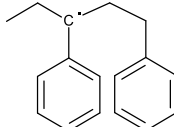
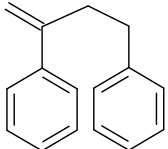
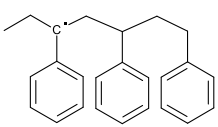
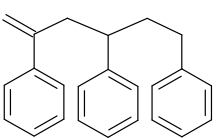
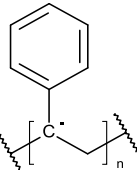


3.4.1.6 Depolymerization Chemistry – PS

The depolymerization of polystyrene is a radical cracking mechanism. Differences between the polymers is due to the stability of the radicals shown in Table 3.5. Unlike polyethylene, the end-group radical is a benzylic radical and is stable allowing for unzipping-type mechanisms to occur. Also, there are two stable intramolecular H-abstraction reactions leading to backbiting and production of dimers and trimers. Finally, as before, intermolecular H-abstraction can occur in a random-scission type mechanism. All of these mechanisms were included in the depolymerization model.

A multi-step breakdown method was used for polystyrene depolymerization. For the initial breakdown from large n-mer, random scission for a generalized polymer size distribution was utilized with 20-mer lumps. For 20-mer and smaller, a standard population balance was used with a differential equation for every mer. Depolymerization reactions for all four mechanisms from Table 3.5 were included on these mers. Finally, for styrene monomers, full pyrolysis and gasification chemistry was allowed to break down the structure into light gases.

Table 3.5: Stable radicals and products from included mechanisms in polystyrene degradation.

Type	Stable Radical	Products
Unzipping		
Dimer Backbiting		
Trimer Backbiting		
Random Scission		Spectrum of mono- and di-olefin n-mers

3.4.2 Pyrolysis of Oligomers

Pyrolysis chemistry occurs without the presence of reactive gases. In the case of plastics, there are two general types of pyrolysis reactions: cracking reactions which serve to break down molecules and charring reactions which serve to build up stable higher-MW species. In this network, the dominant cracking reaction families were acyclic thermal cracking, decarboxylation, and decarbonylation given in Table 3.6. These reaction families are well known and have been used in previous models[74]. Less common cracking mechanisms, ester decarboxylation and rearrangement, were proposed in the PET pyrolysis literature[75], and were included in this model.

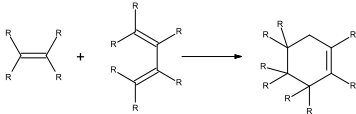
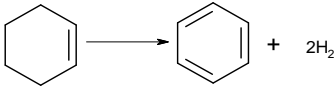
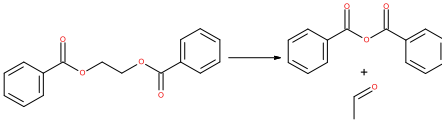
Table 3.6: Pyrolysis cracking reaction families, reaction matrices, and example reactions. The reaction matrix contains -1 for bond-breaking and 1 for bond-making during reaction.

Reaction Type (Family) and Reactive Moety	Reaction Matrix	Example Reaction																									
Decarboxylation Aldehydes	<table border="1"> <tr><td></td><td>H</td><td>O</td><td>C</td><td>R</td></tr> <tr><td>H</td><td>0</td><td>0</td><td>-1</td><td>1</td></tr> <tr><td>O</td><td>0</td><td>0</td><td>1</td><td>0</td></tr> <tr><td>C</td><td>-1</td><td>1</td><td>0</td><td>-1</td></tr> <tr><td>R</td><td>1</td><td>0</td><td>-1</td><td>0</td></tr> </table>		H	O	C	R	H	0	0	-1	1	O	0	0	1	0	C	-1	1	0	-1	R	1	0	-1	0	
	H	O	C	R																							
H	0	0	-1	1																							
O	0	0	1	0																							
C	-1	1	0	-1																							
R	1	0	-1	0																							
Decarboxylation Carboxylic acids	<table border="1"> <tr><td></td><td>H</td><td>O</td><td>C</td><td>R</td></tr> <tr><td>H</td><td>0</td><td>-1</td><td>0</td><td>1</td></tr> <tr><td>O</td><td>-1</td><td>0</td><td>1</td><td>0</td></tr> <tr><td>C</td><td>0</td><td>1</td><td>0</td><td>-1</td></tr> <tr><td>R</td><td>1</td><td>0</td><td>-1</td><td>0</td></tr> </table>		H	O	C	R	H	0	-1	0	1	O	-1	0	1	0	C	0	1	0	-1	R	1	0	-1	0	
	H	O	C	R																							
H	0	-1	0	1																							
O	-1	0	1	0																							
C	0	1	0	-1																							
R	1	0	-1	0																							
Acyclic Thermal Cracking Hydrocarbon side chains and irreducible molecules	<table border="1"> <tr><td></td><td>C</td><td>C</td><td>C</td><td>H</td></tr> <tr><td>C</td><td>0</td><td>-1</td><td>0</td><td>1</td></tr> <tr><td>C</td><td>-1</td><td>0</td><td>1</td><td>0</td></tr> <tr><td>C</td><td>0</td><td>1</td><td>0</td><td>-1</td></tr> <tr><td>H</td><td>1</td><td>0</td><td>-1</td><td>0</td></tr> </table>		C	C	C	H	C	0	-1	0	1	C	-1	0	1	0	C	0	1	0	-1	H	1	0	-1	0	
	C	C	C	H																							
C	0	-1	0	1																							
C	-1	0	1	0																							
C	0	1	0	-1																							
H	1	0	-1	0																							
Ester Decarboxylation Esters	<table border="1"> <tr><td></td><td>H</td><td>O</td><td>C</td><td>C</td></tr> <tr><td>H</td><td>0</td><td>-1</td><td>0</td><td>1</td></tr> <tr><td>O</td><td>-1</td><td>0</td><td>1</td><td>0</td></tr> <tr><td>C</td><td>0</td><td>1</td><td>0</td><td>-1</td></tr> <tr><td>C</td><td>1</td><td>0</td><td>-1</td><td>0</td></tr> </table>		H	O	C	C	H	0	-1	0	1	O	-1	0	1	0	C	0	1	0	-1	C	1	0	-1	0	
	H	O	C	C																							
H	0	-1	0	1																							
O	-1	0	1	0																							
C	0	1	0	-1																							
C	1	0	-1	0																							
Ester Rearrangement Esters adjacent to a double bond	<table border="1"> <tr><td></td><td>H</td><td>O</td><td>C</td><td>C</td></tr> <tr><td>H</td><td>0</td><td>-1</td><td>0</td><td>1</td></tr> <tr><td>O</td><td>-1</td><td>0</td><td>1</td><td>0</td></tr> <tr><td>C</td><td>0</td><td>1</td><td>0</td><td>-1</td></tr> <tr><td>C</td><td>1</td><td>0</td><td>-1</td><td>0</td></tr> </table>		H	O	C	C	H	0	-1	0	1	O	-1	0	1	0	C	0	1	0	-1	C	1	0	-1	0	
	H	O	C	C																							
H	0	-1	0	1																							
O	-1	0	1	0																							
C	0	1	0	-1																							
C	1	0	-1	0																							

The formation of char and tar products is observed throughout the plastics pyrolysis literature. For example, if a PET sample undergoes thermogravimetric analysis (TGA) in a nitrogen atmosphere, 15-20 wt% remains solid even after reaching 700 °C[76]. The literature speculates the formation of a stable anhydride linkage in the

PET backbone [70], [71], [77]; this reaction and other char reactions are detailed in Table 3.7. For PVC, char formation originates from the poly-ene structure following dehydrochlorination. In this work, PVC char is modeled as mass remaining in the poly-ene backbone. For polyethylene, the included char formation pathways involve Diels-Alder[57] reactions followed by dehydrogenation to aromatic rings[68], [73], [78], [79]. While no explicit char formation pathways are included for polystyrene, the monomers fall under the tar category, where tars are defined here as volatile compounds with boiling point greater than or equal to benzene, and are of great importance to gasification processes.

Table 3.7: Pyrolysis reactions used to build aromatic, polyaromatic char molecules.

Reaction Type (Family) and Reactive Moeity	Example Reaction	Reaction Rules
Diels-Alder Addition Diene, dienophile		2 and 6 carbon dieneophiles were allowed to react with 4 carbon dienes.
Multistep Dehydrogenation to Aromatic Rings Naphthenic Rings		Reactions allowed on cyclic enes.
PET Anhydride Linkage Formation Hydrocarbon side chains and irreducible molecules		Only PET linkages on dimers.

3.4.3 Gasification of Oligomers

Gasification chemistry includes reactions with gasification agents such as oxygen, carbon dioxide, or water. As discussed, many polymers produce char or tar products under pyrolysis conditions. Gasification reactions eliminate these heavy molecules through the reaction with gasification agents. For example, although PET forms char under pyrolysis conditions, after inclusion of oxygen, all char is consumed in a TGA experiment[60]. The two primary gasification reaction families included were incomplete combustion and steam reforming as shown in Table 3.8. The model also contained a number of light gas reactions, such as water-gas shift.

Table 3.8: Gasification reactions included in the model. The reversibility of light gas reactions was determined based on the equilibrium constants at reactor conditions.

Reaction Type	Reaction
Incomplete Combustion	Example $C_3H_8 + 3.5O_2 \rightarrow 3CO + 4H_2O$
	General $C_xH_yO_z + \frac{x + \frac{y}{2} - z}{2} O_2 \rightarrow xCO + \left(\frac{y}{2}\right) H_2O$
Steam Reforming	Example $C_3H_8 + 3H_2O \rightarrow 3CO + 7H_2$
	General $C_xH_yO_z + (x - z) H_2O \rightarrow xCO + \left(\frac{y}{2} - (x - z)\right) H_2$
Water-Gas Shift	$CO + H_2O \leftrightarrow CO_2 + H_2$
Steam Reforming Methane to CO	$CH_4 + H_2O \leftrightarrow CO + 3H_2$
Partial Oxidation of Methane	$CH_4 + \left(\frac{1}{2}\right) O_2 \rightarrow CO + 2H_2$
Dry Reforming of Methane	$CH_4 + CO_2 \leftrightarrow 2CO + 2H_2$
Oxidation of CO to CO2	$CO + \left(\frac{1}{2}\right) O_2 \rightarrow CO_2$

3.5 Network Generation

Using the depolymerization, pyrolysis, and gasification chemistries, the reaction network was generated using in-house software tools. First, a reaction network was made for the pyrolysis of each plastic oligomer using the Interactive Network Generator, INGen[44], [80]. These networks were then merged together using INGenNetworkMerge, a C# application; this application also added gasification reactions to the network. Finally, link cleavage reactions (e.g., $PE_{IL} \rightarrow PE_{SC0} + PE_{SC1}$) representing the breakdown of the polymer backbone were added manually to the merged network. The features of the final reaction network are given Table 3.9.

In the final reaction network, the initial depolymerization contained reaction families for each plastic, including four total families for the competition of polystyrene depolymerization mechanisms. The pyrolytic breakdown of oligomers and formation of tar and char molecules was described using five and three reaction families, respectively. Finally, gasification included general incomplete combustion and steam reforming reactions common to all plastics as well as a reaction family specific to PET char breakdown. The final network containing 283 reactions and 85 species was used to build the kinetic model.

Table 3.9: Reaction network diagnostics for the plastics model.

Reaction Family	Reaction Count	Adjustable Parameters	Constraints
<u>Depolymerization</u>			
PE Depolymerization	4	2	0
PET Depolymerization	4	2	0
PVC Depolymerization	3	2	0
Polystyrene Random Scission	102	2	0
Polystyrene Backbiting (dimer)	18	2	0
Polystyrene Backbiting (trimer)	17	2	0
Polystyrene Unzipping	19	2	0
<u>Pyrolysis</u>			
Acyclic Thermal Cracking	27	3	0
Decarboxylation	12	2	2
Decarbonylation	3	2	2
Ester Decarboxylation	2	2	2
Ester Rearrangement	2	2	0
<u>Char Formation</u>			
PET Anhydride Formation	6	2	0
Diels-Alder	4	2	0
Aromatic Ring Formation	4	2	0
<u>Gasification</u>			
Incomplete Combustion	19	2	0
Steam Reforming	18	2	2
PET Anhydride Breakdown	14	2	0
Light Gas Reactions	5	10	2
<u>Total Reactions</u>	283		
<u>Total Species</u>	85		

3.6 Model Equations and Kinetics

The reaction network was used to generate a set of material balance differential equations with one equation per molecular species. This model was built and solved using an in-house software, the Kinetic Model Editor (KME)[40]. In general, the rate laws used standard mass-action kinetics and Arrhenius rate constants. Exceptions to

this rule were in the gasification reactions where the kinetics were assumed to be first order with respect to oxygen and water for incomplete combustion and steam reforming respectively.

The number of adjustable parameters in the model was reduced using the concept of reaction families and linear free energy relationships (LFER). All reactions in a given reaction family are modeled to have the same pre-exponential factor. Furthermore, the activation energies are modeled to follow the Bell-Evans-Polanyi[51], [52] LFER which relates activation energy of individual reactions to the enthalpy of reaction. The final form of the rate constant, derived in prior work[42], [48], is given in Equation 3.15 for reaction i and reaction family j . In general, this constrains the number of adjustable parameters to three per reaction family; however for this work, only acyclic thermal cracking utilizes α_j . All other reaction families contained two adjustable parameters, A_j and $E_{0(j)}$. This modeling approximation states that reaction rate constants for the reactions in the other families are equal for all reactions in the family.

The number of adjustable parameters was further constrained using parameter values from the open literature. In particular, constraints were placed on many of the pyrolysis and gasification parameters. For pyrolysis, rate parameters from the literature were utilized for decarboxylation and decarbonylation[74]. Ester decarboxylation was modeled to have the same rate parameters as decarboxylation. For gasification, reactions with oxygen are much faster than reactions with CO₂ or H₂O. Steam reforming was constrained to be slower and proportional to incomplete combustion. Finally, literature values were assumed for the water-gas shift[81].

$$\ln k_i = \ln A_j - \left(\frac{E_{0(j)} + \alpha_j * \Delta H_i}{RT} \right) \quad (3.15)$$

3.7 Model Evaluation

Literature studies provided the data to evaluate the kinetic model. The polyethylene study was used to probe the kinetics of polyethylene degradation, pyrolysis, gasification, and polyethylene char formation reactions. The PET study was to demonstrate the ability of molecular-level models to predict thermogravimetric analysis (TGA) experiments while analyzing the competition between polymer breakdown, PET char formation, and PET char breakdown. The PVC study was used to obtain rate constants for dehydrochlorination and the subsequent reaction producing benzene. Finally, the polystyrene study allowed for the analysis of the competition between the different depolymerization mechanisms.

3.7.1 Model Evaluation – PE

The polyethylene study utilized a pilot-plant scale fluidized bed gasifier using both oxygen and steam as gasifying agents for polyethylene consumption[23]. The experiments of interest are summarized in Table 3.10. Experimental runs 3-7 from this study were selected because they were uncatalyzed and used air as the oxidation agent. The reported results included input flow rates of polyethylene, air, output syngas composition, and tar flow rate.

Table 3.10: Utilized experiments from Arena et al[23].

	Run 3	Run 4	Run 5	Run 6	Run 7
<i>Polyethylene Flow Rate (kg/hr)</i>	16.7	21.8	27.9	20.0	31.0
<i>Air Flow Rate (kg/hr)</i>	64.3	77.2	90.1	90.1	90.1
<i>Temperature (°C)</i>	850	869	867	898	845
<u><i>Synqas Composition (vol%)</i></u>					
<i>N₂</i>	68.7	65.7	64.6	69	63.9
<i>CO</i>	2.7	2.5	2.4	2.3	2.8
<i>H₂</i>	7.4	9.1	9.6	8.3	9.1
<i>CO₂</i>	9.5	9.6	9.6	10.4	9.1
<i>CH₄</i>	8.3	8.8	9.1	7.1	10.4
<i>C₂H_x</i>	3.4	4.4	4.6	2.9	4.8
<i>Output Tar Flow Rate(kg/hr)</i>	6.2	7.8	12.1	7.0	14.6

The model tuning results are shown in Figure 3.9. The C₂H_x fraction was the combined flow rate of ethane, ethylene, and acetylene. Tars were classified as compounds with a boiling point greater than or equal that of benzene. The model showed good agreement with experimental results with $y_{predicted} = 0.952 * y_{experimental} + 0.0036$. Figure 3.10 shows a comparison between experimental and predicted liquid/gas mass ratio. The model results showed agreement with experimental results, with small under-predictions on runs 5 and 7.

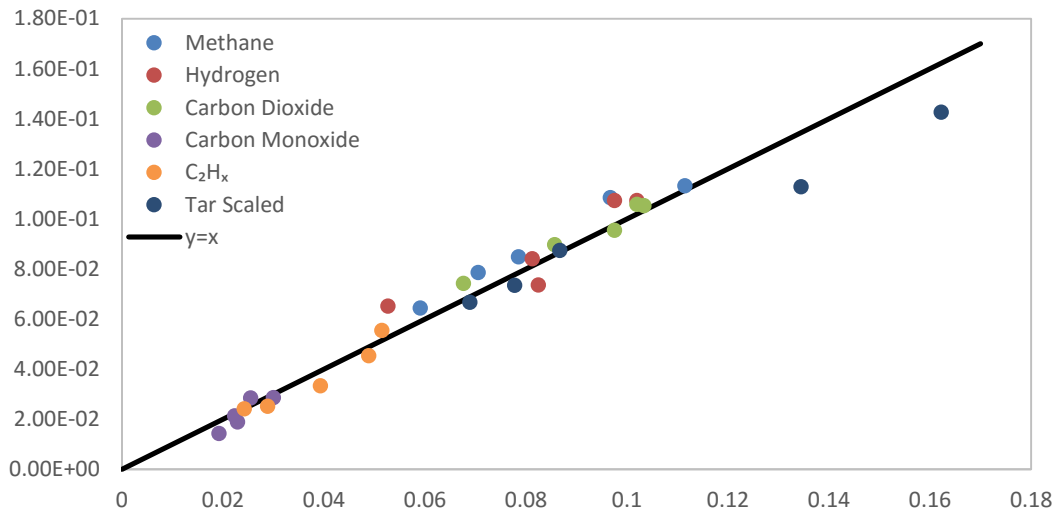


Figure 3.9: Tuning results for all data sets. The linear fit has the equation $y_{\text{predicted}}=0.952*y_{\text{experimental}}+0.0036$. Tar yield is in units of (g/s/25); it was rescaled to have a similar value as the light gas flow rates (mol/s).

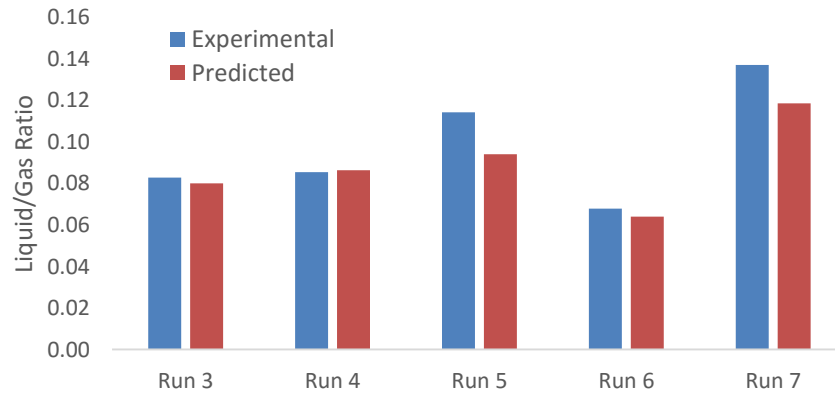


Figure 3.10: Comparison of experimental and model predicted results for liquid/gas ratio (mass basis) for all data sets.

In order to further examine deviations between model and experimental results, the effects of uncertainty in the reported measurements were analyzed in Figure 3.11. For GC measurements, the standard error was 0.05 vol% due to the number of

reported significant figures in Arena et al[23]; similarly, the error in tar flow was 0.05 kg/hr. For tar, the model prediction is as good as the reported significant figures. The experimental results reported an average temperature; however, minor temperature deviations in the reactor are possible. To analyze these effects on model predictions, a 10 degree temperature variation was studied on Run 6. The results were shown to be relatively insensitive to minor changes in temperature, implying that deviations from the average temperatures in Table 3.10 would have little impact on modeling results.

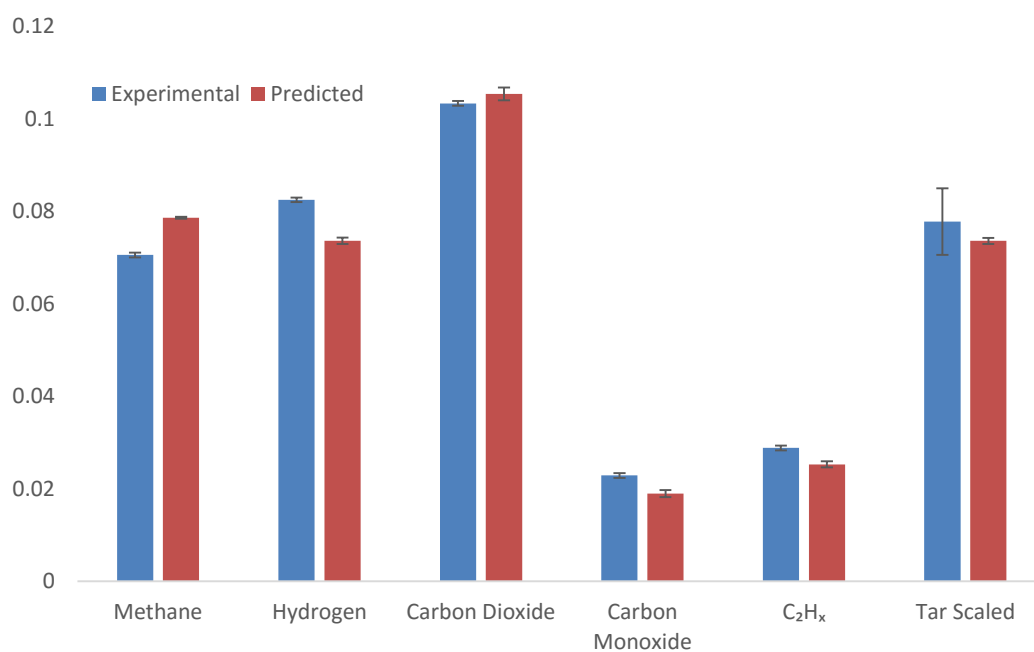


Figure 3.11: Experimental error and the effects of temperature deviation in model predictions for Run 6. Effects of a 10 degree temperature variation are shown using error bars.

3.7.2 Model Evaluation – PET

For polyethylene terephthalate, a thermogravimetric analysis (TGA) [60] study with oxidative depolymerization provided TGA curves for different heating rates of

PET using air as the carrier gas. This allowed for the analysis of PET depolymerization, char formation, and subsequent char breakdown with oxygen. A software tool was developed in order to utilize TGA data in a molecular-level kinetic model.

The simulation of TGA with a molecular-level kinetic model was performed using an in-house software called TGA Simulator; a C# application developed for this work. The logic for the TGA simulator is given in Figure 3.12. In order to simulate a constant heating rate, TGA Simulator repeatedly calls the ODE solver (within KME) using isothermal runs for short duration where the output of one simulation is the input to the next simulation. For example, if the heating rate is 10K per minute starting at 298K then TGA simulator would integrate for 6 seconds at 298K, 6 seconds at 299K, and so forth. The TGA Simulator predicts mass-loss based on the molar amounts, boiling points, and flow rates of each component.

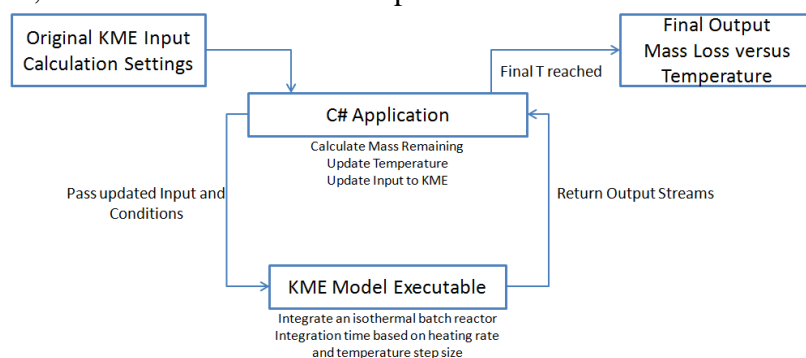


Figure 3.12: Logic for the TGA Simulator C# application

The results in Figure 3.13 show the experimental and predicted TGA curves. There are three regions of interest on this graph: the initial mass loss, char formation, and char consumption. The majority of the initial drop is due to PET

depolymerization; however, any reaction that causes molecular breakdown also plays a role in the initial region of the curve. The relative rates between the breakdown chemistry and PET anhydride formation determine the amount of char initially formed. The char consumption is known to occur under gasification conditions. For instance, an analogous study by Du and coworkers on pyrolysis showed a persistent char.[76] Similarly, Figure 3.14 shows remaining char when oxygen is removed from the simulation. Because our results are the combination of many reaction families and rate parameters, it is difficult to draw a connection to parameters derived from traditional TGA analyses; however, the fit of the raw data implies agreement between experiment and model results.

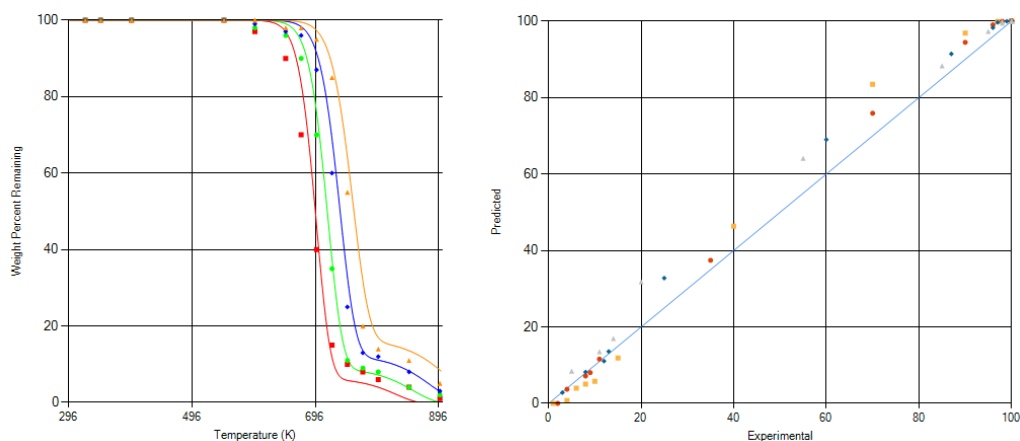


Figure 3.13: TGA model results (lines) compared with experiment (points). Colors correspond to different heating rates: red, 5 °C/min; green, 10 °C/min; blue, 20 °C/min; orange, 40 °C/min. The left plot gives the TGA curves, the right plot is a parity plot of the results. The maximum decomposition rates in units of wt%/°C are 0.018, 0.17, 0.015, and 0.041 in order of increasing heating rate.

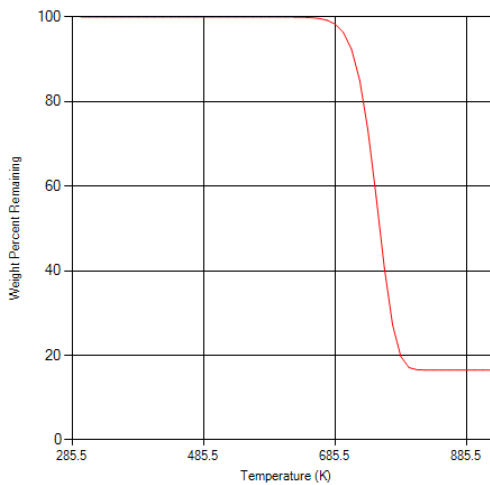


Figure 3.14: TGA Simulator results showing persistence of char in the absence of oxygen for PET depolymerization at a heating rate of 40 °C/min.

3.7.3 Model Evaluation – PVC

The tuning effort for PVC was focused on a study in a bubbling fluidized bed to probe the kinetics of dehydrochlorination and PVC char formation[82]. In this study, there were two uncatalyzed experiments and five catalyzed experiments. In general, the experiments of interest are uncatalyzed as this is more similar to applications such as MSW gasification. However, dehydrochlorination is known to be fast[68], [73] and kinetics are not expected to be limiting which allows for the usage of all seven experiments. The catalyst does affect char formation and therefore only uncatalyzed data sets were used for char analysis.

Table 3.11: HCl and char from all experiments in Slapak et al.[82] Q1 and Q2 are uncatalyzed (quartz sand bed). A1, A2, and all A3 experiments were under alumina support. *- data points not used in char analysis due to catalyst effects on char formation.

Experiment	HCl (wt% PVC)	Char (wt% PVC)
Q1	54	35
Q2	35.2	33
A1	57	16*
A2	54	16*
A3-1150K	54	16*
A3-1200K	54	9*
A3-1250K	54	3*

Results from PVC kinetic parameter tuning are given in Figure 3.15. The char predictions for the two uncatalyzed experiments matched well with the experimental data. For HCl, six of the seven data sets were predicted well. The remaining data point, Q2, is expected to be an outlier or a typographical error because it is well known that approximately 55 wt% of PVC is quickly released in the initial depolymerization step[68], [73].

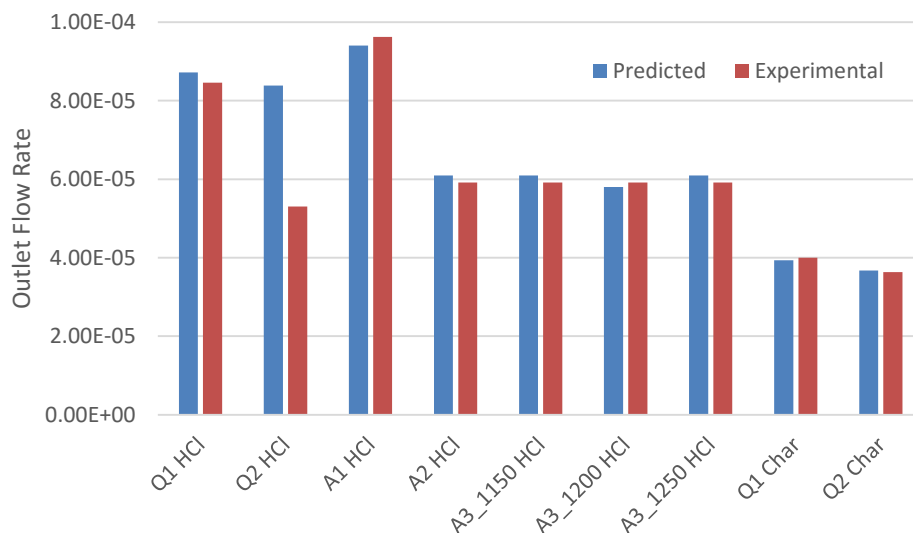


Figure 3.15: Results for HCl (all runs) and Char (only Q1 and Q2). The outlet flow rate units for HCl and char are in mol/s and g/s/50 respectively.

3.7.4 Model Evaluation – PS

The polystyrene tuning study focused on the probing the different depolymerization mechanisms using literature on pyrolysis in a fluidized bed[67]. The results of interest were relative amounts of mono-, di-, and tri- aromatics after pyrolysis over a range of temperatures, as shown in Table 3.12. The kinetic parameters were tuned to these data sets with results shown in Figure 3.16. Overall the fit was good with $y_{predicted} = 0.9595y_{experimental} + 0.0217$. The largest deviation was seen in the 450 °C data set. This data set is less important as the temperature in most gasification applications is significantly higher.

Table 3.12: Experimental weight percent values for monoaromatics, diaromatics and triaromatics in pyrolysis output at different temperatures[67]. All values are in weight percent of initial polystyrene.

Temperature	Monomer	Dimer	Trimer
450 °C	72	11	14
500 °C	76	13.5	7
550 °C	79	15	2
600 °C	87	12	---

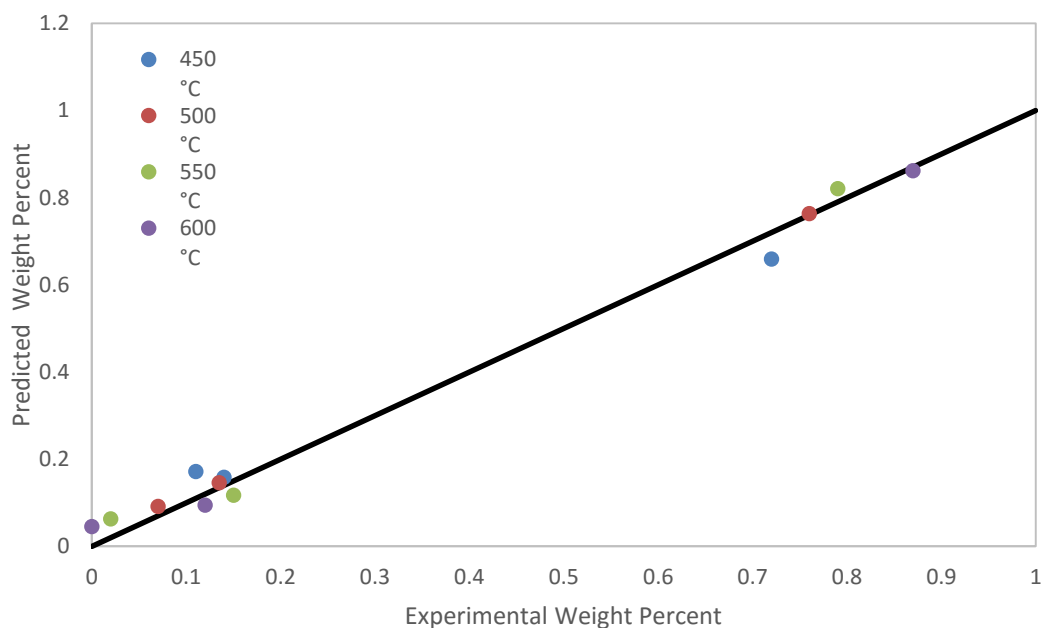


Figure 3.16: Parity plot for monomer-trimer predictions for polystyrene pyrolysis. A least-squares linear fit of the data gives $y_{\text{predicted}} = 0.9595y_{\text{experimental}} + 0.0217$

3.7.5 Reaction Family Rate Constants

After evaluation and optimization with all data sets, a tuned set of kinetic parameters was developed and are given in Table 3.13. In this table, the rate constants are relative to the rate constant for Acyclic Thermal Cracking.

Table 3.13: Reaction family rate constants at 1000 K relative to Acyclic Thermal Cracking. $\log(k)_{\text{relative},1000} = \log(k)_{\text{AcyclicThermalCracking},1000} - \log(k)_{\text{ReactionFamily},1000}$.

Reaction Family	$\log(k)_{\text{rel},1000}$
Depolymerization	
PE Depolymerization	1.60
PET Depolymerization	-2.57
PVC Depolymerization - Dehydrochlorination	-1.95
PVC Depolymerization - Benzene Formation	-8.17
Polystyrene Random Scission	-2.95
Polystyrene Backbiting (dimer)	-7.63
Polystyrene Backbiting (trimer)	-2.49
Polystyrene Unzipping	-5.34
Pyrolysis	
Acyclic Thermal Cracking	0.00
Decarboxylation	2.40
Decarbonylation	2.40
Ester Decarboxylation	2.40
Ester Rearrangement	-2.58
Char Formation	
PET Anhydride Formation	1.98
Diels-Alder	-2.83
Aromatic Ring Formation	-0.76
Gasification	
Incomplete Combustion	-4.00
Steam Reforming	-7.30
PET Anhydride Breakdown	-1.92
Light Gas Reactions	
Water-gas Shift	-6.83
Oxidation CO to CO ₂	-3.14
Partial Oxidation of Methane (forward)	-7.10
Steam Reforming of Methane (reversible)	-5.90
Dry Reforming of Methane (reversible)	-6.84

3.8 Conclusions

A molecular-level kinetic model was developed for the gasification of four common plastics: PE, PVC, PET, and PS. The model's parameters were tuned using literature studies on each of the plastics. The model includes the kinetics of the formation and degradation of tar and char molecules from these wastes, which are important design considerations for waste-to-energy technologies such as MSW gasification.

Furthermore, because this model is at the molecular-level, it can be used to help predict changes in syngas composition in the gasifier outlet as a function of the MSW composition. This could be used to help process engineers design better waste streams for a gasification unit. The robustness of a molecular-level model is especially important in the application of MSW because the waste composition is likely to change as a function of season and location. Only models containing fundamental chemistry have a hope of modeling such a diverse set of conditions.

Chapter 4

MOLECULAR-LEVEL KINETIC MODELING OF BIOMASS GASIFICATION

Scott R. Horton¹, Rebecca Mohr², Yu Zhang², Francis Petrocelli², and Michael T. Klein¹

¹*University of Delaware Energy Institute and Department of Chemical and Biomolecular Engineering, University of Delaware, Newark, DE 19716*

²*Air Products and Chemicals Incorporated. Allentown, PA, 18195*

Reproduced by permission from **Horton, S.R.**; Mohr, R.; Zhang, Y.; Petrocelli, F.; Klein, M.T. “Molecular-level kinetic modeling biomass gasification.” *Energy & Fuels*. 2015 (Web). 10.1021/acs.energyfuels.5b01988. Copyright 2015. American Chemical Society.[83]

4.1 Abstract

A molecular-level kinetic model for biomass gasification was developed and tuned to experimental data from the open literature. The development was divided into two categories: the composition of the feedstock and the construction of the reaction network. The composition model of biomass was divided into three submodels for cellulose, hemicellulose, and lignin. Cellulose and hemicellulose compositions were modeled as linear polymers using Flory-Stockmayer statistics to represent the polymer size distribution. The composition of lignin, a cross-linked polymer, was modeled using relative amounts of structural building blocks, or attributes. When constructing the full biomass composition model, the fractions of cellulose, hemicellulose, and lignin were optimized using literature-reported ultimate analyses.

The reaction network model for biomass contained pyrolysis, gasification, and light-gas reactions. For cellulose and hemicellulose, the initial depolymerization was described using Flory-Stockmayer statistics. The derived monomers from cellulose and hemicellulose were subjected to a full pyrolysis and gasification network. The pyrolysis reactions included both reactions to decrease molecule size, such as thermal cracking, and char formation reactions, such as Diels-Alder addition. Gasification reactions included incomplete combustion and steam reforming. For lignin, reactions occurred between attributes and included both pyrolysis and gasification reactions. The light-gas reactions included water-gas shift, partial oxidation of methane, oxidation of carbon monoxide, steam reforming of methane, and dry reforming of methane. The final reaction network included 1356 reactions and 357 species.

The performance of the kinetic model was examined using literature data that spanned six different biomass samples and had gas compositions as primary results. Three data sets from different biomass samples were used for parameter tuning, and

parity plot results showed good agreement between the model and data ($y_{predicted} = y_{obs} * 0.928 + 0.0003$). The predictive ability of the model was probed using three additional data sets. Again, the parity plot showed agreement between model and experimental results ($y_{predicted} = y_{obs} * 0.989 - 0.007$).

4.2 Introduction

Biomass is the major source of chemical energy that is renewable at a reasonable timescale. The most common way to access that energy is incineration; however, there are technical and environmental issues with large scale implementation. In terms of technical feasibility, biomass has much lower energy density than its fossil fuel counterparts[84]. Environmentally, the incineration of biomass has high production of harmful oxygenates such as dioxins and furans[85]. The gasification of biomass has gained interest in recent years due to lower emissions of pollutants and the production of synthesis gas (syngas), a possible route to liquid fuels. Biomass gasification also makes up the majority of municipal solid waste (MSW) gasification, an up-and-coming waste disposal technology. In the design of biomass gasification units, important parameters are tar production and syngas composition. To study these parameters, kinetic models are often utilized in the literature.

Previous kinetic models of biomass gasification are lumped in nature[86],[87]. Lumped models contain no structural information beyond the definition of the lump. For instance, a lumped model might contain ‘Tar’ where tar is simply defined as ‘liquid product at reactor conditions’. Lumped models in the literature follow some combination of parallel or sequential implementations, as shown in Figure 4.1. More advanced lumped models contain light gasses explicitly. For example, Zhong et al.[88]

contained reactions and material balances for many of the observed light gases. However, the model is still fundamentally lumped as there is no chemical description from the feedstock molecules (e.g., cellulose) to light gas. More examples of kinetic models found in literature can be found in a reviews by Puig-Arnavat[16] and Prakash[89].

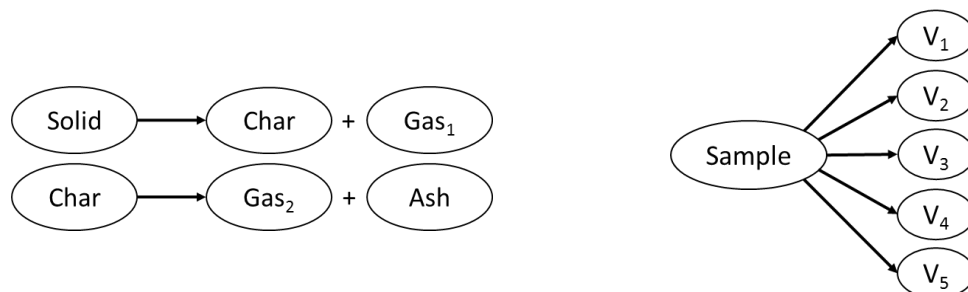


Figure 4.1: Literature lumped kinetic models. (Left) Sequential lumped model[86] of biomass gasification. (Right) parallel lumped model of biomass gasification where V₁-V₅ are lumped volatile products.[87]

Chemical percolation devolatilization (CPD) was developed by Fletcher and coworkers in the early 1990s and has been utilized for two decades in work on the pyrolysis and gasification of coal[90]–[92]. Due to the molecular similarity between coal and lignin, CPD has been successfully applied to biomass in recent years[93]–[95]. In CPD, the chemical structure of the feedstock is modeled as aromatic clusters, labile bridges, and side chains, and the cluster size distribution is described by lattice statistics. The kinetic breakdown of the lattice involves the cleavage of labile bridges into side chains, and the production of light gas, char, and tar molecules. A key advantage of CPD is the direct usage of measurable structural parameters and simple, easy-to-understand kinetic networks. Also, the usage of lattice statistics is

appropriate for cross-linked polymers such as lignin. The main drawbacks of CPD are the minimal information on the molecular descriptions of tar and light gas, and the application of lattice statistics onto predominantly linear polymers such as cellulose and hemicellulose.

For similar reactor conditions on a single biomass sample, lumped kinetic models do an adequate job of describing experimental data[15], [96]. Problems arise when the feedstock or reactor conditions are perturbed. For example, a lumped model of pine sawdust will have different parameters than a lumped model of grass. Fundamentally, a model can only answer questions at the same level of complexity as the model's definition. For example, a lumped model with a single 'tar' component cannot yield any information about the specific tars present in the output stream. In MSW gasification, the biomass feedstock changes over the course of time. For these changes, the questions that are asked of the model are at the molecular-level, and therefore the model must retain the same level of detail.

The current modeling work is the first representation of a molecular-level kinetic model of biomass gasification. This model maps the feedstock to products, tracking each individual molecular species throughout the reactor. With this in mind, there are three fundamental steps to building a molecular-level kinetic model for biomass gasification. First, the feedstock must be defined as a set of molecules. Second, a reaction network describes how the feedstock becomes products. Third, a kinetic model is built which utilizes the feedstock and reaction network to create a system of mass balance differential equations. The output of this process is a model with a set of rate parameters for each reaction chemistry. These rate parameters are then tuned, or optimized, using experimental data from the open literature.

The most interesting results from the model are also at the molecular-level. For example, the model contains reaction chemistries important to biomass gasification. These chemistries convey an underlying understanding of the reactor. Second, the model contains explicit molecular definitions of tar molecules. The amount of produced tar can then be predicted for a range of conditions. Third, the model can predict relative changes in syngas and tar compositions for a variety of biomass feedstocks. This allows for the anticipation of changes in syngas output due to changes in the MSW feedstock composition.

4.3 Molecular Representation of Biomass

In order to model reactor kinetics at the molecular-level, the feedstock must first be represented as a set of molecules and mole fractions. For biomass, an explicit composition cannot be measured experimentally because it contains large polymeric structures; therefore, composition models are required to map available experimental data to molecular compositions.

A molecular-level composition model fundamentally obtains a list of molecules and mole fractions. Here, a composition model is a set of probability distribution functions (PDFs) that describe the relative amounts molecular groups, called attributes within the feed stream. For linear polymers (e.g., cellulose), where the monomer structure is relatively well understood, the composition was modeled with the traditional Flory distribution function[61]. For cross-linked polymers with variable repeat units such as lignin, a more elaborate set of PDFs must be constructed. For both simple and complex systems, the optimal set of PDFs is determined by tuning the PDF parameters to experimental measurements through structure-property

correlations. The complete list of molecules and mole fractions is obtained through juxtaposition of the PDFs.

In this work, composition models for each of the biomass polymers were developed independently using experimental data from literature. These models were combined to build the complete biomass model which was, in turn, used to describe the feedstock to the biomass gasification kinetic model.

4.3.1 Linear Polymer Composition Models: Cellulose and Hemicellulose

The basic composition of a linear polymer is known; for instance the repeat unit of cellulose is α -glucose ($C_6H_{10}O_5$), given in Figure 4.2. Whereas cellulose is comprised solely of glucose, hemicellulose is made up of several pentose sugars, with different branching and functional groups. The primary monomers include xylan, glucronoxylan, arabinoxylan, glucomannan, and xyloglucan[97]. The relative composition of the hemicellulose monomers and degree of crosslinking varies among the different wood types. Consequently, modeling hemicellulose composition is more complex than modeling cellulose. Xylose is the predominate sugar in hemicellulose, so to reduce the composition model complexity, it is often represented as a linear poly-xylan structure[97], [98].

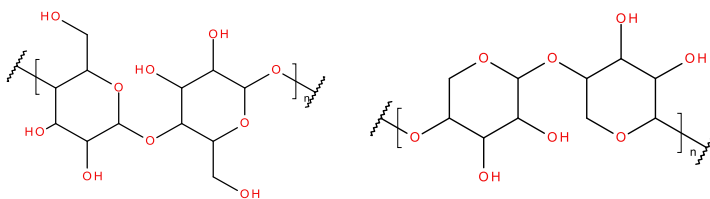


Figure 4.2: Cellulose polymeric n-mer of $\beta(1 \rightarrow 4)$ linked D-glucose units (Left). Hemicellulose representation as an n-mer of poly-xylan (Right).

Composition models are required for linear polymers due to polydispersity, i.e., the presence of differently sized n-mers, and their molecular composition is described using a polymer-size distribution function. In this model, a Flory distribution[61] is used due to its simplicity and wide-spread usage.

$$x_n = (1 - p) * p^{n-1} \quad (4.1)$$

The Flory distribution is given in Equation 4.1, where p is the bridge fraction, or fraction of end-groups that are linkages. Linear polymers can be thought of as cores, side chains (SCs) and inter-core linkages (ILs), a verbiage that will be used later in the analysis of the statistics in cross-linked polymers. By considering each repeat unit as a core, it follows that SCs and ILs are terminal substituents and bridges between cores, respectively. A monomer, therefore, is a core with two SCs, and a dimer contains 2 cores, two SCs, and 1 IL. When this concept is extended to a general linear polymer, an n -mer has $(n - 1)$ ILs, two SCs, and n cores. The concentration of sites in the system is given by Equation 4.2 since every IL represents two previously reactive sites and all unreacted sites are [SC]. The bridge fraction in terms of SCs and ILs is given by Equation 4.3.

$$\textit{Sites in the System} = 2 * [IL] + [SC] \quad (4.2)$$

$$p = \frac{2 * [IL]}{2 * [IL] + [SC]} \quad (4.3)$$

In order to model the molecular composition of a linear polymer using a Flory distribution, the value for p is estimated from experimental measurements. Literature studies have used a variety of methods to characterize a linear polymer. One common metric is the average degree of polymerization, or \overline{X}_n , which can be related to p using Equation 4.4. In biomass gasification literature, the most common representation of

feedstock compositional information is an ultimate analysis. For example, an ultimate analysis for a cellulose sample is shown in Table 4.1.

$$\overline{X}_n = \frac{1}{1-p} \quad (4.4)$$

Table 4.1: Ultimate analysis of cellulose samples in Chang et al. (2011)[99].

Element	Chang et al. (2011)
C (wt%)	44.44
H (wt%)	6.17
O (wt%)	49.38

Given a value for p (or equivalently \overline{X}_n), a predicted ultimate analysis can be calculated through the use of Flory statistics. First, the mole fraction of each n -mer is calculated using Equation 4.1. Second, the weight fraction of each n -mer is calculated by using the average molecular weight of the polymer, \overline{MW} , as shown in using Equation 4.5. Finally, the ultimate analysis is calculated by multiplying the mass fraction of each n -mer by the mass fraction of each element in the n -mer. For example, the predicted weight percent of carbon is found using Equation 4.6. Using this method, an ultimate analysis can be predicted for a given \overline{X}_n and polymer.

$$w_n = x_n * \frac{MW_n}{\overline{MW}} \quad (4.5)$$

$$\text{predicted wt\% Carbon} = \sum_{n=1}^{\infty} w_n * C_{\text{wt\%,n-mer}} \quad (4.6)$$

where $C_{\text{wt\%,n-mer}}$ is the weight percent of carbon in the n – mer

An automated tool called *Linear Polymer Composition Editor* has been developed in a C# application to facilitate the optimization of \overline{X}_n for any linear

polymer and experimental data set. This tool works using a simple optimization loop as shown in Figure 4.3. First, it guesses a value for the degree of polymerization. Next it calculates an ultimate analysis for this degree of polymerization. It then compares to experimental results using a least-squares objective function. Finally, it adjusts the prediction.

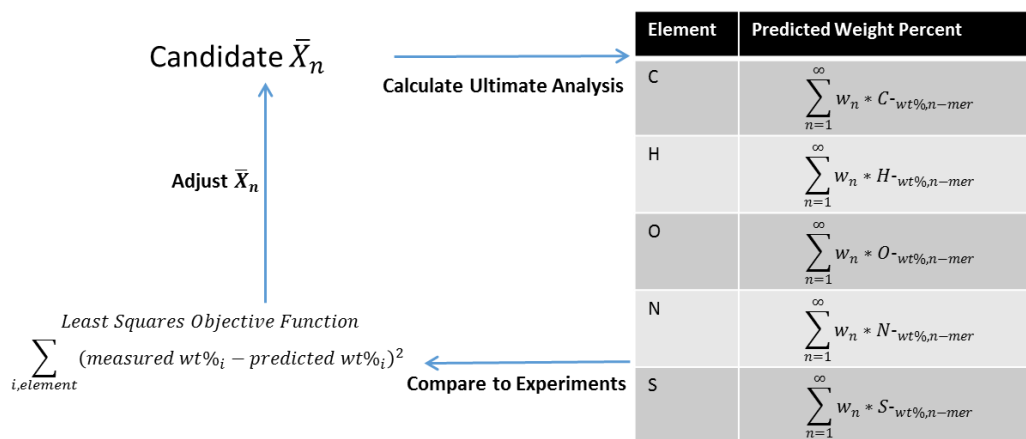


Figure 4.3: Linear Polymer Composition Editor optimization loop.

The linear polymer composition editor was used to simulate the compositions of cellulose and hemicellulose. The composition simulated by the Flory distribution fits very well with the literature as shown in Table 4.2. The agreement is expected as cellulose is known to be composed of a single monomer unit and linear. With hemicellulose, the Flory distribution still fits well; deviations between prediction and experiment are likely due to cross-linking and the exclusion of other possible monomeric units. However, if a mass balance can be achieved using the simpler

polymeric structure, then it is likely that the approximations made would lead to no significant error in gasification products.

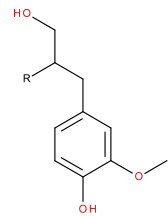
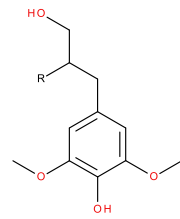
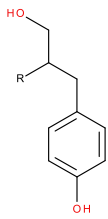
Table 4.2: Comparison between experimental data and predictions from the Linear Polymer Composition Editor. Experimental data came from Chang et al.[99] and Couhert et al.[100], [101] for cellulose and hemicellulose, respectively. The simulated average degree of polymerizations for cellulose and hemicellulose were 232 and 5.

Element	Cellulose Experimental	Cellulose Simulated	Hemicellulose Experimental	Hemicellulose Simulated
C	44.44	44.42	44.3	44.2
H	6.17	6.22	5.4	6.2
O	49.38	49.35	49.9	49.5

4.3.2 Cross-linked Polymer Composition Model: Lignin

The final composition model needed for biomass is for lignin. Lignin is a cross-linked biopolymer present in all plants, and is primarily made of three phenylpropane units: p-coumaryl alcohol, coniferyl alcohol, and sinapyl alcohol (shown in Table 4.3). These units are connected together in a structure reminiscent of an archipelago of islands. The prototypical archipelago structure commonly accepted for lignin is the Freudenberg model[102] (an adapted version is shown in Figure 4.4).

Table 4.3: C9 units of Lignin[103].

Name	Coniferyl Alcohol	Sinapyl Alcohol	P-coumaryl Alcohol
Structure			

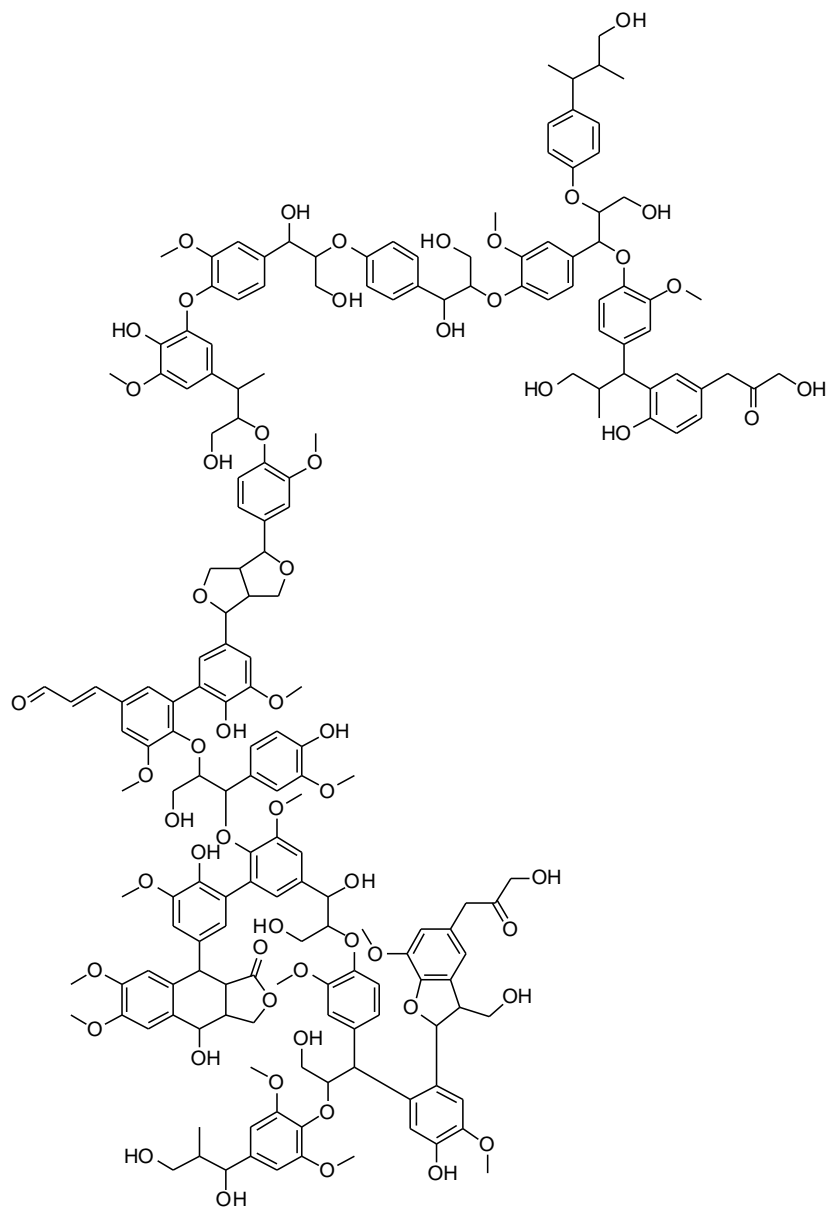
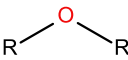
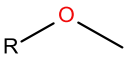
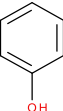
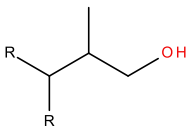
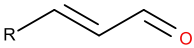
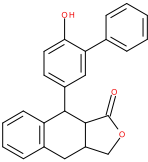
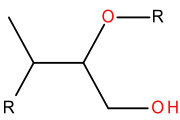
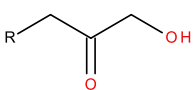
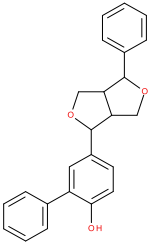
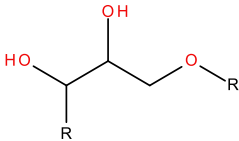
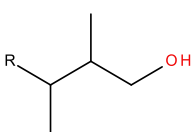
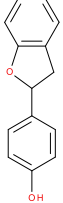
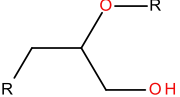
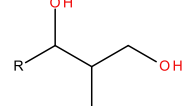


Figure 4.4: Adapted Freudenberg Structure[102]. This structure was parsed to yield the attribute identities.

The Freudenberg model was parsed to obtain identities of cores, ILs, and SCs. The above structure contains 5 cores, 5 ILs, and 5 SCs, shown in Table 4.4. For the

core attributes, there are two characteristics of note. First, the Ph-O bond for a hydroxyl group on an aromatic is a strong bond; therefore, the OH groups are considered part of a core. Similarly, C-C bonds where both carbons are part of separate ring structures, e.g. biphenyl linkages, were considered strong bonds. When parsing inter-core linkages, any IL bonded to three rings in the Freudenberg structure was approximated to contain only two binding sites. This simplifies the configuration of larger core clusters.

Table 4.4: Attribute Identities as parsed by CME from the Freudenberg model for lignin.

Index	Core Identity	IL Identity	SC Identity
1			
2			
3			
4			
5			

Lignin adds complexity to the binding site concept because not all side chains and linkages can bind to all binding sites. An example is seen with side chain binding to the phenol core, given in Figure 4.5. Based on the structure of the C9 units in Table 4.3, the two binding sites ortho to the hydroxyl group can only contain methoxy side chains. The para binding site, on the other hand, must contain a C-C bond, or one of

the other four side chains. Each attribute was associated with R_1 and R_2 binding sites based on the chemical structure.

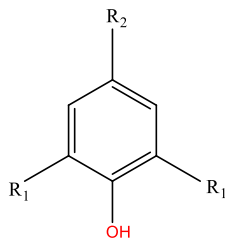
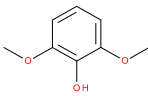
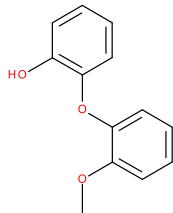


Figure 4.5: Binding site types on the phenol core.

The molecular nature of the composition is retained despite the use of attributes. Individual molecule identities and mole fractions are obtained through the sampling five PDFs. The first three are attribute group PDFs, or the relative amounts of each entry in Table 4.4. Each core has binding sites which can be filled by an IL, SC, or left unfilled (-H side chain). This complexity gives rise to two additional PDFs. First, a polymer size distribution defines the relative amounts of differently sized n -core clusters; or a molecule with n cores and $n-1$ ILs. Finally, the binding site distribution describes how many sites on each core cluster are filled by side chains. The mole fractions of individual molecules are calculated through the combined probabilities from each PDF as shown in Table 4.5. The complete juxtaposition of all five PDFs gives both identities and mole fractions for the molecule list.

Table 4.5: Mole fraction calculation from sampled molecules.

Molecule	Attributes		Filled Binding Sites	Cluster Size	Mole Fraction	
	Cores	SCs and ILs				
				2	1	\propto $P_{\text{core}}(\text{phenol})P_{\text{SC}}(\text{methoxy})^2$ $P_{\text{BS}}(2)P_{\text{Cluster}}(1)$
	 			1	2	$\propto P_{\text{core}}(\text{phenol})$ $P_{\text{core}}(\text{phenol})^*$ $P_{\text{IL}}(\text{ether})$ $P_{\text{SC}}(\text{methoxy})^2$ $P_{\text{BS}}(1)P_{\text{Cluster}}(2)$

In order to model the composition of lignin, experimental measurements were obtained from literature. Compositional measurements of lignin have a strong dependence on the lignin isolation method. For example, Kraft lignin comes from the Kraft pulping process and is significantly degraded from the original plant matter. A less destructive isolation technique is called Milled Wood Lignin (MWL) and the product is considered to be the closest to native lignin[104]. Table 4.6 shows a subset of the experimental measurements on *miscanthus*, a perennial grass[104].

Table 4.6: Experimental Data used in the optimization of the lignin compositional model. All data are from Hage et al. (2009)[104].

Description	Value	Experiment
Ultimate Analysis (wt%)		Unreported
C	63.5	
H	5.7	
O	29.2	
N	0.2	
S	0.0	
Normal Molecular Weight (g/mol)	8300	Gel Permeation Chromatography
Aromatic H per ring	2.5	Carbon NMR
Methoxy (-OCH₃) per ring	0.98	Carbon NMR
Phenolic OH per ring	0.28	Proton NMR

The optimization of lignin's composition was performed using an in-house software, the Composition Model Editor (CME)[43]. Each attribute PDF was modeled using a histogram. Gamma distributions were used to determine the number of filled binding sites on molecules and the polymer size distribution.

For any well-posed optimization problem, the number of adjustable parameters should not exceed the number of data points and constraints. For this simulation, there are 16 total adjustable parameters, and 6 usable data points shown in Table 4.7. Therefore, to have a well-posed problem, 10 constraints must be applied. First, average molecular weight (MW) is primarily controlled by the polymer size distribution. Therefore, the standard deviation was set to a representative value and the MW mean was allowed to vary. Similarly, the only data relevant to the binding site distribution, which controls the number of side chains, is the number of aromatic hydrogen per ring. Again, a representative value was used for the standard deviation and the number of aromatic hydrogens per ring was allowed to vary.

Constraints on the histogram were made using the relative amounts of attributes group members within the Freudenberg structure, as shown in Table 4.7. Two simulations were run to compare a fully constrained model to a second that includes two additional degrees of freedom. In simulation 1, all attribute histograms were set using the Freudenberg structure and only the polymer size distribution mean and the binding site distribution mean were allowed to vary. The results, shown in Table 4.8, were surprisingly accurate given that the attribute PDFs were set entirely using the Freudenberg structure.

In the second simulation, the attribute PDFs were informed by the Freudenberg structure, but selected attribute group member concentrations were allowed to vary. For example, in the SC PDF, the composition of SC1 was allowed to vary and the remaining side chains amounts were constrained to follow the Freudenberg structure (e.g., the probabilities of SC2 and SC3 were equal). Of the substituent PDFs, the methoxy side chain and phenol core were allowed to vary. These decisions were made based on the experimental measurements available. The methoxy side chain correlates very well with the experimentally measured ‘methoxy per ring’ datum, and the phenol core is well described using the ‘phenolic OH per ring’ datum.

Table 4.7: Adjustable parameters in optimization. *obtained by difference, not an adjustable parameter. In simulations 1 and 2, bolded terms were optimized on.

Adjustable Parameter	Simulation 1: Attribute PDFs from Freudenberg	Simulation 2: Attribute PDFs partially constrained by Freudenberg
<u>Polymer Size Distribution</u>		
<u>(Gamma)</u>		
Mean	32	34
Standard deviation	5	5
<u>Binding Site Distribution</u>		
<u>(Gamma)</u>		
Mean	66	66
Standard Deviation	20	20
<u>Core Histogram</u>		
C1	0.571	0.64
C2	0.214	0.18
C3	0.071	0.06
C4	0.071	0.06
C5*	0.071	0.06
<u>IL Histogram</u>		
IL1	0.2	0.2
IL2	0.1	0.1
IL3	0.1	0.1
IL4	0.5	0.5
IL5*	0.1	0.1
<u>SC Histogram</u>		
SC1	0.783	0.89
SC2	0.0435	0.022
SC3	0.0435	0.022
SC4	0.870	0.044
SC5*	0.0435	0.022
Constraint Analysis	16 Adjustable parameters, 6 data points, 14 constraints.	16 Adjustable parameters, 6 data points, 12 constraints.

The results from the second simulation are an improvement on the first simulation especially on the methoxy correlation as shown in Table 4.8. This is unsurprising as lignin from different sources primarily differ in the ratios of guaiacyl, syringil, and p-coumryl units[97]. These units are differentiated based on the number of methoxy groups. Therefore, it follows that the probability of a methoxy side chain would play a key role in tuning to a new biomass type.

Table 4.8: Experimental data currently used in the optimization of the lignin compositional model. All data are from Hage et al. (2009)[104]. The data shown here is a subset of data reported; CME adjustments are required to make use of more data.

Description	Experimental Value	Simulation 1: Attribute PDFs from Freudenberg	Simulation 2: Attribute PDFs partially constrained by Freudenberg
<u>Ultimate Analysis</u>			
<u>(wt%)</u>	63.5	64.98	64.77
C	5.7	6.14	6.18
H	29.2	28.85	29.05
O	0.2	0.0	0.0
N	0.0	0.0	0.0
S			
Average Molecular Weight (g/mol)	8300	8225.7	8304
Aromatic H per ring	2.5	2.44	2.47
Methoxy (-OCH3) per ring	0.98	0.897	0.98
Phenolic OH per ring	0.28	0.315	0.28

4.3.3 Combined Biomass Composition Model

A full biomass sample contains fractions of cellulose, hemicellulose, and lignin. However, literature studies rarely report these fractions, and instead report an ultimate analysis on the full biomass sample. In order to make use of these data, the percentages of each subcomponent, reproduced in Table 4.9, are optimized such that the net ultimate analysis agrees with experimental data.

Table 4.9: Ultimate analysis for each subcomponent of biomass from preceding sections.

Element	Cellulose	Hemicellulose	Lignin
C	44.4	44.3	64.77
H	6.2	6.2	6.18
O	49.4	49.5	29.05

In order to automate this process, an in-house C# application called *MSW Bulk Composition Solver* was developed and utilized. The general logic and equations for the calculation of the ultimate analysis of biomass are given in Figure 4.6. This application, developed for optimizing municipal solid waste (MSW) cuts based on a bulk ultimate analysis, can also be applied to biomass by simply setting all other fractions of MSW to zero. This tool was used to find the optimal fractions, shown in Table 4.10, of cellulose, hemicellulose, and lignin for six biomass samples from Li et al., the gasification study used for the reaction kinetic model. The results showed good agreement with experimental data for C, H, and O. The experimental results showed trace amounts of nitrogen and sulfur that were not included in the model. We have excluded N and S containing function groups due to their relatively insignificant amounts and absence of both composition and gasification experimental results. The

future availability of more detailed experimental data could allow for the inclusion of these functional groups.

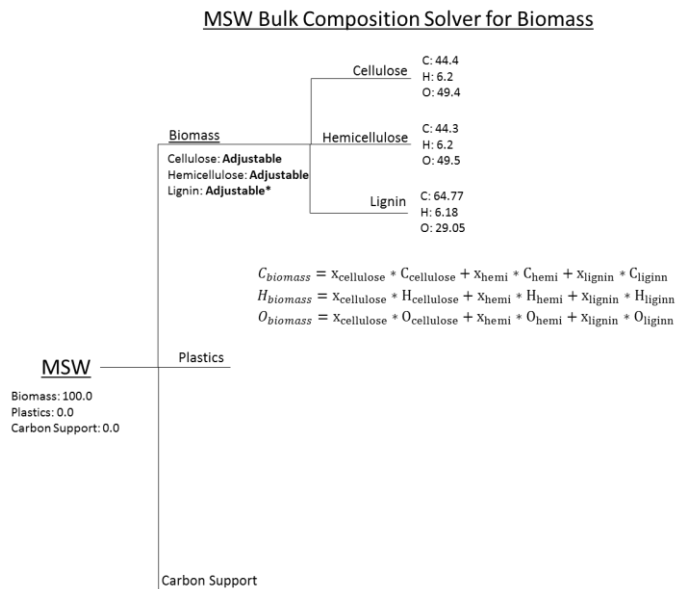


Figure 4.6: Logic of MSW Bulk Composition solver applied for biomass. All numbers in this figure are in wt%. The plastics and carbon support segments of the figure are truncated as the weight fraction within biomass is 0 for each. *-Lignin fraction is dependent on cellulose and hemicellulose.

Table 4.10: Biomass splits for each of the biomasses under study by Li et al.[13] SPF is spruce, pine, fir mixed sawdust. PS is 50% each of pine bark and spruce whitewood mix.

	Cypres	Hemlock	SPF	Cedar	PS	Mixed
S						
<u>Biomass Splits</u>						
Cellulose	0.448	0.448	0.405	0.444	0.425	0.424
Hemicellulose	0.202	0.202	0.3	0.205	0.350	0.350
Lignin	0.35	0.35	0.3	0.35	0.226	0.225
<u>Ultimate Analysis</u>						
C: obs	0.516	0.518	0.504	0.523	0.491	0.489
pred	0.515	0.515	0.504	0.514	0.489	0.489
H: obs	0.062	0.062	0.063	0.0611	0.0786	0.076
pred	0.062	0.062	0.062	0.062	0.0621	0.062
O: obs	0.404	0.406	0.416	0.399	0.403	0.403
pred	0.423	0.423	0.434	0.423	0.448	0.448
N: obs	0.0065	0.0065	0.0062	0.0052	0.0021	0.0051
pred	0	0	0	0	0	0
S: obs	0.0046	0.0070	0.0034	0.0039	0.0007	0.0034
pred	0	0	0	0	0	0

4.4 Reaction Chemistry of Biomass Gasification

After modeling the composition of biomass, the reaction chemistry defines the mapping from molecular inputs to outputs. The reaction chemistry for biomass gasification consists of two major reaction classes: pyrolysis, reactions requiring no reactive gasses, and gasification, here reactions with oxygen and water. Discussion of the reaction chemistry in the biomass gasification model is again divided into linear polymers, cellulose and hemicellulose, and the cross-linked polymer, lignin.

4.4.1 Cellulose and Hemicellulose

For the linear polymers, cellulose and hemicellulose, the composition was represented using a polymer-size distribution and a known repeat unit. Due to the length of these polymers, detailed pyrolysis chemistry, e.g., thermal cracking, could produce a near infinite number of products. Furthermore, the only products measured at gasification conditions are light gasses and tar compounds with undefined compositions[13], [16]. To simplify this process, the initial breakdown of cellulose and hemicellulose is assumed to occur from depolymerization reactions. After breakdown into monomeric units, the reaction network includes more complex pyrolysis and gasification chemistries.

4.4.1.1 Depolymerization

Depolymerization of cellulose can occur via two dominant mechanisms: hydrolysis and thermolysis, which are illustrated in Figure 4.7[105],[106]. Hydrolysis, a bimolecular reaction with water, of a glycosidic linkage produces glucose end-groups on the oligomers formed. At complete conversion, this mechanism produces pure glucose as monomers. The second pathway is a thermolysis mechanism, which produces both a glucose and a levoglucosan end group. Counter-intuitively, this mechanism does not produce a 1:1 ratio of glucose:levoglucosan monomers at complete conversion. Instead, a single glucose monomer is produced for every original cellulose chain. This is illustrated in Figure 4.8 for the breakdown of a cellulose 4-mer. Hydrolysis typically occurs over an acid catalyst[105], whereas thermolysis requires no such catalyst and occurs at temperatures above 300 °C[106]. As biomass gasification is often at extreme temperatures with no acid catalyst, thermolysis is assumed to break down the initial structure.

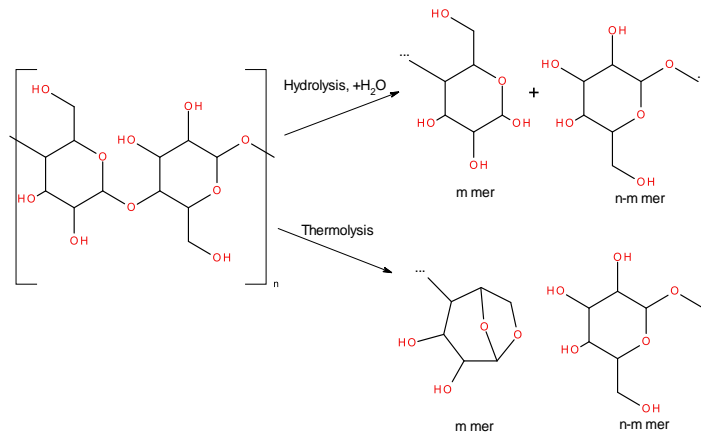


Figure 4.7: Cellulose Depolymerization Pathways.

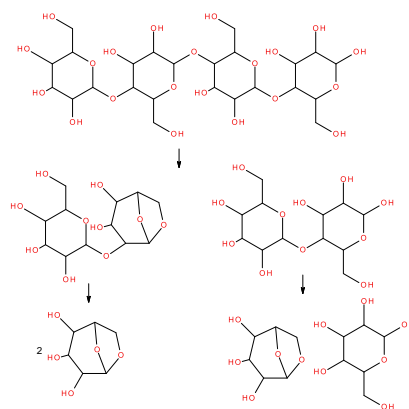


Figure 4.8: Complete cracking of a cellulose 4-mer showing final monomeric products.

After breakdown into glucose and levoglucosan, the monomers then undergo ring opening to form analogous acyclic structures, as shown in Figure 4.9. These molecules are assumed to be the starting point for more detailed pyrolysis and gasification chemistry. Full pyrolysis chemistry was not applied on larger or ring-

containing molecules as it would add unnecessary detail for species that are not measured in gasification literature[13], [100], [101].

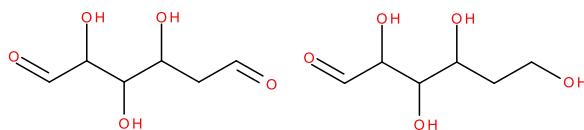


Figure 4.9: Starting molecules of full cellulose pyrolysis network: linear levoglucosan (left) and linear glucose (right).

Hemicellulose depolymerization is similar to that for cellulose in that it can follow both hydrolysis and thermolysis reaction pathways, as shown in Figure 4.10. Unlike that for cellulose, hemicellulose thermolysis can only occur at end-groups rather than at any linkage in the molecule. This is due to the nature of the levoglucosan-like structure, anhydro-xylopyranose, that forms in the thermolysis reaction. In order to have two five-membered rings in the structure, one of the ether linkage sites must participate in ring formation. If this were to occur mid-chain, it would require simultaneous bond-breaking of both ether linkages[98]. Like cellulose, the final yield of an n -mer breakdown via thermolysis is $(n-1)$ anhydro-xylopyranose and one xylose.

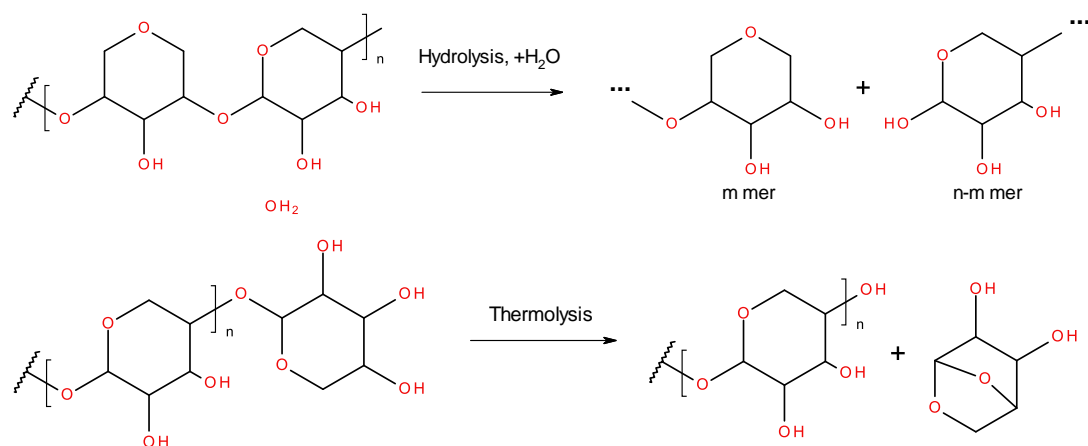


Figure 4.10: Depolymerization pathways for hemicellulose.

Of the two depolymerization mechanisms, thermolysis is likely to dominate based on the observed products[98] at high temperatures. This mechanism follows a stepwise depolymerization rather than a random-scission depolymerization. Every depolymerization reaction produces an anhydroxylopyranose molecule. When the last linkage in each chain breaks, a xylose is also produced. The 5-carbon molecules in Figure 4.11 were the starting points for more detailed pyrolysis and gasification chemistry.

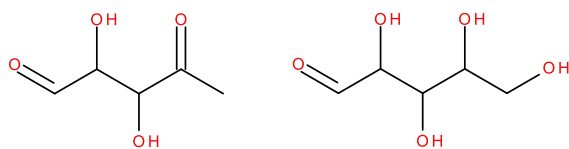


Figure 4.11: Linear forms of anhydro-xylopyranose (left) and xylose (right). These are the starting point of the full pyrolysis network.

For both cellulose and hemicellulose, the linear monomers mark the transition from representing chemical structure using statistics and attributes to representing the structure using explicit molecules. Within the reaction network, this transition is represented using the reactions given in Table 4.11.

Table 4.11: Depolymerization reactions representing conversion of attribute representation to molecular representation for linear polymers.

Hemicellulose	Cellulose
$\begin{aligned} & \textit{Hemicellulose}_{IL} \xrightarrow{\textit{thermolysis}} \\ & \textit{Hemicellulose}_{SC0} \\ & \quad + \textit{Hemicellulose}_{SC1} \end{aligned}$	$\begin{aligned} & \textit{Cellulose}_{IL} \xrightarrow{\textit{thermolysis}} \\ & \textit{Cellulose}_{SC0} + \textit{Cellulose}_{SC1} \end{aligned}$
$\begin{aligned} & \textit{Hemicellulose}_{core} \\ & \rightarrow \textit{Anhydroxylopyranose} \\ & \textit{Hemicellulose}_{core} \\ & \rightarrow \textit{Linear xylose} \end{aligned}$	$\begin{aligned} & \textit{Cellulose}_{core} \rightarrow \\ & \textit{Linear Levoglucosan} \\ & \textit{Cellulose}_{core} \rightarrow \textit{Linear glucose} \end{aligned}$

The equations for the transition from statistical representation to molecular representation are based on the mechanism of depolymerization. For hemicellulose, each link cleavage produces an anhydroxylopyranose due to the unzipping mechanism. Because there is one reaction site per chain, the rate of unzipping is proportional to the number of chains in the system. In the last cleavage of each chain, a linear xylose is also produced. To model this phenomenon, the probability of a linear xylose forming was set to the ratio of total number of initial hemicellulose chains to the total number of repeat units. Shorter chain lengths, i.e., larger initial number of chains, would therefore lead to the production of more linear xylose molecules. These characteristics yield the rate laws given in Table 4.12.

Table 4.12: Depolymerization reaction rate laws representing conversion of attribute representation to molecular representation for hemicellulose.

Index	Reaction	Rate Law
1	$Hemicellulose_{IL}$ <i>thermolysis</i> $\rightarrow Hemicellulose_{SC0}$ + $Hemicellulose_{SC1}$	$Rate_1 = k_1 * [HemiChains]$
2	$Hemicellulose_{core}$ $\rightarrow Anhydroxylopyranose$	$Rate_2 = Rate_1$
3	$Hemicellulose_{core}$ $\rightarrow Linear\ xylose$	$Rate_3 = Rate_1 * \frac{[HemiChains]_0}{[Total\ Repeat\ Units]}$

The mechanism in cellulose depolymerization occurred via random breakdown in the backbone. This characteristic of depolymerization is analogous to the assumptions made in a Flory-distributed polymerization; therefore, a Flory distribution can also be used to model the breakdown. Changes in monomer concentration inform the production of linear levoglucosan and linear glucose.

The production of monomers from random scission can be related to the breakdown of the backbone, or $d[IL]/dt$. First, the number of monomers in a Flory-distributed polymer as a function of p is given below, in Equation 4.7. The parameter, N_0 , corresponds to the number of repeat units in the system, equivalent to the half of the total sites, as each repeat unit has two sites. Differentiation allows for a relationship between the change in monomer concentration and dp/dt , shown in Equation 4.8. The final result, given in Equation 4.9, gives a simple relationship between increase in monomer concentration and decrease in inter-core linkage concentration.

$$N_1 = (N_0) * (1 - p)^2 \quad (4.7)$$

$$where\ N_0 = \frac{2 * [IL] + [SC]}{2}$$

$$\frac{dN_1}{dt} = N_0 * -2 * (1 - p) * \frac{dp}{dt} \quad (4.8)$$

$$\frac{dp}{dt} = \frac{1}{N_0} * \frac{d[IL]}{dt} \quad (4.9)$$

$$\frac{dN_1}{dt} = -2 * (1 - p) * \frac{d[IL]}{dt}$$

The increase in monomer concentration is divided into relative increases in linear levoglucosan and glucose. From the analysis of the depolymerization mechanism, it was found that a single glucose monomer is produced for every original chain of cellulose. The probability of forming a glucose repeat unit is proportional to the total number of chains divided by the number of repeat units given in Equation 4.10. Therefore, if the original system contained shorter polymer chains, then a higher number of glucose monomers would be produced. These results give the rate laws shown in Table 4.13.

$$prob_{glu} = \frac{\text{number of original chains}}{\text{number of repeat units}} \quad (4.10)$$

$$prob_{levo} = 1 - prob_{glu}$$

Table 4.13: Depolymerization reaction rate laws representing conversion of attribute representation to molecular representation for cellulose.

Reaction	Rate Law
$Cellulose_{IL} \xrightarrow{\text{thermolysis}} Cellulose_{SC0} + Cellulose_{SC1}$	$Rate_1 = k_4 * [Cellulose_{IL}]$
$Cellulose_{core} \rightarrow \text{Linear Levoglucosan}$	$Rate_2 = \frac{dN_1}{dt} * prob_{levo}$
$Cellulose_{core} \rightarrow \text{Linear glucose}$	$Rate_3 = \frac{dN_1}{dt} * prob_{glu}$

4.4.1.2 Pyrolysis

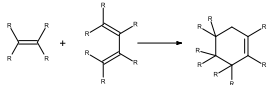
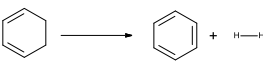
The pyrolysis reactions in the cellulose and hemicellulose networks serve two primary purposes: the breakdown into light hydrocarbons and the formation of char, i.e, stable, heavy molecules. The breakdown of molecules comes in the form of cracking reactions, as shown below in Table 4.14. The enol-aldehyde tautomerization is included for two reasons. First, the aldehyde form of the molecule is energetically more stable. Second, the carbonyl group can undergo decarbonylation, allowing for further breakdown of the molecule.

Table 4.14: Pyrolysis reactions used to breakdown cellulose and hemicellulose into small molecules.

Reaction Type (Family) and Reactive Moiety	Reaction Matrix	Example Reaction	Reaction Rules																									
Decarbonylation Aldehydes	<table border="1"> <tr><td></td><td>H</td><td>O</td><td>C</td><td>R</td></tr> <tr><td>H</td><td>0</td><td>0</td><td>-1</td><td>1</td></tr> <tr><td>O</td><td>0</td><td>0</td><td>1</td><td>0</td></tr> <tr><td>C</td><td>-1</td><td>1</td><td>0</td><td>-1</td></tr> <tr><td>R</td><td>1</td><td>0</td><td>-1</td><td>0</td></tr> </table>		H	O	C	R	H	0	0	-1	1	O	0	0	1	0	C	-1	1	0	-1	R	1	0	-1	0		Any aldehyde (primary carbonyl) is allowed to react.
	H	O	C	R																								
H	0	0	-1	1																								
O	0	0	1	0																								
C	-1	1	0	-1																								
R	1	0	-1	0																								
Decarboxylation Carboxylic acids	<table border="1"> <tr><td></td><td>H</td><td>O</td><td>C</td><td>R</td></tr> <tr><td>H</td><td>0</td><td>-1</td><td>0</td><td>1</td></tr> <tr><td>O</td><td>-1</td><td>0</td><td>1</td><td>0</td></tr> <tr><td>C</td><td>0</td><td>1</td><td>0</td><td>-1</td></tr> <tr><td>R</td><td>1</td><td>0</td><td>-1</td><td>0</td></tr> </table>		H	O	C	R	H	0	-1	0	1	O	-1	0	1	0	C	0	1	0	-1	R	1	0	-1	0		Any carboxylic acid in the system is allowed to react.
	H	O	C	R																								
H	0	-1	0	1																								
O	-1	0	1	0																								
C	0	1	0	-1																								
R	1	0	-1	0																								
Acyclic Thermal Cracking Hydrocarbon side chains and irreducible molecules	<table border="1"> <tr><td></td><td>C</td><td>C</td><td>C</td><td>H</td></tr> <tr><td>C</td><td>0</td><td>-1</td><td>0</td><td>1</td></tr> <tr><td>C</td><td>-1</td><td>0</td><td>1</td><td>0</td></tr> <tr><td>C</td><td>0</td><td>1</td><td>0</td><td>-1</td></tr> <tr><td>H</td><td>1</td><td>0</td><td>-1</td><td>0</td></tr> </table>		C	C	C	H	C	0	-1	0	1	C	-1	0	1	0	C	0	1	0	-1	H	1	0	-1	0		All reactions allowed; however, in cases with multiple reactions for a given site, a single reaction is selected based on radical stability of intermediates as described in the appendix.
	C	C	C	H																								
C	0	-1	0	1																								
C	-1	0	1	0																								
C	0	1	0	-1																								
H	1	0	-1	0																								
Enol-Aldehyde Tautomerization enols	<table border="1"> <tr><td></td><td>C</td><td>C</td><td>O</td><td>H</td></tr> <tr><td>C</td><td>0</td><td>-1</td><td>0</td><td>1</td></tr> <tr><td>C</td><td>-1</td><td>0</td><td>1</td><td>0</td></tr> <tr><td>O</td><td>0</td><td>1</td><td>0</td><td>-1</td></tr> <tr><td>H</td><td>1</td><td>0</td><td>-1</td><td>0</td></tr> </table>		C	C	O	H	C	0	-1	0	1	C	-1	0	1	0	O	0	1	0	-1	H	1	0	-1	0		Reaction allowed on any primary enol.
	C	C	O	H																								
C	0	-1	0	1																								
C	-1	0	1	0																								
O	0	1	0	-1																								
H	1	0	-1	0																								

Pyrolysis reactions were also used in the formation of char as summarized in Table 3.7. The primary reaction family used to create higher molecular weight molecules was Diels-Alder addition. Other reaction families, e.g. dehydrogenation, allowed for the formation of stable aromatic molecules such as benzene and naphthalene.

Table 4.15: Pyrolysis reactions used to build aromatic, polyaromatic char molecules.

<u>Reaction Type (Family) and Reactive Moiety</u>	<u>Reaction Matrix</u>	<u>Example Reaction</u>	<u>Reaction Rules</u>																									
Diels-Alder Addition Diene, dienophile	Bimolecular reaction matrix, more complex		2 and 6 carbon dieneophiles were allowed to react with 4 carbon enes.																									
Double-bond shift Double bonds	<table border="1"> <tr> <td></td> <td>C</td> <td>C</td> <td>C</td> <td>H</td> </tr> <tr> <td>C</td> <td>0</td> <td>-1</td> <td>0</td> <td>1</td> </tr> <tr> <td>C</td> <td>-1</td> <td>0</td> <td>1</td> <td>0</td> </tr> <tr> <td>C</td> <td>0</td> <td>1</td> <td>0</td> <td>-1</td> </tr> <tr> <td>H</td> <td>1</td> <td>0</td> <td>-1</td> <td>0</td> </tr> </table>		C	C	C	H	C	0	-1	0	1	C	-1	0	1	0	C	0	1	0	-1	H	1	0	-1	0		Reactions allowed only on double bonds in a ring.
	C	C	C	H																								
C	0	-1	0	1																								
C	-1	0	1	0																								
C	0	1	0	-1																								
H	1	0	-1	0																								
Dehydrogenation Hydrocarbon side chains and irreducible molecules	<table border="1"> <tr> <td></td> <td>C</td> <td>H</td> <td>H</td> <td>C</td> </tr> <tr> <td>C</td> <td>0</td> <td>-1</td> <td>0</td> <td>1</td> </tr> <tr> <td>H</td> <td>-1</td> <td>0</td> <td>1</td> <td>0</td> </tr> <tr> <td>H</td> <td>0</td> <td>1</td> <td>0</td> <td>-1</td> </tr> <tr> <td>C</td> <td>1</td> <td>0</td> <td>-1</td> <td>0</td> </tr> </table>		C	H	H	C	C	0	-1	0	1	H	-1	0	1	0	H	0	1	0	-1	C	1	0	-1	0		Reactions only allowed on cyclic structures.
	C	H	H	C																								
C	0	-1	0	1																								
H	-1	0	1	0																								
H	0	1	0	-1																								
C	1	0	-1	0																								

4.4.1.3 Gasification

Two forms of gasification reactions were included in the cellulose and hemicellulose networks: incomplete combustion and steam reforming, as shown in Table 4.16. Gasification reactions between hydrocarbons and hydrogen or CO₂, the other gasifying agents in the MSW gasification process, were assumed to be negligible. It should be noted that for the included gasification reactions, the rate laws were assumed to be first order with respect to both reactants. This prevents unrealistic reaction orders with respect to the gasifying agent.

Table 4.16: Gasification reactions in hemicellulose and cellulose networks.

<u>Reaction Type</u>	<u>Example Reaction</u>	<u>General Reaction</u>
Incomplete Combustion	$\text{C}_x\text{H}_y + 3.5\text{O}_2 \longrightarrow 3\text{CO} + 4\text{H}_2\text{O}$	$\text{C}_x\text{H}_y\text{O}_z + \frac{x + \frac{y}{2} - z}{2} \text{O}_2$ $\rightarrow x\text{CO} + \left(\frac{y}{2}\right)\text{H}_2\text{O}$
Steam Reforming	$\text{C}_x\text{H}_y + 3\text{H}_2\text{O} \longrightarrow 3\text{CO} + 7\text{H}_2$	$\text{C}_x\text{H}_y\text{O}_z + (x - z)\text{H}_2\text{O}$ $\rightarrow x\text{CO} + \left(\frac{y}{2} - (x - z)\right)\text{H}_2$

4.4.2 Lignin

4.4.2.1 Interconversion of Attributes

Due to the attribute representation of the composition of lignin, the reaction network of lignin contains reactions between attributes. In biomass gasification, cores are modeled to react via gasification reactions to form smaller cores and light gasses. Side chains and linkages are modeled to react from both pyrolysis and gasification reactions.

4.4.2.2 Core Reactions

The core reactions currently included in the lignin reaction network are incomplete combustion and steam reforming. These reactions occur in a stepwise manner for each of the cores as shown in Figure 4.12. The first core would react with oxygen or steam to produce a reduced size core. This reduced core would then react with oxygen or steam to be completely consumed, forming light gasses.

The reaction network for cores only included gasification reactions. This was due to the high thermal stability of cores in the system. The two dominant cores, accounting for 82 mol% of all cores are benzene and phenol, and they are stable under

pyrolysis conditions and are reacted through gasification. Additionally, in cores that can undergo thermal cracking, the majority of the mass belongs to aromatic rings.

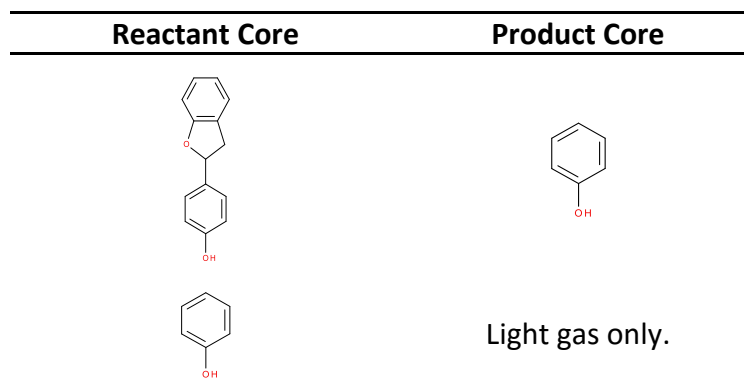
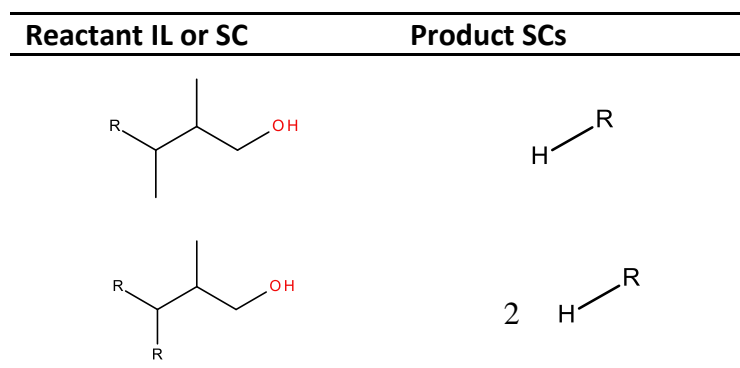


Figure 4.12: Example of stepwise gasification reactions of cores. Each reaction is written for both incomplete combustion and steam reforming. The alternate reactions where the phenol ring is gasified first were also written.

4.4.2.3 Linkage and Side Chain Reactions

The inter-core linkage (IL) and side chain (SC) network contains primarily cracking, incomplete combustion, and steam reforming reactions. The cracking reactions are as described in the cellulose and hemicellulose models and include acyclic thermal cracking and decarbonylation. For side chains, incomplete combustion and steam reforming reactions were written such that a hydrogen side chain remained bound to the core as shown in Table 4.17. This characteristic prevents the product core from having empty binding sites. Similarly, when gasification reactions occur on inter-core linkages, two side chains must remain to fill the binding sites on each core.

Table 4.17: IL and SC gasification to hydrogen side chains to retain stable cores.



4.4.2.4 Light Gas Reactions

In addition to the breakdown of cellulose, hemicellulose, and lignin, light gasses are present in the gasifier and undergo gas-phase reactions. A list of included reactions, along with calculated thermodynamic data, is given in Table 4.18.

Thermodynamic properties were calculated from ground state data and Shomate parameters reported by NIST[107]. These properties were used to determine if reactions were modeled as reversible or irreversible.

Table 4.18: Thermodynamic details of the specific gas-phase reactions. Superscripts represent temperatures (K).

Reaction		K_{eq}^{298}	K_{eq}^{1000}
Water-Gas Shift	$CO + H_2O \leftrightarrow CO_2 + H_2$	1.05E+05	1.44
Steam Reforming Methane	$CH_4 + H_2O \leftrightarrow CO + 3H_2$	1.19E-25	26.74
Partial Oxidation Methane	$CH_4 + \left(\frac{1}{2}\right)O_2 \rightarrow CO + 2H_2$	1.39E+15	3.07E+11
Dry Reforming of Methane	$CH_4 + CO_2 \leftrightarrow 2CO + 2H_2$	1.13E-30	18.62
Oxidation of CO to CO₂	$CO + \left(\frac{1}{2}\right)O_2 \rightarrow CO_2$	1.23E+45	1.65E+10

4.5 Network Generation

The reaction network was generated automatically using in-house software tools. The pyrolysis networks were generated using the Interactive Network Generator, or INGen[44],[40]. In this case, three separate networks were generated: a combined cellulose-hemicellulose network, a lignin core network, and a lignin SC-IL network. An in-house C# application, INGen Network Merge, was developed to both merge these networks and add gasification reactions to the system. The final reaction network features are summarized in Table 3.9. The network contained eight reaction families for depolymerization and pyrolysis, and six reaction families for gasification with oxygen and water. The final network contained 1348 reactions and 357 species. This network was used to construct the kinetic model.

Table 4.19: Reaction network diagnostics for the biomass model.

Reaction Families	Reactions
<u>Depolymerization and Pyrolysis</u>	
	474
Acyclic Thermal Cracking	
Cellulose Depolymerization	3
Double-Bond Shift	76
Decarbonylation	108
Dehydrogenation	10
Diels-Alder	40
Enol-Alde Tautomerization	37
Hemicellulose	3
Depolymerization	
<u>Gasification</u>	
Core Oxidation	26
Core Steam Reforming	26
Incomplete Combustion	231
Incomplete Combustion-Chain	55
Steam Reforming	209
Steam Reforming-Chain	45
<u>Light Gas Reactions</u>	
	5
<u>Total Reactions</u>	1348
<u>Total Species</u>	357

4.6 Model Equations and Kinetics

The model equations in a molecular-level kinetic model are fundamentally a set of differential equations derived from material balances. The reaction rate constants are calculated using a standard Arrhenius equation; this gives two rate parameters, the pre-exponential factor and activation energy, per reaction in the network.

To reduce the parametric complexity of the model, reaction families and linear free energy relationships (LFERs) were utilized. First, all reactions from a given reaction family are modeled to have the same pre-exponential factor. Second, the Bell-

Evans-Polanyi LFER[51], [52] in Equation 4.11 is used to relate the activation energy of reactions within a reaction family, j , to the enthalpy change on reaction, i . This yields the rate constant expression in Equation 4.12. In this relationship, there are three parameters per reaction family in the model: $\ln A$, E_0 , and α . There are few data in the gasification literature on non-light gas species. This makes it difficult to differentiate rate constants within a given family; therefore, most families were modeled to have α equal to zero, thereby removing a third of the adjustable parameters. After parameter reduction, there was a total of 39 adjustable parameters in the model as shown in Table 4.20.

$$E_{i,j}^* = E_{0(j)} + \alpha_j * \Delta H_i \quad (4.11)$$

$$\ln k_i = \ln A_j - \left(\frac{E_{0(j)} + \alpha_j * \Delta H_i}{RT} \right) \quad (4.12)$$

To reduce the complexity of the optimization problem, further constraints were applied to the adjustable parameters in the model, as described in Table 4.20. First, literature values were obtained for the rate constants of decarbonylation, dehydrogenation, and water-gas shift[81],[74]. Further constraints were obtained by allowing thermodynamic equilibrium to dictate two reaction families: double-bond shift and enol-aldehyde tautomerization. Incomplete combustion of small molecules and chains from lignin were modeled using the same rate constant. Steam gasification is known to be significantly slower than oxygen gasification[108]; in this work, the rate constants for steam reforming were constrained to be slower and proportional to the respective incomplete combustion families. Based on this reasoning, dry-reforming and steam-reforming of methane were constrained to be slow relative to the partial

oxidation of methane. After constraints, the optimization problem was reduced to 17 parameters.

Table 4.20: Analysis of adjustable parameters and constraints in the model.

Reaction Families	Adjustable Parameters	Constraints	Justification
<u>Depolymerization and Pyrolysis</u>			
Acyclic Thermal Cracking	3	0	
Cellulose Depolymerization	2	0	
Double-Bond Shift	2	2	Equilibrated
Decarbonylation	2	2	Literature Value
Dehydrogenation	2	2	Literature Value
Diels-Alder	2	2	Equilibrated
Enol-Alde	2	2	Equilibrated
Tautomerization			
Hemicellulose Depolymerization	2	0	
<u>Gasification</u>			
Core Oxidation	2	0	
Core Steam Reforming	2	2	k proportional to Core Oxidation
Incomplete Combustion	2	0	
Incomplete Combustion-Chain	2	2	k same as Incomplete Combustion
Steam Reforming	2	2	k proportional to Incomplete Combustion
Steam Reforming-Chain	2	2	k proportional to Incomplete Combustion
<u>Light Gas Reactions</u>			
	10	6	Literature values and kinetic reasoning
<u>Total</u>	39	22	

The material balances for the attribute reaction model used for lignin are in terms of attributes, rather than species[48], [109]. The equations for the attributes are analogous to the molecular species material balances and are given below in Equation 4.13. All other traits of the reaction kinetics, e.g. reaction family concept, are analogous to the irreducible molecule model discussed previously. It should be noted that despite the attribute representation, the list of molecular species and mole fractions can be generated at any point in the solution[109]; the attribute material balances simply change the relative amounts of attributes in the system.

$$\frac{d\overline{Core}}{dt} = \sum_{i, reactions} \bar{v}_i * rate_i \quad (4.13) \quad a.$$

$$\frac{d\bar{L}}{dt} = \sum_{i, reactions} \bar{v}_i * rate_i \quad b.$$

$$\frac{d\overline{SC}}{dt} = \sum_{i, reactions} \bar{v}_i * rate_i \quad c.$$

4.7 Model Evaluation

To evaluate the model, literature data from Li et al. on uncatalyzed biomass gasification in a circulating fluidized bed were simulated. The paper contained data on five biomass samples and temperatures ranging from 700-815 °C. The reactor was modeled as a continuous stir tank reactor to simulate the experimental fluidized bed. The authors performed 15 experiments varying feedstock, temperature, pressure, oxidation agent, and ash reinjection. The data of primary interest are at atmospheric pressure with air as the oxidation agent, no ash reinjection, and no added catalyst. For these runs, the temperature, feedstock, and gas composition are given in Table 4.21. From this table, runs 3, 4, and 11 were chosen for tuning to test two biomass samples

at a moderate range of temperatures. The remaining data sets were reserved to test the predictive ability of the model.

Table 4.21: Biomass type, temperature, and gas composition for each utilized experimental run from Li et al (2004). For biomass type, the abbreviations are Cyp – cypress, hem – hemlock, SPF- spruce, pine, fir. PS – pine, spruce.

Run Number	2	3	4	11	12	13
Biomass Type	cyp.	SPF	hem.	hem.	PS	mixed
Temperature (°C)	718	766	815	789	701	728
H₂ (mol%)	3.1	3.2	3	4.2	5.4	5.1
N₂ (mol%)	68.1	67.1	68.4	62.6	53.9	56.3
CO (mol%)	11	10.7	9.6	14.6	21.4	19.9
CH₄(mol%)	1.9	1.9	1.9	3	4.6	4.1
CO₂(mol%)	15.9	17.1	17.1	15.7	14.7	14.5

The results, in the form of a parity plot, are given below in Figure 4.13.

Tabulated versions of these results are also given in Table 4.22. The results fit well with experimental data with a best fit line of $y_{predicted} = y_{obs} * 0.928 + 0.0003$.

There are two sources of possible uncertainty. First, there was uncertainty in modeling the ultimate analysis of the biomass, shown previously in Table 4.10. This was most notable in the values for oxygen. This can be partly attributed to the absence of sulfur and nitrogen in the cellulose, hemicellulose, and lignin composition models. Second, the biomass samples contain varying, trace amounts of ash which can have a catalytic effect on gasification reactions[110].

Table 4.22: Observed and predicted values for data sets in Li et al. All values in the table are in mol/s.

Composition	Data Set 3 (exp, pred)	Data Set 4 (exp, pred)	Data Set 11 (exp, pred)
CH ₄	0.017, 0.016	0.020, 0.016	0.024, 0.028
H ₂	0.028, 0.032	0.031, 0.033	0.034, 0.034
CO	0.094, 0.093	0.101, 0.075	0.117, 0.141
CO ₂	0.150, 0.135	0.179, 0.175	0.126, 0.091

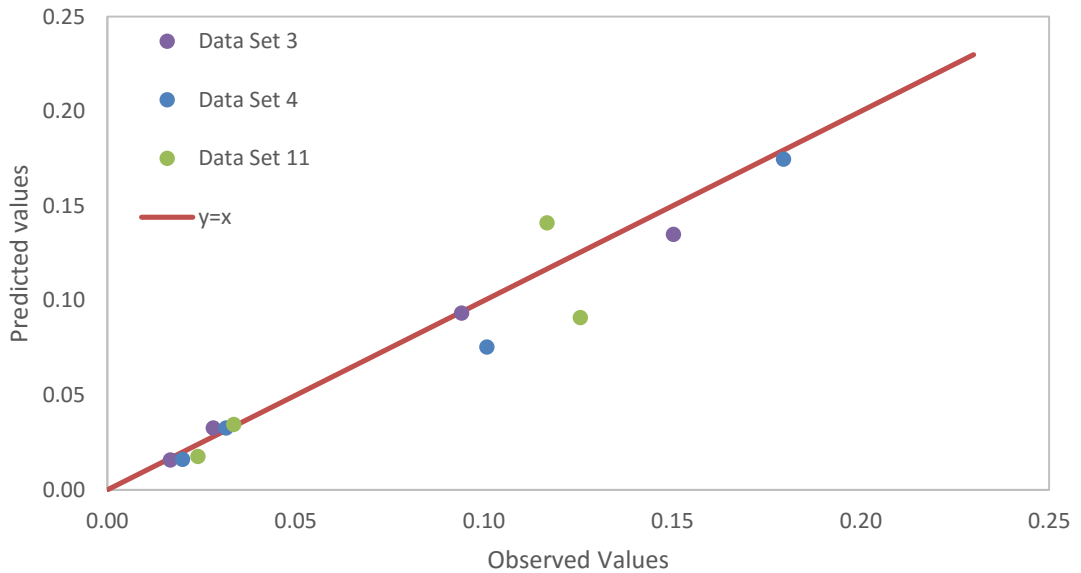


Figure 4.13: Parity plot of tuned data sets for Li et al data. After a linear fit, the formula comparing experiment to model results is $y_{\text{predicted}} = y_{\text{obs}} * 0.928 + 0.0003$. The R^2 relative to $y=x$ is 0.918 for the tuned data sets.

In order to test the tuned kinetic parameters, a once-through simulation was run using all six viable data sets. The parity plot is shown below, in Figure 4.14. The results are summarized as $y_{\text{predicted}} = y_{\text{obs}} * 0.989 - 0.007$ even though the predicted data sets included both a wider temperature range and additional biomass

samples. This suggests model robustness, a key feature for technologies such as MSW gasification.

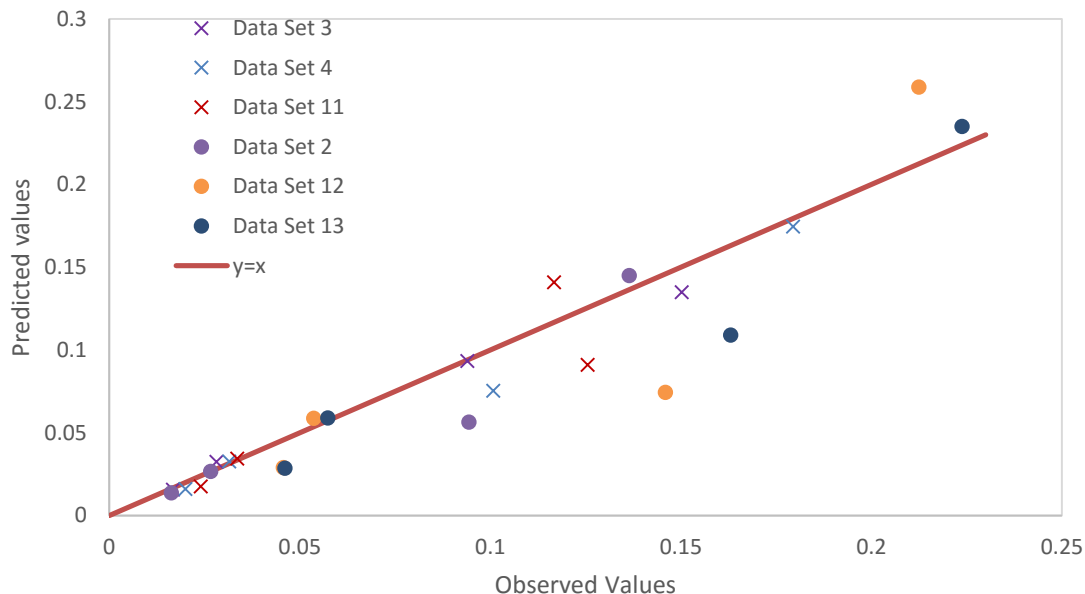


Figure 4.14: All viable datasets from Li et al (2004) using tuned parameters from data sets 3, 4, and 11. Squares represent tuned results, circles are predicted results. After a linear fit, the formula comparing experiment to model results is $y_{\text{predicted}}=y_{\text{obs}}*0.989-0.007$. The R^2 relative to $y=x$ is 0.861 for all data sets.

4.8 Tar Prediction and Reaction Family Analysis

A major advantage of molecular-level kinetic models is the ability to ask the model questions at the molecular level. First, the model predicts both the quantity and composition of tar, defined here as molecules with a higher boiling point than benzene. The relative amounts of tar produced in each of the data sets are given below, in Table 4.23. The trend that data sets 11-13 produced the highest tar agreed with the experimental measurements[13]. The amount of tar also increases as the biomass/O₂

ratio increases as shown in Figure 4.15. The oxygen increase does have a tradeoff in the quality of the syngas; higher tar fractions had a higher fraction of CO and H₂ in syngas. The composition of tar was predominantly lignin-derived components derived from benzene and phenol with methoxy substituents. It is important to note that mass transport, heat transport, and vapor-liquid equilibrium are not taken into account in the modeling of tar in this model. Any tar molecule that is present in the product stream at the reactor outlet is considered part of the tar fraction. This is important to note when comparing with literature studies, such as CPD models by Fletcher and co-workers[93], [94], that model tar release as well as tar formation. It is not a fundamental limitation of molecular-level kinetic models to exclude tar release, or more generally mass and heat transfer effects. An interesting path for future work is to analyze whether these phenomena play a role in discrepancies between model predictions and experimental data.

Table 4.23: Weight fraction of tar in output stream for all data sets.

Data Set	Tar Fraction
Data Set 2	0.028
Data Set 3	0.031
Data Set 4	0.027
Data Set 11	0.058
Data Set 12	0.058
Data Set 13	0.049

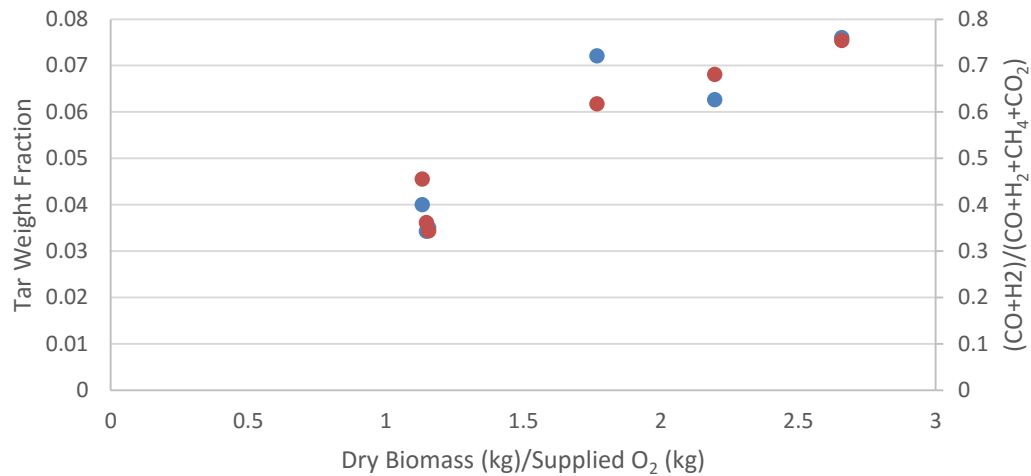


Figure 4.15: Tar weight fraction as a function of the ratio of dry biomass to supplied oxygen (blue, left axis). The fraction of CO and H₂ in overall dry syngas (nitrogen excluded) is also shown (orange, right axis).

The model can also provide additional insight into the process chemistry. First, during reactor integration, the rates of each reaction are recorded as a function of reactor volume. The total molar flux through each reaction can then be quantified using Equation 4.14. For example, if the reaction were the oxidation of CO to CO₂, the summation would return the moles of CO reacted. If the result of Equation 4.14 is calculated for every reaction within a reaction family, then the total flux through the reaction family is quantified. A comparison of the relative sums of all reaction families is given, below, in Figure 4.16. From these results, the dominant pyrolysis reaction families include the depolymerization of each biomass component. Of the gasification chemistries, oxidation was far more prevalent than steam reforming.

$$\text{Molar Flux through reaction} = \sum_{i, \text{ integration points}} (V_{i+1} - V_i) * \text{rate}_i \quad (4.14)$$

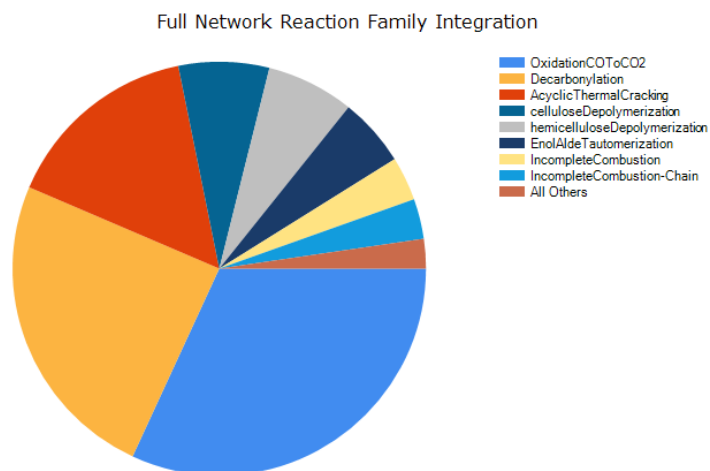


Figure 4.16: Relative importance of reaction families in the reactor model integration for Data Set 11. All analysis was done using an in-house C# application, *KME Results Analyzer*.

4.9 Kinetic Rate Constants

The tuned values for the kinetic rate constants relative to Acyclic Thermal Cracking at 1000K are given in Table 4.24. The initial removal of moisture is important to gasification processes. Here, this removal is incorporated into the rate constants for the initial breakdown of polymeric structures. For cellulose and hemicellulose, the relevant reaction families are cellulose and hemicellulose depolymerization. For lignin, the primary breakdown of polymeric structure is cracking, oxidation, and steam reforming of chains.

Table 4.24: Rate constants at 1000K relative to Acyclic Thermal Cracking.

$\log(k)_{\text{relative},1000} = \log(k)_{\text{AcyclicThermalCracking},1000} - \log(k)_{\text{ReactionFamily},1000}$. Reaction families that were assumed to be equilibrated are not included in the table.

Reaction Family	$\log(k)_{\text{relative}, 1000}$
Depolymerization and Pyrolysis	
Acyclic Thermal Cracking	0.00
Cellulose Depolymerization	0.56
Decarbonylation	1.64
Dehydrogenation	0.84
Hemicellulose Depolymerization	-3.34
Gasification	
Core Oxidation	-0.30
Core Steam Reforming	-10.62
Incomplete Combustion	-2.73
Incomplete Combustion-Chain	-2.73
Steam Reforming	-5.94
Steam Reforming-Chain	-5.94
Light Gas reactions	
Water-gas shift	-7.46
Oxidation CO to CO ₂	-2.10
Partial Oxidation of Methane	-3.71
Steam Reforming of Methane	-5.94
Dry Reforming of Methane	-5.94

4.10 Conclusions

This study has demonstrated that the composition of biomass and kinetics of biomass gasification can be described at the molecular-level. The composition model showed that individual models for cellulose, hemicellulose, and lignin can be linearly combined to produce a full biomass composition model that fit well with literature experimental data. The kinetic model was constructed using a tractable number of tunable parameters, and was shown to agree not only the data sets used for tuning, but

also additional reported results. The results of the kinetic model demonstrated that syngas composition can be predicted across different biomass samples with the same set of parameters, thereby addressing a key weakness of lumped kinetic models. This allows the kinetic model to be used in commercial applications such as municipal solid waste gasification where the biomass type varies as a function of both time and location.

Chapter 5

IMPLEMENTATION OF A MOLECULAR-LEVEL KINETIC MODEL FOR PLASMA-ARC MUNICIPAL SOLID WASTE GASIFICATION

Scott R. Horton¹, Yu Zhang², Rebecca Mohr², Francis Petrocelli², and Michael T. Klein^{1*}

¹University of Delaware Energy Institute and Department of Chemical and Biomolecular Engineering, University of Delaware, Newark, DE 19716

²Air Products and Chemicals Incorporated. Allentown, PA, 18195

Reproduced by permission from **Horton, S.R.**; Mohr, R.; Zhang, Y.; Petrocelli, F.; Klein, M.T. "Implementation of a Molecular-level Kinetic Model for Plasma-arc Municipal Solid Waste Gasification." (Submitted to Energy & Fuels)

5.1 Abstract

A molecular-level kinetic model was developed for a plasma-arc municipal solid waste (MSW) gasification unit. The kinetic model included both MSW and foundry coke. The components included in the MSW kinetic model were biomass and four common plastics, detailed in earlier reports. The relative amounts of these components can be optimized for experimental ultimate analyses using an in-house tool, *The MSW Bulk Composition Solver*. The reaction chemistries included detailed pyrolysis and gasification chemistry totaling 1628 reactions and 433 molecular species. The kinetic model utilized Arrhenius rate laws and contained a material balance for each species in the model. The model of coke gasification included 10 reactions of surface atoms with oxygen and carbon dioxide. The reaction rates were modeled using both surface diffusion and intrinsic kinetics. The plasma arc gasifier was simulated using three zones for MSW: combustion, gasification, and freeboard, and a separate zone for coke gasification. Each bed was simulated using idealized chemical reactors with independent conditions. The simulation of the gasifier was organized in a user-friendly application, organizing measurable inputs and outputs. This application allowed for trending studies, investigating the effects of equivalence ratio, MSW composition, and relative sizes of combustion and gasification zones. The results provided insight into the effects of these variables on tar production, tar composition, and the quality of produced syngas.

5.2 Introduction

In 2013, the United States produced 250 million tons of municipal solid waste (MSW)[1]. The management of this waste has evolved over the years, as shown in Figure 5.1. Historically, MSW was disposed of in landfills; however, in the 1970s,

recycling began to become more prevalent. In recent years, the growth of recycling has tapered off. This begs the question: what should be done with waste that cannot be economically or efficiently recycled? Currently, landfills remain are the primary disposal methodology.

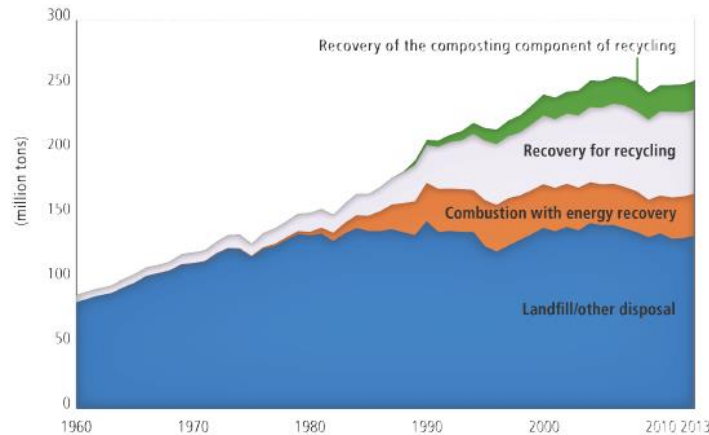


Figure 5.1: MSW management technologies from 1960-2013. Figure from source material[1].

The economic and environmental issues surrounding landfills motivate waste-to-energy (WTE) technologies. Environmentally, landfills are potential sources of groundwater contamination. Also, uncontrolled degradation of waste promotes the formation of greenhouse gases, such as CH_4 [111], that are tens of times more potent than CO_2 . Economically, WTE is attractive due to landfill tipping fees, energy recovery, and political incentives. Landfill tipping fees in the US are shown in Figure 5.2, and are currently on the order of 50 USD/ton. Furthermore, these fees are drastically higher in a more space-limited country; for instance, the UK has tipping fees of around 120 USD/ton[112]. Also, MSW is a remarkable potential source of

energy; it has been estimated that the energy content in only the plastic fraction of US waste is 700 trillion BTU, equivalent to 139 million barrels of oil, per year[113]. Politically, this energy source has been judged renewable in the UK, and thereby provides additional revenue from renewable energy credits.

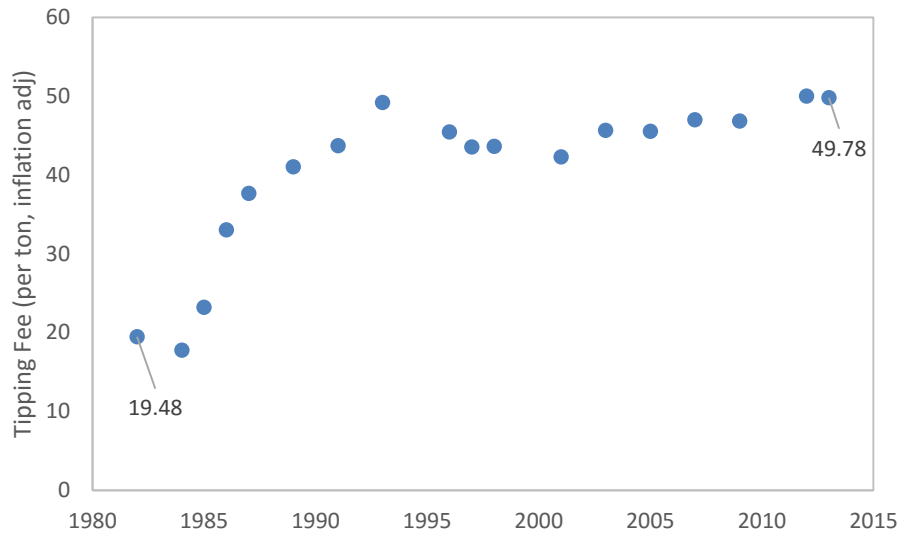


Figure 5.2: Average landfill tipping fees in the US 1982-2013. Prices are in USD.[1]

One of the up-and-coming waste-to-energy technologies is plasma-arc gasification. This technology offers many advantages over traditional incineration. First, oxygen is kept lower than stoichiometric levels, thereby reducing the production of harmful oxygenated pollutants[21]. Second, in gasification the waste is converted to syngas, a ubiquitous product that can be utilized for electricity or liquid fuel synthesis. Finally, due to the extreme temperatures in plasma-arc gasification, the final by-product is a vitrified slag. This slag material passes EPA leech tests and can be utilized for construction purposes[6].

Models allow for prediction and optimization of reactor outlets for a given reactor inlet. In the broad sense, plasma arc gasification has three primary inputs: MSW, Coke, and enriched air. MSW is composed of a variety of components ranging from paper to food to plastics. Furthermore, the composition of MSW is a function of both location and time of year. The second inlet, coke, is fed to the reactor as a heat source and to provide mechanical support for the waste bed. The enriched air stream is fed at various points along the reactors walls and provides gasification agents for the breakdown of MSW. A portion of this air inlet is heated by the plasma torch before entering the main reactor. Interest in modeling MSW gasification stems from the complexity and variability of these input streams. This variability must be captured for a useful and robust model of MSW gasification. In particular, the model must predict response of key outputs, such as syngas and tar composition.

There are many mathematical models of the gasification of MSW, or its components, in the open literature. The most common type of models are based on assuming thermodynamic equilibrium[14], [17], [26]–[33] which predict outlet compositions based only on the temperature of the gasifier. In the outlet composition, the prediction of tar molecules is important in gasification for downstream processing. This prediction is problematic for equilibrium models as the extreme temperatures in the gasifier disallow tar molecules at thermodynamic equilibrium. Therefore, to predict tar molecules, kinetics are necessary. Xiao et al.[37], used an artificial neural net to model MSW gasification. Artificial neural nets can predict tar molecules, however the absence of chemical meaning to connections within the neural net reduces the insight gained from the model. Zhang and coworkers[34], [35] utilized an Eulerian model to study the flow characteristics paired with lumped kinetics. Some

advantages of lumped kinetics include the model solution time, the number of equations, and model simplicity. Lumped kinetics have disadvantages in terms of model robustness if the feed or conditions are perturbed from the data used for parameter tuning.

In kinetic modeling, the type of model is determined by the complexity of both the desired inputs to the model and predictions. In this case, the complexity of both inputs and predictions are at the molecular-level. For instance, a given MSW composition is a set of molecules and mole fractions, and changes in MSW composition are reflected in the mole fractions. The predictions of the model, tar and syngas composition, are also fundamentally represented as a list of molecular structures and amounts. Because of the molecular nature of model inputs and outputs, the optimal kinetic modeling approach is also at the molecular-level.

In this work, we have built a molecular-level kinetic model for a plasma-arc gasifier. For the MSW stream, we have combined models from two prior works on plastics and biomass gasification[54], [83]. The model of coke gasification, detailed in this report, takes into account both diffusional and kinetic limitations. The gasifier was simulated using four zones: combustion, gasification, freeboard, and a coke bed. Each zone was simulated using an idealized reactor, plug-flow or continuously stirred tank, with independent reactor conditions. This model was organized using a user-friendly C# (C sharp) application, allowing for specification of adjustable inputs and rapid analysis of observable outputs. This app enabled trending studies on important design parameters.

5.3 Kinetic Model Development of Municipal Solid Waste Gasification

The kinetic model of MSW gasification includes biomass and four common plastics: polyethylene (PE), polyvinyl chloride (PVC), polyethylene terephthalate (PET), and polystyrene (PS). Kinetic models for biomass and plastic gasification have been individually discussed in prior publications[54], [83]. These models were merged for the full model of MSW utilized in this work. In this section, the details of this model are divided into three categories: the composition model, the reaction chemistry and reaction network, and the automatically constructed kinetic model.

5.3.1 MSW Composition Model

For molecular-level kinetics, the composition of MSW is a list of molecules and mole fractions. The composition model takes a lumped input such as MSW, and, using experimental information, predicts the molecular composition. Model development was a multistep process. First, the waste components in MSW, shown in Figure 5.3, were divided into two modeled categories: plastics and biomass-derived. These two categories were then divided into individual polymers: PE, PVC, PET, PS, cellulose, hemicellulose, and lignin. The molecular composition model was discussed for each of these polymers in prior work; however, in general, polymers were described using known repeat-unit structures and polymer-size distributions. The molecular composition of MSW was modeled as a weighted average of the polymeric compositions, where each weighting was based on the fraction of that polymer in waste.

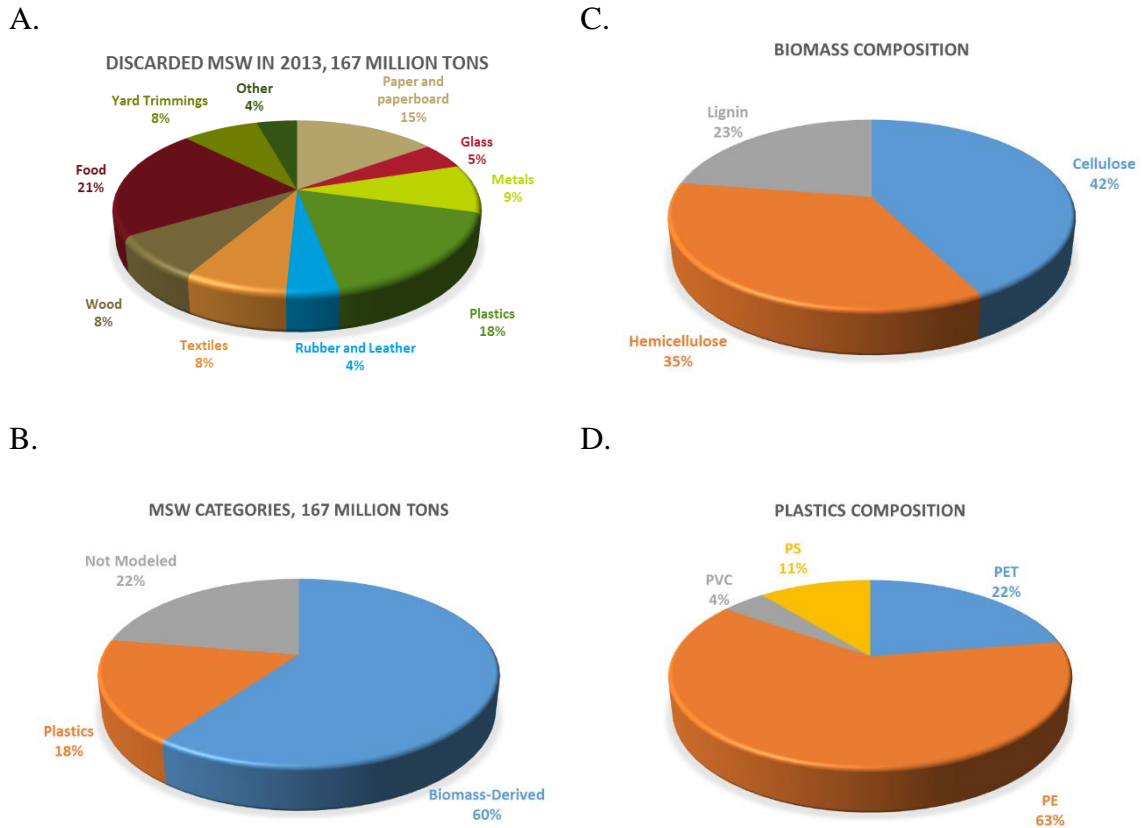


Figure 5.3: MSW Fractions in the United States in 2013. A. Overall fractions as reported by the EPA. B. MSW divided into four categories. The biomass-derived category includes food, wood, yard trimmings, textiles, and paper. The ‘not modeled’ category includes metals, glass, other, and rubber and leather. C. the cellulose hemicellulose and lignin splits predicted in prior work[83] using data from Li and coworkers[13]. D. The relative amounts of included plastics, renormalized from EPA data[1].

The analysis in Figure 5.3 utilizes literature data for the fractional split of MSW components, but MSW is an inherently variable feedstock. To allow these variations, an in-house C# application titled ”MSW Bulk Composition Solver” was developed for tuning new MSW compositions based on simple experimental ultimate

analyses. This application allows the user to vary any of the mass fractions of the seven polymers. The least-squares objective function of the optimization routine compares calculated and experimental ultimate analyses. The optimization proceeds using an in-house simulated annealing algorithm.

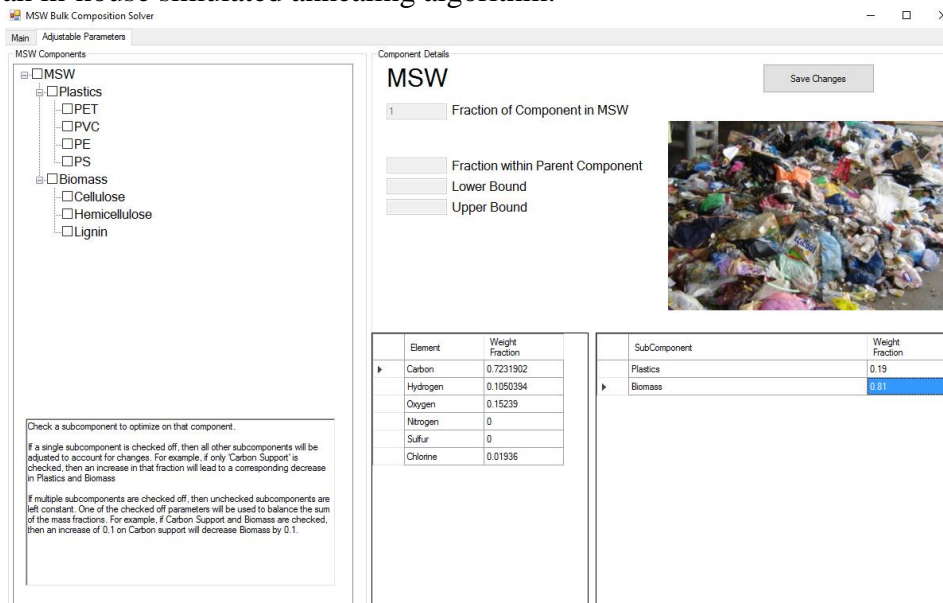


Figure 5.4: Screenshot from the MSW Bulk Composition Solver. In this screen, the checkboxes on the left allow the user to select which fractions are adjusted during the optimization procedure.

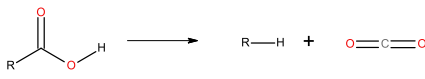
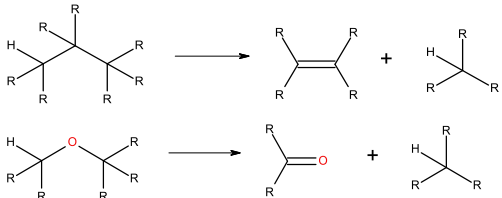
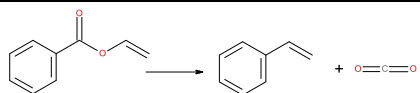
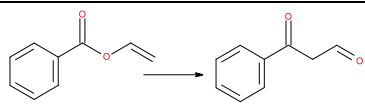
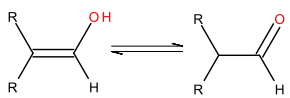
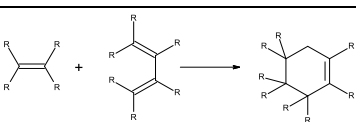
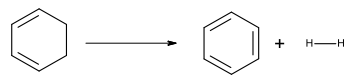
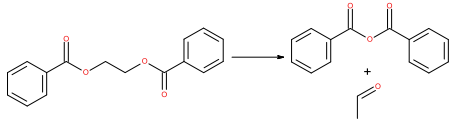
The application in Figure 5.4 allows the user to easily apply ultimate analyses to the kinetic model; however, it is advised that this cursory experiment only be used on feedstocks with similar compositions. The optimization problem is underspecified as there are seven polymers and an ultimate analysis containing only four data points (C, H, O, Cl). It is better to utilize this application with supplemental information to reduce the degrees of freedom of the optimization. For instance, relative amounts of

individual plastics is known, the optimization problem can be constrained. The impact of MSW composition on process variables is analyzed in later results.

5.3.2 Reaction Chemistry and Network

The reaction chemistry of MSW gasification includes pyrolysis and gasification chemistries. Pyrolysis reactions are thermal and take place without the presence of a gasifying agent, as discussed in prior work[54], [83]. There are two primary categories of pyrolysis chemistry discussed in Table 5.1. The first category contains reactions, such as thermal cracking, that break down molecules. The second type of pyrolysis reactions are based on addition and produce stable tar molecules. A good example here is Diels-alder addition where a diene reacts with a dienophile to produce a cyclic olefin.

Table 5.1: Pyrolysis reaction families in MSW gasification. These families include both categories of pyrolysis chemistry: cracking and tar-formation. This table was adapted from tables in prior work[54], [83].

Reaction Type (Family) and Reactive Moeti	Example Reaction
Decarbonylation Aldehydes	
Decarboxylation Carboxylic acids	
Acyclic Thermal Cracking Hydrocarbon side chains and irreducible molecules	
Ester Decarboxylation Esters	
Ester Rearrangement Esters adjacent to a double bond	
Enol-Aldehyde Tautomerization enols	
Diels-Alder Addition Diene, dienophile	
Double-bond shift Double bonds	
Dehydrogenation Hydrocarbon side chains and irreducible molecules	
PET Anhydride Linkage Formation Hydrocarbon side chains and irreducible molecules	

Gasification reactions take place under the presence of a gasification agent such as oxygen, water, or carbon dioxide. In this work, the included gasification reaction families are incomplete combustion and steam reforming, shown below in Table 5.2; also included in this table are important light-gas reactions such as water-gas shift.

Table 5.2: Included gasification reactions. Table is directly from Horton et al[54].

Reaction Type	Reaction
Incomplete Combustion	Example $C_3H_8 + 3.5O_2 \rightarrow 3CO + 4H_2O$
	General $C_xH_yO_z + \frac{x + \frac{y}{2} - z}{2} O_2 \rightarrow xCO + \left(\frac{y}{2}\right) H_2O$
Steam Reforming	Example $C_3H_8 + 3H_2O \rightarrow 3CO + 7H_2$
	General $C_xH_yO_z + (x - z) H_2O \rightarrow xCO + \left(\frac{y}{2} - (x - z)\right) H_2$
Water-Gas Shift	$CO + H_2O \leftrightarrow CO_2 + H_2$
Steam Reforming Methane to CO	$CH_4 + H_2O \leftrightarrow CO + 3H_2$
Partial Oxidation of Methane	$CH_4 + \left(\frac{1}{2}\right) O_2 \rightarrow CO + 2H_2$
Dry Reforming of Methane	$CH_4 + CO_2 \leftrightarrow 2CO + 2H_2$
Oxidation of CO to CO2	$CO + \left(\frac{1}{2}\right) O_2 \rightarrow CO_2$

The reaction network for MSW was constructed via merging the networks for biomass and plastics gasification. Other details of the reaction chemistry can be found in the original publications[54], [83]. After merging the plastics and biomass

networks, the final reaction network for MSW gasification contained 433 species undergoing 1628 reactions.

5.3.3 Kinetic Model Details

The kinetic model contains a material balance differential equation for each of the 433 species in the reaction network. When integrating a reactor, these differential equations are solved simultaneously. The reaction rates are governed using Arrhenius rate parameters; fundamentally two parameters per reaction. Using the concepts of linear free energy relationships (LFERs) and reaction families, the number of adjustable parameters was reduced to three per reaction family[51], [52], [54]. The values of these parameters were optimized in prior work, and they are left invariant for simulations shown in the current work.

5.4 Kinetic Model Development of Coke Gasification

5.4.1 Coke Structure and Composition

Coke is co-fed to the MSW gasification unit as a source of heat and mechanical stability. The particle-size distribution was 4"-6" for the coke in this study. An ultimate analysis is given in Table 5.3. Elementally, the composition of coke was almost entirely carbon with trace amounts of hydrogen, sulfur, and nitrogen. Pure carbon is effectively large sheets of graphene, and therefore the chemical makeup of this coke is large aromatic clusters. Sulfur and nitrogen are likely contained within the aromatic rings; and hydrogen is likely exist at edge sites. These compositional details are key in determining the gasification reactions of coke.

Table 5.3: Ultimate analysis of coke fed to the gasifier.

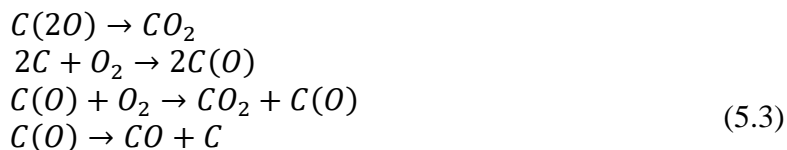
Carbon	98.27
Hydrogen	0.19
Nitrogen	0.96
Sulfur	0.58

5.4.2 Gasification Reactions of Coke

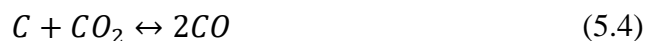
Coke gasification involves between surface atoms and adsorbed gasifying agents. The surface atoms of coke are carbon, hydrogen, nitrogen, and sulfur. The dominant gasifying agents are oxygen and carbon dioxide. While hydrogen is produced and it can react with carbon to form methane, it is not a feed and the reaction with coke will likely be minimal. Although the surface concentrations of H, N, and S are low, their gasification reactions are considered to account for their mass. Simplifications to account for their low concentrations will be discussed.

Carbon can react with oxygen to undergo either complete or incomplete combustion, as shown in Equation 5.1. There is some debate over the surface intermediates and exact steps of the mechanisms for this combustion. Walker et al. gave the mechanism in Equation 5.2 for oxidation where CO originates from carbonyl surface groups and CO₂ originates from lactone surface groups[114]. Later work by Hurt & Calo proposed mechanism in Equation 5.3 after analyzing experimental data with a number of rate law options, including a power law, Langmuir-Hinshelwood-Hougen-Watson, and more complex methods[115]. This mechanism was also the preferred mechanism in a later work by Feng and Bhatia[116].

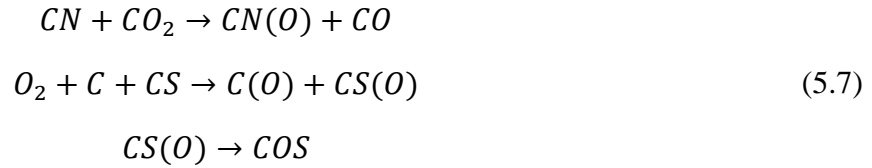
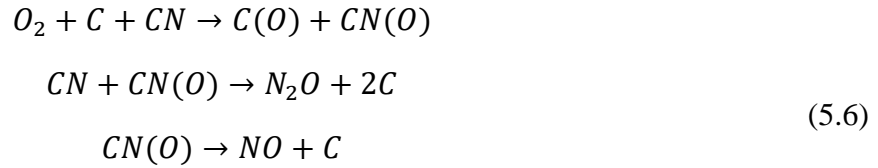




The net surface reaction of CO₂ with carbon to form CO is shown in Equation 5.4, and was studied by its namesake, Boudouard, in 1905. A proposed mechanism was developed by Ergun and is given in Equation 5.5[117]. Rate constants for this mechanism were later studied by Huttinger & Fritz [118]. While more complicated mechanisms exist, this mechanism was reported to explain most experimental observations by Feng & Bhatia[116].



The reactions of nitrogen, sulfur, and hydrogen are less prevalent in the structure of coke and are less well-studied in literature. Surface nitrogen is in low percentages and is likely bound to 5- and 6- member aromatic rings in the surface. The reactions given in Equation 5.6 are proposed by Leppalahti & Koljonen[119] for the gasification with oxygen and CO₂ of surface nitrogen with adjacent surface carbons, CN. For surface sulfur an analogous mechanism produces COS and is proposed in Equation 5.7. Finally, for surface hydrogen, the reaction with oxygen is given in Equation 5.8. For both sulfur and hydrogen, these mechanisms are not based on literature; however, due to the relative scarcity of these surface atoms, the exact details of the mechanism is second order in terms of importance.



5.4.3 Reaction List and Rate Laws

Based on the experimental ultimate and proximate analyses, the coke reaction network has been simplified from the literature mechanisms, and is shown in Table 5.4. Carbon gasification with oxygen is described using two reactions, producing either CO or CO₂. More complex mechanisms involving surface sites are not utilized as the system is known to be diffusion-limited at the reactor conditions. Therefore the combined reaction rate, $r_{net_O_2}$, combines both diffusional limitations and intrinsic kinetics. The relative production of CO and CO₂ is defined using a literature correlation for the $\frac{CO}{CO_2}$ (cR) ratio from Arthur[120] and is given in Equation 5.9.

$$cR = 2500 * e^{-\frac{6420}{T(K)}} \tag{5.9}$$

The rate of consumption of all non-carbon surface elements is assumed to be proportional to the rate of consumption of carbon. For example, after 10% of the surface carbon has been consumed, it is assumed that 10% of H, N, S have also been consumed. These assumptions appear in the rate laws in Table 5.4. Reactions for both oxygen and carbon dioxide are included as either species can consume carbon. It

should be noted that these elements are in small amounts and are not expected to play a major role in gasifier operation; they were included in this model to close the mass balance.

Table 5.4: Reaction network for the coke gasification model. Definitions: $cR = \frac{CO}{CO_2}$ ratio, r_{net} is the net rate taking into account both intrinsic kinetics and diffusional limitations. $[C]_0, [H]_0, [S]_0, [N]_0$ are the relative initial amounts of each element in the coke (Units in either Mol/s or Mol/L).

Reaction	Rate law
$C + \left(\frac{1}{2}\right) O_2 \rightarrow CO$	$r_1 = r_{net_O_2} * \frac{cR}{cR+1}$
$C + O_2 \rightarrow CO_2$	$r_2 = r_{net_O_2} * \frac{1}{cR + 1}$
$2H + 0.5O_2 \rightarrow H_2O$	$r_3 = (r_{net_O_2} + r_5) * \frac{[H]_0}{[C]_0}$
$N + 0.5O_2 \rightarrow NO$	$r_4 = (r_{net_O_2} + r_5) * \frac{[N]_0}{[C]_0}$
$C + S + 0.5O_2 \rightarrow COS$	$r_5 = r_{net_O_2} * \frac{\frac{[S]_0}{[C]_0}}{1 - \frac{[S]_0}{[C]_0}}$
$C + CO_2 \rightarrow 2CO$	$r_6 = r_{net_CO_2}$
$2H + CO_2 \rightarrow H_2O + CO$	$r_7 = (r_{net_CO_2} + r_9) * \frac{[H]_0}{[C]_0}$
$N + CO_2 \rightarrow NO + CO$	$r_8 = (r_{net_CO_2} + r_9) * \frac{[N]_0}{[C]_0}$
$C + S + CO_2 \rightarrow COS + CO$	$r_9 = r_{net_CO_2} * \frac{\frac{[S]_0}{[C]_0}}{1 - \frac{[S]_0}{[C]_0}}$
$CO + \left(\frac{1}{2}\right) O_2 \rightarrow CO_2$	$r_{10} = k * [CO]^{1.5} * [O_2]^{0.25}$ k $= 3.16E12$ $* \exp\left(-\frac{1.67E8 \frac{J}{kmol}}{RT}\right)$

5.4.4 Intrinsic Kinetics and Diffusional Limitations

The net rate given in Equation 5.10 of the reaction of carbon with oxygen takes into account both diffusional limitations and intrinsic kinetics. The Damköhler

number, Da , is defined as the ratio of the rate without diffusion limitations over the diffusion limited rate as shown in 5.11. When Da is small, the reaction rate approaches intrinsic kinetics, or $r_{intrinsic}$. Similarly, when Da is large, the reaction rate approaches the diffusion limited rate, or $r_{diffusionLimited}$. The intrinsic rate follows an Arrhenius relationship, given in Equation 5.12.

$$r_{net_{O_2}} = \frac{r_{intrinsic}}{1 + Da} \left[\frac{mol}{L * s} \right] \quad (5.10)$$

$$Da = \frac{r_{intrinsic}}{r_{diffusionLimited}} \quad (5.11)$$

$$r_{intrinsic} = y[O_2] * A_{O_2,c} * e^{-\frac{E_{O_2,c}}{RT}} \left[\frac{mol}{L * s} \right] \quad (5.12)$$

The diffusion limited rate, shown in Equation 5.13, is proportional to the gas phase oxygen concentration, the surface area to volume ratio of the particle, $\frac{SA_p}{V_p}$, and the oxygen mass transport coefficient, k_{O_2} . The concentration of oxygen depends on the temperature, pressure, and oxygen/air feed composition. The surface area to volume ratio is calculated as a function of time from the initial particle size and the extent of carbon consumption. The mass transport coefficient is calculated using Equation 5.14 and involved calculations of the Sherwood, Schmidt, and Reynolds numbers. The Schmidt number is assumed to be constant as it is a weak function of temperature and contributes little to the Sherwood number.

$$r_{diffusionLimited} = k_{O_2} * y[O_2] * \frac{SA_p}{V_p} = k_{O_2} * y[O_2] * \left(\frac{6}{d_p} \right) \left[\frac{mol}{L * s} \right] \quad (5.13)$$

$$k_{O_2} = \frac{Sh * D_{O_2}}{d_p} \left[\frac{m}{s} \right] \quad (5.14)$$

$$Sh = 2.0 + 1.1 * Re^{0.66} * Sc^{0.33}$$

$$Re = \frac{\rho_g * d_p * v}{\mu}$$

$$Sc = 0.705$$

D_{O_2} : oxygen diffusivity (m^2s^{-1}), d_p : particle diameter (m) v : bed velocity of vapor (m/s)
 μ : viscosity ($kg*m^{-1}*s^{-1}$), ρ_g : vapor density ($kg*m^{-3}$), SA_p : Surface area of particle (m^2)
 V_p : Volume of particle (m^3)

The gasification with CO_2 has analogous formulation as both diffusion and intrinsic rates play a role in determining the kinetics of the reaction. Final equations are given in Equation 5.15 and Equation 5.16.

$$r_{net_CO_2} = \frac{r_{intrinsic} * r_{diffusionLimited}}{r_{intrinsic} + r_{diffusionLimited}} \quad (5.15)$$

$$r_{intrinsic} = y[CO_2] * A_{CO_2,C} * e^{-\frac{E_{CO_2,C}}{RT}} \quad (5.16)$$

$$r_{diffusionLimited} = k_{CO_2} * y[CO_2] * \frac{SA_p}{V_p} = k_{CO_2} * y[CO_2] * \left(\frac{6}{d_p} \right)$$

5.4.5 Analysis of Kinetics in Coke Bed

Diffusional limitation are known to play a role in the gasification of coke at the reaction temperatures. To examine this idea further, Figure 5.5 shows the values of $r_{intrinsic}$, $r_{diffusionLimited}$, and $r_{net_O_2}$ for both 4” and 6” particles at a range of temperatures. As expected from the equations, the intrinsic rate is independent of particle size, and the diffusion limited rate decreases with increasing particle size. In the expected temperature regime of $>1400K$, diffusion limitations dominate. This is

shown in Figure 5.6 which shows the Da as a function of temperature for the two particle sizes. The temperature region of interest has Da much larger than 1, indicating surface diffusion control of the rate.

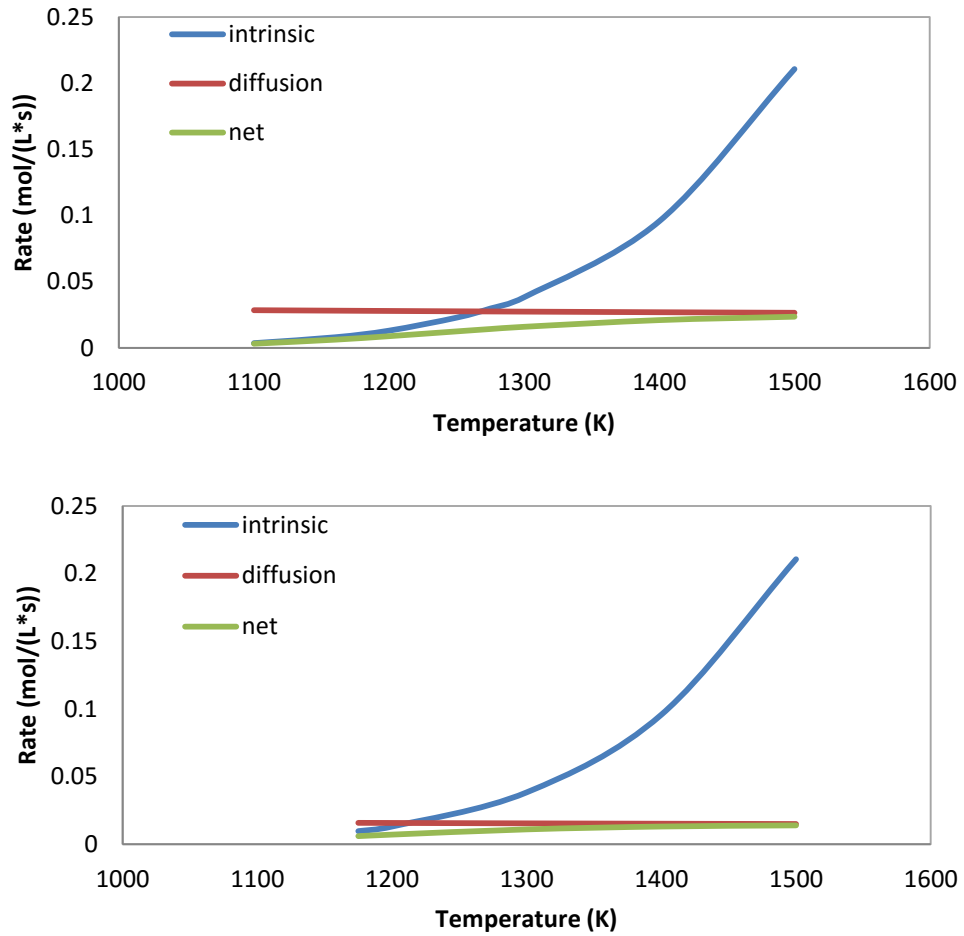


Figure 5.5: Comparison of initial reaction rates for 4'' (top) and 6'' (bottom) particles for gasification with oxygen. Data labels give values for diffusion limitations at 1200K to show comparison in particle sizes.

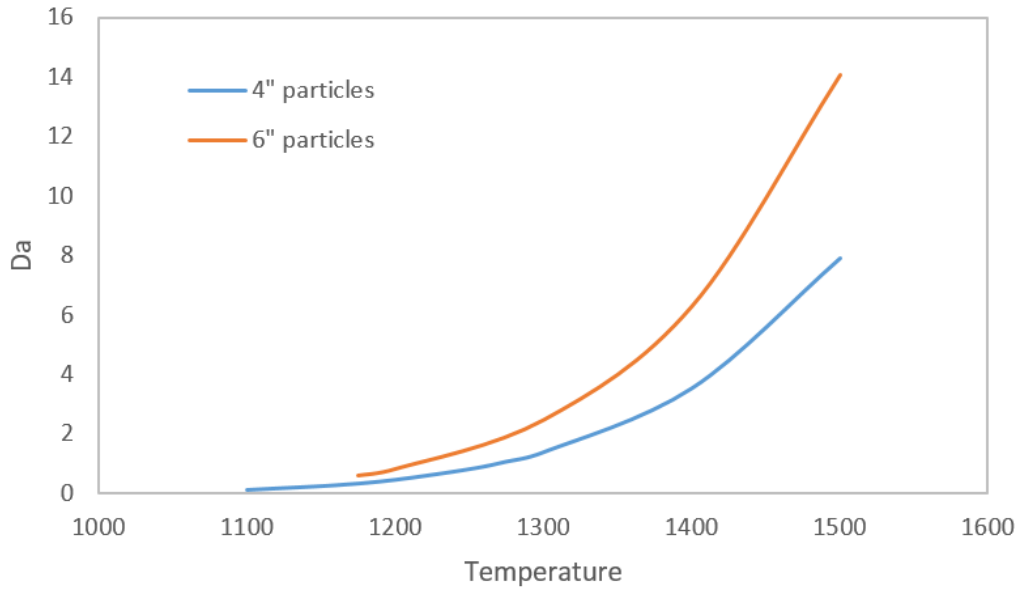


Figure 5.6: Damköhler number as a function of temperature for 4'' and 6'' particles.

The initial diffusion-limited state is expected from the literature. In the cupula handbook[121], diffusional limitations in CO₂ gasification were observed starting at 1000 °C, and diffusion dominated the net rate at 1400 °C as shown in Figure 5.7. The intrinsic kinetics of oxygen gasification is hundreds of times faster than CO₂; therefore, the shift to the diffusion-limited regime occurs at much lower temperatures.

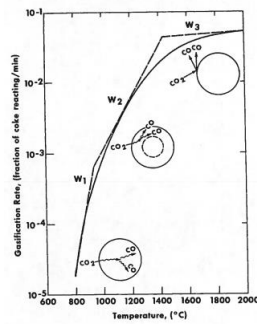


Figure 5.7: Reaction rate contributions as a function of temperature for CO₂ gasification from the Cupula Handbook[121]. In the low temperature region (w₁), kinetic limitations dominate. The middle range temperatures, w₂, both kinetics and diffusion contribute to the overall rate. At high temperatures (w₃), diffusional limitations dominate.

5.5 Reactor Simulation of Plasma-arc Gasifier

The coke and MSW gasification kinetic models were used to simulate a 1000 tonne/day gasification facility. To give an idea of the general layout, a diagram of an Alter Nrg gasifier is given in Figure 5.8[6]. Conceptually, there are four regions of this reactor: the coke bed, the combustion zone, the gasification zone, and the freeboard zone.

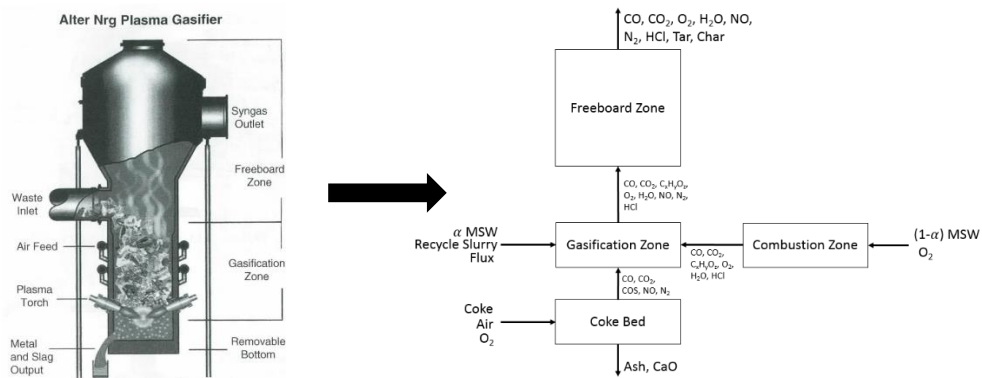


Figure 5.8: Gasification unit depiction from Young[6] (left) and conceptual organization of idealized reactors for each reaction zone(right).

Each region of the gasifier is modeled as an idealized chemical reactor using either the MSW or coke gasification models. Design decisions were based on the flow regimes found in computational fluid dynamic (CFD) simulations performed by APCI (Air Products and Chemicals Inc.). In the coke bed, the coke is gasified using air or enriched air. This is a high-temperature bed and is simulated as a plug-flow reactor using the coke gasification model. The waste inlet is split into both the combustion and gasification zones. The combustion zone are the regions around air inlets with high oxygen concentrations and temperatures. The majority of the waste bed is modeled using the gasification zone which has lower oxygen concentrations and lower temperatures. Both waste bed zones are modeled as a continuously stirred tank reactor (CSTR) using the MSW gasification model. The freeboard zone has the largest volume of any zone and is the region where equilibrium reactions dominate. This zone is modeled as a plug-flow reactor (PFR) using the MSW gasification model.

5.5.1 MSW Gasification I/O Converter

A user-friendly application was developed to organize and run the model of the gasification unit. The focus of this application is on measurable inputs and outputs to the gasification facility. All molecular-level details are abstracted away from the user and occur in the underlying code. The following discussion details the usage and features of this application.

The MSW Gasification I/O Converter is shown in Figure 5.9. To use this application, the user specifies measurable (or known) inputs. Each zone has a volume, temperature, and pressure; this independence is especially important as there are large temperature differences across the reactor. The coke bed has additional flow rates for coke, nitrogen, and oxygen; the independence of the gas flow rates allows for enriched

air input. MSW is fed to both the combustion and gasification zones; where the user-specified α determines the mass flow to each zone. Similar to the coke bed, the combustion zone has independent oxygen and nitrogen flow rates. Moisture is also taken into account in these zones through two parameters: moisture content of MSW and relative evaporation volume. The latter term signifies the volume (per kg/hr of moisture) required for the initial evaporation of moisture within MSW.

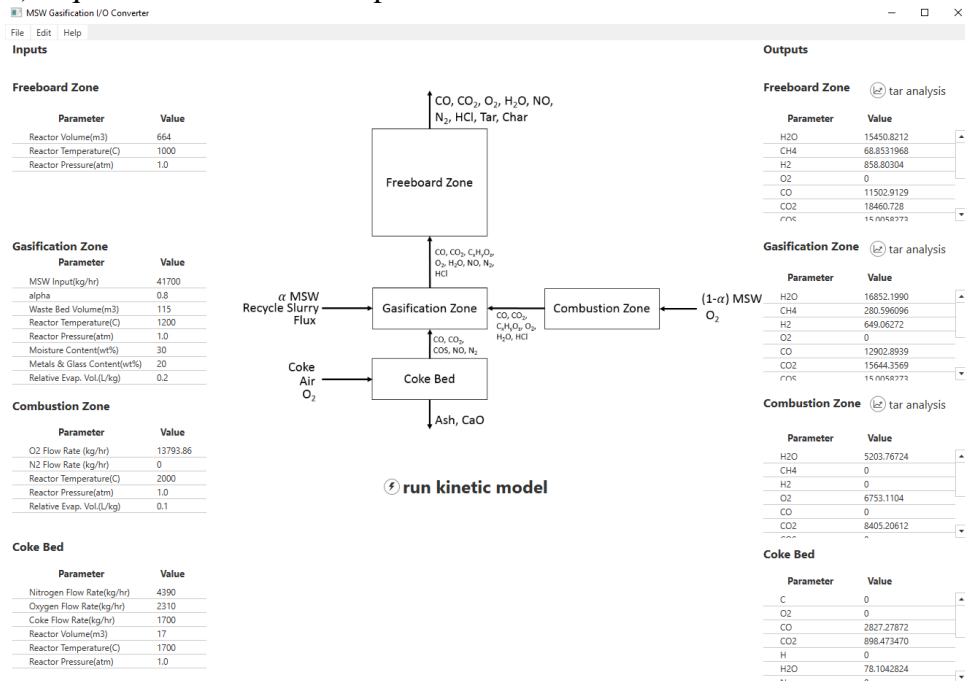


Figure 5.9: Screenshot of the main screen from the MSW Gasification I/O Converter. Measurable process inputs are on the left, the reactor layout is given in the diagram, and measurable process outputs are on the right.

After clicking the *run kinetic model* button, each reactor zone is solved to fill the output tables on the right hand side of Figure 5.9. Due to the linear layout, the solution is straightforward. The coke bed is solved first, followed by the combustion zone. These two zones provide inputs to the gasification zone, solved third, which, in

turn feeds the freeboard zone, solved last. The initial outputs displayed are syngas composition and overall tar weight fraction.

There are two key features to this application that are possible due to the molecular nature of the underlying model. The first is the ability change the composition of MSW, as shown in Figure 5.10. The tool allows the user to uniquely specify the fractions of the seven polymers included in MSW, or the user can load a tuned composition from the MSW Bulk Composition Solver, discussed previously. The second feature is the ability to analyze the molecular composition of tar compounds. For each of the MSW beds, the user can perform analysis of the tar leaving that bed, as shown in Figure 5.11. The form gives a pie chart displaying the fraction of tar for each dominant species, and the user can view the molecular structure of each compound.

Perhaps the most important feature of this application is ease-of-use, enabled by reducing model input and output to measurable quantities. This allows for the user to quickly test ‘what-if’ scenarios relevant to MSW gasifier operation. For instance, the effects of MSW composition can be tested in minutes rather than days or weeks. Furthermore, these tests can be run by anyone from a researcher to an informed engineer on-site.



Figure 5.10: Edit MSW Composition window within the MSW User Friendly Gasification Model.

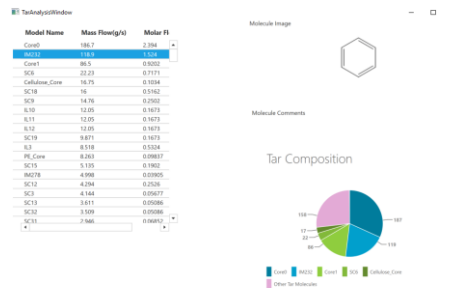


Figure 5.11: Tar composition analysis screen in the MSW Gasification I/O Converter.

5.6 Trending Studies

Trending studies of relevant process parameters were completed using the MSW Gasification I/O Converter. Specifically, the changes in tar flow rate and the quality of syngas were analyzed as functions of equivalence ratio, MSW composition, and α , or the relative flow rate of MSW to the gasification zone. The usage of the user-friendly application allowed these trending studies to be completed in minutes, rather than days or weeks.

Figure 5.12 shows the effects of the equivalence ratio on the relative flowrates of tar molecules and the quality of syngas leaving the freeboard zone. As the equivalence ratio is increased, the relative amount of tar molecules are decreased as the tar molecules are consumed by oxygen. The quality of syngas also decreases with increasing oxygen as CO is oxidized to CO₂. Over the normal equivalence ratio range for gasification, 0.3-0.5, the amount of tar and syngas quality decrease by factors of 2.5 and 1.5 respectively. From the point of view of plant engineers, oxygen flow rate should be set such that tar does not exceed downstream unit specifications; however, exceeding this flowrate reduces the energy content of the syngas and therefore profits from electricity production.

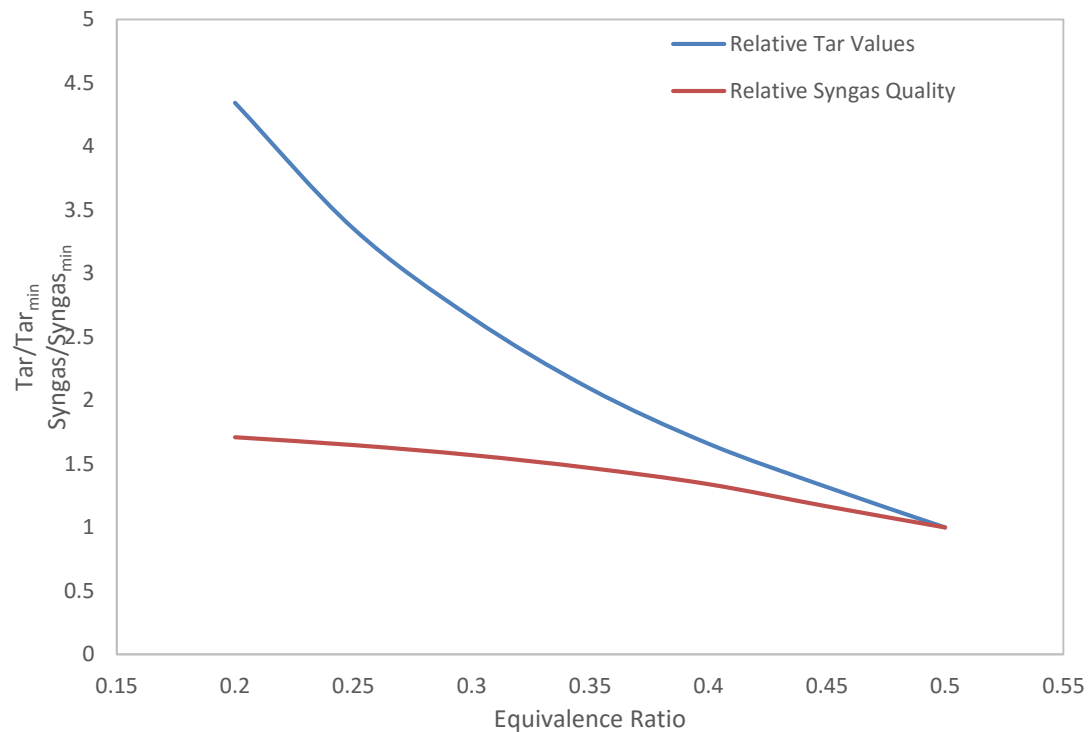


Figure 5.12: Relative tar fraction and relative syngas quality as a function of equivalence ratio. The tar fraction is defined as the weight fraction of species with boiling point greater than or equal to benzene. Syngas quality here is the mass ratio of $\text{CO}+\text{H}_2$ to $\text{CO}+\text{H}_2+\text{CH}_4+\text{CO}_2$.

The composition of tar molecules is described using Figure 5.13. The dominant tar molecules are derived from lignin, benzene, and naphthalene. The aromatic nature of these tar species is expected from gasification literature of related compounds[21]. The lignin reaction model divided lignin into three types of moieties, cores (ring structures), inter-core linkages (connections between cores), and side chains (terminal groups). Most of the mass in lignin tar molecules was contained within benzyl and phenolic cores. The dominant side chains are methoxy, methyl, and hydroxyl. Linkages are less prevalent because in the product stream, most linkages have been

broken from pyrolysis reactions. The remaining linkages are unable to break due to hydrogen deficiency from cracking and require oxygen for further reaction. If more oxygen were fed, as in complete combustion, these linkages would break down, ultimately forming gas phase species.

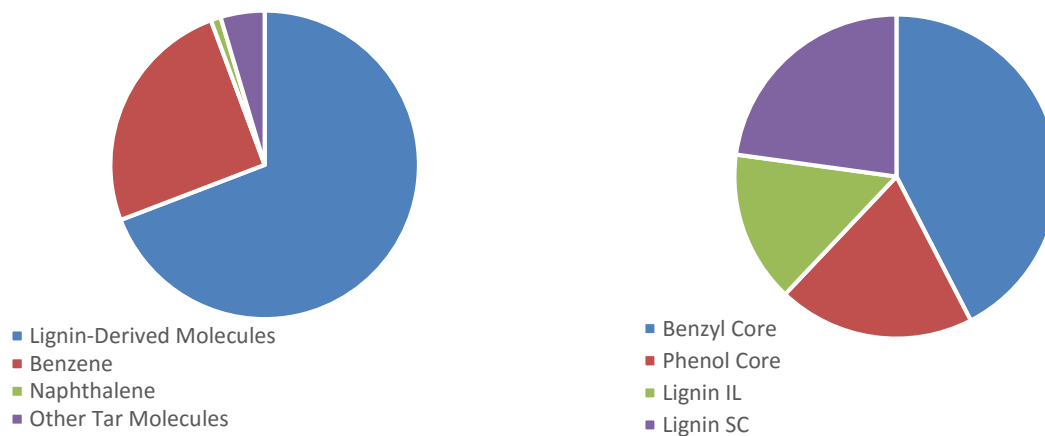


Figure 5.13: Tar composition leaving the freeboard zone. Left: overall tar molecule mass fractions. Right: composition of lignin tar molecules.

A molecular-level kinetic model can predict model results for a variable feedstock. The composition of MSW is variable based on both location and season. For this trending study, the EPA (US Average) results were compared with two sets of seasonal data for the UK: winter and summer as shown in Figure 5.14. The comparisons, given in Table 5.5, show a near constant syngas quality and flow rate for five different MSW compositions. The tar flow rates increased with increasing fraction of plastics; although this was a weak function over the range of expected MSW samples. It should be noted that oxygen flow rates were varied between samples

to hold equivalence ratio constant for the ultimate analyses; this simple experiment remains the most important for gasifier operation. One difference, not immediately evident in Table 5.5, between runs is the composition of tars, shown in Figure 5.15. In this figure, the most extreme cases are compared. In the UK-Summer data set, the tar are almost entirely lignin-derived molecules, or aromatics with high oxygen content. Alternatively, if the feed is mostly plastics, the tar is mostly oxygen-free aromatics. These details are important information for downstream processing.

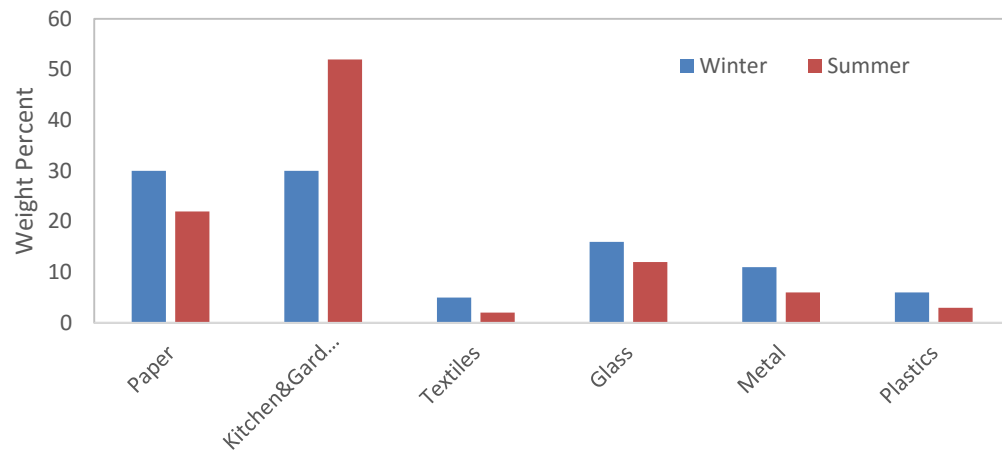


Figure 5.14: Seasonal Dependence of UK MSW, winter and summer[25].

Table 5.5: Comparison of MSW compositions. All data points used equivalence ratio of 0.3. The syngas flow rate was defined as the flow rate sum of CO, CO₂, H₂, and CH₄. Relative syngas flow rate was the ratio of the flow rate to minimum flow rate amount the data sets.

	Plastics Fraction	Biomass Fraction	Relative Tar	Relative Syngas Quality	Relative Syngas Flowrate
EPA	0.23	0.77	1.27	1.01	1.01
UK - Winter	0.085	0.915	1.07	1.00	1.00
UK - Summer	0.038	0.962	1.00	1.00	1.00
Synthesized 1	0.5	0.5	1.64	1.03	1.03
Synthesized 2	0.8	0.2	1.97	1.03	1.03

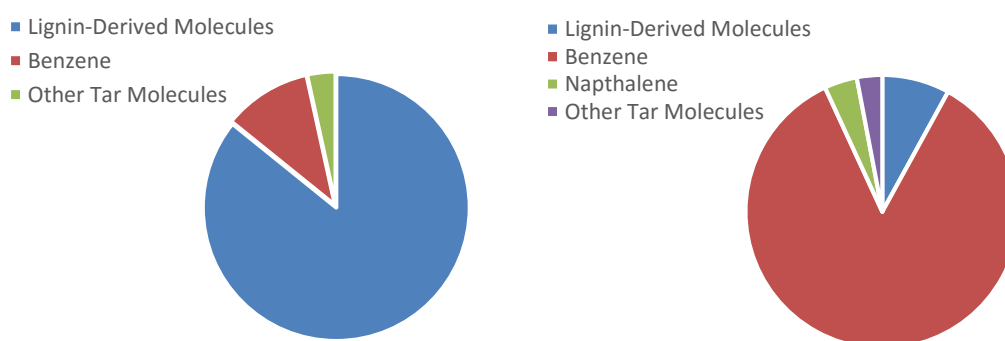


Figure 5.15: Comparison of Tar Compositions for different MSW compositions: Left(UK-Summer), Right(Synthesized 2).

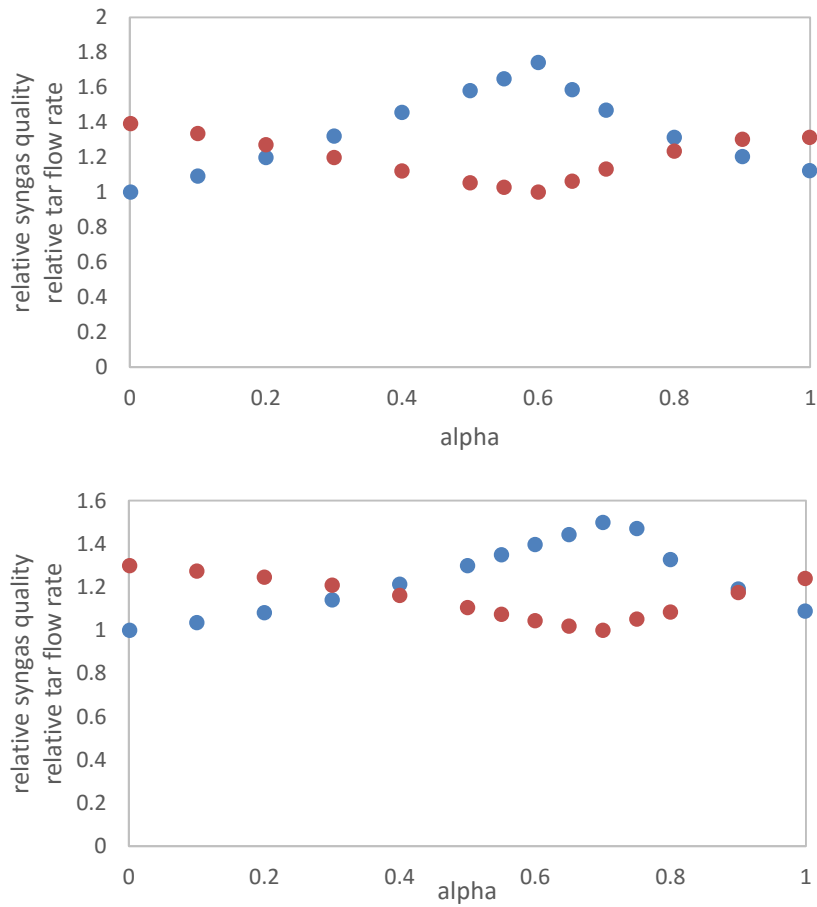


Figure 5.16: Effect of α on relative syngas quality (orange) and tar flow rate (blue) at equivalence ratios of 0.4 (top) and 0.3 (bottom).

The effects of α , or the fraction of the MSW bed in the gasification zone, on relative tar flow rates and syngas quality are given in Figure 5.16. The first observation is an inverse relationship between syngas quality and tar flow rate. This observation can be explained as the simulations were run with constant equivalence ratio, and therefore an increase in tar rate has a corresponding decrease in syngas quality as CO and H₂ are oxidized.

Figure 5.16 also shows a peak in tar flow rate when the fraction of waste entering the combustion zone is equal to the equivalence ratio, or when $\alpha = 1.0 - ER$. The combustion zone is at very high temperature and the waste is completely combusted to CO_2 . The peak then aligns with the definition of equivalence ratio, or the ratio of fuel to O_2 required for complete combustion. If the overall process equivalence ratio is 0.3, and 30% of the MSW is fed to the combustion zone, then the local equivalence ratio in the combustion zone is 1.0, and the oxygen is completely consumed. In this scenario, any waste fed to the gasification zone can only be gasified by H_2O , a much slower set of reaction chemistry. Pyrolysis reactions proceed in the gasification zone, producing tar molecules unabated by incomplete combustion.

The extreme localized temperature in the combustion zone is *not* beneficial to gasifier operation provided that waste is also fed to the relatively cooler portions of the gasification bed. Increasing α above the peak value allows oxygen to be in excess in the combustion zone and reach the gasification bed. Likewise, decreasing α below the peak value, allows a greater portion of the waste to react with oxygen from within the combustion zone. The lowest tar values and highest syngas quality values are shown where α is zero or one; the scenarios where all waste is present in the same zone as the O_2 feed.

5.7 Summary and Conclusions

A plasma-arc gasifier with simulated for a MSW feedstock using a molecular-level kinetic model. The two solid inlets to the reactor were MSW and foundry coke. A molecular-level kinetic model of MSW gasification was developed by combining models of plastics and biomass gasification. A model of coke gasification with oxygen and carbon dioxide was developed utilizing both kinetic and diffusional limitations.

The gasifier was simulated with a coke bed and three zones for MSW: combustion, gasification, and freeboard. These models were organized into a user-friendly C# application called the MSW Gasification I/O Converter. This application prioritized measurable inputs and outputs, to allow for trending studies on important process parameters. Some conclusions from this work are:

- The coke model was surface-diffusion limited at gasifier conditions.
- Increasing equivalence ratio decreases both tar production and syngas quality. Process optimization is required to maximize profit.
- Over normal ranges of waste composition, tar, syngas quality and syngas flowrate are invariant if equivalence ratio is held constant. Therefore, ultimate analysis remains an important tool for gasifier operation. Tar composition requires more in-depth analyses on the fractions of different waste products.
- Tar composition from biomass is primarily aromatics with methoxy, OH, and methyl side chains; tar composition from plastics is predominantly benzene and naphthalene.
- The localized extreme temperature regions of the combustion zone can potentially reduce the quality of syngas produced while increasing the amount of tar exiting the freeboard zone. Tar is minimized in the well-mixed scenario where all MSW contacts all oxygen.
- Kinetic parameters were optimized (in prior work) to literature data at much lower temperatures than plasma arc gasification. In the future, data from gasification facility will allow for trend verification and the validation and/or improvement of kinetic parameters.

Chapter 6

MOLECULAR-LEVEL KINETIC MODELING OF RESID PYROLYSIS

Scott R. Horton¹, Linzhou Zhang², Zhen Hou¹, Craig A. Bennett¹, Michael T. Klein¹,
and Suoqi Zhao²

¹*University of Delaware Energy Institute and Department of Chemical and Biomolecular Engineering, University of Delaware, Newark, DE 19716*

²*State Key Laboratory of Heavy Oil Processing, China University of Petroleum, Beijing 102249, China*

Reproduced by permission from **Horton, S.R.**; Zhang, L.; Hou, Z.; Bennett, C.A.; Klein, M.T.; Zhao, S. "Molecular-level kinetic modeling of resid pyrolysis" *Ind. Eng. Chem. Res.* 2015, 54(16). 10.1021/ie5041572. Copyright 2015. American Chemical Society.[109]

6.1 Abstract

A molecular-level kinetic model of heavy oil pyrolysis was developed for a Venezuelan vacuum residue. Model development proceeded in three major steps: creation of a molecular description of the feedstock, generation of a reaction network, and model solution and parameter tuning. The feedstock composition, as described in previous work[46], was modeled in terms of probability density functions (PDFs) of three finite attribute groups (385 cores, two inter-core linkages, and 194 side chains) and a PDF for each of a cluster-size and binding site distribution. These attributes, or molecule building blocks, represent more than 0.4M molecules. An attribute reaction network was developed using the fundamental reaction chemistry for resid pyrolysis including 6274 reactions that fall into one of 11 reaction families. To make solution time tractable, we used Attribute Reaction Modeling (ARM) which constrained the number of material balances to the number of attributes and irreducible molecules in the system, or 2841 total equations. Therefore, reactor output was a set of reaction-altered attribute PDFs and molar amounts of irreducible molecules. The quantitative molecular composition of the reactor outlet was obtained through the juxtaposition of the final attribute PDFs. The properties of both the sampled molecules and the char fraction were obtained using quantitative structure-property relationships (QSPRs). The kinetic model was tuned using a least-squares objective function comparing the model predictions to measurements from the molecular to bulk-property level for all relevant boiling point fractions. The tuned model showed reasonably good agreement with the experimental measurements.

6.2 Introduction

Petroleum is likely to be of primary importance for the coming decades for the manufacture of liquid fuels. The diminishing supply of conventional, light crude oils has led to a focus in both industry and academia on heavy oil[122]. Heavy oils pose a problem as the light fractions of petroleum are easiest to refine into liquid fuels. A major process to convert heavy oil into lighter fractions is the pyrolysis of vacuum residue, or resid.

Process models assist in making efficient use of this heavy-oil fraction. Originally, models of resid were lumped in nature, often phrased in terms of boiling point cuts[123]. Reactor models therefore contained very few reactions and equations and were easy to solve and understand. Unfortunately, this simplicity also limits the usefulness of lumped models as they contain no chemical structure information and therefore no basis for property estimation beyond the definition of the lump. Two resid samples with different chemical composition would, therefore, require separate rate constants. Furthermore, experimental techniques can now identify tens of thousands of molecular species in a resid sample[124]. By incorporating this detailed information, the overall efficacy and robustness of reactor models can be increased.

The current state-of-the-art in modeling resid pyrolysis is molecular-level modeling. These models attempt to capture the full molecular detail of resid. In the early 1990s, Neurock et al. used Monte Carlo methods to sample 10,000 representative molecules to model reactions of resid[125]. In 2014, Rueda-Velásquez and Gray[126] and Oliveira et al.[127] revisited the use of Monte Carlo techniques for thermolysis, now taking into account modern knowledge of asphaltene composition. Quann and Jaffe developed structure-oriented lumping (SOL) in order to describe both light and heavy fractions of petroleum using structural vectors (building blocks)[128]. Recently,

delayed coking has been described by Tian and coworkers using the SOL methodology[129].

While there is extensive literature on resid pyrolysis, no model has successfully captured the full molecular detail of the reaction of hundreds of thousands of unique resid molecules because reactor models require a material balance differential equation for every species. In the coming years, in order to simulate state-of-the-art experiments, kinetic models must be developed to capture the full molecular detail of resid. Advances in computational or mathematical algorithms will not overcome the sheer intractability of these reacting systems; instead, the development must occur in kinetic modelling approaches.

To address this problem, we will extend previous work[46], [48] that represented 400,000 resid molecules in terms of probability density functions (PDFs) of attributes, or building blocks by introducing a novel approach for the kinetics. As illustrated in Figure 6.1, conventional kinetic modeling would juxtapose the attribute PDFs before reactor model solution. This results in $O(1,000,000)$, or “on the order of” 1,000,000, material balances and an intractable solution. In this work, we instead propose to react the attribute PDFs, rather than molecules. This allows for reactor simulation using only 2839 total material balances. The outlet attribute PDFs are then juxtaposed to generate the full molecular footprint and associated properties.

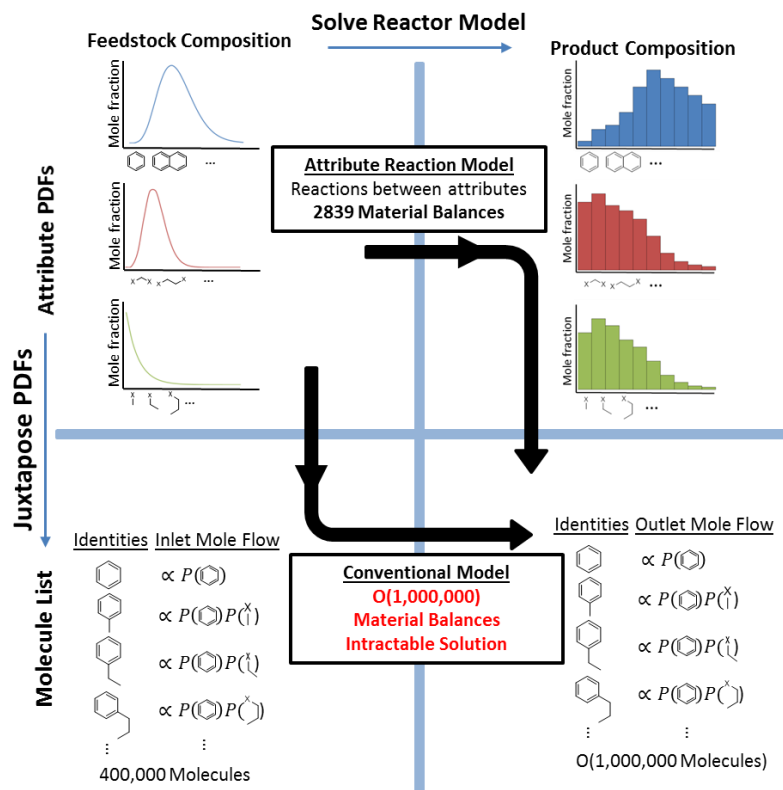


Figure 6.1: Comparison of Attribute Reaction Modeling and Conventional Modeling methods.

In the current work, a molecular-level kinetic model was developed and evaluated for the pyrolysis of a Venezuelan Vacuum Resid. Here, we follow a general procedure laid out in previous work[46], [48] for model construction. Other details of the modeling work have been significantly improved over prior work. First, more detailed reaction chemistries are taken into account. Second, different methods of attribute juxtaposition have been explored. Finally, this work contains kinetic parameter tuning to experimental data. The following sections cover each of the major steps in this process: the molecular representation of the feed, the development of a

reaction network, the construction and solution of a kinetic model, and the comparison of results with experimental measurements.

6.3 Molecular Representation of Resid

Resid is a complex system of molecules, such as the molecule shown in Figure 6.2, where no unique composition defines the feed. Currently, no single analytical technique provides the identities and amounts of every molecule within a given resid; therefore composition models must make use of the information available.

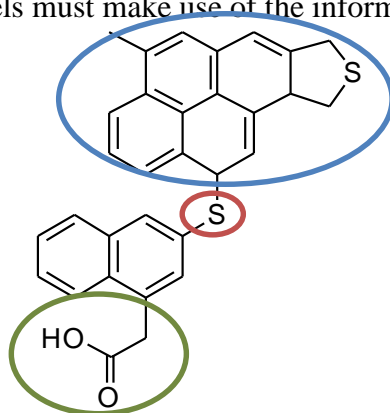


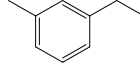
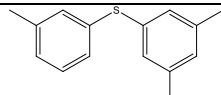
Figure 6.2: Example resid molecule and attribute groups: cores (blue), inter-core linkages (red), and side chains (green).

Conceptually, resid can also be thought of as a collection of structural moieties, or attributes. Despite the complexity and variability of resid, all possible molecules are made up of three attribute types: cores, inter-core linkages, and side chains, as shown in Figure 6.2. Cores are polycyclic molecules containing aromatic rings and naphthenic rings with or without heteroatoms; inter-core linkages are bridges between cores; and side chains are terminal substituents bound to cores. The molecular composition of resid is then a set of probability density functions. First, attribute group

pdfs contain information on the relative amount of each attribute. Second, a cluster-size PDF describes the relative amounts of n-core clusters. Lastly, a binding site PDF describes the number of filled sites on a given core cluster. This description of resid allows for the level of model detail to match the level of available experimental information.

The description of resid as a set of attribute PDFs preserves the molecular-nature of the composition. The PDFs are juxtaposed, by combining the different attributes together, to produce a list of molecules. The identity of the molecule is the combination of the sampled attributes, and the mole fraction is proportional to the relevant PDF values. For example, the mole fraction calculations of selected molecules are given below, in Table 6.1.

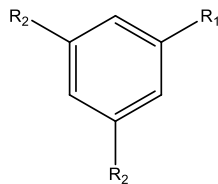
Table 6.1: The mole fraction calculation for selected molecules from attributes. P_{core} , P_{IL} , and P_{SC} represent the three attribute PDFs. P_{BS} and P_{CS} represent the binding site and cluster size distributions.

Molecule	Attributes	Filled Binding Sites	Cluster Size	Mole Fraction
	 	1	1	$\propto P_{core}(\text{benzene})$ $* P_{SC}(x)$ $* P_{BS}(1) * P_{CS}(1)$
	  	2	2	$\propto P_{core}(\text{benzene})$ $* P_{SC}(x)$ $* P_{BS}(2) * P_{CS}(2)$
	  	3	2	$\propto P_{core}(\text{benzene})^2$ $* P_{SC}(x)^3$ $* P_{SC}(x-S-x)$ $* P_{BS}(3) * P_{CS}(2)$

There are numerous methods for building the molecule list. The most intuitive method is complete sampling, where every possible combination of attributes is listed for a given maximum cluster size and filled binding site number. As shown in Table 6.2, the number of sampled molecules in this method is combinatorial in nature and quickly surpasses computational limitations even for simple property calculations. The issue with this method for resid is that many molecules are sampled that cannot be differentiated experimentally. To address this, instead a termed “main methyl method (MMM)”, was developed. In this method, there is a primary binding site where any side chain may be bound. The other binding sites are either unfilled or filled with a methyl group, as shown in Figure 6.3. MMM removes the combinatorial nature of the side chain portion of the model and drastically reduces the number of molecules during sampling.

Table 6.2: Number of molecules for the two common sampling methods for different cluster sizes using 100 cores, 2 linkages, and 50 side chains.

Cluster Size	Max binding sites for side chains	Number of Sampled Molecules – Complete Sampling	Number of Sampled Molecules – Main Methyl Method
1	3	2,210,000	15,000
2	4	4.4 x 10 ⁹	3,030,000



Complete Sampling
R₁ and R₂ all side chains

Main Methyl Method
R₁ all side chains, R₂ only methyl

Figure 6.3: Differences in binding sites for complete sampling and main methyl method.

Further reductions in the sampled molecule list also depend on the available experimental information. For instance, if the experiment of interest is a distillation curve which terminates at 750 °C, then there is no need to sample molecules with boiling points greater than 750 °C. Furthermore, there is no reason to include a higher level of resolution than the experiment. For instance, if the distillation curve is accurate to 10 °C, then the cores can be placed into 10 °C lumps. This reduction is drastic; for instance, if the number of cores was reduced to 50, instead of 100; then the number of molecules for MMM drops to 7,500 and 765,000 for cluster sizes 1 and 2, respectively. Through these methods, the molecule list is tailored to remain finite and representative of the available experimental data.

6.4 Feedstock Composition

The first step in the construction of a molecular-level kinetic model is the description of the feed at the molecular level. The composition model is described, in detail, in our previous work[46], where ~600 attributes were used to describe a molecular composition containing 400,000 molecules after sampling. The first detail of the composition is the identities of the included attributes. These identities came from prior knowledge of resid from both literature and experimental data. The 385

produce over 400,000 molecules and their associated properties. An example of a property prediction is a molecular-weight distribution, reproduced below in Figure 6.9.

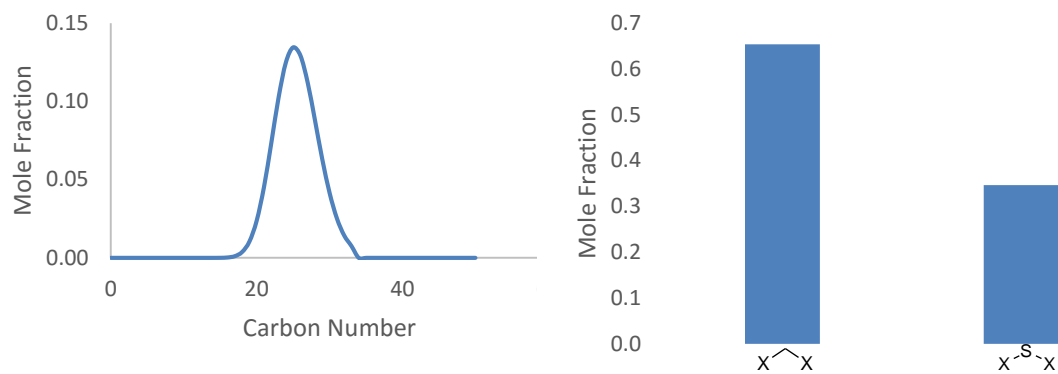


Figure 6.6: Side chain (left) and Inter-core linkage (right) PDFs. The side chain PDF is only shown for n-alkyl side chains (normalized to 1). Similar PDFs can be created for the other side chain types.

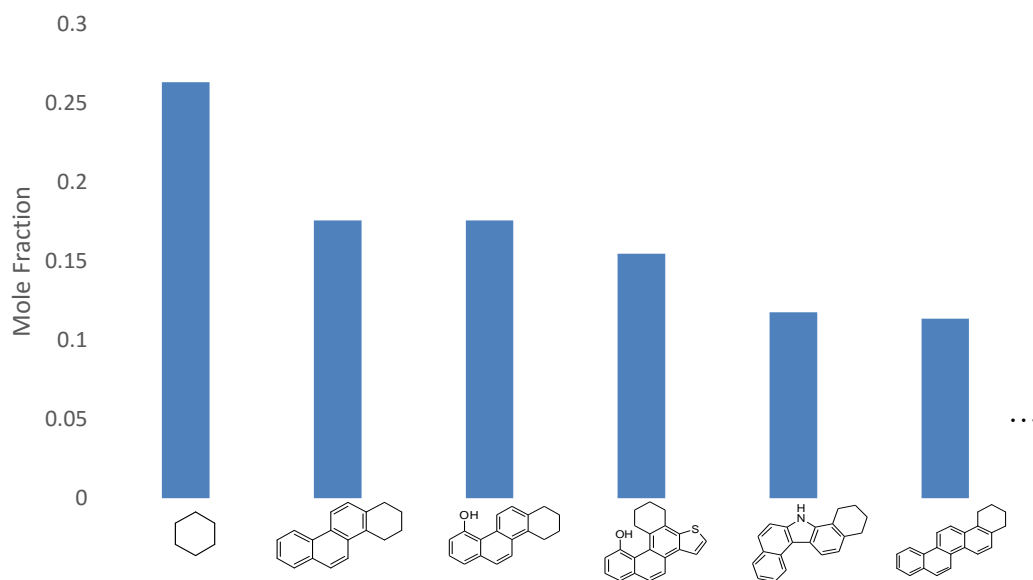


Figure 6.7: Selected cores from the core PDF, mole fractions normalized for the selected cores.

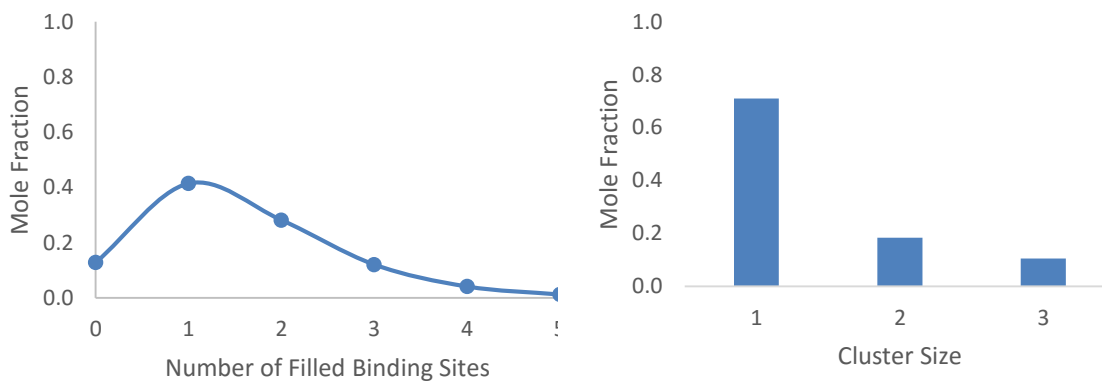


Figure 6.8: Binding site (left) and cluster size (right) PDFs for feedstock composition. Results are from model presented by Zhang et al.[46]

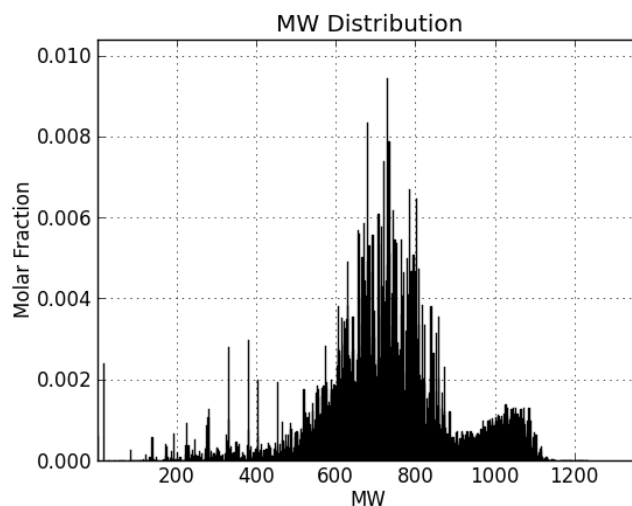


Figure 6.9: Molecular weight distribution of the sampled molecules. Figure reproduced from attribute distributions in Zhang et al[46].

6.5 Reaction Chemistry

Three general reaction types govern resid pyrolysis. First, cracking reactions reduce the molecular weight of some species and produce small molecules. Second, aromatization reactions produce hydrogen and lead to stable polycyclic aromatic hydrocarbons (PAHs). Finally, coking reactions give rise to a high molecular-weight fraction.

The reaction network applies the process chemistry to the attributes in the feedstock. For instance, alkyl side chains can crack to small molecules and shorter side chains. These small molecules can be quantified individually and are therefore termed irreducible molecules. Examples of irreducible molecules include small paraffins, olefins, and hydrogen.

The cracking reaction families include decarboxylation, ring-opening, and the cracking of linear hydrocarbons and C-S bonds. The reaction site and reaction matrices, along with example reactions, can be found below, in Table 6.3. Reaction

rules specify which reaction sites were considered valid sites in reaction network creation. The rules for cracking were based on the stability of radicals in H-Abstraction and β -scission steps. For example, an alkyl side chain on an aromatic ring has a stable radical at the benzylic position as shown below in Figure 6.10. The two most favorable scenarios are a benzylic radical after H-abstraction or a benzylic radical after β -scission. A full list of reaction rules for the reaction families can be found in the supplemental information.

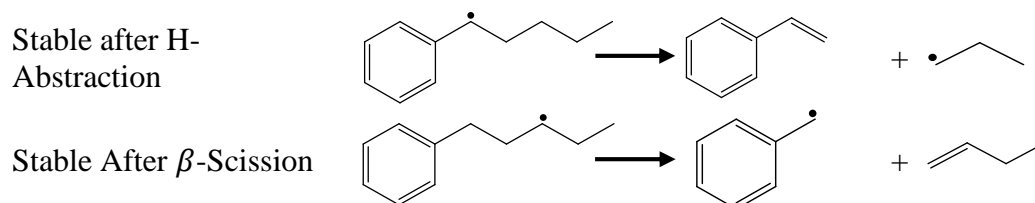


Figure 6.10: Most stable cracking pathways for an alkyl aromatic.

Table 6.3: Cracking reaction families, sites, matrices, and examples. These details are discussed in the PhD Thesis by Zhang[130]. The reaction matrices define the bond making (1) and bond breaking (-1) in a reaction type.

<u>Reaction Type (Family) and Reaction Site</u>	<u>Reaction Matrix</u>	<u>Example Reaction</u>																									
Decarboxylation Carboxylic acid on side chain and irreducible molecules.	<table border="1"> <tr><td></td><td>H</td><td>O</td><td>C</td><td>C</td></tr> <tr><td>H</td><td>0</td><td>-1</td><td>0</td><td>1</td></tr> <tr><td>O</td><td>-1</td><td>0</td><td>1</td><td>0</td></tr> <tr><td>C</td><td>0</td><td>1</td><td>0</td><td>-1</td></tr> <tr><td>C</td><td>1</td><td>0</td><td>-1</td><td>0</td></tr> </table>		H	O	C	C	H	0	-1	0	1	O	-1	0	1	0	C	0	1	0	-1	C	1	0	-1	0	
	H	O	C	C																							
H	0	-1	0	1																							
O	-1	0	1	0																							
C	0	1	0	-1																							
C	1	0	-1	0																							
Naphthenic Ring Opening 6-member naphthenic rings	<table border="1"> <tr><td></td><td>C</td><td>C</td><td>C</td><td>H</td></tr> <tr><td>C</td><td>0</td><td>-1</td><td>0</td><td>1</td></tr> <tr><td>C</td><td>-1</td><td>0</td><td>1</td><td>0</td></tr> <tr><td>C</td><td>0</td><td>1</td><td>0</td><td>-1</td></tr> <tr><td>H</td><td>1</td><td>0</td><td>-1</td><td>0</td></tr> </table>		C	C	C	H	C	0	-1	0	1	C	-1	0	1	0	C	0	1	0	-1	H	1	0	-1	0	
	C	C	C	H																							
C	0	-1	0	1																							
C	-1	0	1	0																							
C	0	1	0	-1																							
H	1	0	-1	0																							
Sulfide Ring Opening 5-member sulfide rings	<table border="1"> <tr><td></td><td>H</td><td>C</td><td>C</td><td>S</td></tr> <tr><td>H</td><td>0</td><td>-1</td><td>0</td><td>1</td></tr> <tr><td>C</td><td>-1</td><td>0</td><td>1</td><td>0</td></tr> <tr><td>C</td><td>0</td><td>1</td><td>0</td><td>-1</td></tr> <tr><td>S</td><td>1</td><td>0</td><td>-1</td><td>0</td></tr> </table>		H	C	C	S	H	0	-1	0	1	C	-1	0	1	0	C	0	1	0	-1	S	1	0	-1	0	
	H	C	C	S																							
H	0	-1	0	1																							
C	-1	0	1	0																							
C	0	1	0	-1																							
S	1	0	-1	0																							
Thermal Cracking – Hydrocarbon Hydrocarbon side chains and irreducible molecules	<table border="1"> <tr><td></td><td>C</td><td>C</td><td>C</td><td>H</td></tr> <tr><td>C</td><td>0</td><td>-1</td><td>0</td><td>1</td></tr> <tr><td>C</td><td>-1</td><td>0</td><td>1</td><td>0</td></tr> <tr><td>C</td><td>0</td><td>1</td><td>0</td><td>-1</td></tr> <tr><td>H</td><td>1</td><td>0</td><td>-1</td><td>0</td></tr> </table>		C	C	C	H	C	0	-1	0	1	C	-1	0	1	0	C	0	1	0	-1	H	1	0	-1	0	
	C	C	C	H																							
C	0	-1	0	1																							
C	-1	0	1	0																							
C	0	1	0	-1																							
H	1	0	-1	0																							
Thermal Cracking – C-S bonds Carbon-Sulfur bonds on side chains and irreducible molecules	<table border="1"> <tr><td></td><td>H</td><td>C</td><td>C</td><td>S</td></tr> <tr><td>H</td><td>0</td><td>-1</td><td>0</td><td>1</td></tr> <tr><td>C</td><td>-1</td><td>0</td><td>1</td><td>0</td></tr> <tr><td>C</td><td>0</td><td>1</td><td>0</td><td>-1</td></tr> <tr><td>S</td><td>1</td><td>0</td><td>-1</td><td>0</td></tr> </table>		H	C	C	S	H	0	-1	0	1	C	-1	0	1	0	C	0	1	0	-1	S	1	0	-1	0	
	H	C	C	S																							
H	0	-1	0	1																							
C	-1	0	1	0																							
C	0	1	0	-1																							
S	1	0	-1	0																							

The aromatization reaction families which increase the aromaticity in the system while releasing hydrogen are given below in Table 6.4. The five reaction families are based on ring type and number of hydrogen atoms released. Here the rules were specified such that the number of hydrogens released from a given reaction step was minimized. For example, an aromatization-2 would take precedence over an aromatization-4 if a molecule contained both reactive sites.

Table 6.4: Aromatization reaction families, sites, matrices, and examples for aromatization reactions. These details are discussed in the PhD Thesis by Zhang[130].

Reaction Type (Family) and Reaction Site	Reaction Matrix	Example Reaction																																																																																	
Naphthenic Ring Aromatization-2	<table border="1"> <tr> <td></td> <td>C</td> <td>C</td> <td>H</td> <td>H</td> </tr> <tr> <td>C</td> <td>0</td> <td>1</td> <td>-1</td> <td>0</td> </tr> <tr> <td>C</td> <td>1</td> <td>0</td> <td>0</td> <td>-1</td> </tr> <tr> <td>H</td> <td>-1</td> <td>0</td> <td>0</td> <td>1</td> </tr> <tr> <td>H</td> <td>0</td> <td>-1</td> <td>1</td> <td>0</td> </tr> </table>		C	C	H	H	C	0	1	-1	0	C	1	0	0	-1	H	-1	0	0	1	H	0	-1	1	0																																																									
	C	C	H	H																																																																															
C	0	1	-1	0																																																																															
C	1	0	0	-1																																																																															
H	-1	0	0	1																																																																															
H	0	-1	1	0																																																																															
Naphthenic Ring Aromatization-4	<table border="1"> <tr> <td></td> <td>C</td> <td>C</td> <td>C</td> <td>C</td> <td>H</td> <td>H</td> <td>H</td> <td>H</td> </tr> <tr> <td>C</td> <td>0</td> <td>1</td> <td>0</td> <td>0</td> <td>-1</td> <td>0</td> <td>0</td> <td>0</td> </tr> <tr> <td>C</td> <td>1</td> <td>0</td> <td>0</td> <td>0</td> <td>0</td> <td>-1</td> <td>0</td> <td>0</td> </tr> <tr> <td>C</td> <td>0</td> <td>0</td> <td>0</td> <td>1</td> <td>0</td> <td>0</td> <td>-1</td> <td>0</td> </tr> <tr> <td>C</td> <td>0</td> <td>0</td> <td>1</td> <td>0</td> <td>0</td> <td>0</td> <td>0</td> <td>-1</td> </tr> <tr> <td>H</td> <td>-1</td> <td>0</td> <td>0</td> <td>0</td> <td>0</td> <td>1</td> <td>0</td> <td>0</td> </tr> <tr> <td>H</td> <td>0</td> <td>-1</td> <td>0</td> <td>0</td> <td>1</td> <td>0</td> <td>0</td> <td>0</td> </tr> <tr> <td>H</td> <td>0</td> <td>0</td> <td>-1</td> <td>0</td> <td>0</td> <td>0</td> <td>0</td> <td>1</td> </tr> <tr> <td>H</td> <td>0</td> <td>0</td> <td>0</td> <td>-1</td> <td>0</td> <td>0</td> <td>1</td> <td>0</td> </tr> </table>		C	C	C	C	H	H	H	H	C	0	1	0	0	-1	0	0	0	C	1	0	0	0	0	-1	0	0	C	0	0	0	1	0	0	-1	0	C	0	0	1	0	0	0	0	-1	H	-1	0	0	0	0	1	0	0	H	0	-1	0	0	1	0	0	0	H	0	0	-1	0	0	0	0	1	H	0	0	0	-1	0	0	1	0	
	C	C	C	C	H	H	H	H																																																																											
C	0	1	0	0	-1	0	0	0																																																																											
C	1	0	0	0	0	-1	0	0																																																																											
C	0	0	0	1	0	0	-1	0																																																																											
C	0	0	1	0	0	0	0	-1																																																																											
H	-1	0	0	0	0	1	0	0																																																																											
H	0	-1	0	0	1	0	0	0																																																																											
H	0	0	-1	0	0	0	0	1																																																																											
H	0	0	0	-1	0	0	1	0																																																																											
Naphthenic Ring Aromatization-6	6-carbon, 6-hydrogen analogue to reaction matrix in Naphthenic Ring Aromatization-4.																																																																																		
Sulfide Ring Aromatization-3	Same matrix as Naphthenic Ring Aromatization-2																																																																																		
Sulfide Ring Aromatization-5	Same matrix as Naphthenic Ring Aromatization-4.																																																																																		

The final reaction family is aromatic ring condensation. This reaction allows for the growth of a char phase. An example is shown below in Figure 6.11. As an attribute reaction, this can be conceptualized as the formation of a biphenyl inter-core linkage. Therefore, only one reaction was written for aromatic ring condensation to represent the possible condensation of any two aromatic cores in the system.

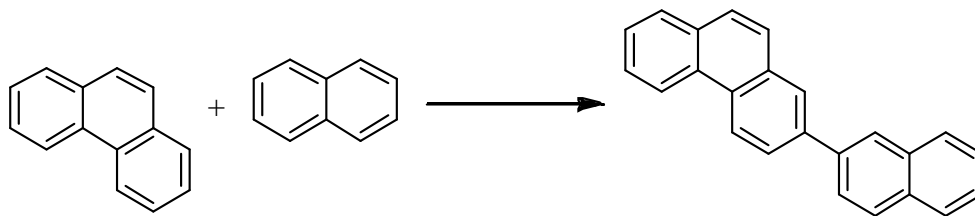


Figure 6.11: Aromatic ring condensation example reaction.

6.6 Network Generation

With these reaction families and reaction rules, the reaction network was generated, automatically, using an in-house software, the Interactive Network Generator, INGen[40], [44]. INGen takes a starting set of reactant molecules as network building seeds, and exhaustively searches the molecules for the reaction sites. The addition of the reaction matrix to the reactant sub-matrix gives product molecules. This is an iterative process as products of reactions can also react. In this case, the seed molecules were the attributes in resid composition. The final network diagnostics for the vacuum resid model are given below in Table 6.5.

INGen builds networks very quickly. For instance, the 6,274 reactions here took ~30 seconds to build on a regular desktop computer (Dell Precision T1500, Processor: Intel (R) Core i7 870@2.93 GHz 2.93 GHz, Memory: 4.00 GB). This allows network generation to become an iterative process where the user can fine-tune the network to include the exact level of desired chemical detail. For instance, in this model, rules were designed for each reaction family.

Table 6.5: Reaction network diagnostics including total number of reactions, attributes, and irreducible molecules. These details are discussed in the PhD Thesis by Zhang[130].

Reaction Family	Number of Reactions
Decarboxylation	137
Naphthenic Ring Opening	224
Sulfide Ring Opening	9
Thermal Cracking – Hydrocarbon	3790
Thermal Cracking – C-S bonds	1097
Naphthenic Ring Aromatization-6	8
Naphthenic Ring Aromatization-4	734
Naphthenic Ring Aromatization-2	13
Sulfide Ring Aromatization-5	9
Sulfide Ring Aromatization-3	6
Aromatic Ring Condensation	1
Total Reactions	6274
Cores	1704
Inter-core Linkages	3
Side-chains	256
Irreducible Molecules	876

6.7 Model Equations

After reaction network construction, a mathematical description of the kinetics is built to model the reactor. In general, a molecular-level kinetic model is a system of ordinary differential equations (ODEs) with one material balance per species and an overall energy balance. In this study, the lab-scale, semi-batch coking reactor that provided experimental data for comparison was isothermal and therefore only material balances are relevant. This would equate to $O(1,000,000)$ differential equations in a conventional kinetic model for resid. Attribute reaction modeling addresses this intractability while retaining molecular-level detail.

First, a balance equation is written for each attribute in the system, as shown in Equation 6.1. Each equation, written in vector notation, uses ν to denote stoichiometry and $-r_{evap}$ to account for the rate of evaporation in the coking semi-batch reactor. In this model, $-r_{evap}$ was taken into account by restricting slow reaction families on smaller molecules. For instance, molecules with less than four rings were not allowed to undergo aromatization. The total number of equations for the attribute portion of the model is equal to the total sum of the attributes. This trait of the model is singularly the most important for computational tractability due to the combinatorial relationship between attributes and molecules. The initial conditions for each attribute originate from the continuous attribute PDFs from the composition model. The generation of initial conditions effectively transforms the continuous probability distributions from the composition into discrete distributions, as illustrated in Figure 6.12.

$$\begin{aligned} \frac{d\overline{Core}}{dt} &= -\bar{r}_{evap} + \sum_{i, reactions} \bar{\nu}_i * rate_i && (6.1) \\ &&& a. \\ \frac{d\overline{IL}}{dt} &= -\bar{r}_{evap} + \sum_{i, reactions} \bar{\nu}_i * rate_i && b. \\ \frac{d\overline{SC}}{dt} &= -\bar{r}_{evap} + \sum_{i, reactions} \bar{\nu}_i * rate_i && c. \end{aligned}$$

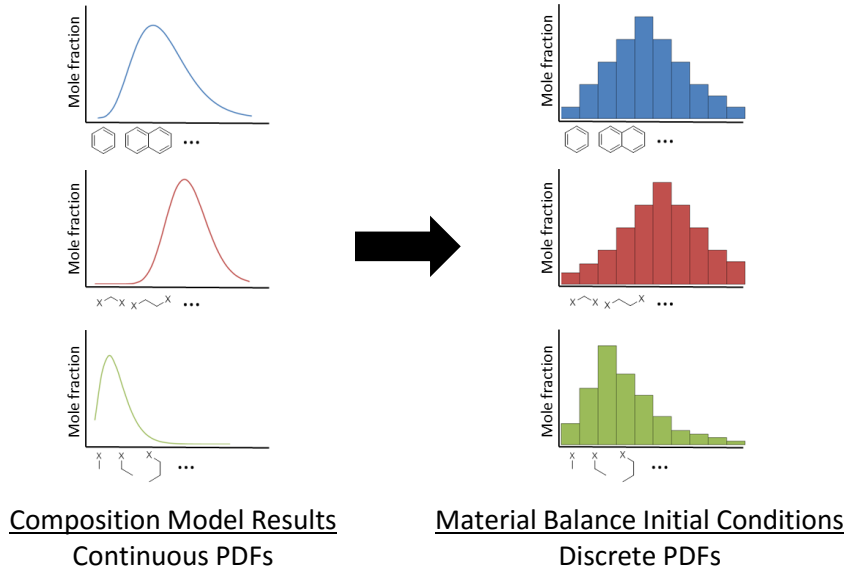


Figure 6.12: Conversion of continuous attribute pdfs to discrete PDFs during the generation of initial conditions for the reactor kinetic model.

Small molecules that are not reducible into attributes were produced in the reaction network. A material balance is written for each of these irreducible molecules as shown in Equation 6.2. The number of irreducible molecules produced is finite, and the model remains tractable. Combined, the attribute and irreducible molecule material balances make up the kinetic model. These equations are integrated using the LSODE suite of differential equation solvers[131].

$$\frac{d\overline{IM}}{dt} = -\overline{r}_{evap} + \sum_{i, reactions} \overline{v}_i * rate_i \quad (6.2)$$

For irreducible molecules, the model solution simply yields molar flows at the outlet, as in a conventional molecular-level model. For attributes, the integration of the reactor model alters the relative amounts of attributes in the system. For example, in

the side chain distribution, cracking would increase the amount of methyl ($x\text{-CH}_3$) side chains relative to longer paraffin side chains. Conceptually, model solution can therefore be represented as the alteration of the discrete attribute PDFs, as shown in Figure 6.13. The molecular products are obtained via juxtaposition.

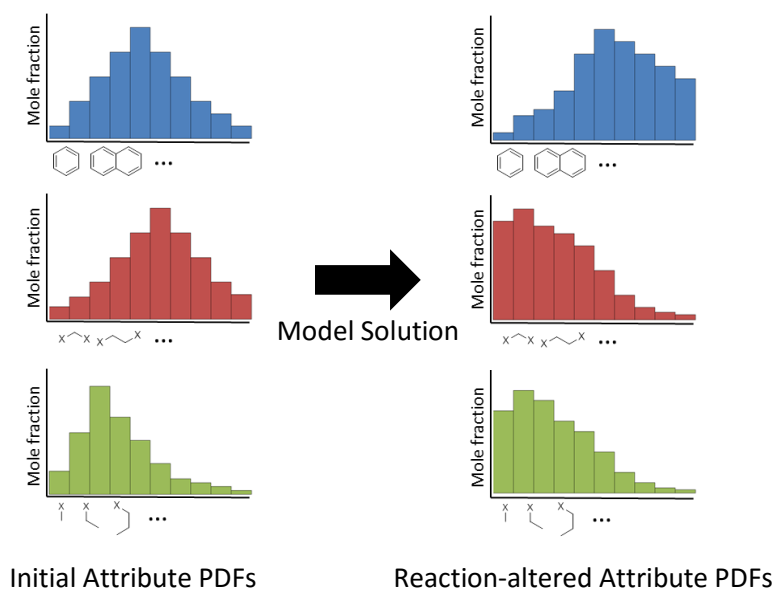


Figure 6.13: The alteration of attribute PDFs through model solution.

6.8 Kinetics

The rate constants in the model were followed the standard Arrhenius expression, given in Equation 6.3. To reduce the parametric complexity, we utilized the concept that the rates of similar reactions, i.e., members of the same reaction family, can be correlated. First, all activation energies for a given reaction family, j , were constrained using a linear free energy relationship (LFER), such as one posed by Bell-Evans-Polanyi[51], [52] shown in Equation 6.4. Second, all pre-exponential factors are assumed to be a function only of reaction family, or $\ln(A_j)$. The expression

for each rate constant in the model, shown in Equation 6.5, is only dependent on known quantities, temperature and the enthalpy change on reaction (ΔH_i), and three reaction-family dependent parameters (A_j , α_j , and $E_{0(j)}$).

$$\ln k_i = \ln A_i - \frac{E_i^*}{RT} \quad (6.3)$$

$$E_{i,j}^* = E_{0(j)} + \alpha_j * \Delta H_i \quad (6.4)$$

$$\ln k_i = \ln A_j - \left(\frac{E_{0(j)} + \alpha_j * \Delta H_i}{RT} \right) \quad (6.5)$$

For instances where the data used for tuning do not contain temperature dependence, the adjustable parameters are reduced to two terms per reaction family. This is shown in Equation 6.6 as a_j and b_j . These are the parameters for ten of the eleven reaction families. For the formation of a biphenyl bond in aromatic ring condensation, the rate is linearly correlated proportional to the average aromatic content in the system, as shown in Equation 6.7. There are a total of 21 adjustable parameters in the model.

$$\begin{aligned} \ln k_i &= a_j + b_j * \Delta H_i \\ a_j &= \ln(A_j) - \frac{E_{0(j)}}{RT} \\ b_j &= -\frac{\alpha_j}{RT} \end{aligned} \quad (6.6)$$

$$k_{aromatic\ ring\ condensation} = a_{arom} * (Average\ Aromatic\ Content) \quad (6.7)$$

6.9 Model Evaluation

The model was evaluated through comparison of its predictions with the experimental results given in Table 6.6. Quantitative structure-property relationships, QSPRs, were used to transform the molecular composition into the higher-level

measurements. After using QSPRs to calculate predictions, the evaluation of model fitness used a least-squares objective function, shown below in Equation 6.8.

$$F = \sum_{i, \text{measurements}} \left(\frac{y_i^m - y_i^p}{w_i} \right)^2 \quad (6.8)$$

Table 6.6: Experimental data for resid pyrolysis at 500 °C and 0.101 MPa for 40 minutes. All data were collected at the State Key Laboratory of Heavy Oil Processing, China University of Petroleum.

Property	Experimental	Property	Experimental
<u>Light Gas Cut</u>	13.6	<u>Diesel Cut</u>	21.1
<u>wt%</u>		<u>wt%</u>	
H ₂ S, wt%	7.31	Density (g/ml)	0.903
H ₂ , wt%	0.35	S, wt%	3.3
CO+CO ₂	0.71	N, wt%	0.26
CH ₄ , wt%	16.65	<u>Gas-Oil Cut</u>	16.5
		<u>wt%</u>	
C ₂ H ₆ , wt%	21.09	Density (g/ml)	0.9859
C ₂ H ₄ , wt%	3.71	C, wt%	85.05
C ₃ H ₈ , wt%	16.26	H, wt%	10.7
C ₃ H ₆ , wt%	9.07	S, wt%	5.6
C ₄ H ₁₀ , wt%	8.51	N, wt%	0.79
C ₄ H ₈ , wt%	7.24	MW (g/mol)	437
C ₅ +, wt%	9.2	Saturates wt%	59.52
<u>Gasoline Cut</u>	13.8	<u>Coke Cut wt%</u>	35.0
<u>wt%</u>			
Density (g/ml)	0.78	C, wt%	86.21
S, wt%	1.9	H, wt%	3.81
N, wt%	0.04	S, wt%	5.6
		N, wt%	2.7

The weight term, w_i , in the objective function is calculated based on two sources of standard error. The first is an error incurred by the property measurement. For instance, there is error in an average molecular weight measurement by GPC. The second source of uncertainty originates in the structure-property correlation. Some properties, such as molecular weight, are calculated exactly from a given composition. Others, such as density, have uncertainty in the structure property correlation. An analysis of a model's predictive ability must take into account both types of error. The total uncertainty, σ_{total} , for a given data point must then take both σ_{exp} and σ_{QSPR} into account, as shown in Equation 6.9. The values for σ_{total} for the data points are given below, in

Table 6.7.

$$w_i = \sigma_{i,total} = \sqrt{\sigma_{i,exp}^2 + \sigma_{i,QSPR}^2} \quad (6.9)$$

Table 6.7: Total error and error associated with experiments and quantitative structure property correlations for the measurements in the objective functions. Values for error were estimated based on experience in our prior work[46] with similar data in the objective function.

Property	Experiment	σ_{exp}	QSPR	σ_{QSPR}	σ_{total}
Boiling Point Cuts	HT-SimDis	1.2	Group contribution Theory	0.05 * y_{obs}	$\sqrt{((0.05 * y_{obs})^2 + 0.012^2)}$
Light Gas Composition	Gas Chrom.	0.05 * y_{obs}	Calculated Exactly	0.00	0.05 * y_{obs}
Elemental Composition	Elemental Analysis	0.01 * y_{obs}	Calculated Exactly	0.00	0.01 * y_{obs}
Density (g/mol)	Pyncometer	0.00003	Gani Theory	0.25 * y_{obs}	0.25 * y_{obs}
Average Molecular Weight	GPC	0.25 * y_{obs}	Calculated Exactly	0.00	0.25 * y_{obs}
SARA	SARA Analysis	0.25 * y_{obs}	Calculated Exactly	0.00	0.25 * y_{obs}

After setting up the objective function, the optimization was performed using a simulated annealing algorithm. The optimization problem was well-posed with over 30 terms in the objective function for 21 adjustable parameters. The parity plot comparing model and experimental results is given below in Figure 6.14. Included in this plot are all data points from Table 6.6. These data agreed reasonably well with experiments with an overall R^2 of the parity plot of 0.939. The tuned values for a_j and b_j used in predicting this data for each reaction family are given below in Table 6.8.

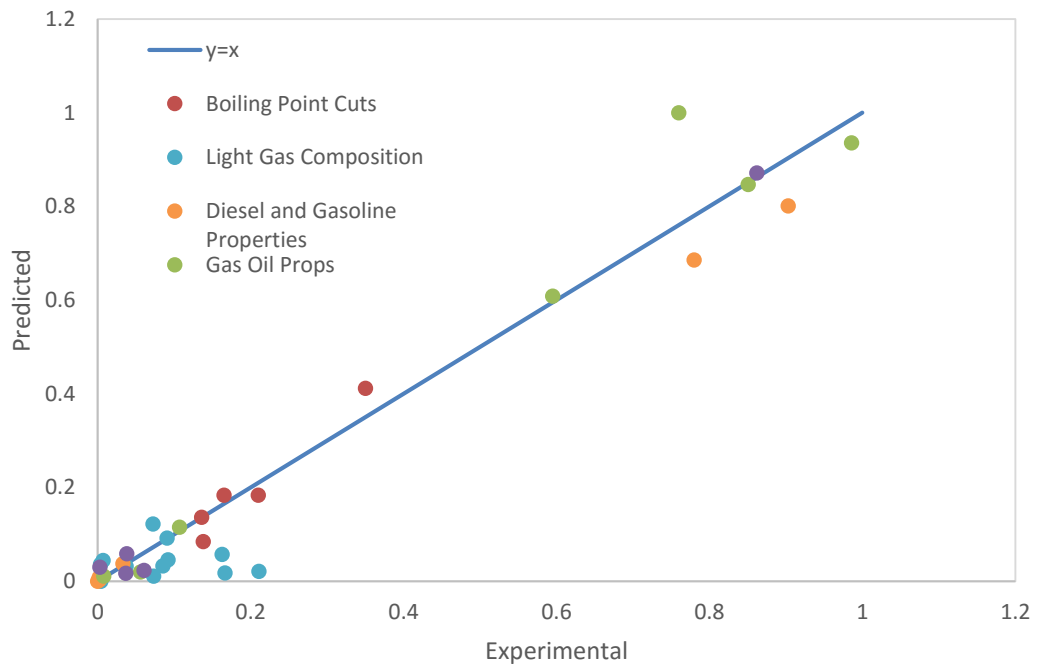


Figure 6.14: Parity plot comparing experimental and predicted results. The $y=x$ line corresponds to exact prediction. All weight percent values were converted to weight fractions, the average molecular weight for gas-oil was normalized to be on the same scale as other data. The R^2 value relative to $y=x$ is 0.944.

Table 6.8: Tuned parameters for kinetic model for each reaction family. $a_j = \ln(A_j) - E_{0(j)}/RT$ and $b_j = -\alpha_j/RT$. For aromatic ring condensation, α_j is the scaling factor, as shown in Equation 6.7. The value for the gas constant used is $R = 1.987 \cdot 10^{-3}$ kcal/(mol*K) and $T = 773$ K.

Reaction Family	a_j	b_j
Decarboxylation	2.041	-0.270
Naphthenic Ring Opening	0.169	-0.275
Sulfide Ring Opening	-1.652	-0.301
Thermal Cracking – Hydrocarbon	-3.645	-0.150
Thermal Cracking – C-S bonds	-3.983	-0.077
Naphthenic Ring Aromatization-6	2.357	-0.255
Naphthenic Ring Aromatization-4	-3.333	-0.278
Naphthenic Ring Aromatization-2	-3.034	-0.112
Sulfide Ring Aromatization-5	-0.006	-0.314
Sulfide Ring Aromatization-3	-1.224	-0.068
Aromatic Ring Condensation	7.800E-05	-----

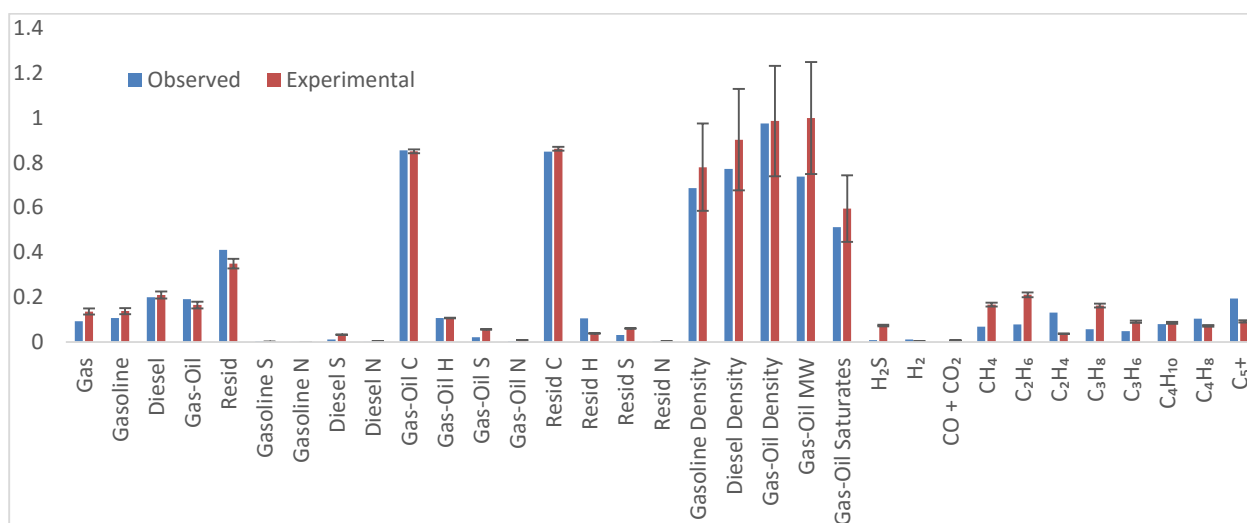


Figure 6.15: Observed versus experimental including error bars for σ_{total} ; the error bars were chosen to be drawn on the experimental values. The average molecular weight for gas-oil was normalized to be on the same scale as other data.

The tuned results including σ_{total} are given in Figure 6.15 and give more detailed information on individual experiments than provided by the parity plot. For instance, the errors in density can be explained by σ_{total} . The predictions that deviate from measurements most notably by the model are in the light-gas composition. The light gas composition is controlled by two reaction families: hydrocarbon cracking and sulfide cracking. One approximation made is that these two reaction families govern the cracking of any resid molecule, regardless of boiling point, and it is likely that the apparent rate constants are different between light gasses and heavy ends. A possible solution is the inclusion of an additional pair of cracking reaction families for light gasses. This alternation would only add four parameters to the model. Therefore, the model would retain its computational tractability. Furthermore, the importance of the predictive ability of a model for light gasses in resid pyrolysis is minor compared to other experiments such as boiling point cuts.

The model also predicts molecular level results such as the molecular weight distribution shown Figure 6.16. When compared to the molecular weight distribution of the feedstock, the outlet stream is more bimodal with a low molecular weight peak corresponding to the low boiling point fractions and a higher molecular weight peak corresponding to coke. The general trend to lower molecular weights correspond to the cracking of side chains from core molecules. The peaks at low molecular weight correspond to irreducible molecules. For aromatic ring number, values of all mole fractions were shifted down due to the production of small molecules. The distribution was also shifted to higher ring numbers due to aromatic ring condensation and aromatization. There were relatively fewer naphthenic rings than aromatics in the

product due to ring opening reactions. These trends were expected based on the reaction network and the feedstock.

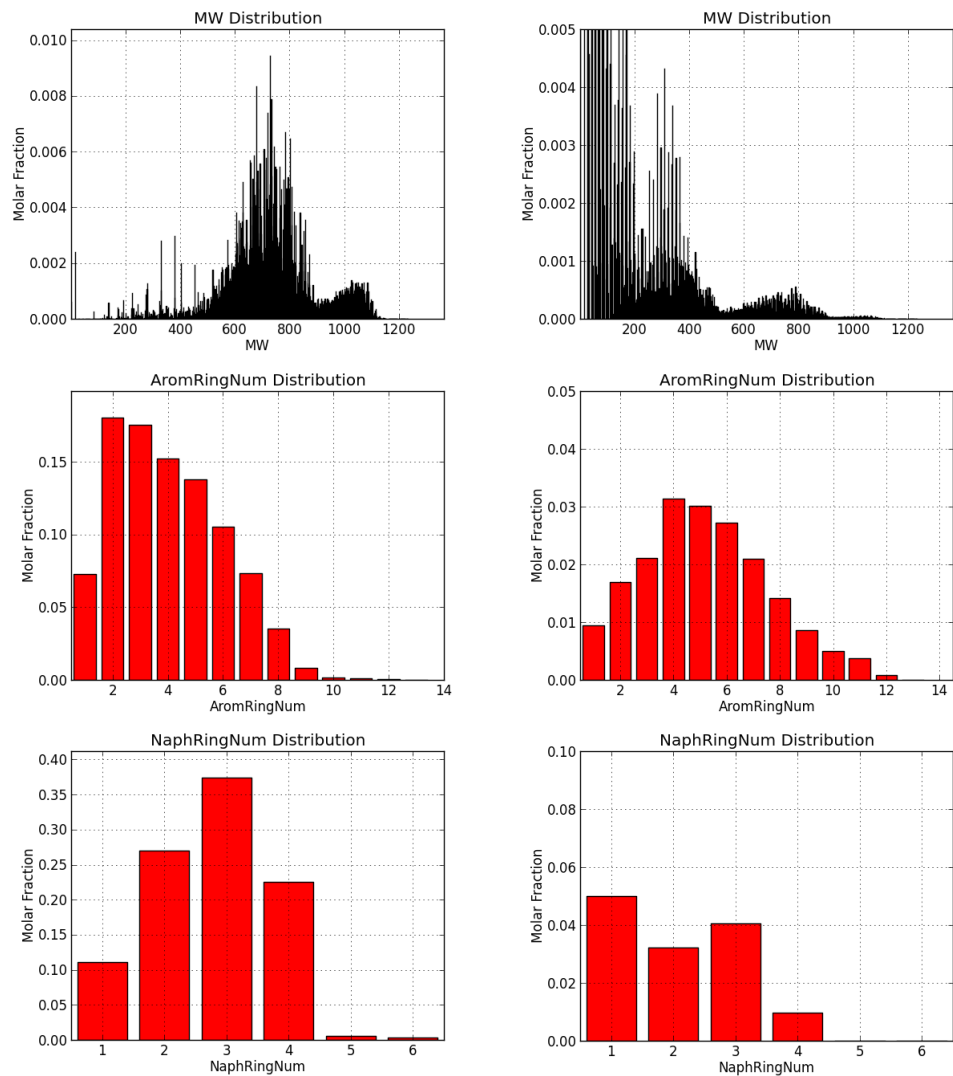


Figure 6.16: Before (left) and After(right) distributions for MW, aromatic ring number, and naphthenic ring numbers.

6.10 Conclusions

We have shown that a model containing only 2839 equations can simulate the pyrolysis of $O(1,000,000)$ resid molecules using an Attribute Reaction Model (ARM). Furthermore, the parametric complexity in the model was reduced to 21 adjustable parameters using Linear Free Energy Relationships and reaction families. Even with this reduced number of equations and adjustable parameters, the model agrees well with experimental data.

The supporting information document contains complete information on the rules for reaction network construction. This information is available free of charge via the Internet at <http://pubs.acs.org/>.

Chapter 7

ENHANCING THE USER-MODEL INTERFACE THROUGH THE DEVELOPMENT OF SOFTWARE APPS

For an industrial reactor kinetic model, there are three types of users, given in Table 7.1. The initial user is the developer of the model. After construction, this model is subsequently used, understood, and evaluated by research collaborators. Once the model is in use, the predominant end-user is a process engineer. There are different goals for the users of kinetic models, yet the common goal is the usage of the model to predict process outputs from specified or experimentally measured inputs. Research collaborators and model developers also hope to gain a mathematical and scientific understanding of the model, model results, and process. Finally, the model developer hopes to further their kinetic model development capabilities for future projects.

Table 7.1: The types and goals of kinetic model users.

User Type	User's Goals
Model Developer	Scientific and mathematical understanding of model and results Usage of model to predict measurable outputs from measurable inputs Furthering kinetic model development capabilities
Research Collaborators	Scientific and mathematical understanding of results Usage of model to predict measurable outputs from measurable inputs
Process Engineer	Usage of model to predict measurable outputs from measurable inputs

To build the kinetic model, the model developer may use the Kinetic Modeler's Toolkit (KMT). There are three software packages within this toolkit, as shown in Figure 7.1: the Composition Model Editor (CME), the Interactive Network Generator (INGen), and the Kinetic Model Editor (KME). The starting points of a kinetic model are experimental data on the feed and reactor outlet, and an understanding of the process chemistry. CME takes experimental data on the feed to create a list of molecules and mole fractions of the inlet. INGen utilizes this molecule list and process chemistry to build a reaction network. Finally, KME uses the reaction network and feed description to create and solve the equations that define the kinetic model.

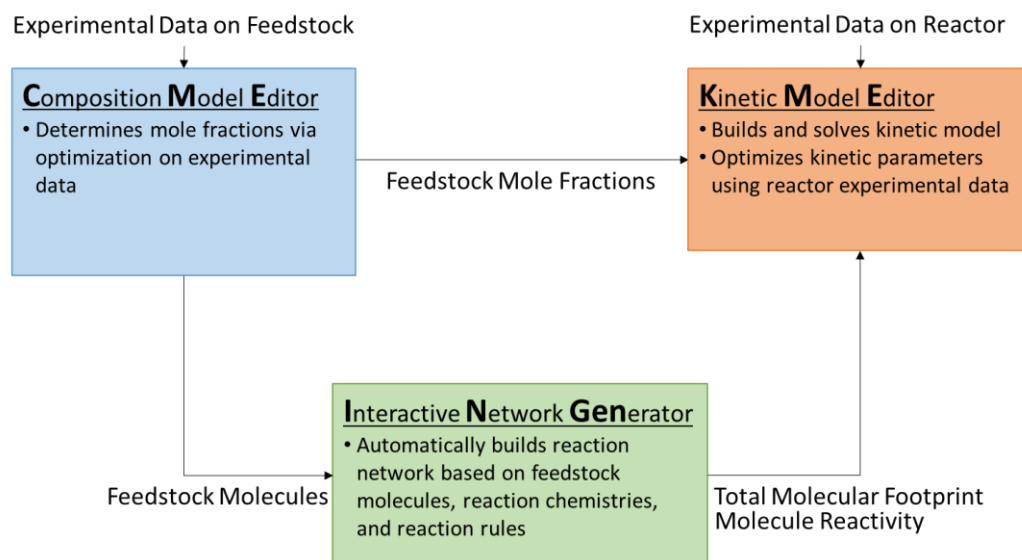


Figure 7.1: Main software packages that make up the Kinetic Modeler's Toolkit

The tools in KMT are designed to be ubiquitous regardless of the kinetic model; *i.e.*, the same tools are used for MSW gasification as heavy oil resid pyrolysis or any other process. The strength of these tools therefore lies in the usage by a model developer. The features of the tools have a very logical progression. When a new project is started, if the tools do not perform all steps necessary for that project, then the tools are expanded to match the new project specifications. Over the years of development, these tools become increasingly more useful to the developers as the features are expanded to include more experimental measurements, process chemistries, and reactor configurations. The unfortunate side effect is that the learning curve for these tools is proportional to the number of features. The tools become less ideal for many research collaborators and process engineers. These users are only using a small fraction of overall features in the toolkit and often don't have the time or resources to spend on the learning curve.

Current expansion of KMT has been in the area of software apps, typically coded in C# (C-Sharp). The use of the colloquial term ‘app’ implies that these tools are lightweight in terms of development and use. Each app targets a specific use case and has one set of features. Alternatively, the larger software suites (CME, INGen, and KME) were designed to take into account as many use cases and features as possible. The consequence of the lightweight design approach is that the apps are very fast to develop, and have an easy learning curve from the point of view of the user. When a user needs new features, a new app is developed to meet their specific needs; this leads to many small programs as shown in Table 7.2.

Software apps target the different objectives for the users of kinetic models. Apps that aim to increase scientific and mathematical understanding focus on organizing the vast quantities of information produced in a molecular-level kinetic model. The organized information is primarily displayed via visualization. It is important to note that these apps retain the molecular information to present to the user. In contrast, apps that focus on the usage of the model for measured inputs and outputs abstract all immeasurable information away from the interface. These apps are typically designed for a specific process and are easy to use regardless of a user’s background in kinetic modeling. Because of the focus on I/O (inputs/outputs), the apps are also useful for scenario testing of varying process parameters. The final category of apps aims to further kinetic model development capabilities. These apps have the most variety in terms of capability, ranging from the simulation of a particular experimental reactor to basic flowsheeting capabilities to a properties database.

Table 7.2: The categories of apps as organized by objective, corresponding design method, and a list of apps developed

App Objective	App Design Method	Apps Developed
Increase scientific and mathematical understanding of the model	Reorganize and visualize information from a molecular-level kinetic model to gain understanding	Reaction Network Visualizer KME Results Analyzer
Usage of the model to predict Measured Outputs from Measured Inputs	Focus on I/O and abstract molecular information away from the user interface.	MSW Gasification I/O Converter Naphtha Reforming I/O Converter
Furthering kinetic model development capabilities	Develop new, lightweight tools to further future kinetic model development.	KME Flowsheet Application TGA Simulator Physical Property Database Interface INGen Network Merge External KME Simulated Annealing CME-Plastics CME-Naphtha MSW Bulk Composition Solver

Most of the C# apps are associated with one or more of the three main software packages in KMT. A good example is the reaction network visualizer where the main use case is to visualize and understand INGen networks; the app supports INGen and assists in the network building process. A second example is the series of I/O converter apps. These tools effectively utilize CME and KME in a behind-the-scenes fashion to allow the users to access only the features of CME and KME that are needed for the project while not being overwhelmed with detail irrelevant to the project at hand.

Table 7.3: The KMT software supported by each App discussed in this thesis.

App	Supported KMT Software
CME-Plastics	CME
CME-Naphtha	CME
MSW-Bulk Composition Solver	CME, KME
MSW Gasification I/O Converter	KME
Naphtha Reforming I/O Converter	CME, KME
Reaction Network Visualizer	INGen
Kinetic Results Analyzer	KME
KME Flowsheet Application	KME
TGA Simulator	KME
INGen Network Merge	INGen
External KME Simulated Annealing	KME
Physical Property Database Interface	CME, KME

The remainder of this chapter discusses each of the three primary app objectives from Table 7.2, and explores the functionality of the apps.

7.1 Increasing the Scientific and Mathematical Understanding of the Model through Apps

Historically, lumped kinetic models had few components and were easy to understand; however, this came at the cost of scientific rigor as shown in Figure 7.2. For instance, a lumped kinetic model of coal pyrolysis might contain four lumped components: coal, tar, volatiles, and char. A few simple plots as a function of operating conditions contain all of the kinetic data produced by the model, and therefore the model is easily understood. However, the absolute quantity of information produced by the model is dwarfed by level of detail actually contained within the process of coal pyrolysis. The information discrepancy between models and reality requires many lumped models to describe the realm of possible operating

conditions, coal types, etc. Rather than a single, universal description, each lumped model only contains a small piece of the information that makes up coal pyrolysis.

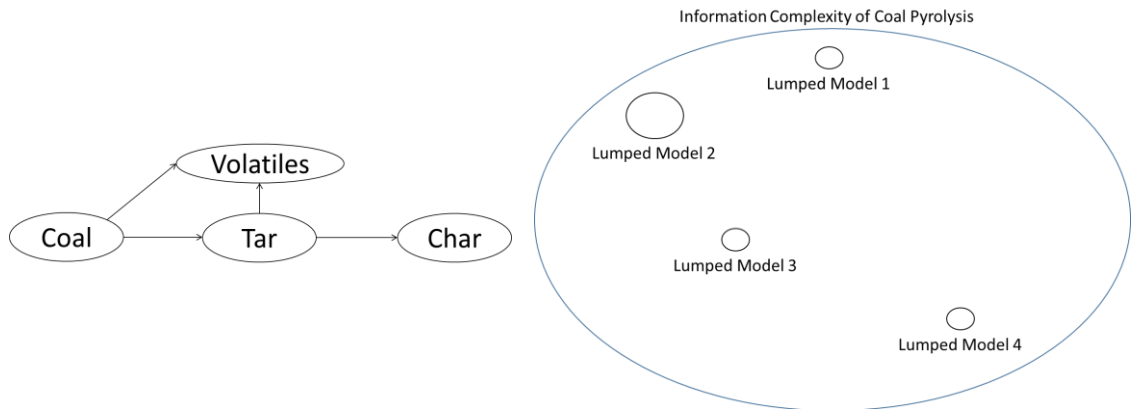


Figure 7.2: (Left) Typical lumped model of coal pyrolysis. (Right) Conceptual representation of the information complexity in coal pyrolysis versus simple lumped models.

Advanced kinetic models are more detailed, but their usefulness is a function of the user's ability to comprehend vast quantities of data. The scientific rigor of modeling has been drastically increased through the advent of advanced experiments, algorithms, and computing. With increased levels of detail in the model, there is a better match between the model and what is physically happening within the process. If a model contained all of the information complexity of coal pyrolysis, then a single, universal model would suffice for every coal and reactor type. However, the incredible amount of information in detailed kinetic models shifts the onus of research onto the user who must understand the model's equations and results. Unaided, a model can be difficult to comprehend, reducing the overall scientific usefulness of the results as shown in Figure 7.3. In order to address the challenge of model comprehension, first

we must go into more detail on the information contained within a detailed kinetic model.

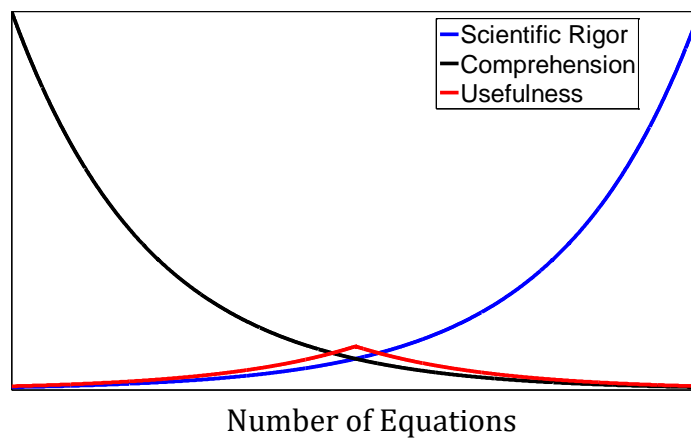


Figure 7.3: Trade-offs of the comprehension and scientific rigor of models as a function of the number of equations.

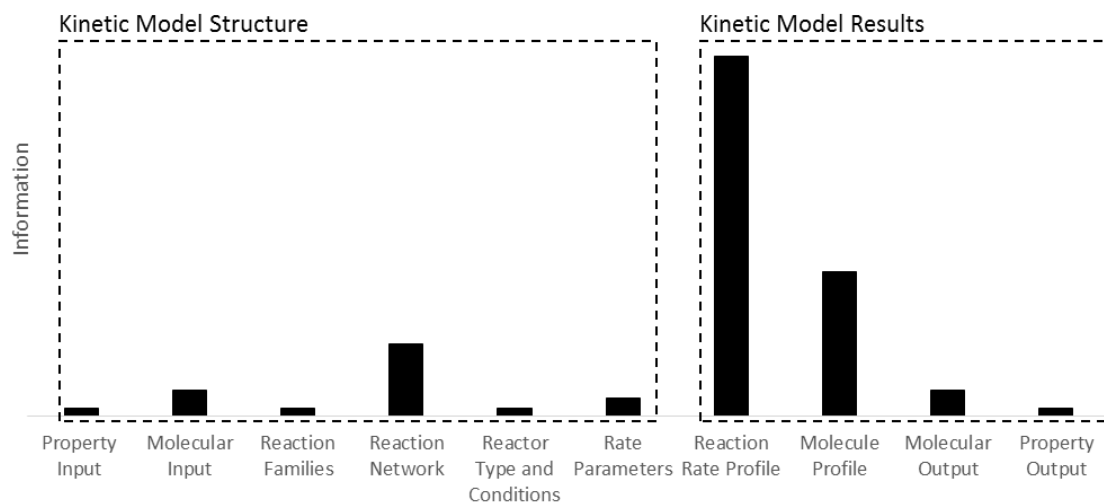


Figure 7.4: Information sources and amounts within a molecular-level kinetic model. Values are relative and qualitative. The relatively low value for rate parameters is due to a linear free energy relationship (LFER) basis.

The sources and quantities of information in molecular-level kinetics are given in Figure 7.4. The measured quantities are typically experimental measurements of the reactor inlets and outlets. Other aspects of the model structure include the reaction families, reactor type, and rate parameters. Typically, models have far more reactions than species; resulting in the smaller relative sizes of the molecular (input or output) compared to the reaction network categories. The largest categories of information are the reaction rate and molecule profiles within the reactor. Each of these categories contains a full set of rate and molecule profiles along the reactor length or the reaction time.

The three main software tools enable the comprehension of many of the categories of information as described in Table 7.4. For example, CME predicts the

molecular input, but it also categorizes the feed using statistical distributions that are based on molecular structure. INGen helps to organize the reaction network via categorization into reaction families. There are opportunities for improvement in understanding the structure of the reaction network. KME also utilizes reaction families in the area of rate parameters. The most information in the kinetic model and the biggest issues in comprehension occur after kinetic model solution.

Table 7.4: Information types, relevant KMT software, how the information is organized, and how well the user comprehends the information. *the comprehension of the reaction network depends on the network size.

Information Type	Relevant Software	Method of Organization	Qualitative Comprehension
Property Input	CME	User-defined and categorized experimental properties	Complete
Molecular Input	CME	Statistical distributions based on molecular structure	High
Reaction Chemistries	INGen	Reaction family list	Complete
Reaction Network	INGen	Organized using reaction families and species	Low-High*
Reactor Type and Conditions	KME	User-input. Flow-profile determines reactor type	Complete
Rate Parameters	KME	User-defined, organized as reaction families	Complete
Reaction Rate Profiles	KME	Tabulated, no categorization	Low
Molecular Profiles	KME	Tabulated, no categorization	Low
Molecular Output	KME	Tabulated, can be categorized based on user-input	Medium
Property Output	KME	Experimental properties and bulk properties	Complete

Two C# apps have been developed to target the hardest to comprehend sources of information in the kinetic model. The *Reaction Network Visualizer* aims to improve the understanding of the structure of the reaction network by allowing the user to

visualize isolated portions of the network. *KME Results Analyzer* targets primarily the rate and molecule profiles in the reactor, but it also helps to address understanding the molecular-output data.

7.1.1 Reaction Network Visualizer

The reaction network visualizer was developed with the purpose of aiding in the creation of reaction networks via INGen. It allows for the graphical visualization of reaction networks, which can aid in viewing the reaction paths from feed molecules to important product molecules. All trees (or mathematical graphs) are rendered using the open-source GraphViz software[132].

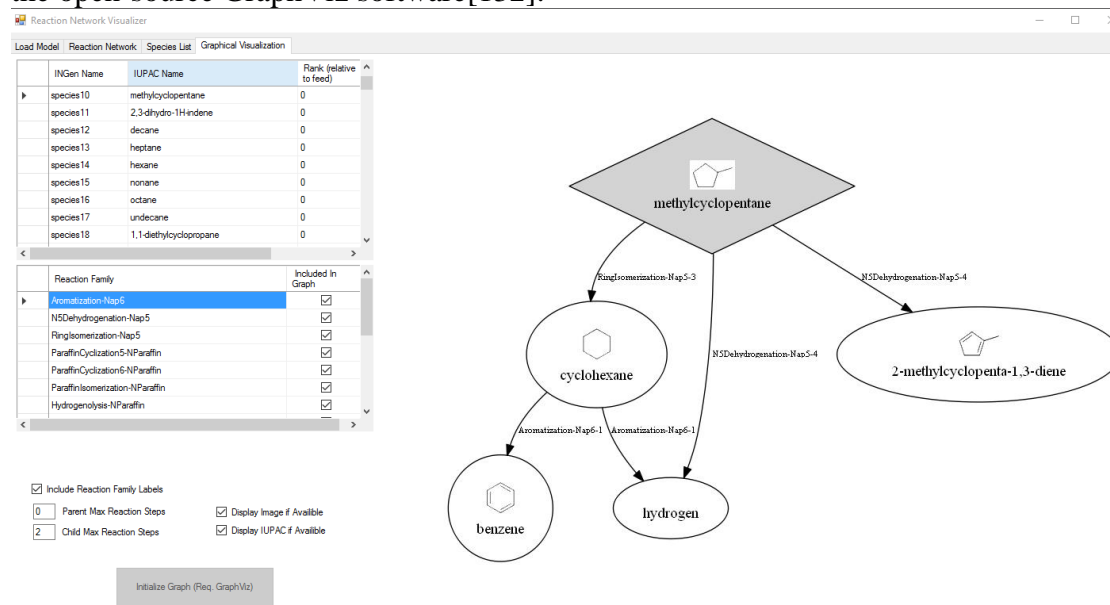


Figure 7.5: Sample screenshot from the Reaction Network Visualizer. Graph image rendered using GraphViz[132].

Because these networks are too large for easy visualization of the full network, there are a few smarter methods of using this software. If there is a species of interest, a user might start from this species with a small number of parent (toward seed³) and child (toward product) reaction steps. The user can then adjust the numbers to visualize the desired network. If the graph is obscured by small, common molecules such as hydrogen or water, the user can elect to remove these molecules from visualization. Likewise, if a user wishes to focus on particular reaction families, this can be done as well.

In any scenario, the Reaction Network Visualizer is used to better understand the reaction network. If the network does contain measured products, then the Visualizer can be used to help find the unreactive end-points of the network. If the network is too large and includes too many intermediates, visualization can help determine the seeds for constrained network building. In order to show the use of this application for the purpose of constrained network building, ethane pyrolysis is used as a case study.

Ethane pyrolysis is a well-understood process where radical chemistries are utilized in models[39], [57]. Because the network is at the mechanistic level, most radicals in the system can interact with most molecules via H-abstraction reactions (see Figure 7.6) leading to a network size explosion as rank (reaction steps away from the network seed, ethane) increases. A qualitative version of this phenomenon is shown in Figure 7.7. This problem is exacerbated as the product of interest, xylene, is many reaction steps away from ethane. This detail brings up a quandary: the model is

³ The seeds of the network are the user-specified starting points for reaction network generation. Often, the seed molecules are synonymous with feed molecules.

either finite and useless or infinite and useful. A finite and useful model of ethane pyrolysis would have xylenes in the finite region of Figure 7.7.

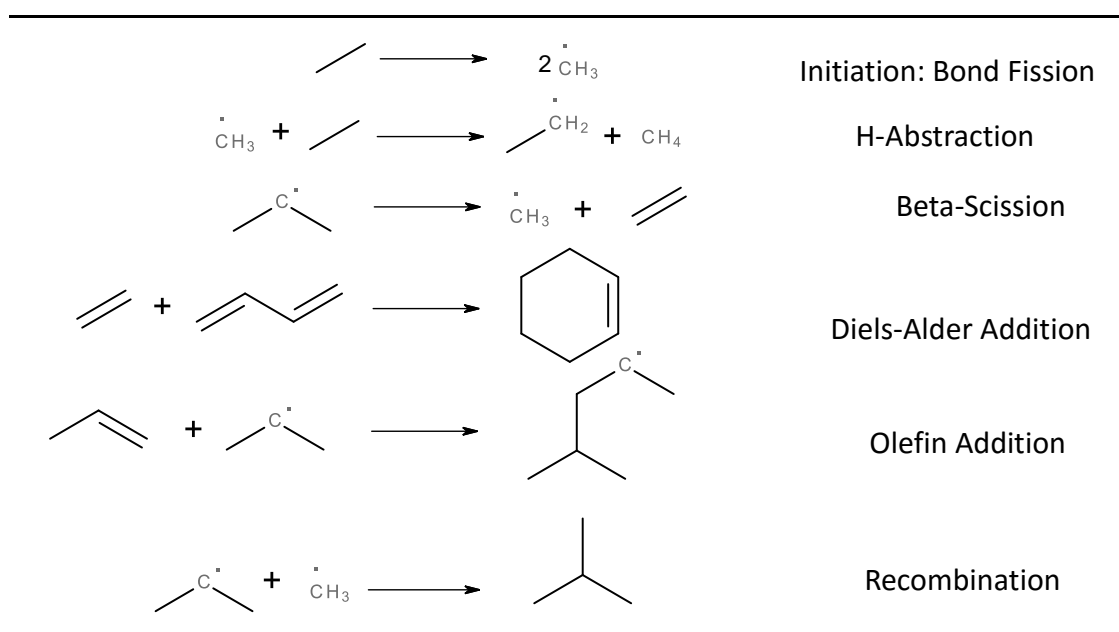


Figure 7.6: Reaction families and some example reactions from ethane pyrolysis. The primary form of mass increase from ethane is first via olefin addition reactions. Once large olefins form, Diels-alder additions allow for the formation of cyclic structures. Beta-scission can then lead to aromaticity and the product of interest, xylene.

The question then arises: is there a way to lower the rank of xylenes such that it is in the finite region of model growth? A logical way to model xylene with a finite number of reactions is by seeding molecules on the path from ethane to xylene. The reaction network generation can then restrict reactions to remain within a few steps (or ranks) of the seeded species. This approach is analogous to creating a roadway between the two molecules, and only allowing for small deviations from that roadway.

Determining the molecular identities of these seeds is where network visualization can play a key role.

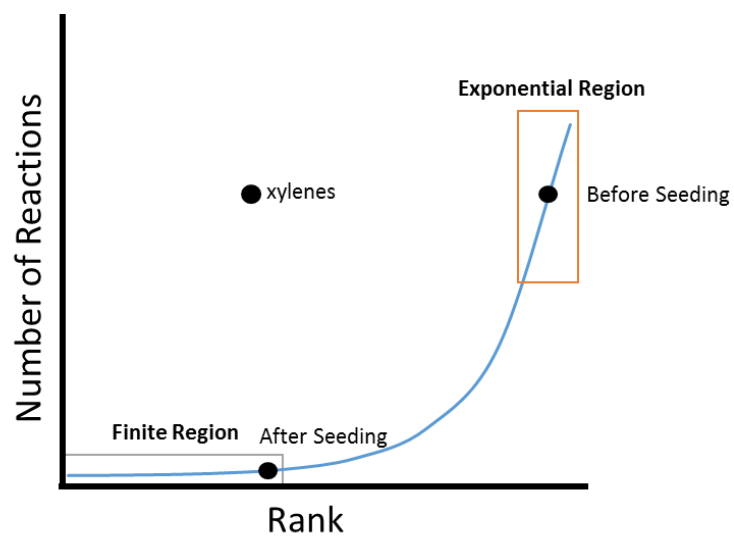


Figure 7.7: Number of equations by rank in an ethane pyrolysis model with ethane as the only seed. The black dots represent the location of xylenes before and after seeding.

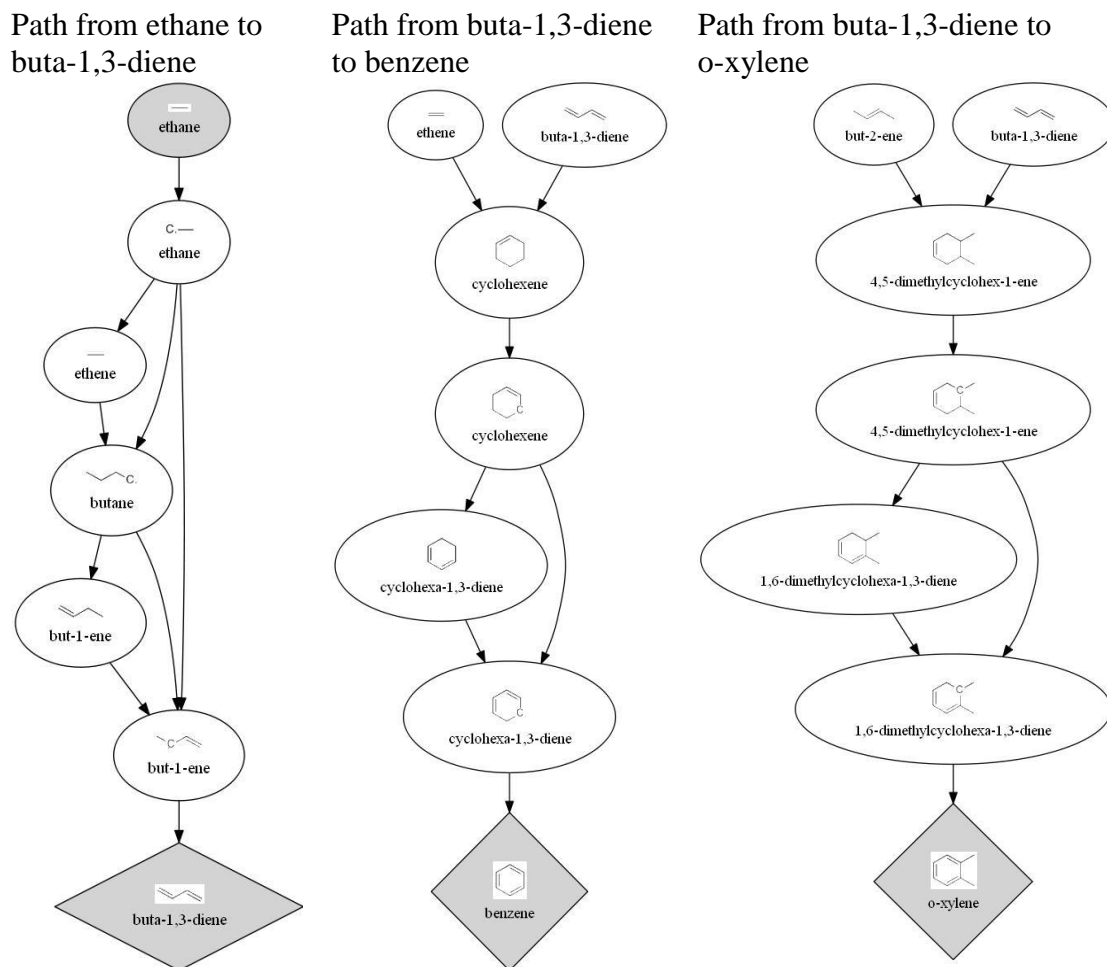


Figure 7.8: Some major reaction paths visualized using the Reaction Network Visualizer. Images rendered using GraphViz.

Using the Reaction Network Visualizer, useful seeds for ethane pyrolysis can be identified as shown in Figure 7.8. The seeds selected are ethene, butadiene, benzene, and methylcyclohexenes. After reproducing the network, the number of reactions required to produce o-xylene is drastically reduced as shown in the

comparison presented in Table 7.5. This case study shows the utility of the reaction network visualizer as an aide to generate finite reaction networks.

Table 7.5: Ethane pyrolysis reaction network before and after seeding.

Reaction Family	Number of Reactions, Only ethane seeded	Number of Reactions, Intermediates seeded
Bond Fission	30	36
H-Abstraction	14,977	2,325
Beta-Scission	325	107
Diels-Alder Addition	4	3
Olefin Addition	17	9
Recombination	153	181
Total Reactions	15,506	2,661

7.1.2 KME Results Analyzer

The KME Results Analyzer was developed for the purpose of gaining additional understanding of the results produced by KME. This app specifically targets reactor profile information and the molecular information of the reactor output. For reactor profile information, the app allows for the user to select specific species in the output stream and graphically see the reaction families responsible for production and consumption of the species of interest. For understanding the molecular output, the app allows the user to specify structural properties (such as aromatic ring class) and visualize the dominant species that match the constraints. The following text examines each of these features in greater detail.

Table 7.6: Reaction rate information from KME.

Distance (or time)	Reaction 1	Reaction 2	Reaction M
d_1	$rate_1(d_1)$	$rate_2(d_1)$	$rate_M(d_1)$
d_2	$rate_1(d_2)$	$rate_2(d_2)$	$rate_M(d_2)$
d_n	$rate_1(d_n)$	$rate_2(d_n)$	$rate_M(d_n)$

$$\begin{aligned}
 & \text{Total Reaction integration for reaction } M \\
 RxnInt_M &= \sum_{i=1}^n (d_i - d_{i-1}) * rate_M(d_i), \quad \text{note } d_0 = 0 \tag{7.1}
 \end{aligned}$$

For profile information, the output of a KME simulation includes the reaction rates in a tabulated format, as shown in Table 7.6. These values can be integrated numerically using Equation 7.1. This result tells the user how many moles actually reacted for each reaction. The reaction integration can help inform a user beyond the reaction rate parameters. A reaction with a high value of the rate constant will not show up numerically if there is no reactant present. Similarly, reactions with low rate constant values might be very important if the reactant concentrations are sufficiently high. For these reasons, in analyzing the results of a kinetic model, it is useful to analyze the total integration of the reaction rates throughout the reactor.

In models with reaction families, the adjustable parameters in the model are a shared pre-exponential factor for the reaction family and the Bells-Evans-Polyani[51], [52] LFER parameters (slope and intercept) of the activation energy correlation. Therefore, interest in analyzing a model's results usually focuses on reaction families rather than individual reactions. A total reaction family integration can then be found by summing the total reaction integrations for each member of that family as in

Equation 7.2. The results can be displayed graphically in a pie chart that demonstrates the mathematical significance, on a molar basis, of each reaction family in the system. For example, the results shown in Figure 7.9 are for naphtha reforming. Key reaction families here are, as expected, the formation of aromatics from naphthenics, paraffin cyclization, and isomerization reactions.

$$RxnFamilyInt_p = \sum_{i=1}^{\text{reactions in family } p} RxnInt_i \quad (7.2)$$

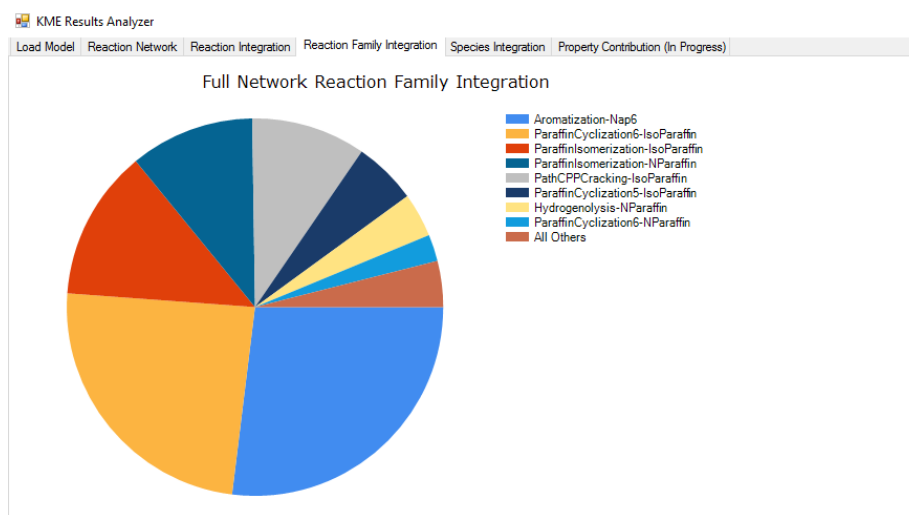


Figure 7.9: Full reaction network generation in a Naphtha Reforming model.

In order to understand the reaction rate and species profiles, the analysis of individual molecular species can yield useful information. For example, the user might be interested in the reaction families that produce or consume that species. Mathematically, this is very similar to the full reaction network integration with an additional term for the stoichiometry, ν , of the species in the reaction, as shown in

Equation 7.3. This analysis is represented visually using pie charts, as shown in Figure 7.10. These graphics can help inform which rate parameters are important for the prediction of the species.

$$\text{Species RxnFamilyInt}_p = \sum_{i=1}^{\text{reactions in family } p} v_i * \text{RxnInt}_i \quad (7.3)$$

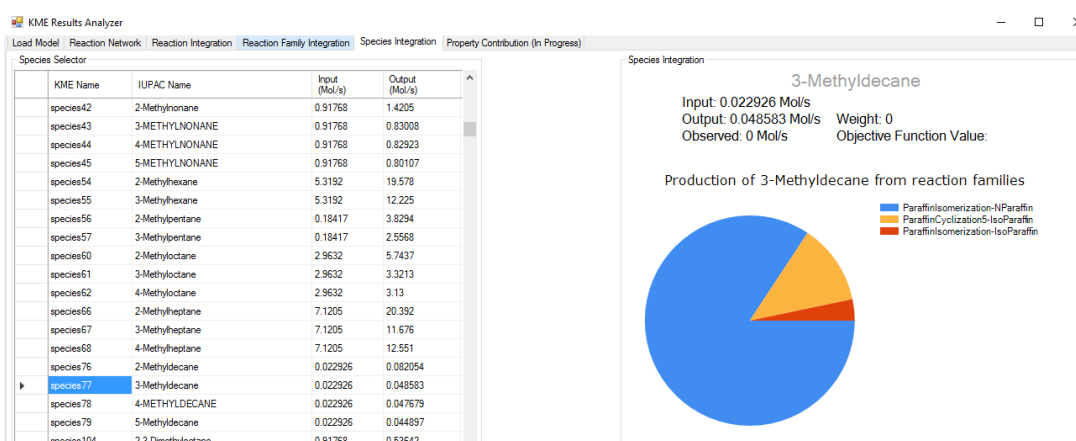


Figure 7.10: Reaction families responsible for the production of 3-methyldecane.

The full list of species outputs can become overwhelming in large models. To understand this output, it then becomes helpful to organize the species based on structural properties. An organization of the species based on structural properties can provide some better insight to the user. For example, Figure 7.11 shows the eight carbon *i*-paraffins in the reactor outlet from a naphtha reforming model. The app also has the ability to organize the species flowrates using any set of conditional statements, involving 70 physical properties. For instance, if the user is interested in 1-

3 ring aromatic species, then they can specify two conditionals, as shown in Figure 7.12. The app automatically gives the eight most significant species that meet the specified criteria.

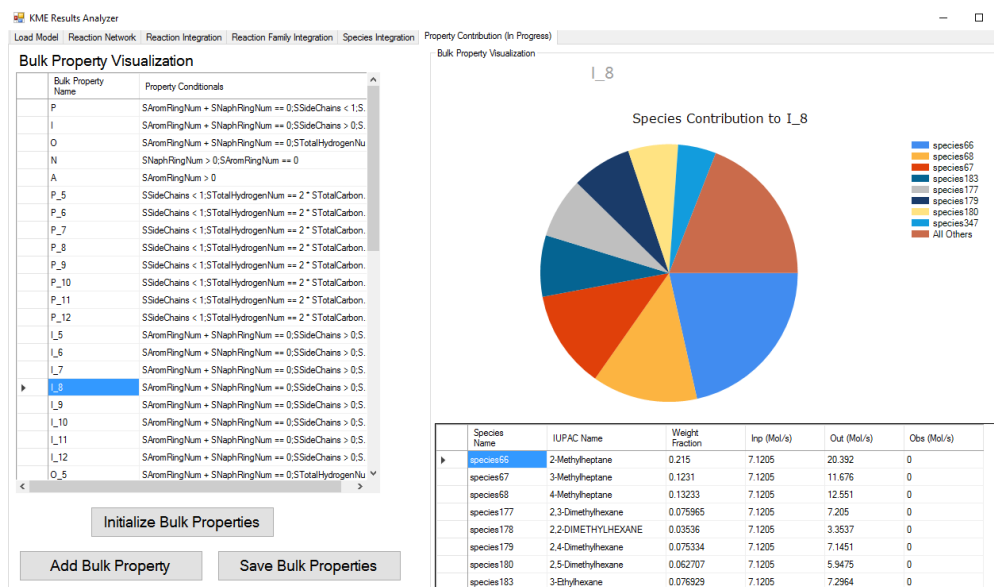


Figure 7.11: Visualization of Bulk Properties in the KME Results Analyzer

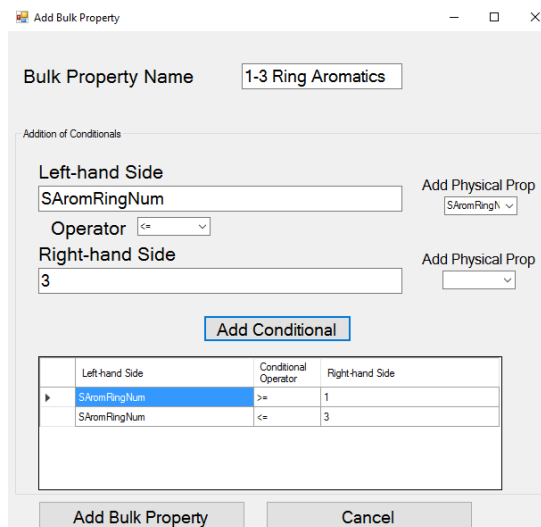


Figure 7.12: Window allowing the addition of bulk properties to the KME Results Analyzer. The bulk property added here is 1-3 ring aromatics.

7.2 Enabling the Usage of Model to Predict Measured Outputs from Measured Inputs

The second category of apps focuses on converting measurable inputs to measurable outputs. These tools are designed for the full spectrum of users from Model Developers to Process Engineers. As such, the assumed background of the user is knowledge of the physical process rather than detailed kinetic modeling. This focus comes into play in the design of the apps. For instance, technical kinetic vocabulary such as linear free energy relationships (LFERs) is avoided, while colloquial terms for experimental measurements are permitted. The apps also minimize user-supplied information required to run the model. For the kinetic model, the user is allowed to input process conditions and measurable properties, but not alter the physical process, equations, or kinetic parameters. The output is customized to suit the user's needs and can be a combination of individual species outputs like H₂ flow, experimentally measured bulk properties like PIONA, and reactor conditions like outlet temperature.

Because of their very nature, these apps are specific to a given project. The two apps discussed here, the MSW Gasification I/O Converter and the Naphtha Reforming I/O Converter, are fundamentally the same concept, but differ in appearance, inputs, and outputs. For instance, the inputs to MSW gasification are typically ultimate analyses, whereas naphtha reforming has detailed molecular information such as detailed PIONA or GC. These apps are currently in use by industrial collaborators and were designed to their specifications.

7.2.1 MSW Gasification I/O Converter

The first I/O converter app was created for a project on MSW gasification and is shown in Figure 7.13. The details of this app are discussed in Chapter 5.

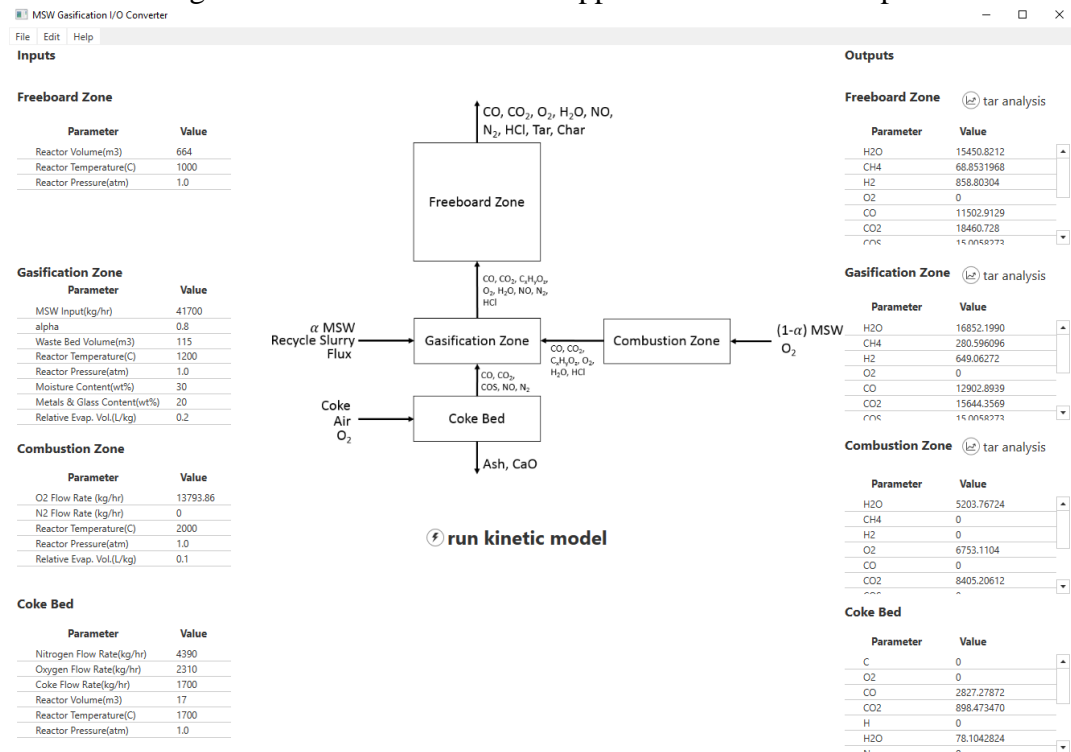


Figure 7.13: Sample Screenshot from the MSW Gasification I/O Converter.

7.2.2 Naphtha Reforming I/O Converter

The Naphtha Reforming I/O Converter, shown in Figure 7.14, was developed to run a detailed kinetic model of a continuous catalytic reforming (CCR) process for naphtha. The measurable inputs to the model are simulated distillation, carbon number based PIONA, density, and reactor conditions. The measurable outputs from the model are light-gas yields, detailed PIONA, and temperature drops across each reactor bed. Because coking is a key phenomenon in this process, coke formation is also reported in the output tables.

Behind the scenes, this app runs both a composition model and kinetic model. In this case, the composition model is a simplified limiting-case of CME (Composition Model Editor), due to the simplicity of a naphtha feed. The KME model involves Langmuir-Hinshelwood-Hougen-Watson (LHHW) kinetics on a bifunctional metal-acid catalyst. Despite this underlying complexity of the kinetic model, the user simply pastes data into the input table and runs the model by selecting the '*Run CCR Model*' button.

A second focus of this app is to enable the blending of feed streams from different sources. The blender portion of the app allows up to four naphtha feeds. This is potentially useful in cost-benefit analyses of different crude oils (straight-run naphtha), or evaluating the effects of feeding naphtha fractions from other refinery unit outlets such as fluid catalytic cracking (FCC). In the underlying code, the app simply runs a CME model for each feed stream. The input to the KME model is then the sum of each of the four feed streams.

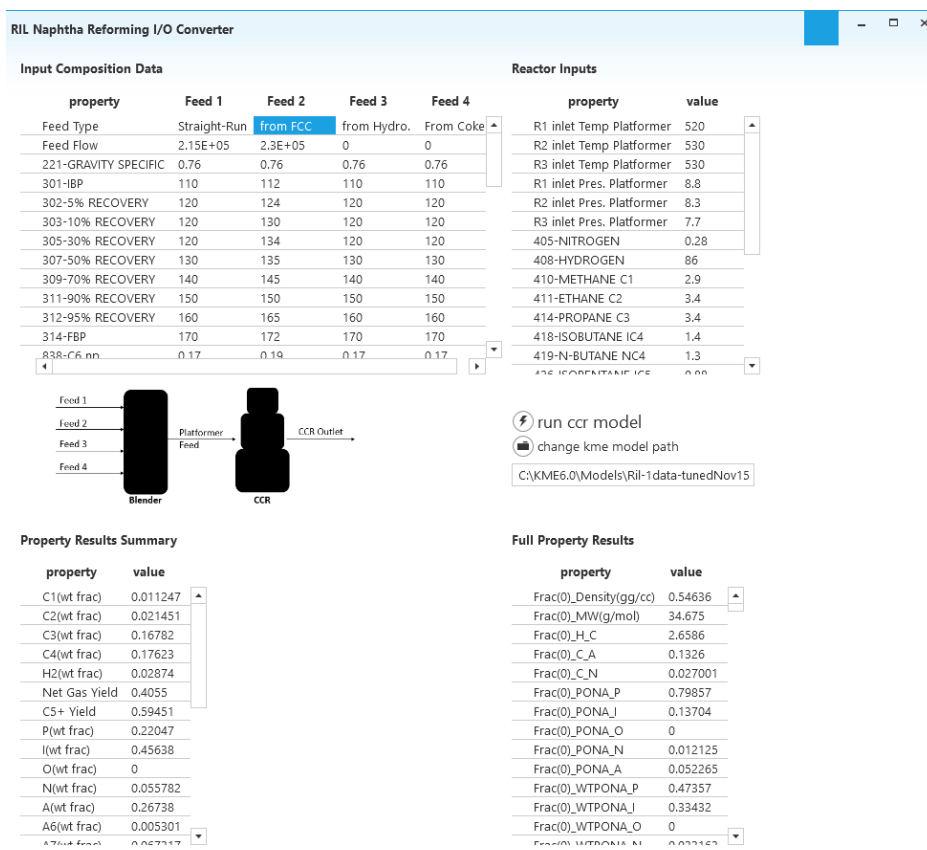


Figure 7.14: Sample Screenshot from Naphtha Reforming I/O Converter

7.3 Furthering Kinetic Model Development Capabilities

The final category of apps is aimed at furthering the kinetic model development capabilities of the Kinetic Modeler’s Toolkit (KMT). These apps are widespread in concept and subject matter. The primary target users of this app are model developers or specific collaborators.

Three apps are discussed here: KME Flowsheet Application, TGA Simulator, and the Physical Property Database Interface. The KME Flowsheet Application provides basic flowsheeting capabilities (e.g., bypass streams) for KME models. TGA Simulator simulates the thermogravimetric analysis (TGA) experiment using a pre-

built KME model. Finally, the Physical Property Database was developed to store previously calculated properties for tens of thousands of molecules.

Many other apps also fall into the category of furthering development capabilities and are listed in Table 7.7; detailed explanations of these apps were excluded from this chapter. For some of these apps, they have been discussed elsewhere (*e.g.*, MSW Bulk Composition Solver). Others are useful to developers but are conceptually less significant, such as External KME Simulated Annealing.

Table 7.7: Apps excluded from the current chapter.

App	Major Functionality
CME-Plastics (or Plastics Composition Editor)	Develop composition models for linear polymers using ultimate analyses as experiments
CME-Naphtha	Develop composition models for naphtha feeds (similar to I/O Converter)
MSW-Bulk Composition Solver	Predict polymer fractions in waste from ultimate analysis, detailed in chapter XX (REFERENCE)
INGen Network Merge	Merge INGen models, modify reaction network to include gasification reactions, detailed in chapter XX (REFERENCE)
External KME Simulated Annealing	Run simulated annealing as a separate application from Excel and allow for visualization of tuning progress and frequent backup of parameters

7.3.1 KME Flowsheet Application

The KME Flowsheet Application, shown in Figure 7.15, was built to incorporate basic flowsheeting capabilities into the Kinetic Modeler's Toolkit (KMT). The strength of the flowsheet app is the reactor block, which incorporate molecular-level kinetics from KME. The advantage this application has over traditional KME is primarily in the ability to split streams and perform reactor bypasses. This is shown in the diagram in Figure 7.15. The Sep1 block is a basic splitter that was added to allow for bypass streams. Finally, heaters were added for reactor models, such as naphtha reforming, where energy balances play a key role in cost analyses.

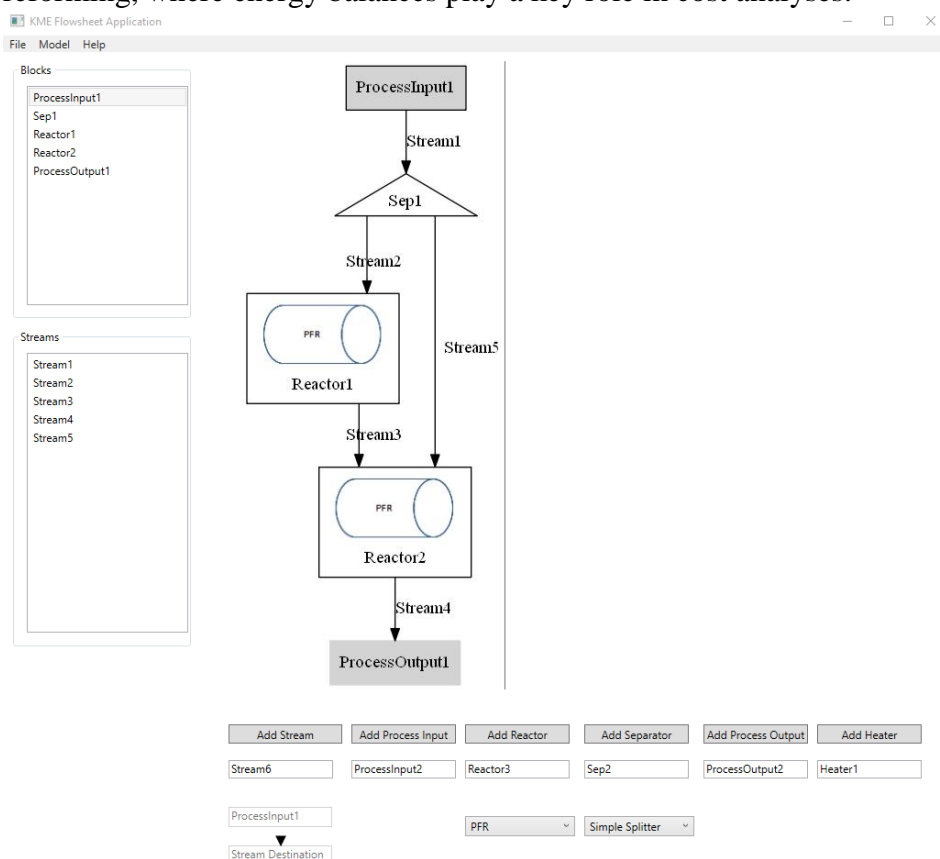


Figure 7.15: Sample screenshot from the KME Flowsheet Application. The flowsheet layout images in the KME Flowsheet Application are rendered using the open-source GraphViz software[132].

A full list of block types and descriptions are given in Table 7.8. Three reactors were included in the flowsheet: PFR, CSTR, and CCR. Of these reactors, CCR requires further explanation. In CCR, there is cross-directional flow of the catalyst and reactant stream. The catalyst flow is much slower than the reactant flow, and therefore the solution is treated as a set of separable ordinary differential equations within KME. In the future, as KME is updated to include more reactor types, the flowsheet will also be updated to include these reactors. For separation, there are three included separators. The simple splitter effectively splits the entire stream evenly; the mole fractions and species within product streams are the same as the inlet stream. The specific splitter allows for the split of each molecular species to be uniquely specified. Finally, the flash allows for a basic temperature-based split, without vapor-liquid equilibrium (VLE) calculations. The final unit is a heater that calculates heat duty for a given outlet stream temperature.

Table 7.8: Block Types and Descriptions included in KME Flowsheet Application.

Block Type	Description
Reactor	Block housing a kinetic model from KME
PFR	Plug-flow reactor
CSTR	Continuously stirred tank reactor
CCR	Continuous Catalytic Reformer
Separator	Block allowing for stream separation
Simple Splitter	Split entire stream on a molar basis, with split governed by a single parameter
Specific Splitter	User-defined molar separation for every species, with n -parameters for n species
Flash	Split based on boiling temperature assuming perfect split with no VLE calculations performed
Heater	Calculate heat required for stream temperature change using a molar-averaged heat capacity of all species in the stream

Solution of a KME Flowsheet Application follows a sequential order. The solution rank is determined automatically by representing the flowsheet as a mathematical graph. Each block is given a solution rank based on its proximity to a process input. For instance, the example flowsheet from Figure 7.15 has solution orders listed in Figure 7.16. If there are loops (*i.e.*, recycle streams), then the current version of this app does not allow for solution. The inclusion of recycles requires iterative solutions and will be included in future versions of this app.

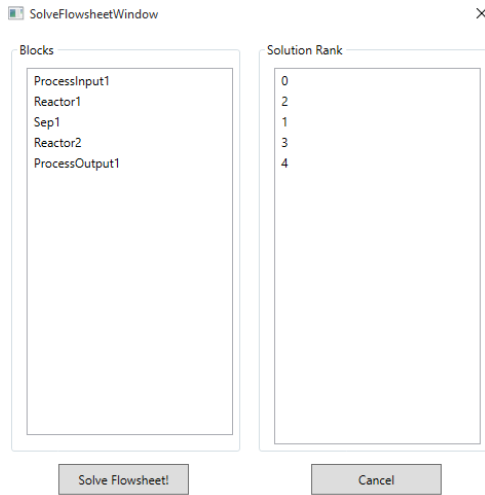


Figure 7.16: Solution order of blocks in the example flowsheet.

7.3.2 TGA Simulator

Thermogravimetric analysis (TGA) is a common lab-scale experiment found in the literature[58], [60], [63], [77], [94], [133]. The technique is ubiquitous and has been applied to feedstocks ranging from biomass to coal to plastics. As shown in Figure 7.17, TGA is a technique where a given mass of a compound, such as coal or biomass, is heated at a constant rate and the mass loss is measured. The vapor phase is either continually vented or quantified using a gas chromatograph. Mass loss occurs from two sources: first, as temperature increases, increasingly heavier components boil and enter the vapor phase; second, pyrolytic and gasification (if air inlet) reactions break down large molecules into lighter molecules with lower boiling points.

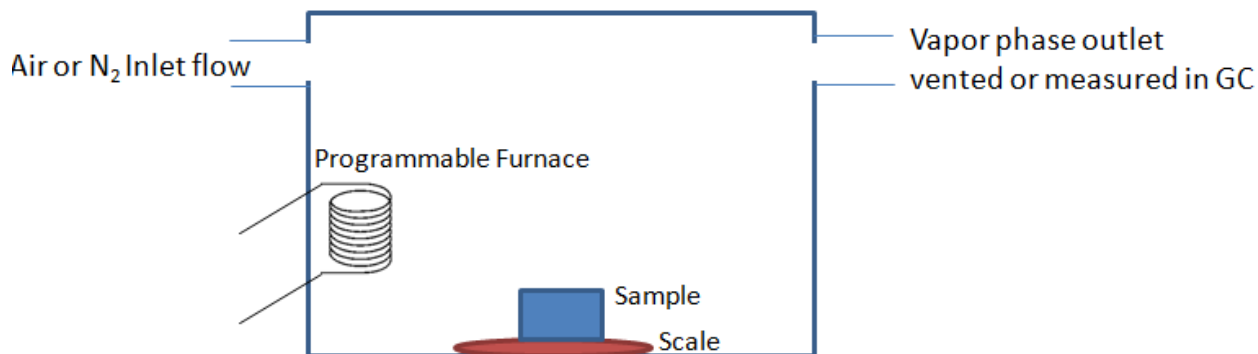


Figure 7.17: Conceptual Diagram of a Thermogravimetric Analysis experiment.

Screenshots from the app are shown in Figure 7.18. The app allows the user to select a KME model, load in experimental data, input calculation settings, and visualize model-experiment comparison of results. The logic of running the KME model is given in Figure 7.19. The simulation begins with the starting temperature from the ‘Settings’ page. It then runs an isothermal batch reactor for a short time period, based on both the heating rate and KME step size. For example, if the heating rate is 30 °C/minute and the KME step size is 1 °C then each isothermal run is 2 seconds long. The output from this simulation is then fed to the next isothermal batch simulation where the temperature is increased by 1 °C. The process continues until the final experimental temperature is reached. At each time (or temperature) step, the vapor and liquid fractions are calculated for comparison with experiments. There are two techniques for calculating the phase of each species shown in Figure 7.20. The most basic technique is to assume the species boils at exactly the boiling point in a step-wise fashion. A slightly more complex technique assumes a logarithmic based method as described by Hou[43].

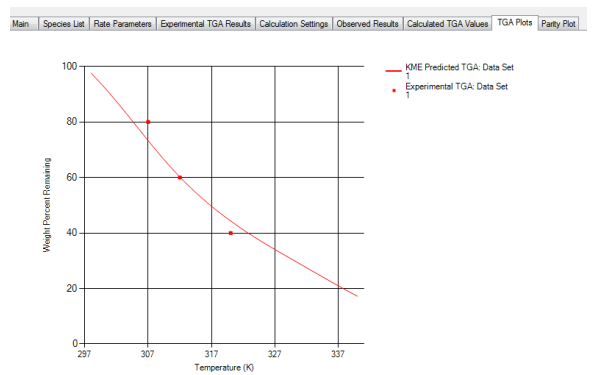
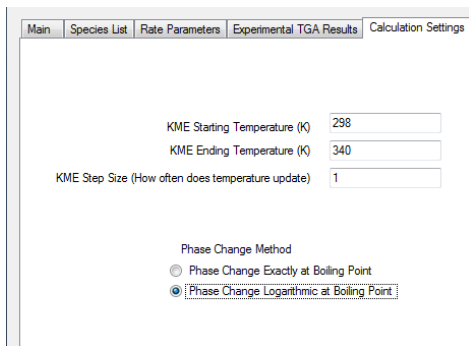
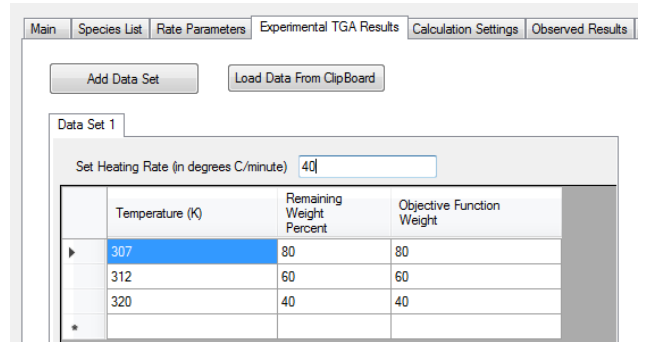
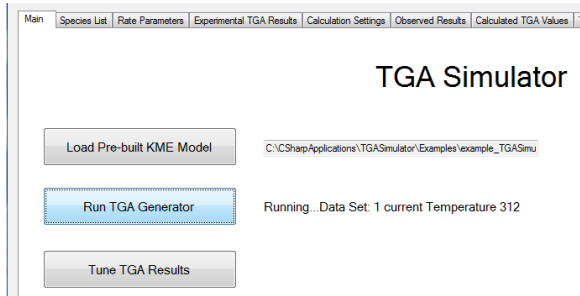


Figure 7.18: Selected screenshots from TGA Simulator. Upper Left: opening screen where user can select the KME model. Upper right: Experimental data Input. Lower Left: simulation settings. Lower right: results and comparison with experiments.

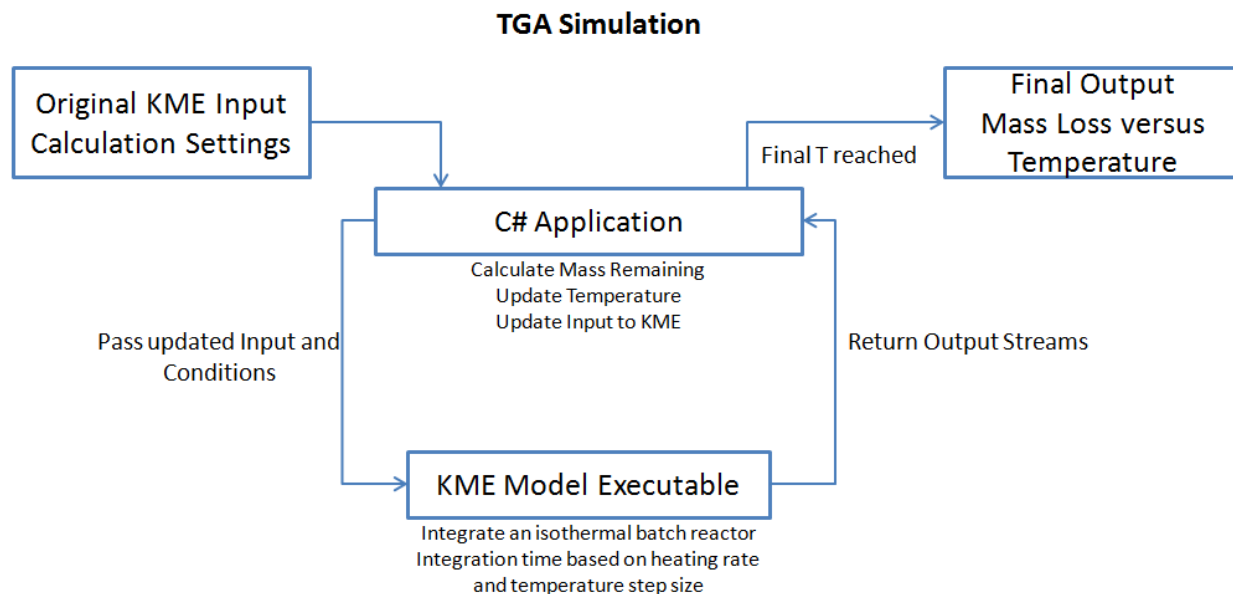


Figure 7.19: TGA Simulator Logic. Image from source [54].

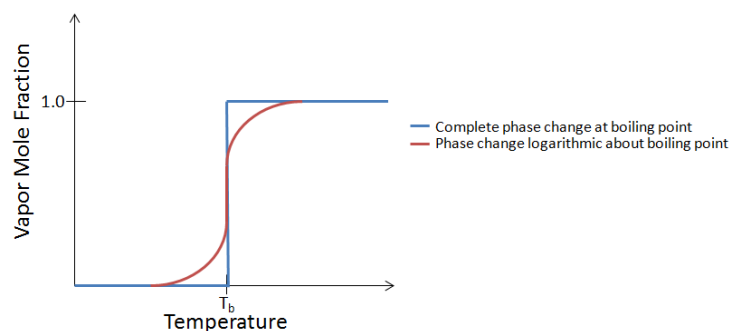


Figure 7.20: Boiling point options in TGA Simulator

7.3.3 Physical Property Database Interface

Physical properties are an integral part to kinetic modeling. Properties play a role in comparison with experimental data, rate constants, equilibrium constants, VLE calculations, and linear free energy relationships (LFERs). For example, the LFER

relationships used for reaction families require ΔH_f . Since the formation energies are temperature-dependent, heat capacity parameters are required for any temperature deviations. Finally, any bulk property requires property values for the individual species. For example, if the bulk property is a boiling point distribution, then the boiling points of each species are required.

Some of these properties, such as molecular weight, are known exactly based on the molecular structure. Others, such as heat capacity, density, or heats of formation must either be measured or approximated. Ideally, all molecular properties would come directly from experiments. Realistically, the properties of many species have not yet been measured. Even if measurements do exist, finding properties for every species every time a model is made can be an onerous task. In lieu of experimental data, group-contribution methods can be used to approximate properties.

Group contribution methods assume that a molecule's properties can be predicted based on the groups that compose the molecule. One of the oldest and still most commonly used group-contribution method was developed by Benson[134]. Benson's theory divides a molecule into groups, with one group per non-hydrogen atom. For example, ethane would have two groups (both CH_3) and propane would have three (two CH_3 groups and one CH_2 group). The groups' properties are a function of the neighboring atoms; a CH_3 group bound to an oxygen atom would have a different set of properties than if it were bound to a carbon atom. Applying this concept to ethane, the molecule contains two $\text{CH}_3\text{-C}$ groups. The groups of some common molecules are shown in Table 7.9. Properties are calculated as a function of these groups. For example, the heat of formation of a molecule is calculated using Equation 7.4.

$$\Delta H_f = \sum_{i, \text{groups}} n_i * \Delta H_i \quad (7.4)$$

where n_i is the number of group i within a molecule

Table 7.9: Some common molecules divided into Benson Groups and predicted heats of formation versus the values found in the NIST database.

Molecule	Structure	Groups	Predicted Heat of Formation (kJ/mol)	Heat of formation from NIST (kJ/mol)
Ethane		2 CH ₃ -C	-84.38	-84. ± 0.4
Propane		2 CH ₃ -C, 1 CH ₂ -2C	-105.32	-104.7 ± 0.50
Methanol		1 CH ₃ -C, 1 OH-C	-200.75	-205 ± 10
Ethanol		1CH ₃ -C, 1 CH ₂ -C, O, 1 OH-C	-234.66	-232± 2

The validity of a given group contribution method is often dependent on molecule type and size. For instance, another system of grouping, Gani groups, predict polycyclic aromatics acceptably well; however, they are not useful for predicting properties of small molecules or biomolecules. Benson's model, on the other hand, predicts properties of small molecules and biomolecules relatively well but falls short on predictions of more complex molecules. Within KMT, group-contribution methods are employed by the program PropGen (a component within CME). PropGen makes use of a combination of these methods to make the best possible property predictions.

Ultimately, any group contribution method is still a model of the properties; experimental data is preferred in cases where it exists.

Table 7.10: Order of preference for sources of molecular properties.

Order of Preference for Molecular Properties	Relevant Molecules
Experimental measurements	Any experimental properties available should be used; however, they are likely only available for small molecules
Group Contribution Methods	
Benson	Benson Groups are useful for small molecules that do not have experimental data, and they are also useful for biomolecules
Gani	Gani Groups are most useful for larger molecules such as polycyclic aromatic hydrocarbons (PAHs)

For some molecules, experimental measurements are available in the open literature. This is especially true for low-molecular weight molecules. Furthermore, these small molecules are common to many different process chemistries. Often in model building, there is the necessary tedium of looking up experimental properties and correcting the group contribution approximations. This process is both error-prone and repetitive. The best way to address this issue is a physical property database.

An app titled the Physical Property Database Interface, shown in Figure 7.21, was developed and utilized to build a database that currently contains ~10,000 molecules with 70 properties per molecule. When molecules are added to the database,

the initial property predictions are from group contribution using PropGen. The app allows for easy addition of literature values for a given molecule.

The screenshot shows the 'Property Database Interface' window. It features a menu bar with 'File' and 'Edit'. Below the menu is a search bar and a dropdown menu for 'Any Search Field'. The main area is divided into two panes. The left pane displays a table with columns 'IUPACName' and 'StringCode'. The right pane displays a table with columns 'property', 'value', 'source', and 'units'. A chemical structure of p-xylene is shown in the top right corner.

IUPACName	StringCode
benzene	C(H)C(H)C(H)C(H)C(H)C(H)
m-xylene	C(C(H3))C(H)C(C(H3))C(H)C(H)C(H)
o-xylene	C(C(H3))C(C(H3))C(H)C(H)C(H)C(H)
p-xylene	C(C(H3))C(H)C(H)C(C(H3))C(H)C(H)
hydrogen	(H2)
1,1,4-trimethylcyclohexane	C(C(H3)C(H3))C(H2)C(H2)C(C(H3))H)C(H)
1,3,5-trimethylcyclohexane	C(C(H3)H)C(H2)C(C(H3)H)C(H2)C(C(H3)H)
cyclohexane	C(H2)C(H2)C(H2)C(H2)C(H2)C(H2)
cyclopentane	C(H2)C(H2)C(H2)C(H2)C(H2)
methylcyclopentane	C(C(H2)C(H2)C(H2)C(H2)C(H3)H)
2,3-dihydro-1H-indene	CC(H)C(H)C(H)C(H)C(C(H2)C(H2)C(H2))
decane	C(C)C(C)C(C)C(H2)C(H2)C(H2)C(C)C(C)C(C)C
heptane	C(C)C(C)C(H3)H2)C(C)C(C)C(H3)H2)H2)
hexane	C(C)C(H3)H2)C(C)C(C)C(H3)H2)H2)
nonane	C(C)C(C)C(C)C(H3)H2)H2)C(C)C(C)C(H3)H2)
octane	C(C)C(C)C(H3)H2)H2)C(C)C(C)C(H3)H2)H
undecane	C(C)C(C)C(C)C(H3)H2)H2)C(C)C(C)C(C)C(C)C
1,1-diethylcyclopropane	C(C)C(C)C(H3)H2)C(C)C(H3)H2)C(H2)C(H2))
1,2-diethylcyclobutane	C(C)C(C)C(H3)H2)C(C)C(C)C(H3)H2)C(H2)C(C)
1,2-dimethylcyclooctane	C(C)C(H3)H)C(C)C(H3)H)C(H2)C(H2)C(H2)C(C)
1-methyl-2-methylenecyclopentane	C(C)C(H2)C(C)C(H3)H)C(H2)C(H2)C(H2)
(Z)-1-methylcyclooct-1-ene	C(C)C(H)C(H2)C(H2)C(H2)C(H2)C(H2)C(H2)C(H2)
1-methylcyclopent-1-ene	C(C)C(H)C(H2)C(H2)C(H2)C(H3))
2-ethylthiophene	C(C)C(H)C(H)C(H)S)C(C)C(H3)H2)
3-methylthiophene	C(C)C(H)C(H)S)C(H)C(H3))
4-ethylcyclohex-1-ene	C(C)C(H2)C(H)C(H)C(H2)C(H2)H)C(C)C(H3)H
5-methylundecane	C(C)C(C)C(C)C(H3)H2)H2)C(H3)H)C(C)C(C)C
isopropylcyclobutane	C(C)C(H2)C(H2)C(H2)C(H2)C(H3)C(H3)H)
methylcycloheptane	C(C)C(H2)C(H2)C(H2)C(H2)C(H2)C(H2)C(H)
methylenecyclohexane	C(C)C(H2)C(H2)C(H2)C(H2)C(H2)C(H2))
1-methyl-2-propylcyclohexane	C(C)C(H3)H)C(H2)C(H2)C(H2)C(H2)H)C(C)

property	value	source	units
Tc	611.054756	Group Contribution	K
Pc	33.893294	Group Contribution	bar
Vc	399.1506	Group Contribution	cm ³ /mol
Tb	415.903642	Group Contribution	K
Tm	206.772417	Group Contribution	K
Hform	15.5807	Group Contribution	kcal/mol
Gform	112.5651	Group Contribution	kcal/mol
CPa	-23.99	Group Contribution	Cal/mol/K
CPb	0.62544	Group Contribution	Cal/mol/K ²
CPc	-0.000376	Group Contribution	Cal/mol/K ³
CPd	0	Group Contribution	Cal/mol/K ⁴
Hfusion	-0.5775	Group Contribution	kcal/mol
Hvap	39.8932	Group Contribution	kcal/mol
LogKw	2.2747	Group Contribution	Unitless
Fp	299.4603	Group Contribution	K
Hvp	33.8065	Group Contribution	kJ/mol
Svp	83.064	Group Contribution	Cal/mol/K
SigmaD	18.5739	Group Contribution	Mpa ^{1/2}
SigmaP	0.8383	Group Contribution	Mpa ^{1/2}
SigmaH	2.7202	Group Contribution	Mpa ^{1/2}
Sigma	19.7694	Group Contribution	Mpa ^{1/2}
Omega	0.345003	Group Contribution	Unitless
Vm	0.1224	Group Contribution	cm ³ /kmol
Vica	0	Group Contribution	Unitless

Figure 7.21: Screenshot of Physical Property Database Interface.

The underlying database uses SQLite allowing for portability and local storage. SQLite is a database management system (DBMS) that utilizes a relational model of data. Benefits of using a DBMS instead of simpler storage systems such as Excel or text files include search speed and the ability to perform easy queries to return data of interest. In the physical property database, tables include molecule names, physical properties, units, property methods, and property values. As a result of these design decisions, searching the database, changing properties, adding new properties, and adding new molecules occurs in real time.

The database interface allows for the export of properties for a selected list of molecules, as shown in Figure 7.22. The user can search the full database based on molecule name or property information. When properties are exported, the user can select which property to export, however, by default, literature values are preferred over group contribution.

Select Molecule List

isSelected	IUPACName	isSelected	
<input checked="" type="checkbox"/>	benzene	<input checked="" type="checkbox"/>	C(H)C(H)C(H)C(H)C(H)C(H)
<input checked="" type="checkbox"/>	m-xylene	<input checked="" type="checkbox"/>	C(C(H3))C(C(H3))C(H)C(H)C(H)C(H)
<input checked="" type="checkbox"/>	o-xylene	<input checked="" type="checkbox"/>	C(C(H3))C(H)C(H)C(C(H3))C(H)C(H)
<input checked="" type="checkbox"/>	p-xylene	<input checked="" type="checkbox"/>	CC(H)C(H)C(H)C(H)CC(H2)C(H2)C(H2)
<input checked="" type="checkbox"/>	2,3-dihydro-1H-indene	<input checked="" type="checkbox"/>	C(C(H)C(H)SC(H)C(H3))
<input type="checkbox"/>	2-ethylthiophene	<input checked="" type="checkbox"/>	C(C(C(H3))C(H)C(H)C(H)C(H))C(C(C(H3)H2)H2)
<input checked="" type="checkbox"/>	3-methylthiophene	<input checked="" type="checkbox"/>	C(C(C(H3)H2))C(C(C(H3)H2))C(H)C(H)C(H)C(H)
<input type="checkbox"/>	mesitylene	<input checked="" type="checkbox"/>	C(C(C(H)C(H)C(H)C(H)C(H)C(H)H2)C(C(H3)H2)H2)
<input checked="" type="checkbox"/>	1-methyl-2-propylbenzene	<input checked="" type="checkbox"/>	C(C(H)C(H)C(H)C(H)C(H)C(H3))
<input checked="" type="checkbox"/>	1,2-diethylbenzene	<input checked="" type="checkbox"/>	C(C(C(H)C(H)C(H)C(H)C(H)C(H))C(C(H3)H2)H2)
<input type="checkbox"/>	1-ethyl-2-methylbenzene	<input checked="" type="checkbox"/>	C(C(H)C(H)C(H)C(H)C(H)C(H))C(C(H3)H2)
<input checked="" type="checkbox"/>	butylbenzene	<input checked="" type="checkbox"/>	C(C(C(C(H)C(H)C(H)C(H)C(H)C(H)H2)C(C(H3)H2)H2)H2)H2)
<input checked="" type="checkbox"/>	toluene	<input checked="" type="checkbox"/>	C(C(C(H3))C(H)C(H)C(H)C(H)C(H))C(C(C(H3)H2)H2)H2)

Molecule Name Any Search Field

advanced search by property toggle select all

select from ingen model

property	LB	isSelected	property	value	source
TotalCarbonNum		<input checked="" type="checkbox"/>	Tc	638.354892	Group Contribution
AromCNum		<input checked="" type="checkbox"/>	Pc	37.782282	Group Contribution
NaphCNum		<input checked="" type="checkbox"/>	Vc	379.8818	Group Contribution
AromRingNum	1	<input checked="" type="checkbox"/>	Tb	416.589948	Group Contribution
NaphRingNum		<input checked="" type="checkbox"/>	Tm	217.39198	Group Contribution
MW		<input checked="" type="checkbox"/>	Hform	27.9796	Group Contribution
Density		<input checked="" type="checkbox"/>	Gform	128.153	Group Contribution

export molecule properties export in kme order



Figure 7.22: Export molecule list window in the Physical Property Database Interface. The left side shows a search of the database for all species with 1 or more aromatic ring. The right side gives the current list of selected molecules and details on which properties are being exported.

7.4 Current and Future App Development

A key benefit to the app-based style of software design is that development is quick and ongoing. Unlike with major software packages, the timeframe between idea conception and availability of a usable tool is much shorter. This section details the Data Audit Application, a project currently still in the conception stage. A second advantage of app development is the ease of version updates. Currently, many of the apps are going through a general UI update. Over the last two years of developing apps, the quality of the user interfaces has improved drastically.

7.4.1 Data Audit Application

In the future, the idea of a ‘data audit’ will be explored. As a modeler, the default is to trust experimental data and, instead, question the correctness of the model if model and experiment do not agree. The typical course of action is to then go back to tuning the kinetic model or explore the reaction network to understand if any process chemistry is missing from the model. The idea of the data audit is to perform a heuristic to analyze the experimental data. There are two tiers currently being considered: analyzing the data alone, and analyzing the data and reaction network simultaneously.

The first tier heuristic is to analyze the consistency of experimental data with itself. Basic examples of this are mass balances: *i.e.*, do the measured weight fractions sum to 1.0? This type of analysis catches many types of human errors such as erroneous entry of data. Comparing experimental data on the input and output can provide more useful information. This is most useful if there are molecular measurements on both streams. In this case, a carbon balance can be calculated using

Equation 7.5. If the carbon balance is nonzero, then no amount of tuning of model parameters will return perfect results.

$$\begin{aligned}
 \text{Carbon Balance} & & (7.5) \\
 &= \sum_{i=0}^{\text{numInputs}} (C_{\#,i} * \text{molarFlow}_i) \\
 &- \sum_{j=0}^{\text{numObs}} (C_{\#,j} * \text{molarFlow}_j)
 \end{aligned}$$

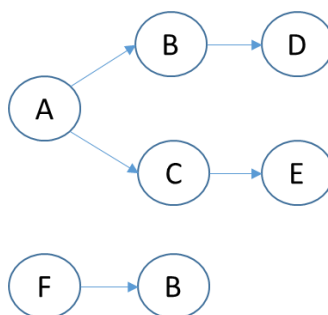


Figure 7.23: Basic reaction network layout for heuristic example.

Table 7.11: Inputs, observed quantities, minimum and possible values at reactor outlet, and whether a heuristic returns a red flag.

Species	Input (Mol/s)	Observed (Mol/s)	Min, Max	Red Flag from Heuristic
A	1	0	0, 1	N
F	2	0	0, 2	N
B	0	2	0, 3	N
E	0	2	0, 1	Y

A second tier heuristic is to analyze both the data and reaction network. The major question asked by this heuristic is: can the data be predicted given the structure of the reaction network? A simple, conceptual example is shown below in Figure 7.8

and Table 7.11. Based on the input of A and F into the network, the maximum production of B is 3 Mol/s if all of both A and F react to B . In this example, the observed amount of B is 2 Mol/s, which is less than the maximum, and the heuristic does not flag the measurement. For E , the observed value is 2 Mol/s and the maximum possible production is 1 Mol/s based on the structure of the reaction network. The heuristic returns a flag, which means that either the data or the reaction network needs to be edited. No amount of kinetic parameter tuning will ever produce the observed value of E .

7.4.2 Update of User Interfaces

Currently, many of the older apps are going through an update of their user interfaces. Specifically, app development has switched from Windows Forms Applications to the more modern Windows Presentation Foundation (WPF). From the point of view of app development, the main advantage of WPF is ability of elements (*e.g.*, menus) to be easily replicated across applications. The built-in objects in WPF are also much more visually appealing.

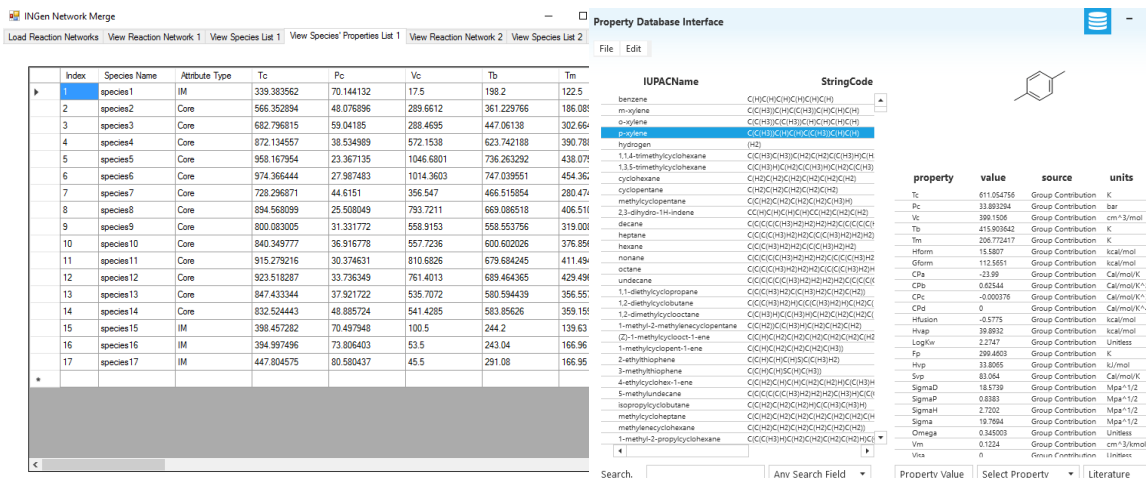


Figure 7.24: Comparison of user interfaces in Windows Forms Applications (Left, App: INGen Network Merge) and Windows Presentation Foundation (WPF, Physical Properties Database Interface).

7.5 Summary

In summary, software development in KMT has shifted toward lightweight software apps. These apps target the objectives of the kinetic model's users. The first category of apps aimed at elucidating the detailed results from kinetic models to help improve model comprehension. These apps included the visualization of reaction networks and the visualization of reactor profile data. The second category of apps focused on measured inputs and outputs to the process. These apps are tailored to individual processes and collaborators. Most importantly, by focusing on inputs and outputs, the learning curve to using KMT is minimized. The final group of apps focuses on enhancing the capabilities of KMT. These apps are wide-ranging and include flowsheeting, simulating TGA, and an interface to a physical properties database. As a developer, the apps of KMT are inherently rewarding as they target the needs of specific users. All apps are currently in use by either researchers or industrial collaborators.

Chapter 8

SUMMARY AND CONCLUSIONS

8.1 Summary and Conclusions

In summary, this dissertation presented two orthogonal goals: the development of kinetic models and the development of model building tools. A model for the gasification of MSW was generated and solved using the in-house KMT software. This was accomplished in three phases. In the first two phases, gasification models for biomass and plastics were developed, independently, and optimized using literature data. These models were merged to form a gasification reaction model for MSW. This model, combined with a coke gasification reaction model, provided the basis for a reactor model of a plasma-arc gasifier. The reactor model represented the gasifier using four beds, corresponding to different zones in the overall gasification unit.

The plasma-arc gasifier reactor model was utilized for trending studies and helped to understand the effects of the extreme temperatures in the combustion zone of the reactor, the impact of MSW composition, and the effects of changing the oxygen flow rates, or the equivalence ratio. The extreme temperatures of the combustion zone were found to potentially increase tar production and reduce syngas quality due to a localized conversion of CO to CO₂. Realistic variations of MSW composition was found to have a minor impact on syngas quality, provided that equivalence ratio remained constant. The effects on tar composition were more pronounced, with higher

biomass fractions leading to increased production of oxygenated aromatics, and higher plastics fractions leading to increased production of benzene and naphthalene. Finally, increasing oxygen flow rate to the bed decreased both tar flow rate and syngas quality. This provides room for optimization by process engineers to maximize syngas quality while keeping tar formation within the design specifications for downstream operations.

In the process of modeling MSW gasification, modeling strategies were developed for both linear and cross-linked polymers. These strategies extend to other feedstocks such as additional plastics and entirely different complex feedstocks. For instance, the same modeling strategies utilized for lignin were applied to the pyrolysis of heavy oil. Going forward, the study of additional plastics and other, more complex feedstocks such as coal will be expedited due to the development of modeling strategies in this dissertation.

While building the models for MSW gasification and resid pyrolysis, software ‘apps’ were developed to aid in future model development. A key aim of software development was to target the user-model interface. Specifically, there are three groups of users: model developers, research collaborators, and process engineers; each group has their own goals while using the model. Process engineers are most interested in the ability of the model to predict measurable outputs from measurable inputs. The perfect tool for a process engineer is just that: an I/O converter. In addition to the measurable I/O, research collaborators care about the scientific and mathematical understanding of the model. These users wish to understand the process chemistry to improve results in the long run. Model developers share these aims with the research collaborators; however, they are also interested in the future development

of models. Apps that are exclusive to model developers add features to KMT to aid in future projects.

8.2 Recommendations for Future Work

8.2.1 MSW Composition

The composition of MSW is one major area for future research in both the composition of individual polymers and the overall composition of waste. For the composition of linear polymers, there are two potential areas of future work. First, the assumptions of this model led to deviations between measured and modeled ultimate analyses for some polymers. Second, real MSW contains more than a single sample of each polymer. For the overall composition of waste, the suggested focus area for research is a method of quantification of polymer fractions in daily gasifier operation.

8.2.1.1 Individual Polymer Composition

In the modeling of the composition of linear polymers, the data utilized were from ultimate analyses. To utilize this limited data, two constraints were imposed in the composition model. First, the linear polymers were assumed to have known and constant repeat unit structure. Second, the polymer size distribution was assumed to follow an idealized distribution, *e.g.*, a Flory distribution[61]. Although these assumptions worked well for some polymers, others—such as PVC—showed deviations when compared with experimental ultimate analysis. A preliminary analysis of these deviations is given in the following text; however, this is suggested as an area for future consideration.

The comparison of the PVC composition model with literature experimental results is given in Table 8.1. The deviations are seen in the relative amounts of carbon

and chlorine in the polymer sample. For PVC, a Flory distribution was assumed to model the polymer size distribution. If this assumption is relaxed, one can imagine two extremes: all monomers or an infinite polymer. In either of these scenarios, the amount of carbon is still below that of the experimental value. Therefore, polymer size distribution alone cannot explain this discrepancy.

The second possible reason for deviation between experiments and model predictions is the assumption of a constant repeat unit in the polymer sample. This assumption is a bit more interesting. First, real PVC waste can contain many plasticizers. However, these plasticizers typically originate from phthalates, which contain oxygen. The absence of oxygen from the ultimate analysis excludes plasticizers from consideration. However, it is also known that the first step of depolymerization is fast in PVC, forming a polyene structure with C_2H_2 repeat unit. If the polymer backbone is assumed to be a mixture of polyene and PVC repeat units, then the predicted and experimental analyses are significantly closer.

Table 8.1: Experimental[64] and predicted ultimate analyses for PVC. Also given are the ultimate analyses if the for a monomer and infinite polymer, and pure polyene structure. The partially depolymerized polymer was 93.6% PVC repeat units with 6.4% polyene repeat units.

Element	Polyvinyl Chloride					
	Experimental	Predicted	Monomer	Infinite Polymer	Polyene	Partial Depoly.
C	41.55	38.1	37.2	38.4	92.3	41.55
H	4.81	5.44	7.8	4.81	7.6	5.57
O	0.00	0.00	0.00	0.00	0.00	0.00
Cl	52.95	56.38	55.0	56.8	0.00	52.78

The only significant change to model results is the amount of HCl produced by depolymerization. In the original model, depolymerization would convert

approximately 56 weight percent of the polymer to HCl; in contrast, the updated composition would only convert 53 weight percent to HCl. The partial depolymerization hypothesis did correct the modeled composition to match experimental results; however future work is needed to verify the results.

Real MSW is inherently complex with multiple sources of each polymer. For instance, there are many types of polyethylenes, including high-density polyethylene and low-density polyethylene. In the model presented in this dissertation, each polymer fraction was optimized using a single ultimate analysis. An area for future work in MSW composition is in relaxing these assumptions.

One possible route forward is an extensive analysis of common polymer types, polymer size distributions, and the effects on the output from a kinetic model. In order to pursue this method, detailed input and output data are required for each polymer in question. For the inlet, polymer size distributions can be obtained from Gel Permeation Chromatography[66]. This information can be paired with detailed gas chromatography results to study the effect of polymer type (*e.g.*, HDPE) for each polymer on the reaction kinetics. Ultimately, this methodology would allow the model to take into account a combination of polymers and polymer types. To utilize this level of detail in a gasifier, additional work is required in modeling the combined composition of MSW.

8.2.1.2 Combined Composition of MSW

Currently, the composition of the polymeric fractions of MSW is based on an ultimate analysis, potentially taken daily, during gasifier operation. In this model, MSW is represented using four plastics and three biopolymers, and an ultimate analysis likely contains only four usable data points (C, H, O, and Cl). Optimization is

therefore under-constrained, and there are infinite solutions for any ultimate analysis. In current simulations, known samples of MSW (such as the US average distribution) are utilized; however, in gasifier operation, these values—while representative—will not be exactly correct.

A potential route for future research lies in relaxing the assumption that the only available data are from ultimate analyses. This could be done at the plant operation level, *i.e.*, a method of efficiently quantifying polymeric fractions of waste. A second option would be to perform a study of the average MSW composition over time for a given MSW gasifier. This would inform the quantification of individual MSW fractions beyond that of an ultimate analysis.

8.2.2 Parameter Tuning and Confidence Intervals

In this dissertation, the final set of parameters for the MSW gasification model was based on literature studies on plastics and biomass. In the future, with the availability of plant data, we hope to assess the validity of our current parameter values in a commercial scale gasifier. If intrinsic values of kinetic parameters were obtained in literature studies, then the model results should match the full gasifier. Issues could arise as the temperatures of the plasma gasifier are much more extreme than the literature studies utilized for parameter tuning. Also, the plant is at a large scale of 1,000 metric tons/day. If there are mass or heat transfer limitations, there is opportunity for future model development and parameter tuning.

The parameters in a kinetic model can be assessed using statistics. For example, using the seven data sets in the biomass gasification study, confidence intervals can be calculated for the tuned parameters. Specifically, we have predicted 95% confidence intervals using methodology described in prior work by Hou[43]. The

relative confidence intervals on the pre-exponential, or A, factors are given in Figure 8.1. The confidence intervals were smallest on depolymerization and gasification chemistries. The A-factors were less certain on cracking and dehydrogenation; at the reactor conditions, these reaction families are relatively fast and small changes do not appear in the objective function. In contrast, the objective function was insensitive to the dry reforming of methane because the reaction rate is too slow. In this case, minor increases in the A-factor do not increase the rate enough to impact the objective function. In the future, with the availability of data for MSW gasification we can extend this methodology to the reactor model of the plasma-arc gasifier.

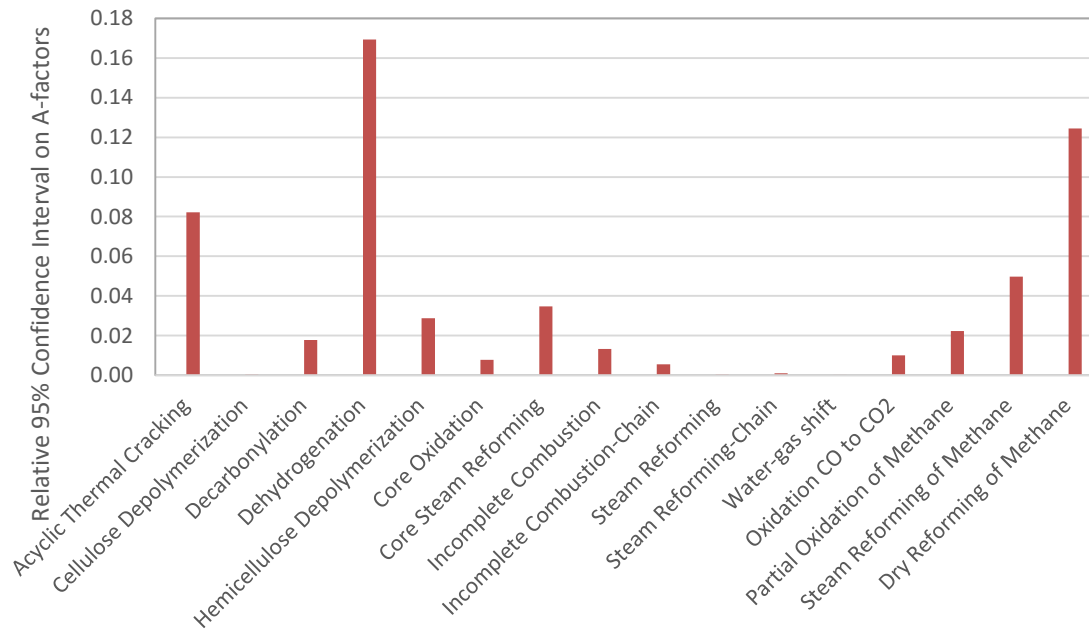


Figure 8.1: 95% confidence intervals on A-factors relative to the value of the A-factor. For instance, the confidence interval is $\pm 0.169 * \log A$ for dehydrogenation.

8.2.3 Optimizing Experimental Data for Molecular Models

The current limits to molecular-level modeling of MSW gasification are imposed, not by the modeling methods or computational power, but by the experimental information available in gasification literature. In order to enable the use of molecular models, future gasification literature should focus on molecular detail of both the reactor inlet and reactor outlet. For the reactor inlet, currently ultimate analyses are the most common characterization. For the reactor outlet, the common results are tar weight fraction and molecular predictions from gas chromatography on the most common species (CO, CO₂, H₂, and CH₄). On both the inlet and outlet, this status quo lacks molecular detail. This is not necessarily due to a lack of experimental techniques; a full spectrum of advanced experiments is seen in the literature on refinery reactors. These experiments have aided in the development of detailed kinetic models on a wide range of boiling point ranges from naphtha[135]–[140] to vacuum gas oil[141] to vacuum resid[46], [48], [127]–[130].

In naphtha reforming, molecular models are enabled through extensive molecular detail on both the input and output. For instance, standard measurements include simulated distillation, density, and carbon number PIONA. Advanced measurements such as GCxGC can give many isomers of species with up to 14 carbons[142], [143]. These measurements enable molecular models by allowing for mechanism discrimination and accurate kinetic parameter tuning.

The most complex refinery units also utilize advanced experiments to enable molecular modeling. For example, in heavy oil coker, FTICR-MS (Fourier Transform Ion Cyclotron Resonance-Mass Spectrometry) is utilized to elucidate the molecular identities of up to 50,000 unique species[46],[124]. These measurements can be utilized in molecular models as shown in Figure 8.2[46]. The degree of complexity in

heavy oil is on the same order of magnitude as MSW. This gives cause for optimism for the future pairing of detailed experiments and detailed kinetic models.

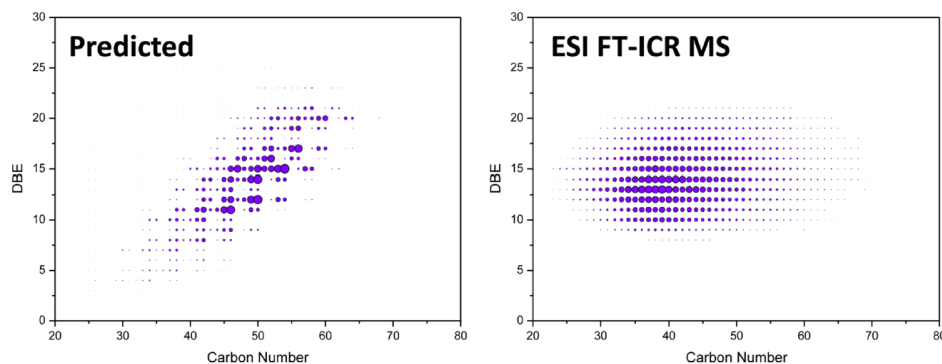


Figure 8.2: Comparison of DBE versus Carbon Number for single pyrrolic ring structures for experimental(right) and predicted (left) results. Figure taken directly from source and was Figure 15 in the source material.[46]

8.3 Closing Remarks on MSW Gasification

Currently, much of the waste in the United States is discarded in landfills. MSW is a valuable energy resource that is one of the low-hanging fruits in the energy market, and is able to provide a significant amount of cheap energy with little research and development. In order to pursue this source of energy, there are a number of useful Waste-to-Energy (WTE) technologies. This dissertation focused on gasification of waste, and culminated in a reactor model for the most environmentally friendly WTE option: plasma-arc gasification. In building this model, it was shown that the process could be modeled at the molecular-level. This model is based on fundamental process chemistry and can account for changes in process conditions and MSW composition. Gasification and other WTE technologies have been, and will continue to be, a future topic of research. Undoubtedly, detailed kinetic models will play a central role in the future conversion of waste to energy.

REFERENCES

- [1] EPA, “Advancing Sustainable Materials Management: Facts and Figures 2013,” 2015.
- [2] B. W. Mosher, P. M. Czepiel, R. C. Harriss, J. H. Shorter, C. E. Kolb, J. B. McManus, E. Allwine, and B. K. Lamb, “Methane Emissions at Nine Landfill Sites in the Northeastern United States,” *Environ. Sci. Technol.*, vol. 33, no. 12, pp. 2088–2094, Jun. 1999.
- [3] EPA, “LFG Energy Project Development Handbook,” 2015.
- [4] E. Braw, “Dirty power: Sweden wants your garbage for energy,” *Aljazeera America*, 2015.
- [5] Department for Environmental and Rural Affairs, “Incineration of Municipal Solid Waste,” 2013.
- [6] G. C. Young, *Municipal Solid Waste to Energy Conversion Processes Economic, Technical, and Renewable Comparisons*. Hoboken, NJ: John Wiley & Sons, Inc., 2010.
- [7] H. . Chagger, A. Kendall, A. McDonald, M. Pourkashanian, and A. Williams, “Formation of dioxins and other semi-volatile organic compounds in biomass combustion,” *Appl. Energy*, vol. 60, no. 2, pp. 101–114, 1998.
- [8] EPA, *Clean Air Act*. 42 U.S.C. §7401, 1990.
- [9] D. A. Bell, B. F. Towler, and M. Fan, *Coal Gasification and Its Applications*. William Andrew Applied Science Publishers, 2011.
- [10] A. Gruppig, “Coal Gasification Method,” 4,243,101, 1981.
- [11] J. L. Johnson, *Kinetics of Coal Gasification A Compilation of the Research by the late Dr. James Lee Johnson*. John Wiley & Sons, Inc., 1979.
- [12] J. Rezaiyan and N. P. Cheremisinoff, *Gasification Technologies a primer for engineers and scientists*. Taylor & Francis Group, 2005.

- [13] X. T. Li, J. R. Grace, C. J. Lim, a. P. Watkinson, H. P. Chen, and J. R. Kim, "Biomass gasification in a circulating fluidized bed," *Biomass and Bioenergy*, vol. 26, no. 2, pp. 171–193, Feb. 2004.
- [14] H. J. Huang and S. Ramaswamy, "Modeling biomass gasification using thermodynamic equilibrium approach," *Appl. Biochem. Biotechnol.*, vol. 154, no. 1–3, pp. 193–204, 2009.
- [15] Y. Wang and C. M. Kinoshita, "Kinetic model of biomass gasification," *Sol. Energy*, vol. 51, no. 1, pp. 19–25, 1993.
- [16] M. Puig-Arnavat, J. C. Bruno, and A. Coronas, "Review and analysis of biomass gasification models," *Renew. Sustain. Energy Rev.*, vol. 14, no. 9, pp. 2841–2851, Dec. 2010.
- [17] M. Ruggiero and G. Manfrida, "An equilibrium model for biomass gasification processes," *Renew. Energy*, vol. 16, no. 1–4, pp. 1106–1109, 1999.
- [18] D. C. Elliott, "Catalytic Hydrothermal Gasification of Biomass," *Biofuels, Bioprod. Biorefining*, vol. 2, pp. 254–265, 2008.
- [19] P. R. Solomon, D. G. Hamblen, R. M. Carangelo, M. A. Serio, and G. V. Deshpande, "General Model of Coal Devolatilization," vol. 24, no. 3, pp. 405–422, 1988.
- [20] H. Wang, B. Z. Dlugogorski, and E. M. Kennedy, "Coal oxidation at low temperatures: oxygen consumption, oxidation products, reaction mechanism and kinetic modelling," *Prog. Energy Combust. Sci.*, vol. 29, no. 6, pp. 487–513, Jan. 2003.
- [21] U. Arena, "Process and technological aspects of municipal solid waste gasification. A review," *Waste Manag.*, vol. 32, no. 4, pp. 625–639, 2012.
- [22] E. Leal-Quirós, "Plasma Processing of Municipal Solid Waste," *Brazilian J. Phys.*, vol. 34, no. 4B, pp. 1587–1593, 2004.
- [23] U. Arena, L. Zaccariello, and M. L. Mastellone, "Tar removal during the fluidized bed gasification of plastic waste.," *Waste Manag.*, vol. 29, no. 2, pp. 783–91, Feb. 2009.
- [24] B. Lemmens, H. Elslander, I. Vanderreydt, K. Peys, L. Diels, M. Oosterlinck, and M. Joos, "Assessment of plasma gasification of high caloric waste streams," *Waste Manag.*, vol. 27, no. 11, pp. 1562–1569, 2007.

- [25] A. J. Griffiths, K. P. Williams, and N. Owen, "Engineering value recovery from municipal solid waste," *Proc. Inst. Mech. Eng. Part C J. Mech. Eng. Sci.*, vol. 224, no. 3, pp. 559–570, 2010.
- [26] S. Jarunthammachote and A. Dutta, "Equilibrium modeling of gasification: Gibbs free energy minimization approach and its application to spouted bed and spout-fluid bed gasifiers," *Energy Convers. Manag.*, vol. 49, no. 6, pp. 1345–1356, 2008.
- [27] S. Jarunthammachote and A. Dutta, "Thermodynamic equilibrium model and second law analysis of a downdraft waste gasifier," *Energy*, vol. 32, no. 9, pp. 1660–1669, 2007.
- [28] A. K. Sharma, "Equilibrium modeling of global reduction reactions for a downdraft (biomass) gasifier," *Energy Convers. Manag.*, vol. 49, no. 4, pp. 832–842, 2008.
- [29] H. Tang and K. Kitagawa, "Supercritical water gasification of biomass: Thermodynamic analysis with direct Gibbs free energy minimization," *Chem. Eng. J.*, vol. 106, no. 3, pp. 261–267, 2005.
- [30] Z. A. Zainal, R. Ali, C. H. Lean, and K. N. Seetharamu, "Prediction of performance of a downdraft gasifier using equilibrium modeling for different biomass materials," *Energy Convers. Manag.*, vol. 42, no. 12, pp. 1499–1515, 2001.
- [31] I. Janajreh, S. S. Raza, and A. S. Valmundsson, "Plasma gasification process: Modeling, simulation and comparison with conventional air gasification," *Energy Convers. Manag.*, vol. 65, pp. 801–809, 2013.
- [32] X. Li, J. R. Grace, A. P. Watkinson, C. J. Lim, and A. Ergudenler, "Equilibrium modeling of gasification: A free energy minimization approach and its application to a circulating fluidized bed coal gasifier," *Fuel*, vol. 80, no. 2, pp. 195–207, 2001.
- [33] A. Mountouris, E. Voutsas, and D. Tassios, "Solid waste plasma gasification: Equilibrium model development and exergy analysis," *Energy Convers. Manag.*, vol. 47, no. 13–14, pp. 1723–1737, 2006.
- [34] Q. Zhang, L. Dor, A. K. Biswas, W. Yang, and W. Blasiak, "Modeling of steam plasma gasification for municipal solid waste," *Fuel Process. Technol.*, vol. 106, pp. 546–554, 2013.
- [35] Q. Zhang, L. Dor, W. Yang, and W. Blasiak, "Eulerian model for municipal

- solid waste gasification in a fixed-bed plasma gasification melting reactor,” *Energy and Fuels*, vol. 25, no. 9, pp. 4129–4137, 2011.
- [36] J. M. Zurada, *Introduction to artificial neural systems*, vol. 8. West publishing company St. Paul, 1992.
- [37] G. Xiao, M. jiang Ni, Y. Chi, B. Jin, R. Xiao, Z. Zhong, and Y. Huang, “Gasification characteristics of MSW and an ANN prediction model,” *Waste Manag.*, vol. 29, no. 1, pp. 240–244, 2009.
- [38] L. Broadbelt, S. Stark, and M. Klein, “Computer generated reaction modelling: decomposition and encoding algorithms for determining species uniqueness,” *Comput. Chem. Eng.*, vol. 20, no. 2, pp. 113–129, 1996.
- [39] L. J. Broadbelt, S. M. Stark, and M. T. Klein, “Computer Generated Pyrolysis Modeling: On-the-Fly Generation of Species, Reactions, and Rates,” *Ind. Eng. Chem. Res.*, vol. 33, no. 4, pp. 790–799, Apr. 1994.
- [40] W. Wei, C. A. Bennett, R. Tanaka, G. Hou, M. T. J. Klein, and M. T. Klein, “Computer aided kinetic modeling with KMT and KME,” *Fuell Process. Technol.*, vol. 89, p. 350, 2008.
- [41] M. T. Klein, G. Hou, R. J. Quann, W. Wei, K. H. Liao, R. S. H. Yang, J. a Campain, M. a Mazurek, and L. J. Broadbelt, “BioMOL: a computer-assisted biological modeling tool for complex chemical mixtures and biological processes at the molecular level.,” *Environ. Health Perspect.*, vol. 110 Suppl , pp. 1025–9, Dec. 2002.
- [42] M. T. Klein, G. Hou, R. J. Bertolacini, L. J. Broadbelt, and A. Kumar, *Molecular Modeling in Heavy Hydrocarbon Conversions*. Boca Raton, FL: Taylor and Francis Group, 2006.
- [43] Z. Hou, “Software Tools for Molecule-based Kinetic Modeling of Complex Systems,” Rutgers University, 2011.
- [44] C. A. Bennett, “User-Controlled Kinetic Network Generation with INGen,” Rutgers University, 2009.
- [45] B. M. Moreno, “Thermochemical Conversion of Biomass: Models and Modelling Approaches,” University of Delaware, 2014.
- [46] L. Zhang, Z. Hou, S. R. Horton, M. T. Klein, Q. Shi, S. Zhao, and C. Xu, “Molecular Representation of Petroleum Vacuum Resid,” *Energy & Fuels*, vol. 28, pp. 1736–1749, Mar. 2014.

- [47] S. Horton and M. Klein, "Reaction and Catalyst Families in the Modeling of Coal and Biomass Hydroprocessing Kinetics," *Energy & Fuels*, vol. 28, no. 2013, pp. 37–40, 2013.
- [48] S. R. Horton, Z. Hou, B. M. Moreno, C. A. Bennett, and M. T. Klein, "Molecule-based modeling of heavy oil," *Sci. China Chem.*, vol. 56, no. 7, pp. 840–847, Jun. 2013.
- [49] I. Mochida and Y. Yoneda, "Linear free energy relationships in heterogeneous catalysis: II. Dealkylation and isomerization reactions on various solid acid catalysts," *J. Catal.*, vol. 7, pp. 393–396, 1967.
- [50] C. Read, "Reactor and Catalyst Structure/function Relationships in the Hydrocracking of Alkyl-substituted Biphenyl Compounds," University of Delaware, 1995.
- [51] M. Evans and M. Polanyi, "Some applications of the transition state method to the calculation of reaction velocities, especially in solution," *Trans. Faraday Soc.*, 1935.
- [52] R. Bell, "The theory of reactions involving proton transfers," *Proc. R. Soc. London. Ser. A*, 1936.
- [53] K. Radhakrishnan and A. Hindmarsh, "Description and use of LSODE, the Livermore solver for ordinary differential equations," NASA, 1993.
- [54] S. R. Horton, J. Woekener, R. J. Mohr, Y. Zhang, F. P. Petrocelli, and M. T. Klein, "Molecular-Level Kinetic Modeling of the Gasification of Common Plastics," *Energy Fuels (In Press.)*, 2015.
- [55] T. M. Kruse, O. S. Woo, H.-W. Wong, S. S. Khan, and L. J. Broadbelt, "Mechanistic Modeling of Polymer Degradation: A Comprehensive Study of Polystyrene," *Macromolecules*, vol. 35, no. 20, pp. 7830–7844, Sep. 2002.
- [56] T. M. Kruse, O. Sang Woo, and L. J. Broadbelt, "Detailed mechanistic modeling of polymer degradation: application to polystyrene," *Chem. Eng. Sci.*, vol. 56, no. 3, pp. 971–979, Feb. 2001.
- [57] D. M. Matheu and J. M. Grenda, "A systematically generated, pressure-dependent mechanism for high-conversion ethane pyrolysis. 1. Pathways to the minor products," *J. Phys. Chem. A*, vol. 109, no. 24, pp. 5332–5342, 2005.
- [58] T. Faravelli, G. Bozzano, M. Colombo, E. Ranzi, and M. Dente, "Kinetic modeling of the thermal degradation of polyethylene and polystyrene

- mixtures,” *J. Anal. Appl. Pyrolysis*, vol. 70, no. 2, pp. 761–777, 2003.
- [59] E. Henrich, S. Bürkle, Z. I. Meza-Renken, and S. Rumpel, “Combustion and gasification kinetics of pyrolysis chars from waste and biomass,” *J. Anal. Appl. Pyrolysis*, vol. 49, no. 1, pp. 221–241, 1999.
- [60] X. H. Du, C. S. Zhao, Y. Z. Wang, Q. Zhou, Y. Deng, M. H. Qu, and B. Yang, “Thermal oxidative degradation behaviours of flame-retardant thermotropic liquid crystal copolyester/PET blends,” *Mater. Chem. Phys.*, vol. 98, no. 1, pp. 172–177, 2006.
- [61] P. J. Flory, *Principles of Polymer Chemistry*. New York: Cornell, 1953.
- [62] Kirk-Othmer, *Kirk-Othmer Encyclopedia of Chemical Technology*, vol. 24. 1997.
- [63] J. M. Heikkinen, J. C. Hordijk, W. De Jong, and H. Spliethoff, “Thermogravimetry as a tool to classify waste components to be used for energy generation,” *J. Anal. Appl. Pyrolysis*, vol. 71, no. 2, pp. 883–900, 2004.
- [64] H. M. Zhu, X. G. Jiang, J. H. Yan, Y. Chi, and K. F. Cen, “TG-FTIR analysis of PVC thermal degradation and HCl removal,” *J. Anal. Appl. Pyrolysis*, vol. 82, no. 1, pp. 1–9, 2008.
- [65] C. Bouster, P. Vermande, and J. Veron, “Evolution of the product yield with temperature and molecular weight in the pyrolysis of polystyrene,” *J. Anal. Appl. Pyrolysis*, vol. 15, pp. 249–259, 1989.
- [66] C. M. Stafford, T. P. Russell, and T. J. McCarthy, “Expansion of polystyrene using supercritical carbon dioxide: effects of molecular weight, polydispersity, and low molecular weight components,” *Macromolecules*, vol. 32, no. 22, pp. 7610–7616, 1999.
- [67] Y. Liu, J. Qian, and J. Wang, “Pyrolysis of polystyrene waste in a fluidized-bed reactor to obtain styrene monomer and gasoline fraction,” *Fuel Process. Technol.*, vol. 63, no. 1, pp. 45–55, 2000.
- [68] N. Grassie and G. Scott, *Polymer Degradation and Stabilisation*. Great Britain: Press Syndicate of the University of Cambridge, 1985.
- [69] J. D. Peterson, S. Vyazovkin, and C. A. Wight, “Kinetics of the Thermal and Thermo-Oxidative Degradation of Polystyrene, Polyethylene and Poly(propylene),” *Macromol. Chem. Phys.*, vol. 202, no. 6, p. 775, 2001.

- [70] G. Montaudo, C. Puglisi, and F. Samperi, "Primary thermal degradation mechanisms of PET and PBT," *Polymer Degradation and Stability*, vol. 42, no. 1, pp. 13–28, 1993.
- [71] L. H. Buxbaum, "The Degradation of Poly(ethylene terephthalate)," *Angew. Chemie Int. Ed.*, vol. 7, no. 3, p. 182, 1968.
- [72] B. B. Troitskii, L. S. Troitskaya, V. N. Myakov, and A. F. Lepaev, "Mechanism of the thermal degradation of poly(vinyl chloride)," *J. Polym. Sci.*, vol. 1361, no. 42, pp. 1347–1361, 1973.
- [73] Y. Tsuchiya and K. Sumi, "Thermal decomposition products of poly(vinyl alcohol)," *J. Polym. Sci. Part A-1 Polym. Chem.*, 1969.
- [74] B. M. Moreno, N. Li, J. Lee, G. W. Huber, and M. T. Klein, "Modeling aqueous-phase hydrodeoxygenation of sorbitol over Pt/SiO₂-Al₂O₃," *RSC Adv.*, vol. 3, no. 45, p. 23769, 2013.
- [75] J. Zhang, Q. Ji, P. Zhang, Y. Xia, and Q. Kong, "Thermal stability and flame-retardancy mechanism of poly(ethylene terephthalate)/boehmite nanocomposites," *Polym. Degrad. Stab.*, vol. 95, no. 7, pp. 1211–1218, 2010.
- [76] X. H. Du, Y. Z. Wang, X. T. Chen, and X. D. Tang, "Properties of phosphorus-containing thermotropic liquid crystal copolyester/poly(ethylene terephthalate) blends," *Polym. Degrad. Stab.*, vol. 88, no. 1, pp. 52–56, 2005.
- [77] J. Zhang, Q. Ji, P. Zhang, Y. Xia, and Q. Kong, "Thermal stability and flame-retardancy mechanism of poly(ethylene terephthalate)/boehmite nanocomposites," *Polym. Degrad. Stab.*, vol. 95, no. 7, pp. 1211–1218, 2010.
- [78] V. Cozzani, C. Nicolella, M. Rovatti, and L. Tognotti, "Influence of Gas-Phase Reactions on the Product Yields Obtained in the Pyrolysis of Polyethylene," *Ind. Eng. Chem. Res.*, vol. 36, no. 2, pp. 342–348, 1997.
- [79] V. Cozzani, "Characterization of coke formed in the pyrolysis of polyethylene," *Ind. Eng. Chem. Res.*, vol. 36, pp. 5090–5095, 1997.
- [80] C. A. Bennett and M. T. Klein, "Using Mechanistically Informed Pathways to Control the Automated Growth of Reaction Networks," *Energy & Fuels*, vol. 26, no. 1, pp. 41–51, Jan. 2012.
- [81] F. Bustamante, R. M. Enick, R. P. Killmeyer, B. H. Howard, K. S. Rothenberger, a. V. Cugini, B. D. Morreale, and M. V. Ciocco, "Uncatalyzed and wall-catalyzed forward water-gas shift reaction kinetics," *AIChE J.*, vol. 51,

no. 5, pp. 1440–1454, May 2005.

- [82] M. J. P. Slapak, J. M. N. Van Kasteren, and B. a a H. Drinkenburg, “Hydrothermal Recycling of PVC in a Bubbling Fluidized Bed Reactor : the Influence of Bed Material and Temperature,” *Polym. Adv. Technol.*, vol. 602, pp. 596–602, 1999.
- [83] S. R. Horton, R. J. Mohr, Y. Zhang, F. P. Petrocelli, and M. T. Klein, “Molecular-Level Kinetic Modeling of Biomass Gasification,” *Energy & Fuels*, p. acs.energyfuels.5b01988, 2015.
- [84] T. L. Richard, “Challenges in scaling up biofuels infrastructure.,” *Science*, vol. 329, pp. 793–796, 2010.
- [85] H. . Chagger, a Kendall, a McDonald, M. Pourkashanian, and a Williams, “Formation of dioxins and other semi-volatile organic compounds in biomass combustion,” *Appl. Energy*, vol. 60, no. 2, pp. 101–114, 1998.
- [86] D. K. Shen, S. Gu, K. H. Luo, a. V. Bridgwater, and M. X. Fang, “Kinetic study on thermal decomposition of woods in oxidative environment,” *Fuel*, vol. 88, no. 6, pp. 1024–1030, Jun. 2009.
- [87] M. Broström, a. Nordin, L. Pommer, C. Branca, and C. Di Blasi, “Influence of torrefaction on the devolatilization and oxidation kinetics of wood,” *J. Anal. Appl. Pyrolysis*, vol. 96, pp. 100–109, Jul. 2012.
- [88] L. Zhong and W. Mei, “Kinetic Model Establishment and Verfication of the Biomass Gasificaiton on Fluidized Bed,” no. July, pp. 12–15, 2009.
- [89] N. Prakash and T. Karunanithi, “Kinetic Modeling in Biomass Pyrolysis – A Review,” vol. 4, no. 12, pp. 1627–1636, 2008.
- [90] D. M. Grant, R. J. Pugmire, T. H. Fletcher, and A. R. Kerstein, “Chemical model of coal devolatilization using percolation lattice statistics,” *Energy & Fuels*, vol. 3, no. 2, pp. 175–186, Mar. 1989.
- [91] T. H. Fletcher, A. R. Kerstein, R. J. Pugmire, M. S. Solum, and D. M. Grant, “Chemical Percolation Model for Devolatilization . 3 . Direct Use of 13C NMR Data To Predict Effects of Coal Type,” no. 10, pp. 414–431, 1992.
- [92] T. H. Fletcher, A. R. Kerstein, R. J. Pugmire, and D. M. Grant, “Chemical Percolation Model for Devolatilization. 2. Temperature and Heating Rate Effects on Product YieMst,” no. 1, pp. 54–60, 1990.

- [93] T. H. Fletcher, H. R. Pond, J. Webster, J. Wooters, and L. L. Baxter, "Prediction of tar and light gas during pyrolysis of black liquor and biomass," *Energy and Fuels*, vol. 26, no. 6, pp. 3381–3387, 2012.
- [94] A. D. Lewis and T. H. Fletcher, "Prediction of sawdust pyrolysis yields from a flat-flame burner using the CPD model," *Energy and Fuels*, vol. 27, pp. 942–953, 2013.
- [95] C. Sheng and J. L. T. Azevedo, "Modeling biomass devolatilization using the chemical percolation devolatilization model for the main components," *Proc. Combust. Inst.*, vol. 29, no. 1, pp. 407–414, 2002.
- [96] D. Fiaschi and M. Michelini, "A two-phase one-dimensional biomass gasification kinetics model," *Biomass and Bioenergy*, vol. 21, pp. 121–132, 2001.
- [97] R. Pettersen, "The chemical composition of wood," *Chem. solid wood*, 1984.
- [98] D. K. Shen, S. Gu, and a. V. Bridgwater, "Study on the pyrolytic behaviour of xylan-based hemicellulose using TG–FTIR and Py–GC–FTIR," *J. Anal. Appl. Pyrolysis*, vol. 87, no. 2, pp. 199–206, Mar. 2010.
- [99] A. C. C. Chang, H.-F. Chang, F.-J. Lin, K.-H. Lin, and C.-H. Chen, "Biomass gasification for hydrogen production," *Int. J. Hydrogen Energy*, vol. 36, no. 21, pp. 14252–14260, Oct. 2011.
- [100] C. Couhert, J.-M. Commandré, and S. Salvador, "Failure of the component additivity rule to predict gas yields of biomass in flash pyrolysis at 950°C," *Biomass and Bioenergy*, vol. 33, no. 2, pp. 316–326, Feb. 2009.
- [101] C. Couhert, J.-M. Commandre, and S. Salvador, "Is it possible to predict gas yields of any biomass after rapid pyrolysis at high temperature from its composition in cellulose, hemicellulose and lignin?," *Fuel*, vol. 88, no. 3, pp. 408–417, Mar. 2009.
- [102] K. Freudenberg, "Lignin: Its Constitution and Formation from p-Hydroxycinnamyl Alcohols: Lignin is duplicated by dehydrogenation of these alcohols; intermediates explain formation and structure.," *Science*, vol. 148, pp. 595–600, 1965.
- [103] A. Tejado, C. Peña, J. Labidi, J. M. Echeverria, and I. Mondragon, "Physico-chemical characterization of lignins from different sources for use in phenol-formaldehyde resin synthesis.," *Bioresour. Technol.*, vol. 98, no. 8, pp. 1655–63, May 2007.

- [104] R. El Hage, N. Brosse, L. Chrusciel, C. Sanchez, P. Sannigrahi, and A. Ragauskas, "Characterization of milled wood lignin and ethanol organosolv lignin from miscanthus," *Polym. Degrad. Stab.*, vol. 94, no. 10, pp. 1632–1638, Oct. 2009.
- [105] A. Demirbas, "Products from Lignocellulosic Materials via Degradation Processes," *Energy Sources, Part A Recover. Util. Environ. Eff.*, vol. 30, no. 1, pp. 27–37, Nov. 2007.
- [106] F. Shafizadeh, R. H. Furneaux, T. G. Cochran, J. P. Scholl, and Y. Sakai, "Production of levoglucosan and glucose from pyrolysis of cellulosic materials," *J. Appl. Polym. Sci.*, vol. 23, no. 12, pp. 3525–3539, Jun. 1979.
- [107] P. J. Linstrom and W. G. Mallard, "NIST Chemistry WebBook, NIST Standard Reference Database Number 69," 2015. [Online]. Available: <http://webbook.nist.gov>.
- [108] W. F. DeGroot and G. N. Richards, "Relative rates of carbon gasification in oxygen, steam and carbon dioxide," *Carbon N. Y.*, vol. 27, no. 2, pp. 247–252, 1989.
- [109] S. R. Horton, L. Zhang, Z. Hou, C. a. Bennett, M. T. Klein, and S. Zhao, "Molecular-Level Kinetic Modeling of Resid Pyrolysis," *Ind. Eng. Chem. Res.*, vol. 54, no. 16, pp. 4226–4235, 2015.
- [110] G. Löffler, V. J. Wargadalam, and F. Winter, "Catalytic effect of biomass ash on CO, CH₄ and HCN oxidation under fluidised bed combustor conditions," *Fuel*, vol. 81, pp. 711–717, 2002.
- [111] B. W. Mosher, P. M. Czepiel, and R. Harriss C., "Methane Emissions at Nine Landfill Sites in the Northeastern United States," *Environ. Sci. Technol.*, vol. 33, no. 12, p. 2088, 1999.
- [112] WRAP, "Comparing the cost of alternative waste treatment options," 2012.
- [113] N. J. Themelis, M. J. Castaldi, J. Bhatti, and L. Arsova, "Energy and Economic Value of Non-recycled Plastics (NRP) and Municipal Solid Wastes (MSW) that are Currently Landfilled in the Fifty States."
- [114] P. L. Walker, R. L. Taylor, and J. M. Ranish, "An update on the carbon-oxygen reaction," *Carbon N. Y.*, vol. 29, no. 3, pp. 411–421, Jan. 1991.
- [115] R. Hurt and J. Calo, "Semi-global intrinsic kinetics for char combustion modeling," *Combust. Flame*, vol. 2180, no. 01, 2001.

- [116] B. Feng and S. K. Bhatia, "On the validity of thermogravimetric determination of carbon gasification kinetics," *Chem. Eng. Sci.*, vol. 57, no. 15, pp. 2907–2920, 2002.
- [117] S. Ergun, "Kinetics of the Reaction of Carbon Dioxide with Carbon," *Phys. Chem.*, vol. 60, pp. 480–485, 1940.
- [118] K. Hüttinger and O. Fritz, "The carbon-carbon dioxide reaction: an extended treatment of the active-site concept," *Carbon N. Y.*, vol. 2, no. 4, 1991.
- [119] J. Leppälähti and T. Koljonen, "Nitrogen evolution from coal, peat and wood during gasification: Literature review," *Fuel Process. Technol.*, vol. 43, 1995.
- [120] J. R. Arthur, "Reactions between Carbon and Oxygen," *Trans. Faraday Soc.*, vol. 47, pp. 164–178, 1951.
- [121] "chap8@Cupola_HB.pdf," in *Cupola Handbook*, 1997, pp. 8–1 – 8–37.
- [122] E. J. Swain, "Sulfur, coke, and crude quality -- Conclusion: US crude slate continues to get heavier, higher in sulfur," *Oil Gas J.*, vol. 93, no. 2, p. 37, 1995.
- [123] W. I. Beaton and R. J. Bertolacini, "Resid Hydroprocessing at Amoco," *Catalysis Reviews*, vol. 33, pp. 281–317, 1991.
- [124] R. P. Rodgers and A. M. McKenna, "Petroleum Analysis," *Anal. Chem.*, vol. 83, p. 4665, 2011.
- [125] M. Neurock, C. Libanati, A. Nigam, and M. Klein, "Monte Carlo simulation of complex reaction systems: Molecular structure and reactivity in modelling heavy oils," *Chem. Eng. Sci.*, vol. 45, no. 8, pp. 2083–2088, 1990.
- [126] R. Rueda-Velásquez and M. Gray, "Monte Carlo simulation of asphaltenes and products from thermal cracking," *Energy & Fuels*, vol. 28, pp. 2352–2364, 2014.
- [127] L. P. de Oliveira, J. J. Verstraete, and M. Kolb, "Simulating vacuum residue hydroconversion by means of Monte-Carlo techniques," *Catal. Today*, vol. 220–222, pp. 208–220, Mar. 2014.
- [128] R. Quann and S. Jaffe, "Structure-oriented lumping: describing the chemistry of complex hydrocarbon mixtures," *Ind. Eng. Chem. Res.*, pp. 2483–2497, 1992.
- [129] L. Tian, B. Shen, and J. Liu, "A Delayed Coking Model Built Using the Structure-Oriented Lumping Method," *Energy & Fuels*, vol. 26, no. 3, pp.

1715–1724, Mar. 2012.

- [130] L. Zhang, “Molecular-Level Characterization and Process Modeling for Heavy Petroleum Fractions,” China University of Petroleum, 2014.
- [131] L. Nationai, “Description and Use of LSODE , the Livermore Solver for Ordinary Differential Equations,” 1993.
- [132] E. R. Gansner and S. C. North, “An open graph visualization system and its applications to software engineering,” *Softw. Pract. Exp.*, vol. 30, no. 11, pp. 1203–1233, 2000.
- [133] Z. Gao, I. Amasaki, and M. Nakada, “A thermogravimetric study on thermal degradation of polyethylene,” *J. Anal. Appl. Pyrolysis*, vol. 67, no. 1, pp. 1–9, Mar. 2003.
- [134] S. W. Benson and J. H. Buss, “Additivity Rules for the Estimation of Molecular Properties. Thermodynamic Properties,” *J. Chem. Phys.*, vol. 29, no. 3, p. 546, 1958.
- [135] W. S. Kmak, “A Kinetic simulation model of the powerforming process,” in *AICHE National Meeting*, 1971.
- [136] M. P. Ramage, K. R. Graziani, P. H. Schipper, F. J. Krambeck, and B. C. Choi, “Kinptr (Mobil’s Kinetic Reforming Model): A Review Of Mobil’s Industrial Process Modeling Philosophy,” *Adv. Chem. Eng.*, vol. 13, no. C, pp. 193–266, 1987.
- [137] W. S. Kmak and A. N. J. Stuckey, “Powerforming process studies with a kinetic simulation model,” in *AICHE National Meeting*, 1973.
- [138] G. F. Froment, “Fundamental kinetic modeling of catalytic hydrocarbon conversion processes,” *Rev. Chem. Eng.*, vol. 29, no. 6, pp. 385–412, 2013.
- [139] M. Z. Stijepovic, A. Vojvodic-Ostojic, I. Milenkovic, and P. Linke, “Development of a Kinetic Model for Catalytic Reforming of Naphtha and Parameter Estimation Using Industrial Plant Data,” *Energy & Fuels*, vol. 23, no. 2, pp. 979–983, 2009.
- [140] W. Wei, C. A. Bennett, R. Tanaka, G. Hou, and M. T. Klein, “Detailed kinetic models for catalytic reforming,” *Fuel Process. Technol.*, vol. 89, no. 4, pp. 344–349, 2008.
- [141] H. Kumar and G. F. Froment, “Mechanistic kinetic modeling of the

- hydrocracking of complex feedstocks, such as vacuum gas oils,” *Ind. Eng. Chem. Res.*, vol. 46, no. 18, pp. 5881–5897, 2007.
- [142] S. R. Horton, L. Zhang, Z. Hou, C. a. Bennett, M. T. Klein, and S. Zhao, “Molecular-Level Kinetic Modeling of Resid Pyrolysis,” *Ind. Eng. Chem. Res.*, vol. 54, no. 16, pp. 4226–4235, 2015.
- [143] M. Adahchour, J. Beens, and U. A. T. Brinkman, “Recent developments in the application of comprehensive two-dimensional gas chromatography,” *J. Chromatogr. A*, vol. 1186, no. 1–2, pp. 67–108, 2008.
- [144] C. Vendevre, F. Bertoncini, D. Espinat, D. Thiébaud, and M. C. Hennion, “Multidimensional gas chromatography for the detailed PIONA analysis of heavy naphtha: Hyphenation of an olefin trap to comprehensive two-dimensional gas chromatography,” *J. Chromatogr. A*, vol. 1090, no. 1–2, pp. 116–125, 2005.

Appendix

PUBLISHED WORK COPYRIGHT CLEARANCE PERMISSIONS

The following screenshots give the RightsLink permissions for the first-author publications included in this dissertation. The order of the screenshots is in the order of appearance of the published work.

The screenshot shows the RightsLink interface for ACS Publications. At the top left is the Copyright Clearance Center logo. The main header includes the RightsLink logo and navigation buttons for Home, Create Account, Help, and Live Chat. Below the header, the ACS Publications logo is displayed with the tagline 'Most Trusted. Most Cited. Most Read.' The article details are as follows:

- Title:** Reaction and Catalyst Families in the Modeling of Coal and Biomass Hydroprocessing Kinetics
- Author:** Scott R. Horton, Michael T. Klein
- Publication:** Energy & Fuels
- Publisher:** American Chemical Society
- Date:** Jan 1, 2014

Below the article details is a 'Quick Price Estimate' section with a red text box containing the following permission text: 'Permission for this particular request is granted for print and electronic formats, and translations, at no charge. Figures and tables may be modified. Appropriate credit should be given. Please print this page for your records and provide a copy to your publisher. Requests for up to 4 figures require only this record. Five or more figures will generate a printout of additional terms and conditions. Appropriate credit should read: "Reprinted with permission from {COMPLETE REFERENCE CITATION}. Copyright {YEAR} American Chemical Society." Insert appropriate information in place of the capitalized words.'

Figure A.1: RightsLink permission obtained from ACS for reproduced work published by author[47].

Copyright Clearance Center RightsLink[®] Home Create Account Help

ACS Publications Most Trusted. Most Cited. Most Read.

Title: Molecular-Level Kinetic Modeling of the Gasification of Common Plastics
Author: Scott R. Horton, James Woeckener, Rebecca Mohr, et al
Publication: Energy & Fuels
Publisher: American Chemical Society
Date: Nov 1, 2015
 Copyright © 2015, American Chemical Society

LOGIN
 If you're a copyright.com user, you can login to RightsLink using your copyright.com credentials. Already a RightsLink user or want to learn more?

Quick Price Estimate

Permission for this particular request is granted for print and electronic formats, and translations, at no charge. Figures and tables may be modified. Appropriate credit should be given. Please print this page for your records and provide a copy to your publisher. Requests for up to 4 figures require only this record. Five or more figures will generate a printout of additional terms and conditions. Appropriate credit should read: "Reprinted with permission from { COMPLETE REFERENCE CITATION }. Copyright {YEAR} American Chemical Society." Insert appropriate information in place of the capitalized words.

Figure A.2: RightsLink permission obtained from ACS for reproduced work published by author[54].

Copyright Clearance Center RightsLink[®] Home Create Account Help Live Chat

ACS Publications Most Trusted. Most Cited. Most Read.

Title: Molecular-Level Kinetic Modeling of Biomass Gasification
Author: Scott R. Horton, Rebecca J. Mohr, Yu Zhang, et al
Publication: Energy & Fuels
Publisher: American Chemical Society
Date: Nov 1, 2015
 Copyright © 2015, American Chemical Society

LOGIN
 If you're a copyright.com user, you can login to RightsLink using your copyright.com credentials. Already a RightsLink user or want to learn more?

PERMISSION/LICENSE IS GRANTED FOR YOUR ORDER AT NO CHARGE

This type of permission/license, instead of the standard Terms & Conditions, is sent to you because no fee is being charged for your order. Please note the following:

- Permission is granted for your request in both print and electronic formats, and translations.
- If figures and/or tables were requested, they may be adapted or used in part.
- Please print this page for your records and send a copy of it to your publisher/graduate school.
- Appropriate credit for the requested material should be given as follows: "Reprinted (adapted) with permission from (COMPLETE REFERENCE CITATION). Copyright (YEAR) American Chemical Society." Insert appropriate information in place of the capitalized words.
- One-time permission is granted only for the use specified in your request. No additional uses are granted (such as derivative works or other editions). For any other uses, please submit a new request.

Figure A.3: RightsLink permission obtained from ACS for reproduced work published by author[83].

Copyright Clearance Center **RightsLink** Home Create Account Help Live Chat

ACS Publications **Title:** Molecular-Level Kinetic Modeling of Resid Pyrolysis
Author: Scott R. Horton, Linzhou Zhang, Zhen Hou, et al
Publication: Industrial & Engineering Chemistry Research
Publisher: American Chemical Society
Date: Apr 1, 2015
 Copyright © 2015, American Chemical Society

LOG IN
 If you're a copyright.com user, you can login to RightsLink using your copyright.com credentials. Already a RightsLink user or want to learn more?

PERMISSION/LICENSE IS GRANTED FOR YOUR ORDER AT NO CHARGE

This type of permission/license, instead of the standard Terms & Conditions, is sent to you because no fee is being charged for your order. Please note the following:

- Permission is granted for your request in both print and electronic formats, and translations.
- If figures and/or tables were requested, they may be adapted or used in part.
- Please print this page for your records and send a copy of it to your publisher/graduate school.
- Appropriate credit for the requested material should be given as follows: "Reprinted (adapted) with permission from (COMPLETE REFERENCE CITATION). Copyright (YEAR) American Chemical Society." Insert appropriate information in place of the capitalized words.
- One-time permission is granted only for the use specified in your request. No additional uses are granted (such as derivative works or other editions). For any other uses, please submit a new request.

Figure A.4: RightsLink permission obtained from ACS for reproduced work published by author[109].